Summary

The miniaturization of microwave components is one of the challenges of present and future communication devices. For this reason, this thesis is focused on the study of new miniaturization strategies for planar non-radiating microwave components. Throughout this work, different miniaturization approaches have been applied to the design of several microwave components such as multi-band devices and filters, including also electronically tunable implementations.

To obtain the required compact sizes and/or multi-band functionality, new artificial lines based on the semi-lumped open split ring resonators (OSRRs) and open complementary split ring resonators (OCSRRs) are proposed. Firstly, composite right-left handed (CRLH) transmission lines are presented, applying such lines to the design of dual-band impedance inverters and Y-junction power dividers, as well as wideband band pass filters. In addition, by combining these resonators with additional semi-lumped components, extended composite right-left handed (E-CRLH) transmission lines are also reported and applied to implement quad-band impedance inverters, power dividers, branch-line couplers and dual-band band pass filters. To demonstrate and validate its functionality, different proof-of-concept demonstrators for all the aforementioned devices are implemented and fabricated, where a good agreement between simulations and measurement is obtained. Furthermore, the circuit models and the design methodology for all the presented devices are also reported, based on a parameter extraction method. Through this method it is demonstrated that the circuit models provide an accurate description of the considered structures.

The tunability of such CRLH lines is also analyzed by means of barium-strontium-titanate (BST) thick-films. With this approach, a tunable CRLH line with simulated and measured tunability range of 36.6% is demonstrated. Once this approach is experimentally validated, the previously presented mono-band and dual-band components based on the CRLH lines are provided with this tunability, exploring both its methodology and limitations.

Finally, new compact filters with sharp responses are also presented based on stepped-impedance-resonators (SIRs) coupled to coplanar waveguide (CPW) host transmission lines. After analyzing the isolated resonator and its circuit model, elliptic-type low pass and high pass filters, as well as band pass filters with transmission zeros are designed through the conventional filter theory, where a high-degree of compactness as well as good performance is demonstrated.

M. Durán-Sindreu   Miniaturization of Planar Microwave Components Based on Semi-Lumped Elements and Artificial Transmission Lines

UAB CEI
CAMPUS OF INTERNATIONAL EXCELLENCE

Miniaturization of Planar Microwave Components Based on Semi-Lumped Elements and Artificial Transmission Lines

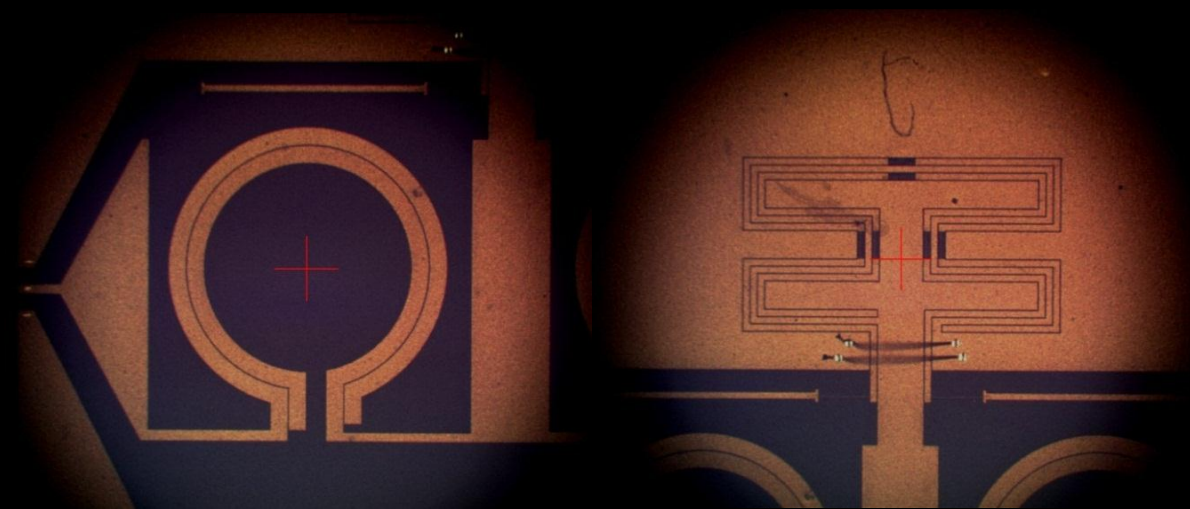## Application to Multi-Band Devices and Filters

Ph.D. Thesis written by:

Miguel Durán-Sindreu Viader

Advisors:

Ferran Martín Antolín

Jordi Bonache Albacete

UAB

Universitat Autònoma de Barcelona

Miniaturization of Planar Microwave Components Based on Semi-Lumped Elements and Artificial Transmission Lines: Application to Multi-Band Devices and Filters

Ph.D. Thesis written by

Miguel Durán-Sindreu Viader

Under the supervision of

Ferran Martín Antolín

and

Jordi Bonache Albacete

Bellaterra (Cerdanyola del Vallès), July 2011

The undersigned, Prof. **Ferran Martín Antolín** and Dr. **Jordi Bonache Albacete**,
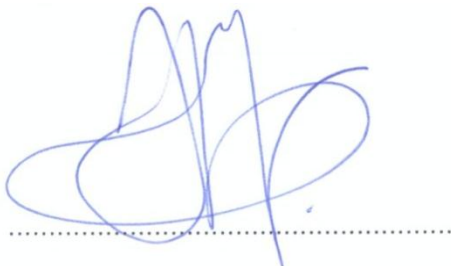
Professors of the Electronic Engineering Department (Engineering School) of the *Universitat Autònoma de Barcelona*,
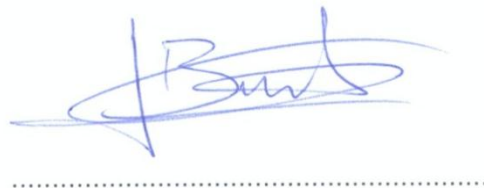
CERTIFY:

That the thesis entitled "*Miniaturization of Planar Microwave Components Based on Semi-Lumped Elements and Artificial Transmission Lines: Application to Multi-Band Devices and Filters*" has been written by **Miguel Durán-Sindreu Viader** under their supervision.

And hereby to acknowledge the above, sign the present.

Signature: Ferran Martín Antolín   **Signature:** Jordi Bonache Albacete

....

Bellaterra, July 4th 2011.

Contents

Acknowledgements

The present work was possible thanks to the many people who helped me during these last years, and hence this also belongs in part to them.

I would like to give special thanks to my supervisors, Ferran Martín and Jordi Bonache, for their constant guidance, help and never-ending novel ideas. I also want to thank the people from GEMMA/CIMITEC, the Electronic Engineering Department and the Engineering School, who supported me and provided me with so many laughs and good times. In addition, I would like to thank all the friends and colleagues who I met during my placement in the Microwave Engineer Group at the *Technishe Universität Darmstadt*, and who I will never forget: *danke, dass ich mich bei Euch in Darmstadt wie zu Hause fühlen konnte!!.*

Of course, I also want to express my gratitude to those people who, by being so separate from my research field, helped me with the most basic and important things. Thanks to my family (including the new members: *¡Alex esto va por ti!*) and friends.

And last but not least, this is also a tribute to the person who knows the pains of this thesis better than I: *gracias Débora*.

Summary

The miniaturization of microwave components is one of the challenges of present and future communication devices. For this reason, this thesis is focused on the study of new miniaturization strategies for planar non-radiating microwave components. Throughout this work, different miniaturization approaches have been applied to the design of several microwave components such as multi-band devices and filters, including also electronically tunable implementations.

To obtain the required compact sizes and/or multi-band functionality, new artificial lines based on the semi-lumped open split ring resonators (OSRRs) and open complementary split ring resonators (OCSRRs) are proposed. Firstly, composite right-/left-handed (CRLH) transmission lines are presented, applying such lines to the design of dual-band impedance inverters and Y-junction power dividers, as well as wideband band-pass filters. In addition, by combining these resonators with additional semi-lumped components, extended composite right-/left-handed (E-CRLH) transmission lines are also reported and applied to implement quad-band impedance inverters, power dividers, branch-line couplers and dual-band band-pass filters. To demonstrate and validate its functionality, different proof-of-concept demonstrators for all the aforementioned devices are implemented and fabricated, where a good agreement between simulations and measurement is obtained. Furthermore, the circuit models and the design methodology for all the presented devices are also reported, based on a parameter extraction method. Through this method it is demonstrated that the circuit models provide an accurate description of the considered structures.

SUMMARY

The tunability of such CRLH lines is also analyzed by means of barium-strontium-titanate (BST) thick-films. With this approach, a tunable CRLH line with simulated and measured tunability range of 36.6% is demonstrated. Once this approach is experimentally validated, the previously presented mono-band and dual-band components based on the CRLH lines are provided with this tunability, exploring both its methodology and limitations.

Finally, new compact filters with sharp responses are also presented based on stepped-impedance-resonators (SIRs) coupled to coplanar waveguide (CPW) host transmission lines. After analyzing the isolated resonator and its circuit model, elliptic-type low-pass and high-pass filters, as well as band-pass filters with transmission zeros are designed through the conventional filter theory, where a high-degree of compactness as well as good performance is demonstrated.

CHAPTER 1

Motivation and objectives

The information society is an ever-expanding community. As society evolves, so does technology, re-defining how people communicate with each other using cell phones, Global Positioning System (GPS) receivers, satellites, personal computing, radio, television or high-speed Internet, among other devices. In fact, even these concepts are also being constantly re-defined, with most of the aforementioned applications now available in one single device, able to make a phone call, browse the web or even know its geolocation at the same time.

Thus, this work arises from the need to study new strategies for the miniaturization of communication components, in order to meet the requirements of these upcoming devices, as well as the all-in-one device merging trend. Specifically, this thesis is focused on the design of planar passive non-radiative elements present in common transceivers, focusing on power dividers, couplers and filters.

This desired size reduction can be obtained either by miniaturizing each component or by providing the component with multi-band functionality, hence reducing the total

number of elements in the device. Moreover, the multi-band functionality can also be obtained with tunable structures, since they can adapt to the environmental changes or to the application requirements.

Throughout this work, all the aforementioned options will be examined, mainly considering for this purpose the recently appeared approach based on the metamaterials theory. By means of these new concepts, additional or enhanced functionality and performance can be provided to state of the art components. In particular, this thesis will analyze the implementation of metamaterial inspired devices by means of the semi-lumped resonators open split ring resonators (OSRRs) and open complementary split ring resonators (OCSRRs). However, other non-metamaterial based components, such as stepped-impedance-resonators (SIRs), will be considered as a way of achieving size reduction, and will be applied to the design of planar elliptic or quasi-elliptic filters. Therefore, the outline of this work is as follows:

- The second chapter presents a brief introduction of the state of the art of microwave device miniaturization. Moreover, the concepts of metamaterials, as well as their applications are analyzed.

- In chapter three, the semi-lumped resonators OSRRs and OCSRRs are exploited to implement artificial or metamaterial transmission lines. Then, these fully planar artificial lines are applied to the implementation of miniaturized wideband band-pass filters, as well as dual-band and quad-band devices.

- The fourth chapter analyzes the possibility of tuning the artificial lines presented in the third chapter by means of ferroelectric materials. Therefore, additional functionality is obtained, applying these concepts to tunable filters, phase shifters or dual-band components.

- In chapter five, the miniaturization of planar filters by means of SIRs is also studied, illustrating the design of elliptic low-pass and high-pass filters, as well as band-pass filters with transmission zeros.

- Lastly, in chapter six, the conclusions and future research that result from this thesis are outlined.

The work conducted during the realization of this thesis was carried out within the Group GEMMA/CIMITEC, which is part of the Electronics Engineering Department of the *Universitat Autònoma de Barcelona*. GEMMA/CIMITEC has been part of the European Network of Excellence NoE 500252-2 METAMORPHOSE (Metamaterials organized for radio, millimeter wave and photonic super lattice engineering), the main objective of which was to research, study and promote artificial electromagnetic materials and metamaterials within the European Union. It has recently given rise to the Virtual Institute for Artificial Electromagnetic Materials and Metamaterials (METAMORPHOSE VI AISBL). Furthermore, CIMITEC is one of the centers of the Technological Innovation Network of TECNIO (ACC1Ó) of the Catalan Government, created with the objective of promoting the transference of technology to industry in the

field of Information and Communication Technology and has been recognized as a Consolidated Group by the Catalan Government (AGAUR). This work was, thus, supported by the European, Spanish and Catalan Governments by means of several projects and contracts and, specially, a grant from the UAB (PIF) and from the Catalan Government (BE grant number 2010 BE1 00834). The *Universitat Autònoma de Barcelona* contributes through the *Vicerectorat de Projectes Estrategics - Parc de Recerca*. Among the projects and contracts with the different institutions and companies that have given support to the developed research activities, we would like to highlight:

- Project TEC2007-68013-C02-02 METAINNOVA from the Spanish Government (*Dirección General de Investigación*). Project co-coordinated by the *Universitat Autònoma de Barcelona* and the *Universidad de Sevilla*. Title: *Tecnologías basadas en metamateriales y su aplicación a la innovación en componentes y subsistemas de RF microondas y milimétricas: circuitos de radiocomunicación*.

- International Project Eureka METATEC granted to a consortium composed of two companies and three research institutions from Serbia and Spain and funded in Spain by a PROFIT and an AVANZA I+D project. Title: *METAmaterial-based TEchnology for broadband wireless Communications and RF identification*.

- Project CSD2008-00066 CONSOLIDER INGENIO 2010 granted to a consortium composed of eight research groups from different Spanish Universities and funded by the Spanish Government. Title: *Ingeniería de Metamateriales (EMET)*.

- International Project Eureka 5014 METASENSE granted to a consortium composed of two companies and two research institutions from Serbia and Spain and funded in Spain by AVANZA I+D projects. Title: *Miniature METAmaterial-Based SENsing Devices for Agricultural, Environmental and Geological Applications*.

- Project VALTEC08-1-0009 granted to the *Universitat Autònoma de Barcelona* by the Catalan Government. Title: *Nuevos componentes de comunicaciones multibanda basados en metamateriales electromagnéticos (COMPATIBLE)*.

- Project TEC2010-17512 METATRANSFER granted to the *Universitat Autònoma de Barcelona* by the Spanish Government. Title: *Nuevas estrategias de diseño y síntesis de componentes de microondas basados en conceptos de METAmateriales con orientación a la TRANSFERrencia tecnológica*.

CHAPTER 2

Introduction and state of the art

Once the solid foundations of the microwave circuit theory were established [1] - [3], significant effort focused on device miniaturization. Since a complete list of size reduction procedures would require a lengthy introduction and it is beyond the scope of this thesis, only a brief number of techniques will be considered in section 2.1. Thus, some advances highlighted by the author in the field of passive planar non-radiating components will be presented, focusing on power dividers, couplers and filters, which are the main topics of this thesis. This state of the art will be the starting point for both the miniaturized components obtained by means of metamaterial concepts as well as the compact filters based on SIRs.

The rest of the chapter will be dedicated to the metamaterial theory, which will facilitate a new path towards the design of miniaturized and multi-band devices. We will study its origin, as well as the main relevant advantages and some applications in great detail. These metamaterial concepts have been used for the design of the microwave components presented in chapters 3 and 4.

2.1 State of the art on miniaturization of planar microwave devices

A very common procedure to obtain compact devices consists of replacing the transmission lines and stubs that make up the conventional distributed designs with other electrically smaller components with equivalent properties. This can be done either by coupling stubs [4] - [7], coupling resonators [8], non-uniform transmission lines [9], fractal elements [10], or by means of slow wave structures [11] - [14], among others. Moreover, these latter miniaturized slow wave structures have also been applied to filters by periodically cascading these cells to create electromagnetic band gaps (EBGs) with a rejected band due to the interference phenomena, or Bragg effect [15] - [17].

Another possibility of further miniaturizing the devices consists of using additional layers, commonly implemented (although not exclusively) in low-temperature co-fired ceramic (LTCC) technology or the more recently liquid crystal polymer (LCP) substrates [18] - [21].

Nonetheless, most of the previous techniques still have stubs or resonators with moderately large electrical lengths (a quarter or an eighth of the wavelength). This leads to still very big structures at the lower region of the microwave spectrum with the corresponding higher cost. Consequently, a different approach to that based on distributed stubs or transmission line sections is required. To this end, the use of lumped or semi-lumped elements/resonators, with a size much smaller than the wavelength, can drastically reduce the dimensions of the devices. Moreover, these elements have the additional advantage of being easily integrated in Microwave Integrated Circuits (MIC) or Monolithic MIC (MMIC) technologies. Their major drawback is their low quality factor inherent to their size, with the consequent higher losses [22] - [24].

On the other hand, in the filter community special emphasis has been placed on miniaturizing the resulting devices by means of different types of distributed resonators, as well as with the aforementioned solutions, which are widely reported in the literature [25] - [28].

A different way of achieving size reduction is to provide the components with multi-band functionality, hence reducing the total number of elements present in the device. For this purpose, different solutions arise. The first technique consists of incorporating additional distributed elements to those present in the conventional designs in order to have a higher degree of freedom and force the additional multi-band functionality. These strategies have successfully been applied by means of additional distributed sections or stubs in power dividers [29], [30] or couplers [31] - [33]. In addition, in the filter community, a higher degree of freedom is frequently obtained by additional free parameters on the dimensions of certain distributed resonators, enabling the control of two or more frequency bands, renaming them as dual- or multi-mode resonators, respectively [34] - [36]. Moreover, another solution like dual-behavior resonators (DBR)

based on the parallel association of band-stop structures [37], [38] or the coupling theory [39], [40], among others, have also been applied to achieve these same goals.

Multi-band functionality can also be achieved by considering the lumped-element equivalent circuit models of dual- or multi-band components, implementing the resulting circuits either by lumped or semi-lumped elements. In [41], a dual-band balun and divider was presented and implemented by means of this approach. In Figure 2.1(a) the lumped-element equivalent circuit of the dual-band balun is shown, in which two dual-band branches of ±90⁰ and ∓90⁰ at two arbitrary frequencies f_1 and f_2 are implemented as shown, in order to satisfy the ±180⁰ difference between the outputs. In general filters, additional transformation from the low-pass prototype can be applied in order to achieve the multi-band functionality [27], [42], [43]. In [43], this procedure was followed to obtain a dual-band Chebyshev band-pass filter with the resulting equivalent circuit reproduced in Figure 2.1(b), in which additional transformations were applied in order to implement the device with distributed stubs.

The introduction of tunable components in microwave circuits provides re-configurability, which is also a path to achieving functionality at various bands, with the ability to adapt itself to environmental changes or application requirements. To this end, most of the aforementioned techniques can be used, adding or replacing the capacitances or coupling schemes with tunable capacitors. Several approaches can be found, with some examples being micro-electro-mechanical systems (MEMS) or ferroelectric materials or varactors. The issue has been broadly studied in the filter community [44], [45]. In this thesis, ferroelectric tunable devices will be considered, showing in chapter 4 a brief state of the art of these tunable materials as well as the implementation of tunable filters, power dividers and phase shifters.

Finally, throughout the last decade, another alternative to miniaturizing has emerged, using concepts of metamaterials. This method makes use of the advantage and methodology developed in the field to create metamaterial devices, which enables a systematic procedure to design compact and/or multi-band components. By these means, planar quad-band devices such as power dividers or couplers, scarcely present in the state of the art will be possible, showing in this thesis some examples in chapter 3.
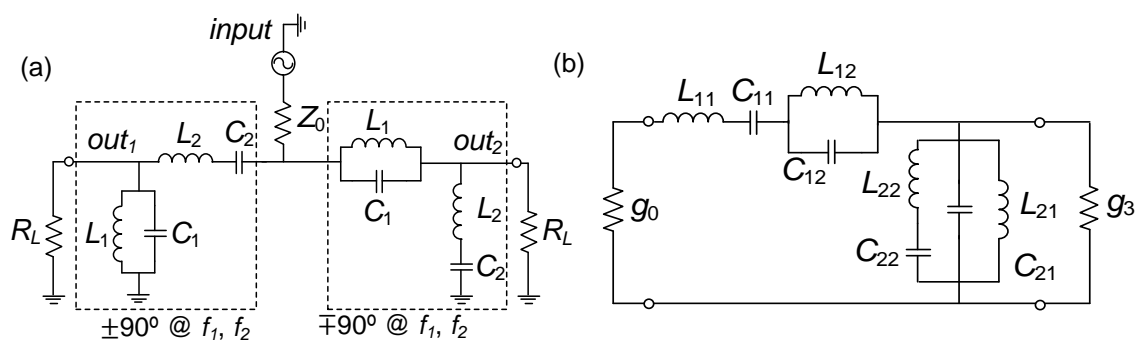
Figure 2.1. Circuit model of a dual-band balun (a) and of a dual-band band-pass filter (b). Extracted from [41] (a) and [43] (b).

In the following section, the concept of metamaterials, as well as the basic properties of these artificial materials will be explained, with special emphasis on one-dimensional planar metamaterials, that is, metamaterial transmission lines.

2.2 Metamaterial transmission lines

Ever since the recent appearance of the metamaterial field, a lot of interest has arisen in the scientific community, with several books having dealt with these new concepts [46] - [50]. Nonetheless, a general consensus on the definition of the term "metamaterial" has not yet been established. Based on [46], metamaterials are defined as *artificial effectively homogeneous electromagnetic structures with unusual properties not readily available in nature*. On the other hand, in [47] and [48] a more general definition is considered, designating the same term as *artificial media with unusual electromagnetic properties*. Therefore, the former statement considers metamaterials to be those artificial structures in which the unit cell size is much smaller than the guided wavelength of the effective artificial medium λ_{gam}[1] (and therefore satisfying the condition of *effectively homogeneous* structure). Alternatively, the latter also includes in the definition structures where the unit cell size can be comparable to the wavelength of the signal (such as electromagnetic band gaps among others).

Throughout this work we will focus mainly on planar one dimensional structures inspired by effective homogeneous media, although periodicity, inherent to such media, will not be a factor. The key aspect, rather than periodicity and homogeneity will be the control of the electromagnetic properties of such structures, i.e., metamaterial transmission lines, as well as the small size of the constitutive blocks. However, the next paragraphs will review the main properties of metamaterials and their implementations.

Since an effective medium has a much smaller period than the wavelength, the refractive phenomena will dominate over the scattering or diffraction phenomena if a wave propagates through the medium [46]. For this reason, it is possible to consider the constitutive cells as "atoms" or "particles", giving rise to the possibility of analyzing the structure considering constitutive parameters such as effective permeability, permittivity or the refraction index, which do not have to necessarily be the same as those of its constituent materials. Therefore, we can study their electromagnetic behavior considering the propagation of electromagnetic waves in a certain medium with effective parameters ε and μ, being defined for an isotropic medium as [2]

$$n = \pm c\sqrt{\varepsilon\mu} \qquad (2.1)$$

---

[1] The sub index in the term λ_{gam} is considered to differentiate it from the general guided wavelength λ_g of the constitutive medium.

[2] Note that although in continuous media the propagation constant is usually referred by k, in circuit theory this same concept is normally expressed by β, and hence this latter definition has been considered throughout this thesis.

$$\beta = \frac{\omega}{c} n \tag{2.2}$$

with n being the refractive index, ω the angular frequency, c the speed of light in vacuum, β the propagation constant, ε the dielectric permittivity and μ the magnetic permeability. From equations (2.1) - (2.2) it follows that if permeability and permittivity both have same sign (either positive or negative), then the propagation of electromagnetic waves is allowed, given that the propagation constant β is real. Of these two cases, structures with $\varepsilon < 0$, $\mu < 0$ do not exist in nature. These latter structures can, however, be artificially fabricated.

The properties of a simultaneously negative ε and μ medium were firstly analyzed by Veselago [51] in 1968. In [51], these media were named as "Left-Handed", since the electric (*E)* and magnetic (*H)* field vectors, as well as the propagation vector (*β)* form a left-handed triplet (unlike the conventional materials with $\varepsilon > 0$, $\mu > 0$, where a right-handed triplet is formed). As pointed out by Veselago, the consequences of the negative valued permeability and permittivity are the antiparallel phase and group velocities as well as the reversal of the Doppler effect and Snell law (at the interface between a conventional and a left-handed medium), the latter interpreted as being due to the negative refraction index of the left-handed medium.

However, it was not until 1999 that Pendry *et al.* [52] proposed the first effective medium with a negative effective permeability $\mu < 0$ by means of the so-called split ring resonator (SRR), with a small unit cell size. For this to happen, a periodic array of SRRs with the incident radiation polarized with the magnetic field parallel to the axis of the rings was required. This particle, shown in Figure 2.2 with its equivalent circuit model, is formed by two open concentric metallic rings with slits etched in opposite sides. Due to its small electrical size, the quasi-static condition can be considered in order to analyze its behavior. Thus, the resulting equivalent circuit is a parallel *LC* tank, where C_o corresponds to the distributed capacitance between rings ($C_o = 2\pi r_o C_{pul}$), with C_{pul} being the per unit length capacitance between rings. Similarly, L_s can be approximated as the inductance of a single ring of average radius r_o and strip width c. A year later, in 2000, David Smith *et al.* [54] synthesized the first left-handed medium (i.e., achieving both $\varepsilon < 0$ and $\mu < 0$) combining an array of SRRs to introduce the negative permeability, with metallic posts to introduce the negative permittivity. Such a configuration is shown in Figure 2.3, where propagation is allowed (although with high losses) in a certain region due to the simultaneous $\varepsilon < 0$ and $\mu < 0$, whereas in the rest of the band no propagation is allowed since both parameters have opposite signs.
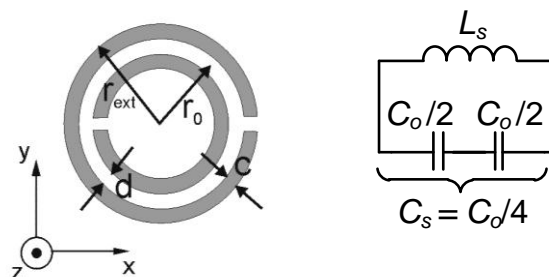
Figure 2.2. Topology and equivalent circuit of a SRR, extracted from [53].
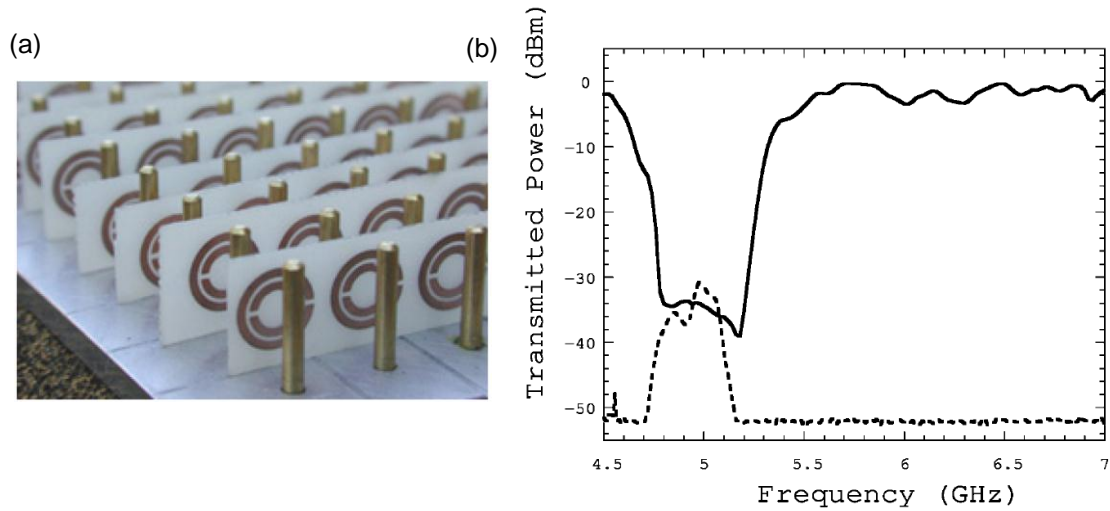
Figure 2.3. Photograph (a) and response (b) of the first left-handed medium composed by an array of SRRs and metallic posts, extracted from [54].
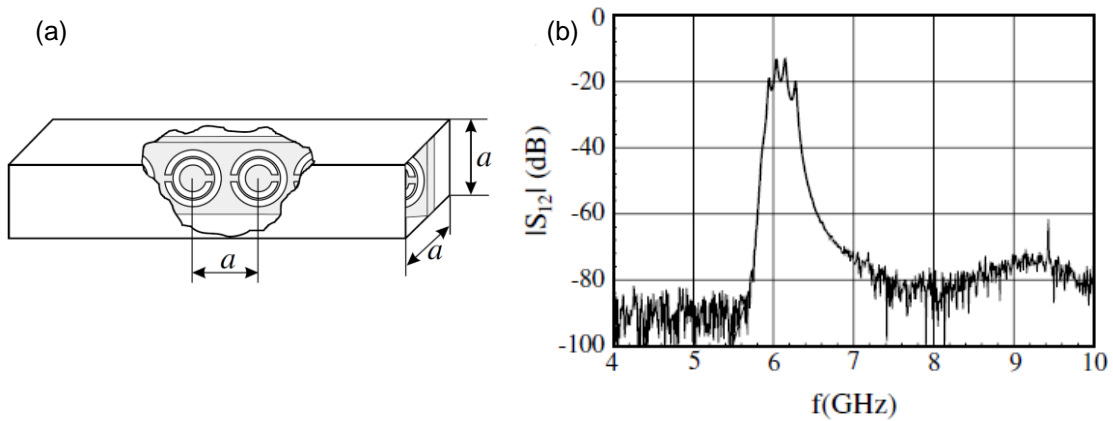
Figure 2.4. Layout (a) and transmission response (b) of a left-handed medium composed by a waveguide with an array of SRRs, extracted from [55].

Another possibility of obtaining a left-handed medium in the microwave region is to introduce SRRs in a rectangular waveguide with a resonance frequency smaller than the cut-off frequency of the waveguide, as shown in Figure 2.4. In this region, the waveguide behaves as an effective negative permittivity medium whereas the SRR behaves as an effective negative permeability medium, hence obtaining a backward propagation [55].

Two-dimensional left-handed structures were also fabricated. The first experimental verification of a left-handed 2D structure was implemented with square SRRs and metallic wires printed in a fiberglass substrate (reproduced in Figure 2.5), experimentally demonstrating the negative index of refraction [56].

After these results were published, additional experimental and numerical works were presented [57] - [59], supporting the pioneering work by Veselago [51], Pendry [52] and Smith [54]. Over recent years, these concepts have been applied in as many diverse fields as cloaking or magnetic resonance imaging applications, as well as expanding their functionality to the optical range through three dimensional structures [60] - [62].

Figure 2.5. Photograph of the first 2D left-handed structure used to demonstrate the negative refraction, extracted from [56].

2.2.1 Transmission line theory of artificial media

Metamaterials or artificial media can also be analyzed by means of the transmission line theory. Through the forthcoming analysis, metamaterials may be applied in microwave engineering applications implementable in different planar or multi-layer technologies. For this purpose, a relation between the effective parameters of the artificial medium ε_{eff} - μ_{eff} with those of a transmission line is required.

Let us assume a plane wave propagating in a homogeneous and isotropic lossless medium. In this case, the propagation constant β and the wave impedance η are related as

$$\eta = \sqrt{\frac{\mu}{\varepsilon}} \tag{2.3}$$

$$\beta = \omega\sqrt{\mu\varepsilon} \tag{2.4}$$

whereas in a conventional lossless transmission line, assuming its representation as an infinite periodic structure with an incremental circuit model of infinitesimal length Δx such as that shown in Figure 2.6(a), with per unit length series impedance $Z' = Z/\Delta x$ and shunt admittance $Y' = Y/\Delta x$, and using the telegrapher's equations, the same conditions yield

$$Z_0 = \sqrt{\frac{Z'}{Y'}} = \sqrt{\frac{L'}{C'}} \tag{2.5}$$

$$\beta = \pm\sqrt{-Z'Y'} = \omega\sqrt{L'C'} \tag{2.6}$$

with Z_0 being the characteristic impedance and $L' = L/\Delta x$, $C' = C/\Delta x$ the per unit length inductance and capacitance, respectively. Thus, from equations (2.3) - (2.4) and (2.5) - (2.6) it follows that the propagation in a transmission line is equivalent to that of a plane wave in a homogenous and isotropic medium if

$$L' = \mu_{eff} \tag{2.7}$$

$$C' = \varepsilon_{eff} \qquad (2.8)$$

where the index "*eff*" has been added to differentiate the permittivity or permeability of the constitutive materials from those of the resulting effective medium.

As can be seen, for the case of a transmission line, $\varepsilon_{eff} > 0$, $\mu_{eff} > 0$ and consequently propagation is allowed. To fulfill the condition of a left-handed medium by means of this study, negative inductances and capacitances such as those shown in Figure 2.6(b) would be required to satisfy the condition of $\varepsilon_{eff} < 0$, $\mu_{eff} < 0$. Since the impedances of the incremental circuit of Figure 2.6(b) are not equivalent to any reactive element such as capacitors or inductors, in 2002 [63], [64] an alternative equivalent circuit (Figure 2.6c) was proposed that also allows left-handed wave propagation in a certain region. This case is the so-called left-handed transmission line or dual transmission line, since the impedances are the dual of the conventional transmission line (the inductance is exchanged for capacitance and vice versa). The characteristic impedance and propagation constant of the model of Figure 2.6(c) are [3]

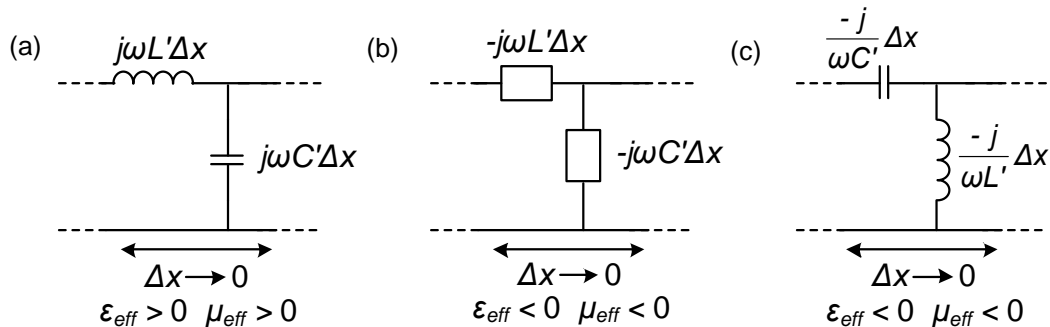$$Z_0 = \sqrt{\frac{Z'}{Y'}} = \sqrt{\frac{L'}{C'}} \qquad (2.9)$$

$$\beta = \pm\sqrt{-Z'Y'} = -\frac{1}{\omega\sqrt{C'L'}} \qquad (2.10)$$

Then, using the same procedure as with the case of the lossless transmission line, taking into account equations (2.3) - (2.4) and (2.9) - (2.10) the result is

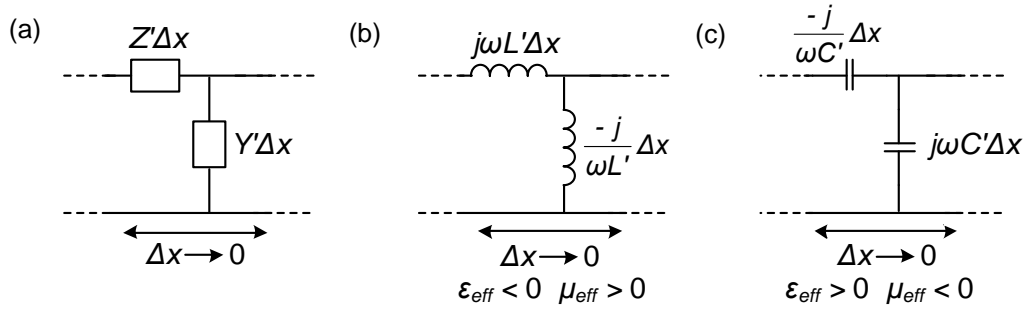$$\mu_{eff} = -\frac{1}{\omega^2 C'} \qquad (2.11)$$

$$\varepsilon_{eff} = -\frac{1}{\omega^2 L'} \qquad (2.12)$$

thereby demonstrating that the circuit of Figure 2.6(c) also satisfies $\varepsilon_{eff} < 0$, $\mu_{eff} < 0$ and hence, left-handed wave propagation is obtained.

Figure 2.6. Incremental circuit model of a conventional (a), non-conventional (b) and dual transmission line (c). The values depicted in the series branch correspond to the impedance, whereas for the shunt branch corresponds to the admittance.

---

[3] Notice that in (2.9) - (2.12) *L'* and *C'* have units of H·m and F·m, respectively, reflecting that an increase of length reduces the inductance and capacitance [46].

(a) $Z'\Delta x$ $Y'\Delta x$ $\Delta x \rightarrow 0$

(b) $j\omega L'\Delta x$ $\dfrac{-j}{\omega L'}\Delta x$ $\Delta x \rightarrow 0$ $\varepsilon_{eff} < 0 \quad \mu_{eff} > 0$

(c) $\dfrac{-j}{\omega C'}\Delta x$ $j\omega C'\Delta x$ $\Delta x \rightarrow 0$ $\varepsilon_{eff} > 0 \quad \mu_{eff} < 0$

Figure 2.7. Incremental circuit model of a generic transmission line (a) and for non-propagation media (b) - (c). The values depicted in the series branch correspond to the impedance, whereas for the shunt branch corresponds to the admittance.

Note that for the validity of (2.11) and (2.12) an infinite periodic structure composed of the incremental circuit of Figure 2.6(c) should be required, although if periodicity and homogeneity are sacrificed, a left-handed behavior is still obtained.

The more general analogy between a plane wave propagating in a homogeneous and isotropic lossless medium with that of an incremental generic impedance model such as that shown in Figure 2.7(a) can also be considered. Since no assumption on the nature of the reactance is taken in this case, this will enable us to study the effective permeability or permittivity of any kind of artificial media, composed of either inductances, capacitances, or a combination of both. By applying the telegrapher's equation to this general case and following the same procedure as before, it can be concluded that the propagation in an incremental circuit model of generic impedance satisfies the following relation

$$Z'(\omega) = j\omega\mu_{eff} \tag{2.13}$$

$$Y'(\omega) = j\omega\varepsilon_{eff} \tag{2.14}$$

Therefore, propagation is only allowed when the series and shunt reactances are opposite in sign (since the propagation constant β will only be real in these cases). Moreover, it can easily be seen how for the equivalent circuits of Figure 2.6(a) or Figure 2.6(c) the impedance conditions of equation (2.13) - (2.14) lead to the same results shown in (2.7) - (2.8) or (2.11) - (2.12), respectively, as was expected.

Finally, artificial media such as those shown in Figure 2.7(b)-(c) can also be analyzed with this approach, resulting in a permeability and permittivity opposed in sign and consequently not allowing wave propagation.

2.2.2 Network theory of artificial lines

The analysis of the previous section was formulated on periodicity and homogeneity. Nonetheless, in order to design microwave components, homogeneity can be sacrificed. In other words, the unit cell does not need to be electrically small in the region of interest, nor is it necessary to satisfy $\beta l \approx 0$. [4]

---

[4] A clear example of this case occurs with impedance inverters, in which an electrical length of $\beta l = \pm 90^0$ is required, leading to a unit cell size of $\lambda_{gam}/4$, which is considered to be the effective-
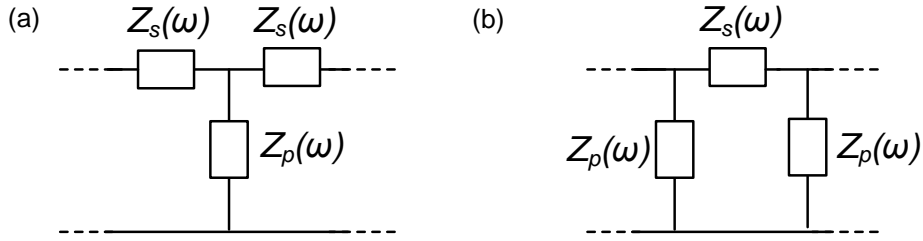
Figure 2.8. Generic T (a) - and π (b) - circuit model.

In more specific terms, in such non-homogeneous artificial media, the use of effective parameters such as permittivity or permeability, as well as the telegrapher's equations cannot be considered. For this reason, an alternative method based on network or also renamed Bloch wave theory is required to analyze these structures. This will provide the dispersion characteristics and the characteristic impedance for any structure with arbitrary cell size. Specifically, a periodic two-port network structure composed of the cascade of identical unit cells of length l is assumed. In such conditions, the complex propagation constant γ is related as [1]

$$cosh(\gamma l) = \frac{A + D}{2} \tag{2.15}$$

where A and D correspond to the diagonal terms of the [ABCD] matrix. If we now consider the [ABCD] matrix of a symmetric T- or a π-model with series and shunt impedance $Z_s(\omega)$ and $Z_p(\omega)$, respectively (Figure 2.8), the following equation in the transmission bands (excluding losses) results [5]

$$cos(\beta l) = 1 + \frac{Z_s(\omega)}{Z_p(\omega)} \tag{2.16}$$

A relation between the propagation constant β and the S-parameters can also be obtained considering the equivalence between these parameters with the [ABCD] matrix. Specifically, the propagation constant can be expressed as

$$cos(\beta l) = \frac{1 - S_{11}S_{22} + S_{12}S_{21}}{2S_{21}} \tag{2.17}$$

which for the case of a lossless, reciprocal, symmetric and passive network can be reduced to

$$cos(\beta l) = \frac{cos(\Phi_{21})}{|S_{21}|} \tag{2.18}$$

---

homogeneity limit [46]. In fact, the case of a cascade of n unit cells with $\beta l \approx 0$ could also be considered to obtain the same results, but in the latter case the maintenance of homogeneity would lead to a lower degree of miniaturization.

[5] Note that if the T- or π-model of the incremental circuits of Figure 2.6(a) or Figure 2.6(c) are considered and a second-order Taylor approximation is applied to equation (2.16) forcing the long wavelength condition (and thus $\beta l \rightarrow 0$), then the propagation constant of equation (2.6) or (2.10) results, respectively.

14

Φ_{21} being the phase of S_{21}. Thus, for networks satisfying the aforementioned conditions it follows that

$$\beta l|_{|S_{21}|=1} = \pm\Phi_{21} + 2k\pi, \; k \in Z \qquad (2.19)$$

Moreover, considering a positive group velocity, it can be deduced that the physical solution corresponds to $\beta l = -\Phi_{21}$, i. e., if total transmission is satisfied the electrical length is equal to the phase shift of S_{21}, but with an opposite sign.

Another relevant parameter is the characteristic impedance. Since the infinitesimal unit cell condition is not necessarily satisfied, we cannot consider the previous concepts of characteristic impedance. Therefore, we will consider the so-called Bloch impedance, which relates the voltage and currents at the terminals of the unit cell in periodic structures (either infinite or matched to the ports). In general circuit terms, this is also called image impedance, since the Bloch impedance can also be obtained as the impedance seen at the input when its value is equal to the load impedance at the output [48]. For this reason, in artificial lines it plays the same role as the characteristic impedance on a conventional transmission line (and for this reason it is sometimes renamed as such). Taking this into account, the Bloch impedance for the T- and π-model is [6]

$$Z_{B_T}(\omega) = \sqrt{Z_s(\omega)\big[Z_s(\omega) + 2Z_p(\omega)\big]} \qquad (2.20)$$

$$Z_{B_\pi}(\omega) = \sqrt{\frac{Z_p^{\,2}(\omega)Z_s(\omega)}{2Z_p(\omega) + Z_s(\omega)}} \qquad (2.21)$$

Z_{BT} and $Z_{B\pi}$ being the Bloch impedance of the T- and π-model, respectively. By inspecting equations (2.20) - (2.21), it can be deduced that if a lossless passive circuit is only composed of reactive elements, then the Bloch impedance will be either pure real or pure imaginary depending on whether propagation is allowed or not, respectively. Considering this, in the following chapters, only the real part of this impedance will be represented unless otherwise specified.

Thus, with both propagation constant and Bloch impedance, it will be possible to analyze and control the behavior of the magnitude transmission and/or phase of any kind of lossless artificial lines that can be modeled by reactive elements at any frequency region, where the long wavelength limit will not be necessary.

Figure 2.9 and Figure 2.10 show the dispersion diagram and Bloch impedance for an artificial line that allows either right-handed (RH) or left-handed (LH) wave propagation, such as those shown in Figure 2.6(a) or Figure 2.6(c), respectively. In each graph, the results derived from the network theory are compared with those inferred from the transmission line theory (HLW denoting the latter case where the additional homogeneity and hence long wavelength limit restrictions are satisfied).

---

[6] Note that if the T- or π-model of the incremental circuits of Figure 2.6(a) or Figure 2.6(c) are considered forcing the long wavelength condition, then the Bloch impedance results in the characteristic impedance of equations (2.5) or (2.9).
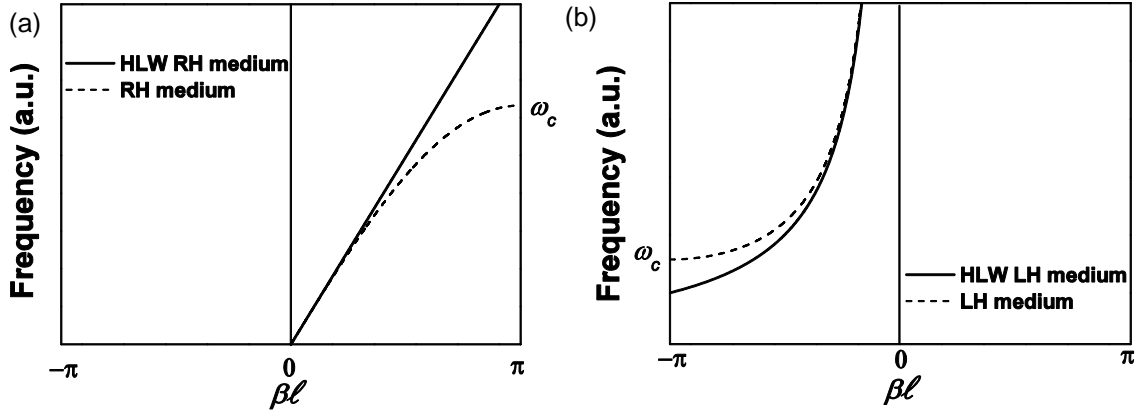
Figure 2.9. Dispersion diagram for the media of Figure 2.6(a) and Figure 2.6(c) with right-handed (a) and left-handed (b) wave propagation, respectively. In the graph is shown the cases with and without the restriction of homogeneity and long wavelength (restriction denoted as HLW).
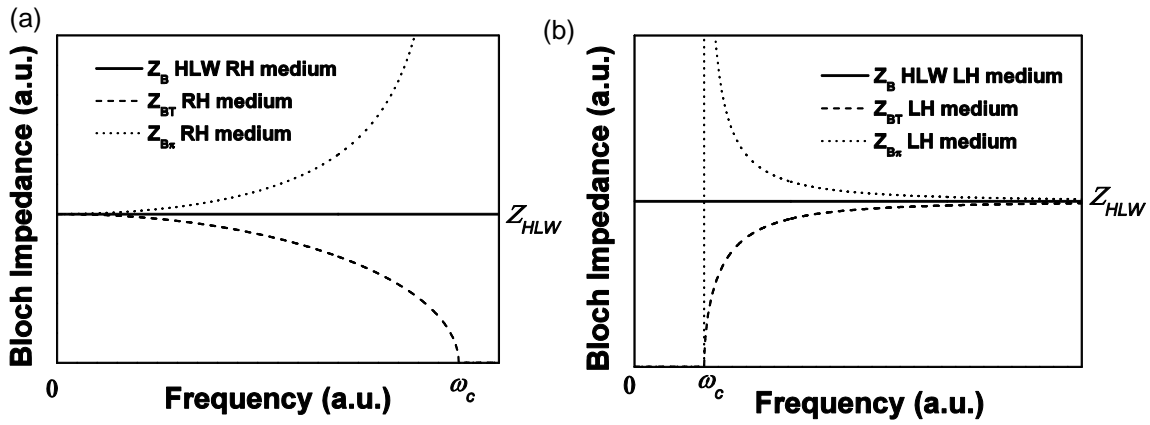
Figure 2.10. T- and π- characteristic impedance for the media of Figure 2.6(a) and Figure 2.6(c) with right-handed (a) and left-handed (b) wave propagation, respectively. In the graph is shown the cases with and without the restriction of homogeneity and long wavelength (restriction denoted as HLW).

If no assumption or restriction is applied to the incremental circuits of Figure 2.6(a) or Figure 2.6(c), dispersion is present, and the limits of propagation are between [0, π] and [-π, 0], respectively, ±π corresponding to the cut-off frequency ω_c given by the arccosine delimitation [-1, 1]. On the other hand, if the constraint of homogeneity is applied there is no cut-off frequency, and a non-dispersive linear dependence with frequency is obtained for the conventional transmission line, as expected from equation (2.6). Alternatively, the resulting propagation for the dual or left-handed transmission line is dispersive even in the homogeneous condition, and the phase constant is delimited by (-∞, 0], as predicted from equation (2.10).

The Bloch impedance is frequency dependent, with different limits (either zero or infinite) depending on the model used (as opposed to the dispersion diagram where both T- and π-models lead to the same results). However, if the restriction of homogeneity or long wavelength is applied, both models lead to a constant impedance Z_{HLW}, corresponding to the characteristic impedance shown in equations (2.5) or (2.9).

16

2.2.3 Composite right-/left-handed lines

Although all the artificial transmission lines analyzed so far present either left- or right-handed wave propagation, it is also possible to design artificial structures with both left- and right-handed wave propagation depending on the frequency region. These lines are called composite right-/left-handed (CRLH) transmission lines [65] - [68]. The design of metamaterial-based microwave circuits is based on the controllability of the dispersion diagram and Bloch impedance of CRLH lines (also called dispersion and impedance engineering). For this reason, different types of artificial CRLH lines have been presented in recent years. Throughout this section, different artificial lines will be analyzed, and it will be envisaged how these artificial media are of interest for multi-band devices and/or to enhance the performance of microwave devices. In addition, given that all the artificial lines that are going to be presented from now on will be considered for microwave engineering applications with non-infinitesimal unit cell sizes and not necessarily satisfying the long wavelength condition, only the models and equations presented in section 2.2.2 will be employed. Nonetheless, if a homogeneous structure fulfilling the long wavelength condition formed by the unit cells that will to be presented is considered, then equations (2.13) - (2.14) could be used to extract the effective parameters of the medium by means of a straight-forward procedure.

2.2.3.1 Conventional and dual CRLH lines

The first implementations of CRLH lines were presented in [65] - [68], and are composed of the combination of the right-handed and left-handed cells presented in Figure 2.6(a) and Figure 2.6(c), as shown in Figure 2.11. In fact, this cell was initially obtained seeking the implementation of a pure left-handed transmission line in planar technology, but as will be seen in section 2.2.4, the right-handed contribution of the host line could not be neglected [65] - [68].

In Figure 2.12(a), the dispersion diagram considering equation (2.16) is plotted. Taking into account the circuit elements of Figure 2.11, it follows that left-handed wave propagation at low frequencies is allowed since the dominant reactances are those of the capacitance C_L and the inductance L_L.
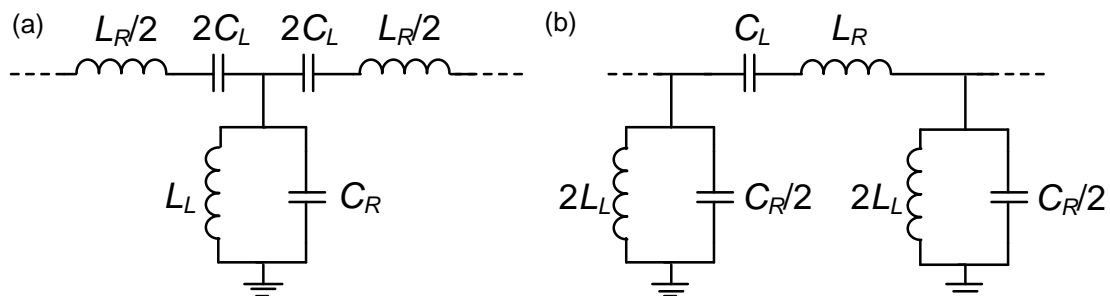
Figure 2.11. *T-* (a) or *π-* (b) model of the CRLH transmission line.
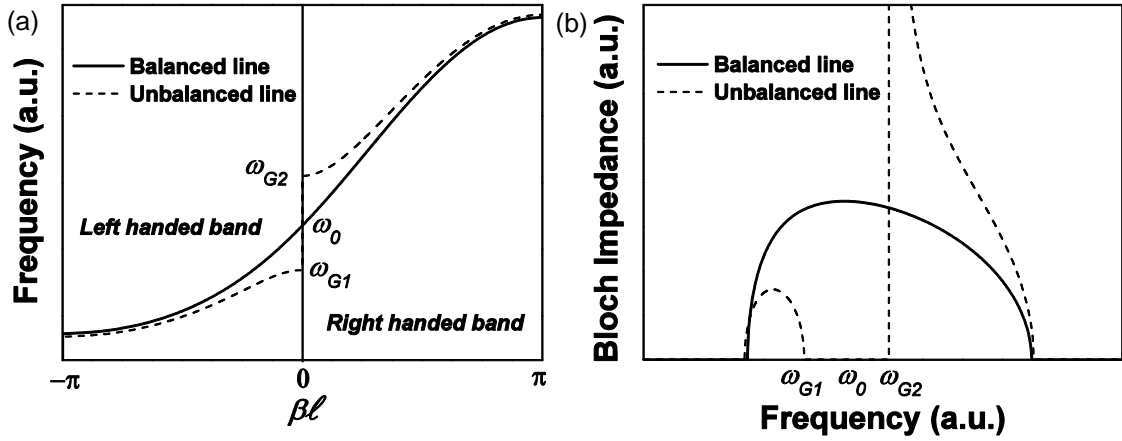
Figure 2.12. Typical dispersion diagram (a) and Bloch impedance (b) of a balanced and unbalanced *T*-model CRLH transmission line.

On the other hand, at high-frequencies the dominant reactances are those of the capacitance C_R and the inductance L_R and therefore a right-handed band appears. The band gap between both bands is determined by the resonance frequencies of the series branch ω_s and the shunt branch ω_p

$$\omega_s = \frac{1}{\sqrt{L_R C_L}} \tag{2.22}$$

$$\omega_p = \frac{1}{\sqrt{L_L C_R}} \tag{2.23}$$

with its limits ω_{G1} and ω_{G2} defined as [48]

$$\omega_{G1} = min(\omega_s, \omega_p) \tag{2.24}$$

$$\omega_{G2} = max(\omega_s, \omega_p) \tag{2.25}$$

Then, if $\omega_s = \omega_p = \omega_0$ a continuous transition between both bands appears. This condition is normally denoted as the balanced case (whereas a non-continuous transition is normally referred to as unbalanced). In Figure 2.12(b) the Bloch impedance of a balanced and unbalanced CRLH transmission line considering the *T*-model of Figure 2.11 is plotted, obtained by means of equation (2.20). As can be observed, the unbalanced CRLH line has a band gap between the same frequency positions as on the dispersion diagram. In this region, the impedance is purely imaginary, proving to be useful for the impedance matching of arbitrary impedances [69]. On the other hand, the balanced case presents a continuous transition with a maximum impedance value set at ω_0 defined as

$$Z_B|_{\omega=\omega_0} = \sqrt{\frac{L_R}{C_R}} = \sqrt{\frac{L_L}{C_L}} \tag{2.26}$$

which will be useful for devices in which a flat band-pass response over a wide frequency range is required.
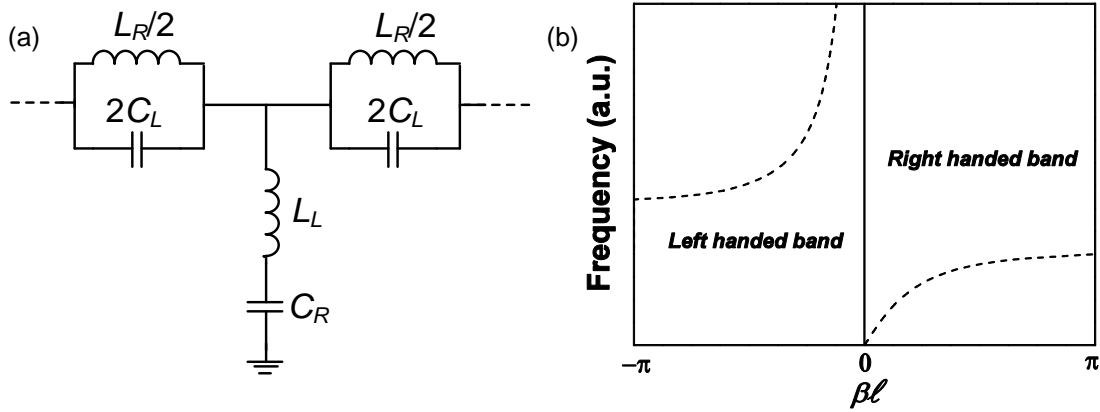
Figure 2.13. Unit cell (a) and typical dispersion diagram (b) of the D-CRLH line.

In addition, since its unit cell is identical to that of a third-order band-pass filter, the usefulness of these artificial lines to implement microwave filters can already be envisaged.
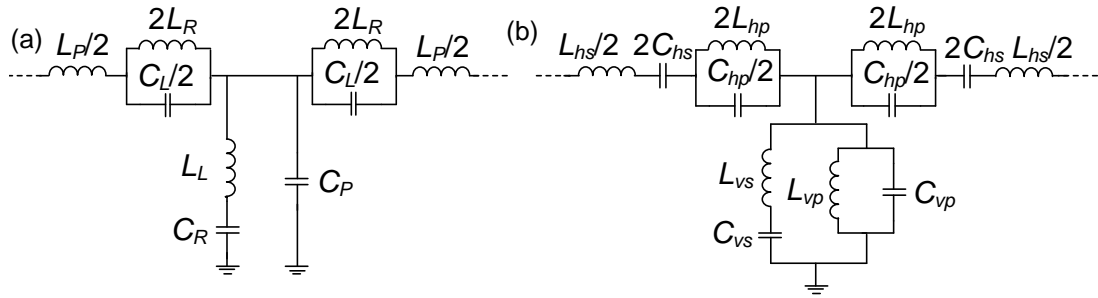
Another type of artificial line exhibiting forward and backward wave propagation is the so-called dual-CRLH or D-CRLH line, presented by Caloz [70] and reproduced in Figure 2.13(a). The term "dual" makes reference to the fact that the series and shunt reactances of this artificial line are exchanged from the conventional CRLH line. By means of this procedure, a duality in the dispersion diagram also results, presenting right-handed behavior at low frequencies and left-handed behavior at high frequencies. Nonetheless, in a D-CRLH line, even when the series and parallel LC tank resonates at the same frequency, as is the case in the dispersion diagram of Figure 2.13(b), a band gap between the left- and right-handed bands appears, only presenting a continuous band if a homogeneous medium is considered [70].

2.2.3.2 Generalized CRLH lines

Artificial lines with more than two propagation bands are also possible. This feature enhances the conventional or dual CRLH line functionality and allows the realization of devices with a higher number of bands. Nonetheless, in the same way that the CRLH line with two propagation bands requires twice as many reactive elements as the pure left- or right-handed line, the requirement of a higher number of bands will also lead to an artificial line with a higher number of reactive elements.

In [71], the Double-Lorentz transmission line was proposed, which facilitates the propagation of three alternating left- and right-handed bands. To obtain this unit cell, a combination of the D-CRLH line shown in Figure 2.13(a) and the pure right-handed line shown in Figure 2.6(a) is applied, obtaining the unit cell of Figure 2.14(a).

Thus, the dispersion diagram begins with right-handed wave propagation and then alternates to left-handed and right-handed wave propagation, respectively. It is worth mentioning that if the same D-CRLH line is combined with the pure left-handed line shown in Figure 2.6(c), then the same three bands appear, but beginning with a left-handed band at low frequencies [72].

19

Figure 2.14. Unit cell of a Double-Lorentz (a) (extracted from [71]) and E-CRLH line (b).

Moreover, in [73], [74] a CRLH line exhibiting four different bands was proposed, renaming the resulting artificial line as an extended CRLH line or E-CRLH line. In Figure 2.14(b) one possible unit cell that satisfies the aforementioned conditions that result from combining the conventional CRLH line with the D-CRLH line is shown. Thus, to obtain four bands the number of reactive elements must be doubled in comparison with the conventional CRLH line (which presented only four different elements and two different bands). Figure 2.15 shows the dispersion diagram and Bloch impedance of an arbitrary *T*-model E-CRLH line such as that shown in Figure 2.14(b), obtained by means of equations (2.16) and (2.20), respectively.

We again can distinguish between the balanced or unbalanced cases, with the same consequences in dispersion and impedance as those explained in the conventional CRLH line (although in this case two band gaps between left- and right-handed bands can arise). Moreover, the way in which the structure presents a left-handed behavior at low frequencies and then alternates to right-handed and left-handed bands with frequency can be appreciated.

The same analysis can be applied to a generalized CRLH line of *N* bands. From this study, carried out by different authors in [72], [75], it can be deduced that to design an artificial line with *N* bands, 2*N* reactive elements will be required (with this condition being satisfied in all the artificial lines presented in this chapter). Moreover, in [75] a generalized CRLH line model to implement *N* bands was presented, demonstrating that to design an *N* band artificial line such as that reproduced in Figure 2.16, *N*/2 series resonators in parallel on the series branch and *N*/2 shunt resonators in series on the parallel branch are required.

The previous statement can be deduced by studying the poles and zeros of each branch. Both series and shunt branches present a reactance with *N*/2 zeros and *N*/2 poles. For the case of the series branch the zeros corresponds to the resonance frequency of each series *LC* tank and the first pole is at the origin, whilst for the shunt branch the poles corresponds to the resonance frequency of each shunt *LC* tank and the first zero is at the origin. In addition, Foster's reactance theorem [76] also applies, which states that the reactance of a passive lossless two-port network is always monotonically increasing with frequency, leading to a reactance function that always alternates from poles to zeros with frequency and vice versa.
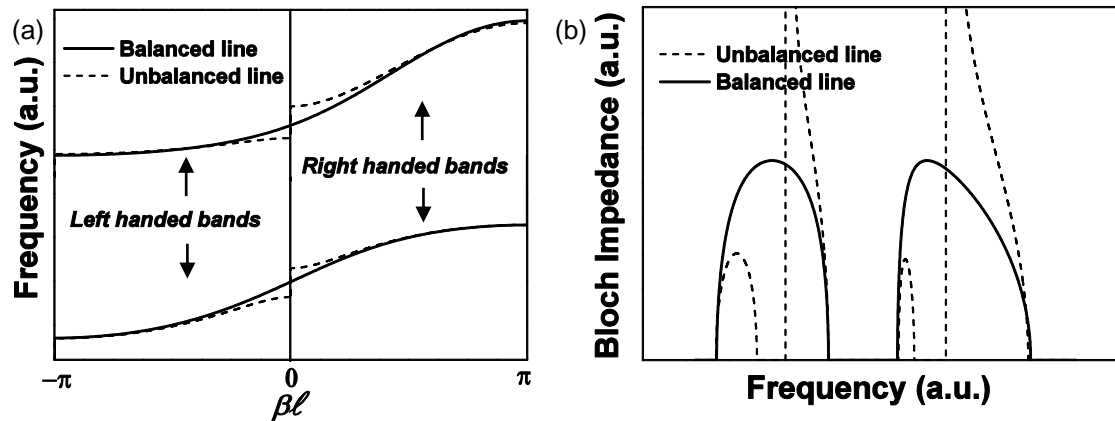
Figure 2.15. Typical dispersion diagram (a) and Bloch impedance (b) of a *T*-model E-CRLH line as the one shown in Figure 2.14(b).
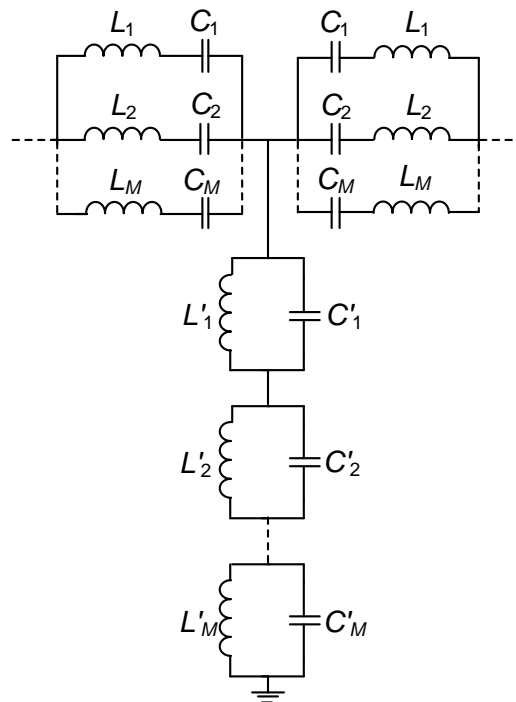

Figure 2.16. Generalized circuit model of an arbitrary *N*-band CRLH line, extracted from [75].

Thus, considering the two aforementioned statements, as well as considering that propagation is only allowed when the series and shunt impedances are opposite in sign (as analyzed in equations (2.13) - (2.14)), it is deduced that a unit cell such as that depicted in Figure 2.16 can achieve a maximum of *N* bands. Lastly, it has to be considered that this statement can be expanded to any resulting artificial line such as the conventional CRLH, the D-CRLH or the E-CRLH line, and not only the artificial line that results from the generalized CRLH line.

2.2.4 Planar implementation of CRLH lines: The resonant-type approach

The planar implementation of the artificial lines shown in section 2.2.3 can be implemented by means of different ways or approximations.

21
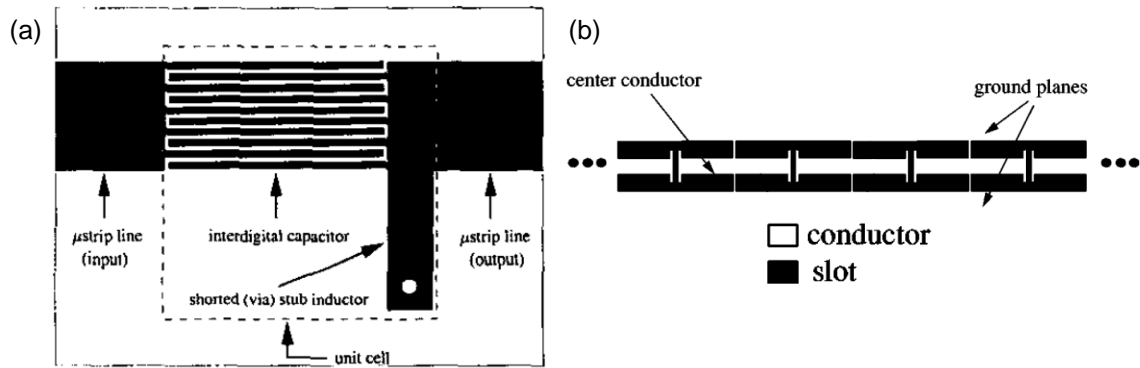
Figure 2.17. Layout of the microstrip (a) and CPW based artificial line (b), extracted from [65] (a) and [67] (b).

A possible approximation consists of using discrete elements (capacitors and inductors), although these can only operate up to a limited frequency range due to the parasitic effects, in addition to having the element values fixed by the manufacturer. Another approach to implement artificial lines is by means of planar semi-lumped elements that act as the capacitors or inductors required in a certain range of interest. This avoids the need to solder components and lowers the cost of production. With this approach, typically a host line is loaded with series gaps (or interdigital capacitors) and shunt vias acting as inductances, frequently referred to as the *CL*-loaded approach. Examples of *CL*-loaded lines were first reported in microstrip [65], coplanar waveguide (CPW) [67] or strip line technology [68], showing in Figure 2.17 the layout for the case of microstrip and CPW technology.

It is worth noting that although all of these configurations sought the implementation of a pure left-handed medium (by means of series capacitors and shunt inductors), since the elements need to be hosted in a conventional medium with a distributed series inductance and shunt capacitance to ground, a CRLH line behavior due to the right-handedness of the host transmission line was obtained.

Soon after these results were published and the CRLH line pointed out, different authors presented additional approaches to obtain the same CRLH behavior. One of these approaches, on which we will focus throughout this thesis, is the so called resonant-type approach, which makes use of electrically small resonators coupled to a host line to obtain the CRLH line behavior. Depending on the resonator used, different responses and models result. In this section, we will analyze the responses obtained with the resonator SRR and with its complementary counterpart CSRR. Lastly, in chapter 3, the implementation of CRLH lines based on open resonators will be seen as novel results of this thesis.

2.2.4.1 CRLH lines loaded with SRRs

Figure 2.18(a) shows the layout of a CRLH transmission line implemented with SRRs in CPW technology, extracted from [77]. The SRRs are etched on the bottom of the substrate below the slot regions of the CPW transmission line to excite the SRR with the required axial magnetic field.
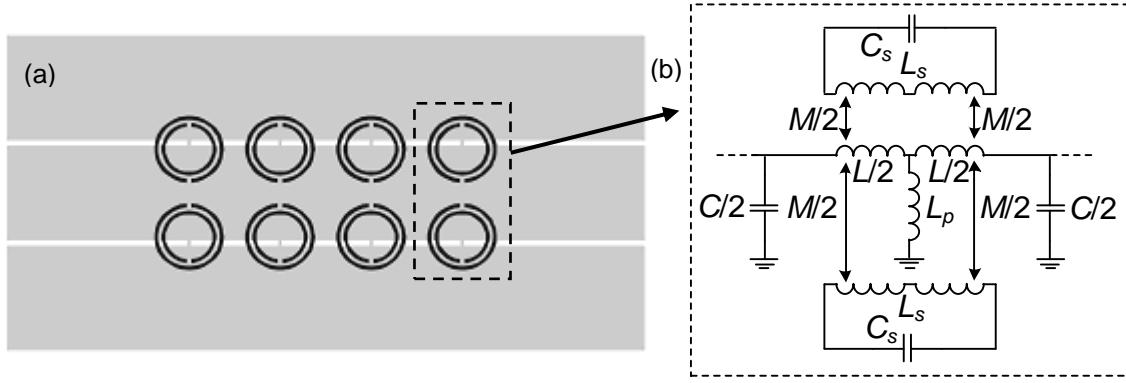
Figure 2.18. Layout (a) and equivalent circuit (b) of the CRLH transmission line unit cell based on SRRs coupled to a CPW host line with metallic strips to ground. Extracted from [77] (a) and [78] (b).
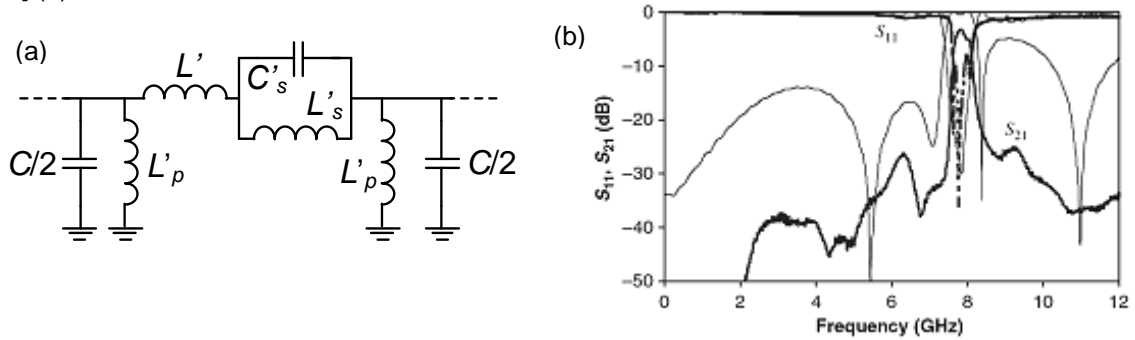
Figure 2.19. Transformed equivalent circuit (a) and frequency response (b) of the layout shown in Figure 2.18(a). Equivalent circuit extracted from [78]. Frequency response extracted from [77].

Additionally, inductive strips from the main line to the ground plane are added to obtain the required shunt inductance. The equivalent circuit, analyzed in [77], [78], is that shown in Figure 2.18(b) where the SRRs, modeled as parallel *LC* tanks, are coupled by a mutual inductance *M*/2 to the host line with inductance *L*/2 and shunt capacitance *C/2*, as well as with an inductive effect to ground, L_p, due to the narrow strips to the ground plane.

The equivalent circuit of Figure 2.18(b) can be transformed using equations (2.27) - (2.30) to that shown in Figure 2.19(a) [78]. Hence, this structure behaves as a CRLH transmission line with an additional parameter L'_s which generates a transmission zero due to the resonance of the parallel *LC* tank (i.e., the resonance frequency of the SRR).

$$C'_s = \frac{L_s}{2\omega_o^2 M^2}\left(\frac{1+\dfrac{M^2}{2L_pL_s}}{1+\dfrac{L}{4L_p}}\right)^2 \tag{2.27}$$

$$L'_s = 2\omega_o^2 M^2 C_s \frac{\left(1+\dfrac{L}{4L_p}\right)^2}{1+\dfrac{M^2}{2L_pL_s}} \tag{2.28}$$

23

$$L' = \left(2 + \frac{L}{2L_p}\right)\frac{L'}{2} - L'_s \tag{2.29}$$

$$L'_p = 2L_p + \frac{L}{2} \tag{2.30}$$

The frequency response is depicted in Figure 2.19(b), where neither the transmission zero nor the right-handed band can be appreciated due to the high number of cells and the limited frequency region depicted, respectively.

2.2.4.2 CRLH lines loaded with CSRRs

Another way to implement a CRLH line is by means of the dual or complementary particle of the SRR, that is, the complementary split ring resonator (CSRR), shown in Figure 2.20 with its equivalent circuit, initially presented in [79].

The CSRR can be obtained by exchanging the metal for slots and vice versa from a SRR resonator. Considering the Babinet principle, it can be deduced that if the effects of the metal thickness and losses, as well as those of the dielectric substrate are neglected, given the same dimensions and size, the CSRR resonates at the same frequency as the SRR if an electric field excitation on the axial direction is applied (whilst the SRR required a magnetic excitation in the same direction) [53], [80]. Thus, if CSRRs and series gaps are loaded to a microstrip line, a CRLH line behavior can be obtained. Figure 2.21 shows the layout and equivalent circuit of a CRLH line implemented with CSRRs, where the CSRRs are allocated below the host line (etched in the ground plane) to be excited by an axial electrical field. The CSRR is modeled as a shunt parallel LC tank electrically coupled to the host line with inductance $L/2$ and shunt capacitance C_L.

Moreover, the series capacitance C_s adds a fringing capacitance which also affects the coupling with the CSRR. The model of Figure 2.21(b) can be simplified to that shown in Figure 2.22(a) if the following conditions are considered

$$C_{par} = C_f + C_L \tag{2.31}$$

$$2C_g = 2C_s + C_{par} \tag{2.32}$$

$$C = \frac{C_{par}(2C_s + C_{par})}{C_s} \tag{2.33}$$

where it can be seen that the model is the same as that of a conventional CRLH line but with an extra capacitance C. Figure 2.22(b) shows the measured magnitude response of the layout of Figure 2.21(a), in which it can be appreciated that if both CSRRs and capacitive gaps are present, then a left-handed behavior is obtained with the resulting band-pass transmission, the right-handed band being allocated at higher frequencies than the depicted region.
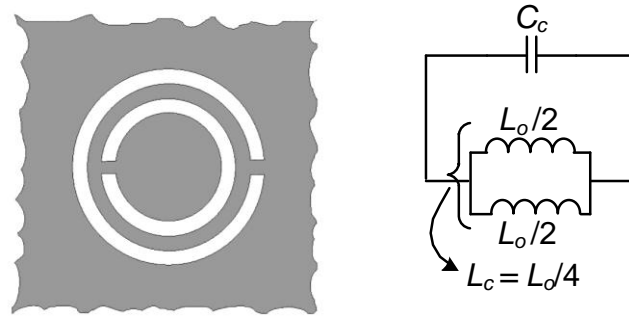
Figure 2.20. Topology and equivalent circuit of a CSRR, extracted from [53].
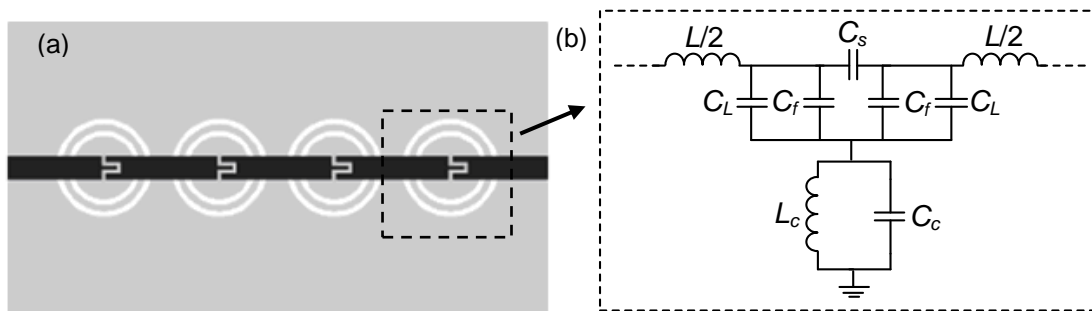
Figure 2.21. Layout (a) and equivalent circuit (b) of a CRLH line loaded with CSRRs and series gaps. Extracted from [48] (a) and [81] (b).
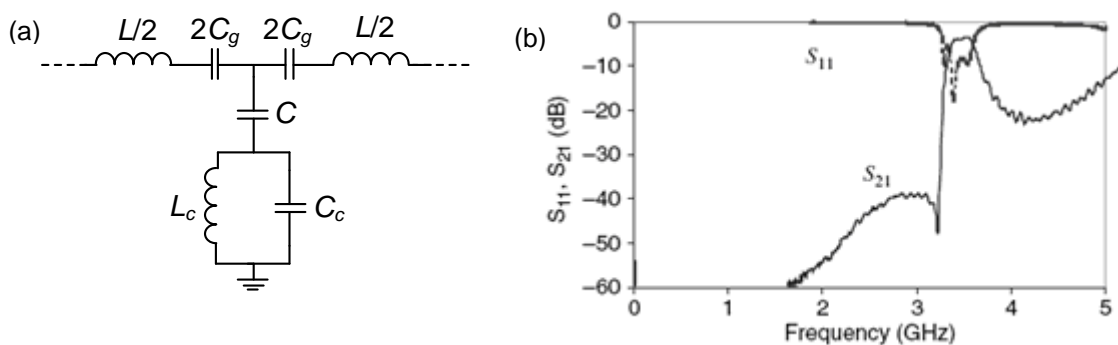

Figure 2.22. Simplified equivalent circuit (a) and measured response (b) of the layout of Figure 2.21(a). Extracted from [81] (a) and [48] (b).

Moreover, an additional transmission zero below the band (as occurred with the CRLH loaded with SRRs) also appears, due to the resonance of the shunt branch (i.e., the resonance of the *LC* tank and the capacitance *C*). The presence of a transmission zero below the band in both SRR or CSRR loaded CRLH lines can be of interest for certain applications such as filters. Nonetheless, for other applications where severe conditions of bandwidth are required, this aspect can be a drawback. In chapter 3, an alternative to obtain a CRLH line that does not present any transmission zero below the band will be presented. To this end, the open resonators will be considered, which will result in a behavior similar to that obtained with the *CL*-loaded approach presented in [65] - [68].

2.3 Applications of metamaterial transmission lines

Based on the theory exposed in section 2.2, specifically on the concepts of artificial or metamaterial transmission lines, a vast number of microwave applications have emerged which take advantage of the controllability of both the dispersion and impedance of these lines, as well as their small electric size.

In this section, different applications will be presented, focusing only on passive non-radiating-wave applications. In particular, we will review some of the applications reported in the literature for size reduction, multi-band functionality and band-pass filter design, which are the aspects that will be treated in chapters 3 and 4. Additionally, in [46] - [49] a broader review can also be found analyzing active devices or antennas, as well as other passive applications such as coupled-line couplers, enhanced-bandwidth devices, implementation of extreme impedance transmission lines, or other filter topologies and responses.

2.3.1   Size reduction

One of the advantages of metamaterial transmission lines is the small electrical size of their unit cells, as well as the controllability of both dispersion diagram and characteristic impedance. The former aspect can be applied to reduce the size in certain applications.

In [82], the CRLH line based on CSRR and series gaps implemented in microstrip technology, presented in section 2.2.4.2, was applied to the design of impedance inverters. For this purpose, a condition of $\beta l = -90^{o}$ and an impedance of $\sqrt{2}Z_{0}$ was forced by means of equations (2.16) and (2.20), where the negative sign condition in the electrical length was applied to work at the left-handed band and thus increase the degree of miniaturization.

Since the CRLH line has additional elements in comparison with the conventional transmission line, the direct relation between physical length and phase shift is no longer valid. As a result, it is now possible to force a phase shift of -90° with a size much smaller than $\lambda_{g}/4$, with λ_{g} being the guided wavelength of the host medium (i.e., the microstrip line). In fact, the quarter wavelength condition will still be satisfied, but for the guided wavelength of the effective artificial medium λ_{gam}, which is much smaller than λ_{g}, hence obtaining the desired miniaturization.

Figure 2.23 shows the layout of a power divider implemented with the resulting artificial lines compared with a conventional power divider, where roughly 50% size reduction can be appreciated. Figure 2.23(c) also shows the frequency response of the artificial line based divider and conventional power divider. With the artificial line approach, a good performance is obtained, although in a narrower band as compared to the conventional approach. In [82], this study is extended to other types of power dividers, as well as multi-output power dividers, obtaining a similar performance.
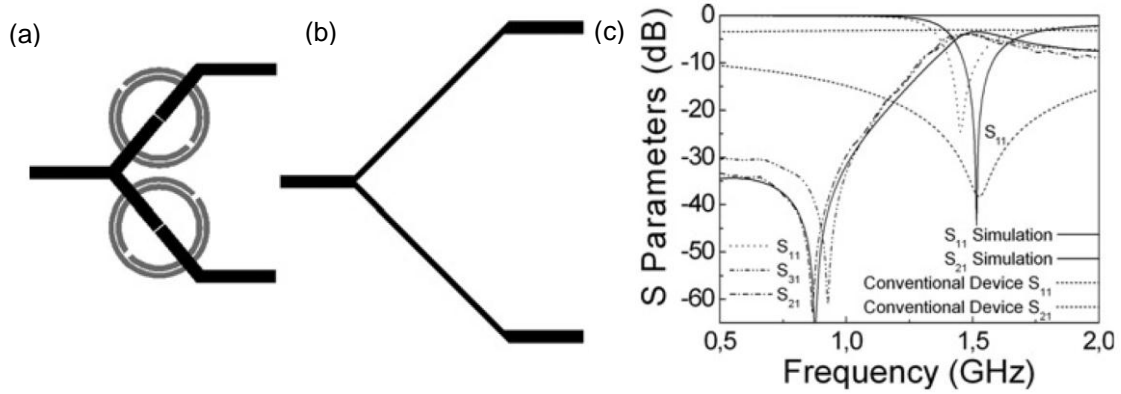
Figure 2.23. Layout of the power divider based on CRLH lines (a) and conventional transmission lines (b) with same operating frequency. The frequency responses are compared in (c). The CSRRs of the ground plane are indicated in gray color. Extracted from [82].

CRLH lines can also be applied to miniaturize phase shifters. Since a CRLH line has both left- and right-handed wave propagation, it can lead to a positive, negative or zero phase shift, whereas a conventional transmission line can only exhibit a negative phase shift due to a positive group and phase velocity. Moreover, the relation of a higher phase with a higher length is not required for CRLH lines, since additional elements are present. These aspects make the metamaterial based phase shifters very suitable to be applied for phase compensation. In [47], [49], zero-degree CRLH lines were presented in order to use them on feeding networks for antenna arrays. These artificial lines avoid the use of -360º conventional phase-shifters, which are normally very large. Figure 2.24(a) shows the photograph of the implementation of a CPW based 2-stage and 4-stage zero-degree phase shifting lines.

These lines are implemented by means of series capacitances and shunt inductances to obtain the left-handed behavior and conventional transmission line sections to obtain the right-handed behavior. Figure 2.24(b) also shows its phase and magnitude response in comparison with a conventional -360º phase shifter. As can be seen, the metamaterial approach enables the possibility of designing a more compact and flatter response than the conventional phase shifters, with the additional ability of forcing either a positive or negative phase shift.
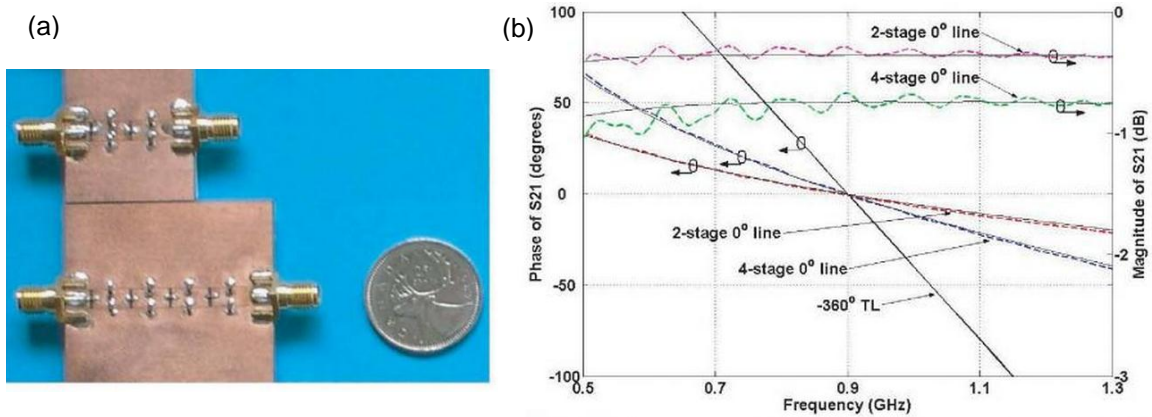

Figure 2.24. Two-stage and four-stage phase shifters (a); Phase and insertion loss (b) of the metamaterial-based zero-degree phase shifters and a conventional -360º phase shifter. Extracted from [49].

2.3.2   Multi-band applications

Another main advantage of the CRLH lines presented in chapter 2.2.3 is that they present *N* different propagation bands (*N* depending on the combination and number of reactive elements). One potential application of this feature is the possibility of forcing a characteristic impedance and phase condition in each band, with this aspect being very suitable for multi-band microwave devices, since it reduces the size and number of components present in communication systems.

In Figure 2.25 the dispersion diagram and Bloch impedance of a balanced CRLH line with two propagation bands based on the circuit model of Figure 2.11 is depicted, as well as that of a conventional transmission line based on the incremental circuit model of Figure 2.6(a). As can be seen, the conventional transmission line has constant impedance with frequency and a mono-band propagation nature.[7] Therefore, due to the limited number of reactive elements (circuit model) as well as the linear-frequency dependence, if the values of inductance and capacitance of the conventional transmission line are set to force an arbitrary phase and impedance at a certain frequency ω_1, additional conditions cannot be satisfied. On the other hand, since the CRLH line presents two propagation bands, as well as frequency-dependent impedance, a condition of an arbitrary (and not necessarily the same) phase and impedance can be forced at two different arbitrary frequencies ω_1 and ω_2, which are allocated in the right- and left-handed propagation band, respectively. Moreover, this procedure is straight-forward since the model of a CRLH line has four different reactive elements and four requirements (an impedance and phase at two arbitrary frequencies). In addition, this procedure is extendible to a CRLH line of arbitrary order.

Using these concepts, an *N*-band impedance inverter with a phase shift alternating from 90º and -90º (or equivalently 270º) and specified impedance can be designed. By means of this impedance inverter, different multi-band microwave applications such as branch line couplers, rat-race couplers or Wilkinson power dividers can be implemented among others.
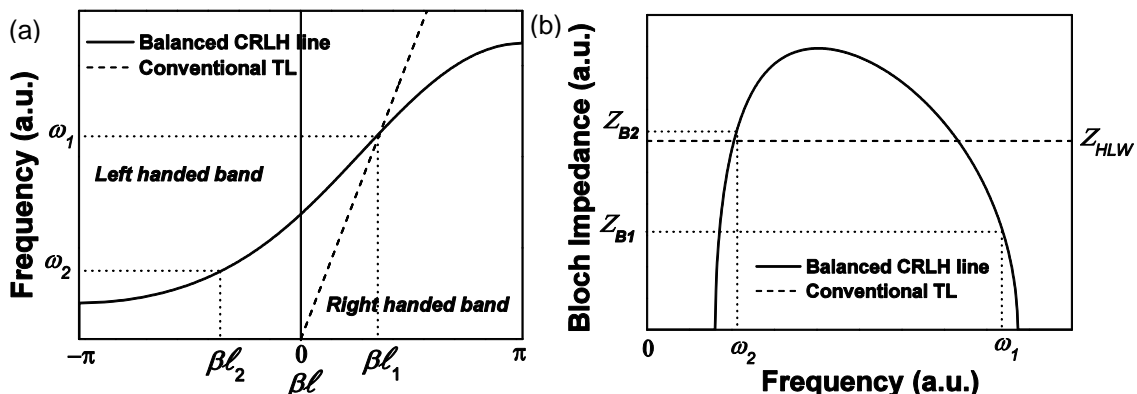
Figure 2.25. Dispersion diagram (a) and Bloch impedance (b) of a balanced CRLH line and a conventional transmission line.

---

[7] Note that although the same functionality appears at the odd harmonics, this is not considered as multi-band nature since the frequency position as well as the values of impedance and phase at these other bands cannot be controlled without altering the response at the first band.
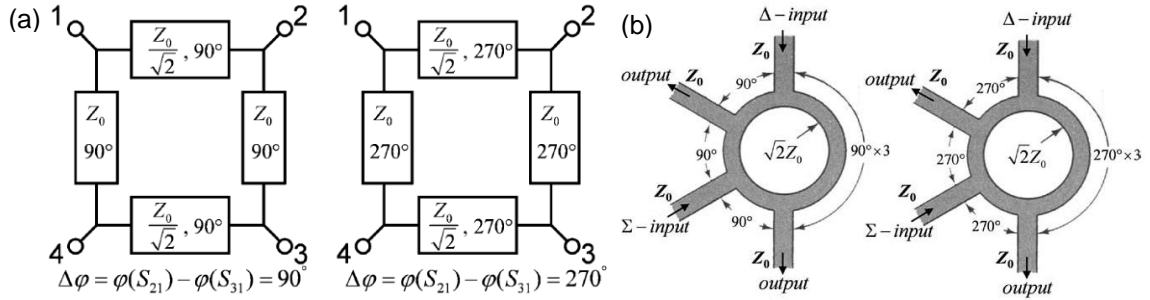
Figure 2.26. Conceptual schematic for each operation frequency for the dual-band branch line (a) and rat-race (b) coupler. Extracted from [83].

In [83], a dual-band branch line and rat-race couplers implemented by means of SMT chip components (to obtain the left-hand contribution) and microstrip-line sections (to obtain the right-hand contribution) was presented. To compensate for the effects of the frequency-dependent reactance of the chip inductors and capacitors, an additional tuning stub was added to the left-handed section of the dual-band branch line. Figure 2.26 and Figure 2.27 show the resulting conceptual schematic for each operation frequency and the photograph of the fabricated devices with its equivalent circuit for the case of the branch line and rat-race coupler, respectively. Figure 2.28 also shows the measured magnitude response for the dual-band branch line and rat-race couplers. For the case of the dual-band branch line coupler the required functionality is achieved at the GSM bands of 930 MHz and 1.78 GHz, whereas for the dual-band rat-race coupler the frequency operations are chosen at 1.5 GHz and 3 GHz. In both cases, a transmission very close to -3 dB can be appreciated.

Lately, these devices were also implemented in fully-planar technology by means of the resonant-type approach. Specifically, the CRLH line based on CSRRs can be designed to satisfy the conditions of a dual-band impedance inverter. This approach was considered in [84] to implement a dual-band branch line coupler at the GSM frequencies 0.9 GHz and 1.8 GHz, showing in Figure 2.29 the layout as well as the magnitude response, where a similar behavior as that obtained with the *CL*-loaded approach can be obtained but with neither vias nor SMT components.
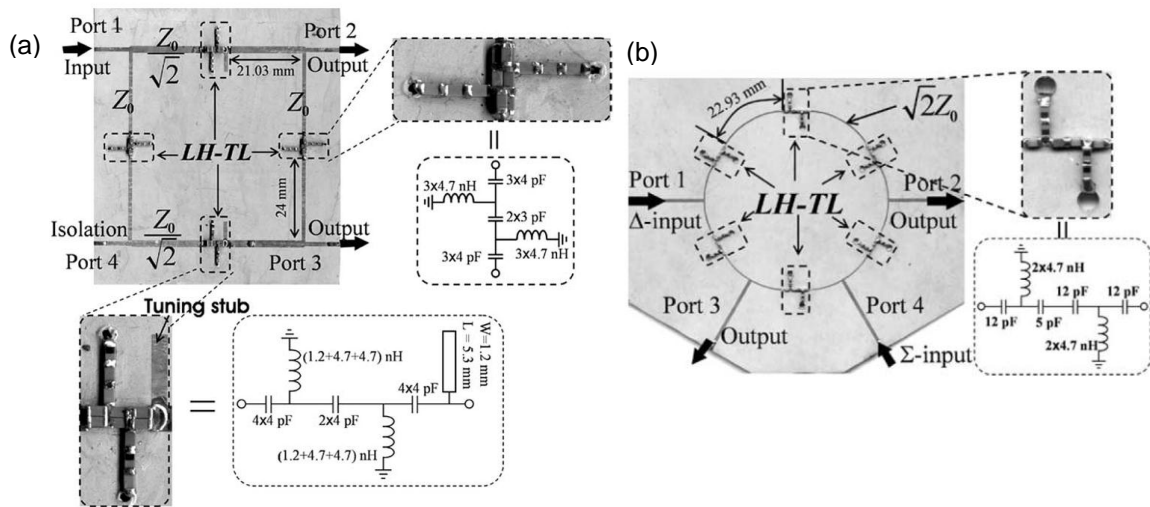
Figure 2.27. Photograph of the fabricated device and equivalent circuit for the dual-band branch line (a) and rat-race (b) coupler. Extracted from [83].
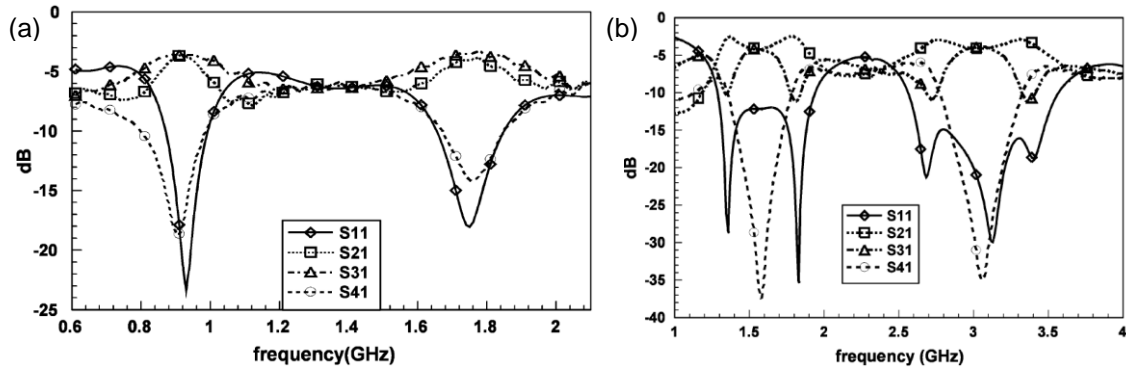
Figure 2.28. Measured S-parameters for the dual-band branch line (a) and rat-race (b) couplers of Figure 2.27. Extracted from [83].
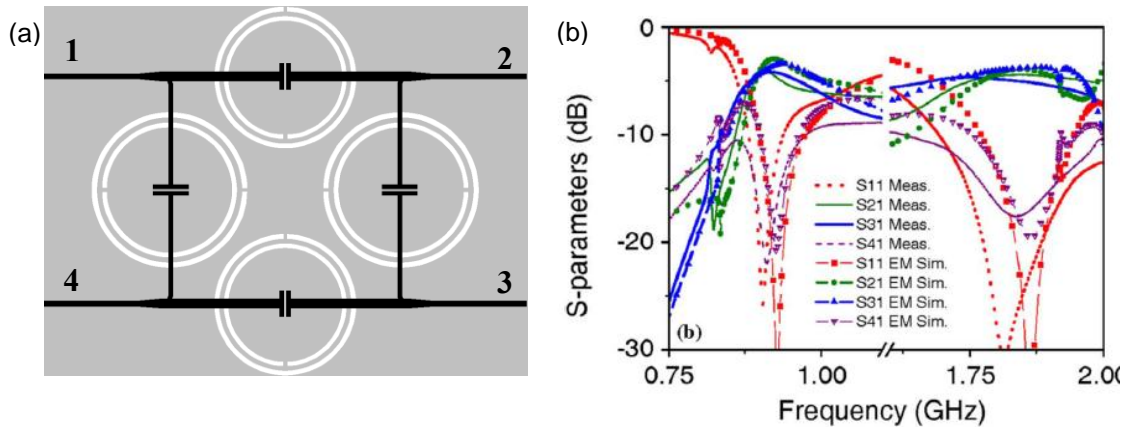
Figure 2.29. Layout (a) and frequency response (b) of the dual-band branch line coupler implemented by the resonant approach. Extracted from [84].
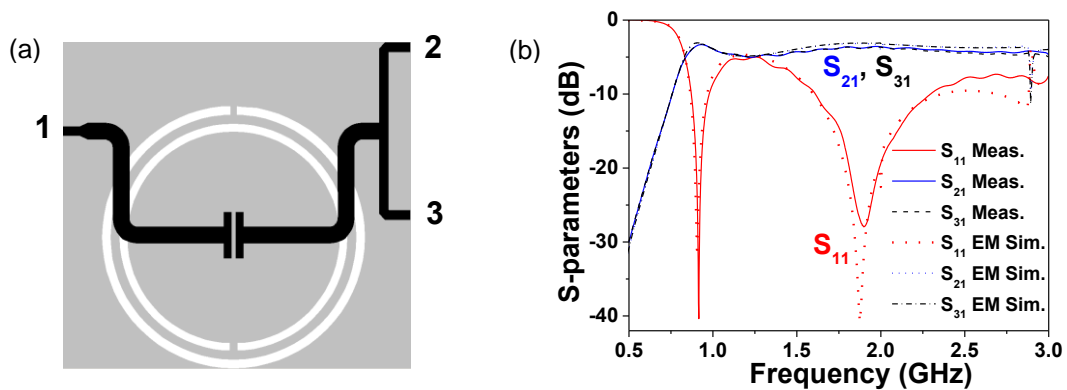
Figure 2.30. Layout (a) and frequency response (b) of the dual-band Y-junction power divider implemented by the resonant approach. Extracted from [85].

In addition, in [85] this cell was also employed to implement dual-band Y-junction power dividers operative at the same GSM frequencies, as shown in Figure 2.30 with its frequency response. Moreover, in order to further miniaturize the devices, in [85] and [86] the same branch line coupler and power divider presented in Figure 2.29 and Figure 2.30 was also presented, but with the so called complementary spiral resonator (CSR), which presents roughly half the electrical size of the CSRR, obtaining similar results to those depicted but with reduced size. Furthermore, both dual-band approaches based on CSRRs and CSRs presented smaller electrical dimensions than the conventional mono-band devices.

After the appearance of these applications, different authors ([71], [87], [88]) investigated the possibility of designing tri-band and quad-band unit cells in planar technology by means of the Double-Lorentz and E-CRLH lines presented in Figure 2.14. In [87], the quad-band planar artificial line topology of Figure 2.31 was proposed requiring discrete chip elements to implement the capacitors of the series branch. By means of this planar unit cell, a quad-band Wilkinson power divider was presented in [89], where due to the application requirements all the inductive elements were also replaced for chip inductors, only implementing in planar technology the capacitances of the shunt branch. Figure 2.32 shows the layout, as well as the matching response, appreciating the quad-band functionality at the frequencies of 775 MHz, 1.40 GHz, 2.72 GHz and 3.80 GHz.

In [90], the unit cell of Figure 2.31 was also employed to implement a dual-band band-pass filter. This can be achieved by forcing a continuous transition between the left-handed and right-handed propagation bands. Hence, two bands appear, in the same way that a continuous propagation band appeared in a conventional CRLH line if the condition of a balanced transmission line was forced. Figure 2.33 shows the layout and response of the proposed dual-band band-pass filter, requiring only chip capacitors in this case to implement the capacitances of the series branch as initially proposed in [87]. A dual-band behavior is obtained, but with a poor matching in each band. This is due to an erroneous application of the balanced conditions, which led to a wrong design, as explained and corrected in [91], [92]. If the correct equations are applied, then a filter characteristic such as that shown in Figure 2.33(d) is obtained.
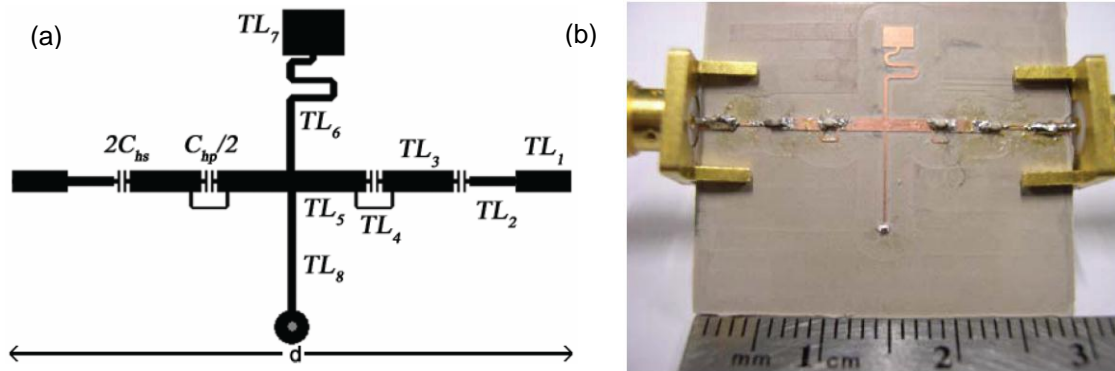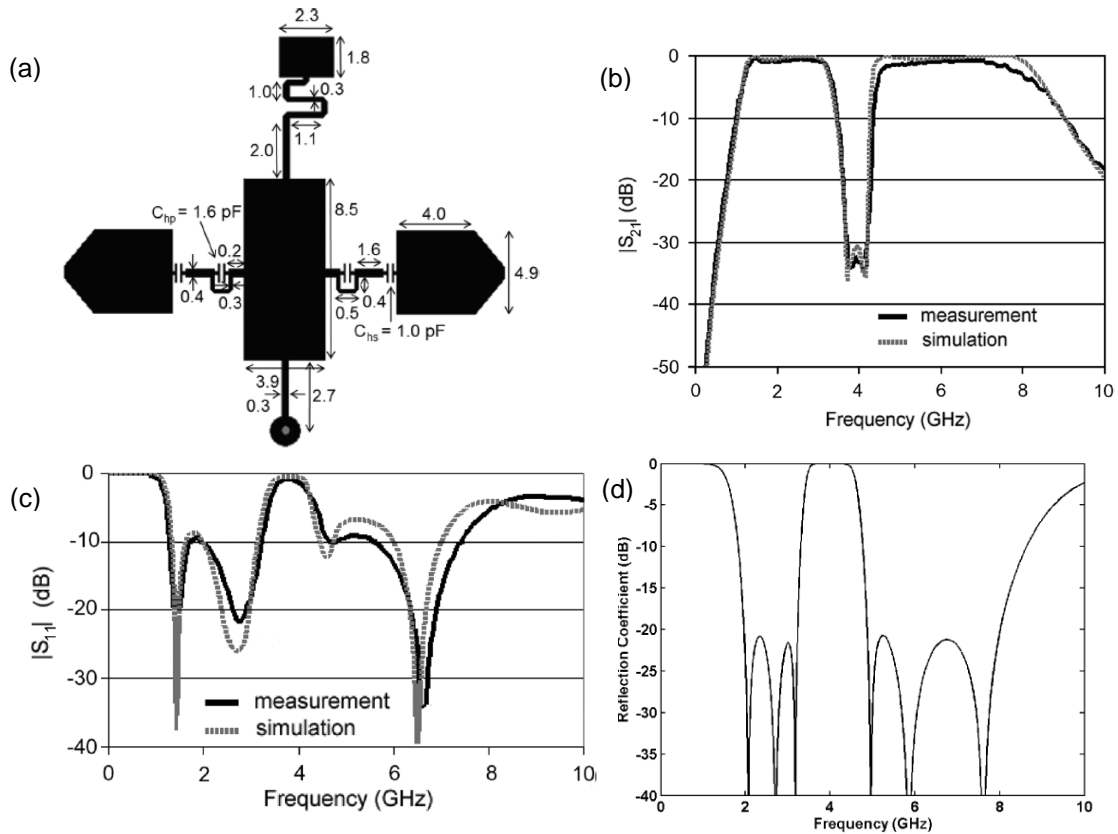

Figure 2.31. Layout (a) and photograph (b) of a planar unit cell of an E-CRLH line. Extracted from [87].
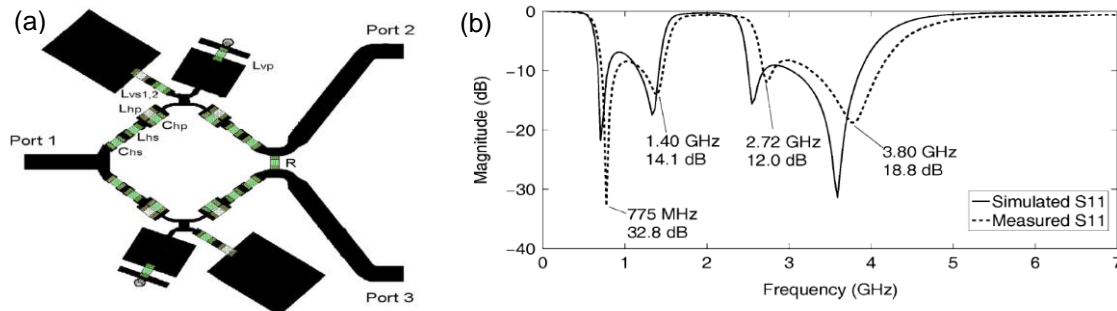
Figure 2.32. Layout (a) and matching (b) of a quad-band Wilkinson power divider. Extracted from [89].

Figure 2.33. Layout (a), insertion losses (b) and return losses (c) of the dual-band band-pass filter extracted from [90]. The return losses of the circuit response with same requirements but with a correct design is also depicted (d), extracted from [91].

In fact, it can be observed that the resulting response is that of a third-order dual-band filter, since both circuit models are the same (in the same way that the conventional CRLH model is the same as that of a third-order mono-band band-pass filter). Thus, in this case, the same characteristics could be obtained by means of the classical Chebyshev filter design with the corresponding additional transformations to obtain the dual-band nature [27], [43]. In section 3.3.3, it will be shown that similar dual-band band-pass filters to those of [90], but based on open resonators, can be implemented in a fully planar configuration.

In [88], an alternative topology to implement fully-planar E-CRLH lines was presented, reproducing the resulting topology in Figure 2.34(a)-(b). As can be seen from the dispersion diagram of Figure 2.34(c), four bands appear in the electromagnetic simulation, although there is a considerable disagreement between the electromagnetic and circuit simulation. Moreover, to our knowledge an application based on this approach has not yet been presented. Consequently, although an application of the fully-planar unit cell of Figure 2.34 has not been presented so far, the up-to-date limited agreement between circuit and electromagnetic response would lead to a higher level of difficulty to implement quad-band devices with specific requirements.

Although several applications have been presented based on the CRLH unit cells of Figure 2.30 and the E-CRLH unit cells of Figure 2.31, none of these applications presented a comparison between circuit and electromagnetic simulation or analyzed the parasitic behavior that could lead to the discrepancies between both.
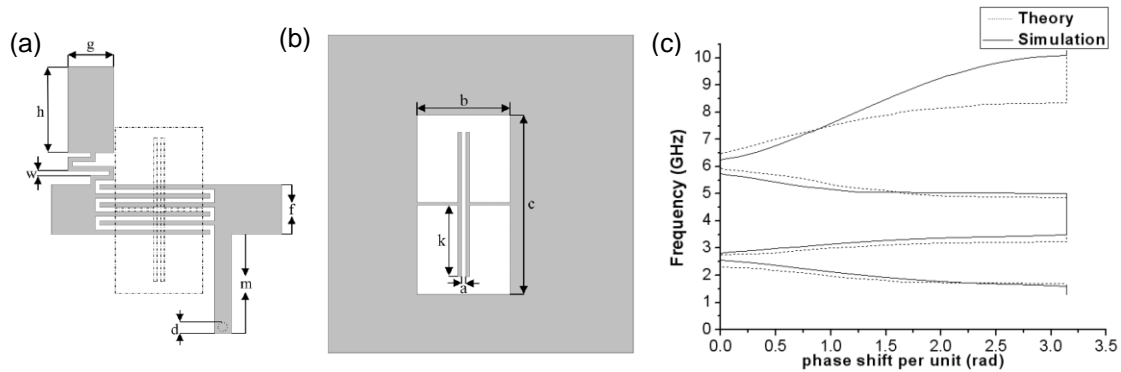
Figure 2.34. Top (a) and bottom (b) view of the layout and dispersion diagram (c) of a fully-planar E-CRLH line. Extracted from [88].

Therefore, since the design is strongly dependent on the dispersion diagram and Bloch impedance, these latter approaches will also lead to a complex procedure to meet a set of real specific requirements. In chapter 3, a fully-planar approach of CRLH and E-CRLH lines based on open particles will be provided and applied to the design of dual-band and quad-band components. A comparison of the circuit model and electromagnetic simulation will be presented and considered, which will be of huge help for the design process, making it easier to control all the bands and understand the full response behavior.

2.3.3   Band-pass filters

Given the small electric size of the SRRs or CSRRs, these metamaterial resonators have highly contributed to offering new strategies for filter design. Considering the most basic structure, that is, SRRs or CSRRs coupled to a host line, a notch in the response appears thanks to these resonators, having applied these structures to the design of stop-band filters both in CPW [93] and microstrip [94] technology with SRRs and CSRRs, respectively. These resonators can also be added to conventional filters for spurious suppression [94], showing in Figure 2.35 a microstrip coupled-line band-pass filter loaded with SRR in order to suppress the harmonics, achieving a rejection level better than 30 dB for the first spurious, as well as also suppressing the second harmonic.
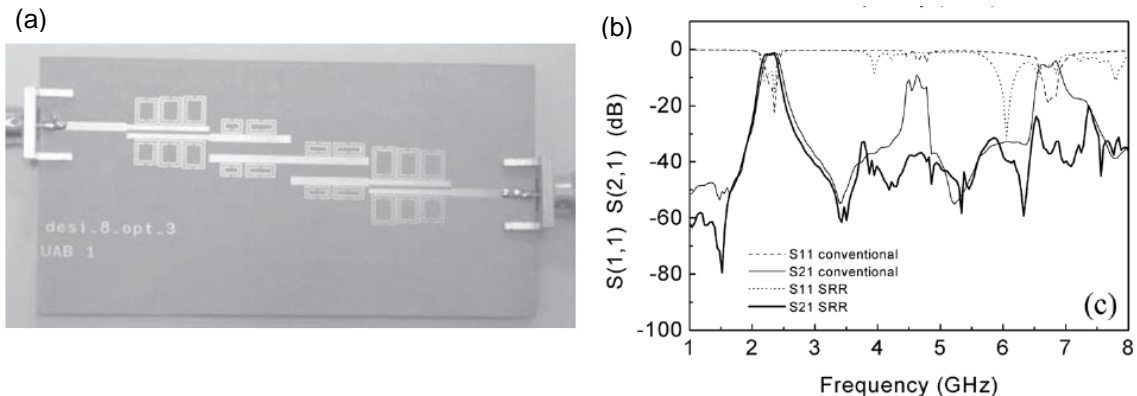
Figure 2.35. Layout (a) and measured frequency response (b) of a microstrip coupled-line band-pass filter loaded with SRR. In (b) the simulation of a conventional microstrip coupled-line filter is also added for comparison purposes. Extracted from [94].

In addition, since the conventional CRLH line has the same circuit model as that of a third-order band-pass filter, several authors have presented different topologies based on or inspired by metamaterial concepts.

In [95], the CRLH line based on CSRRs was applied to the design of a wideband band-pass filter. To this end, three identical balanced CRLH lines were cascaded. In Figure 2.36(a) the layout of the filter is depicted, in which interdigitated capacitors were required to meet the specifications. Figure 2.36(b) also shows the frequency response, where a wideband and flat response is obtained, albeit with the drawback of a poor frequency selectivity at the upper band edge.
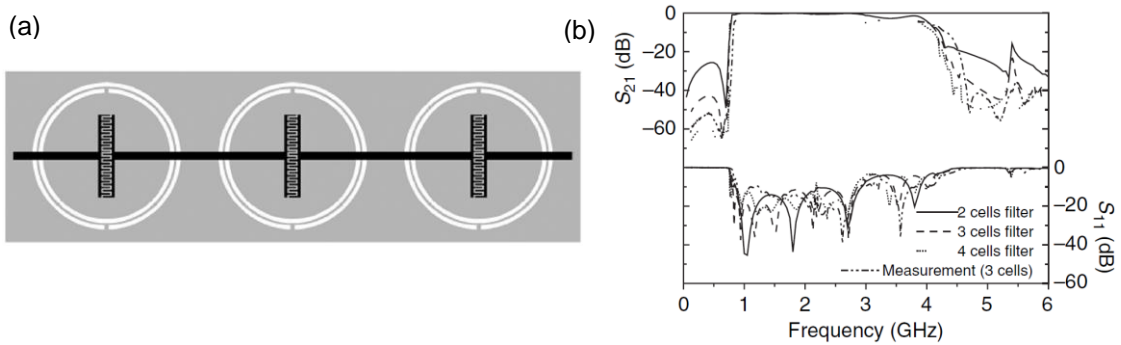
Figure 2.36. Layout (a) and frequency response (b) of a filter formed by three identical balanced CRLH lines. Extracted from [95] (a) and [48] (b).
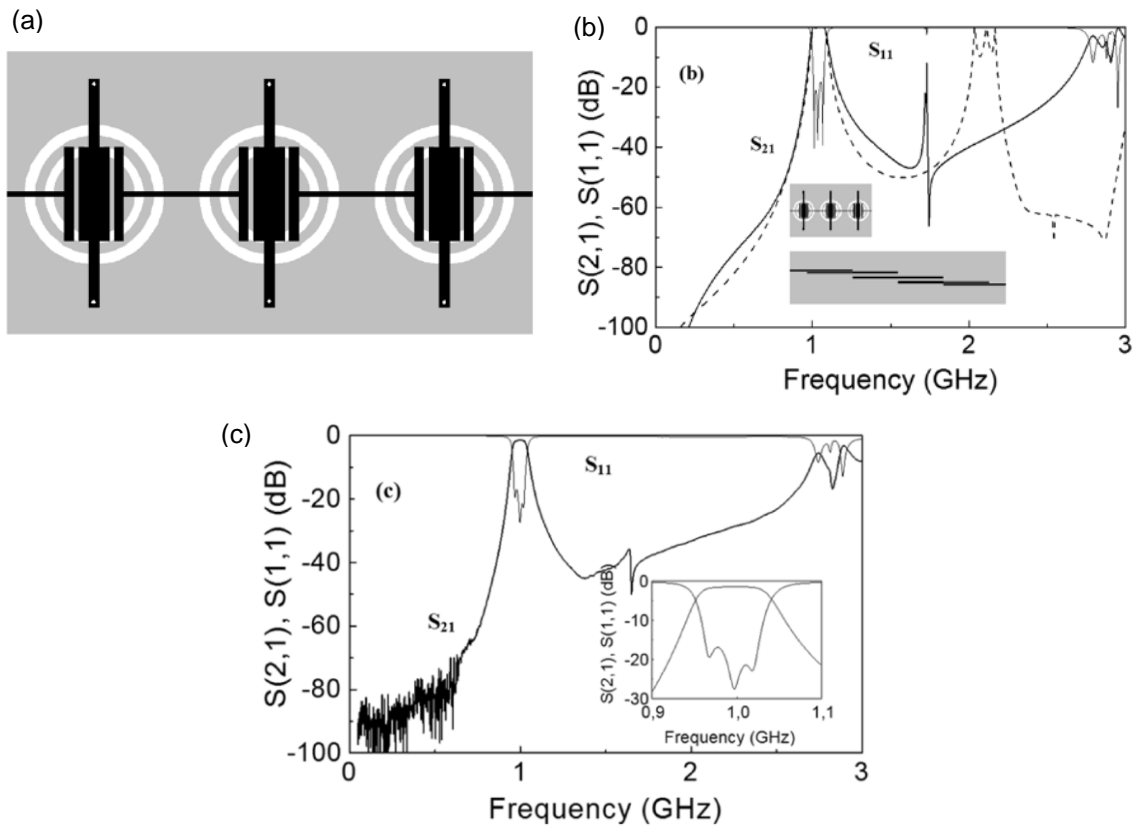
Figure 2.37. Layout (a), simulated (b) and measured (c) frequency response of a filter formed by three identical hybrid CRLH lines. In (b) the simulation of a conventional microstrip coupled-line filter is also added for comparison purpose. Extracted from [97].

34
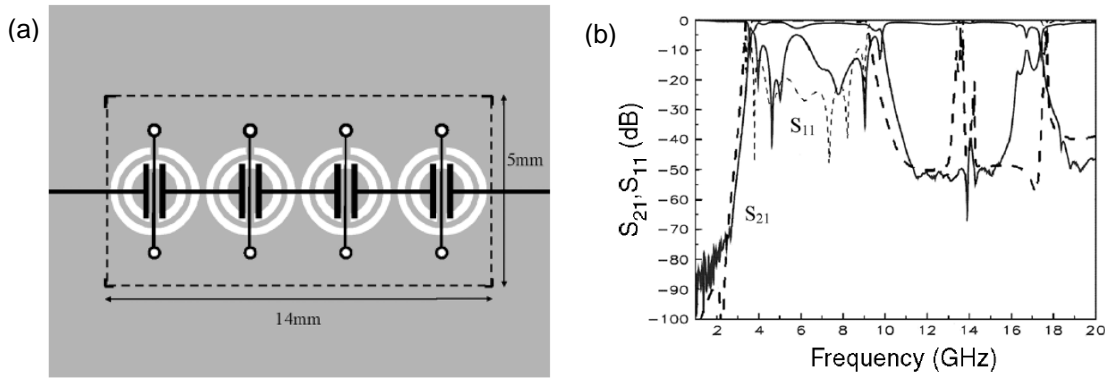
Figure 2.38. Layout (a) and frequency response comparison of the electromagnetic simulation (dashed line) and measurement (solid line) (b). Extracted from [95].

In order to improve this latter aspect, in [96], [97] an additional shunt inductance was added to the basic CSRR unit cell, renaming the resulting line as the hybrid cell, shown in Figure 2.37(a). A richer dispersion diagram arises, with three propagation bands and a transmission zero. This transmission zero can be applied for narrow-band band-pass filters if the first left-handed band is considered, as shown in Figure 2.37(b), where a better stop-band rejection is obtained if compared with the initial CSRR unit cell or with a conventional microstrip coupled-lines filter (the latter is also depicted in the figure).

Moreover, if the balanced condition is forced on these hybrid cells, wideband responses such as those shown in Figure 2.38 can be obtained [95], with the resulting compact dimensions. Nonetheless, in these latter cases an accurate equivalent circuit that models the whole band has been found to be very complex, thus complicating the design process and/or the fulfillment of specific requirements. To this end, in chapter 3, an alternative approach based on open resonators will be considered for wideband filters, with the main advantage of presenting an accurate circuit model that is valid throughout the band, thus simplifying the design process.

In **summary**, this has been an introductory chapter, where the state of the art on miniaturization of planar microwave components (mainly focused on the devices considered in this thesis) has been reviewed. We have also introduced the metamaterial transmission line concept, with special emphasis on the CRLH line. Additionally, we have provided the fundamental theory for the design of devices based on metamaterial transmission lines and some applications have been reviewed, with an eye towards size reduction, multi-band components and planar filters.

CHAPTER 3

Artificial lines based on OSRRs and OCSRRs and applications

After applying the SRR to the synthesis of left-handed structures and artificial transmission lines, several authors have studied the possibility of implementing split rings with smaller size or different properties. By these studies, new particles such as the non-bianisotropic split ring resonator (NB-SRR), the archimedean spiral resonator (ASR) or the already mentioned spiral resonator (SR) and its dual counterpart CSR have appeared, among others [53], [98] - [100].

In 2004, Martel *et al.* presented the OSRR, considering this resonator as the open version of the SRR [101]. In this case, the term "open" denotes that this resonator presents two metallic terminals by which the particle can be excited either by a voltage or current source, unlike the SRRs or CSRRs, which are driven by magnetic or electric coupling. Afterwards, in 2009 Vélez *et al.* presented the OCSRR, obtained by applying duality to the OSRR, in the same manner that the CSRR was obtained from the SRR

[102]. Through these works, as well as [103], [104], these particles have been proven to be suitable for the design of band-pass filters by means of coupling either OSRRs or OCSRRs through impedance inverters.

In this chapter, the study to design artificial lines through the combination of these particles altogether will be presented. As will be seen, if these lines are applied to band-pass filters, a further miniaturization will be achieved in comparison with the above-mentioned approaches due to substitution of the impedance inverters with electrically small resonators.

In addition, the resulting artificial lines will have a similar behavior to those implemented by the *CL*-loaded approach, where no additional transmission zero below the frequency band will be present compared to the case of the SRR- or CSRR-based CRLH lines. Although this transmission zero could be useful for certain application such as filters, for other applications like dual-band components it tends to limit the operating bandwidth of the first band [84]. This new approach overcomes this drawback. To demonstrate this, a dual-band impedance inverter and power divider will be presented.

Furthermore, these open particles (combined with additional semi-lumped elements), will also be applied in section 3.3 to the design of E-CRLH lines. Such lines will enable the design of quad-band components and dual-band Chebyshev band-pass filters, where the full compatibility with planar technology as well as the detailed procedure for the synthesis of these lines using its circuit models will reveal a clear advantage in comparison to the already existing E-CRLH lines [87] - [91].

The electromagnetic and circuit simulation of all the devices that will be presented are obtained by means of the commercial software *Agilent ADS/Momentum.* The fabrication process of all these devices is based on standard photo/mask etching techniques. The measurement is obtained by means of the *Agilent E8364B* vector network analyzer.

3.1 The open resonators: topology and circuit model

Figure 3.1 shows the topology and equivalent circuit model of the OSRR and OCSRR. As was discussed in [101], the OSRR can be considered as a series *LC* resonator, where L_s is equivalent to the inductance of the SRR, i.e., the inductance of a closed ring of average radius $r_o = r_{ext}$ - c - d/2 and width c. On the other hand, C_s is four times the capacitance of the SRR, since in the SRR the upper and lower halves were series connected, whereas in the OSRR a distributed capacitance between the whole inner and outer rings is obtained. Thus, given the same dimensions and substrate, the resonance frequency of the OSRR is roughly half that of the SRR. In a similar manner, the OCSRR can be modeled as a parallel *LC* resonator, where C_p is equivalent to the capacitance of the CSRR, i.e., the capacitance of a disk of radius r_o - c/2 surrounded by a metallic plane at a distance c from its edge.

38
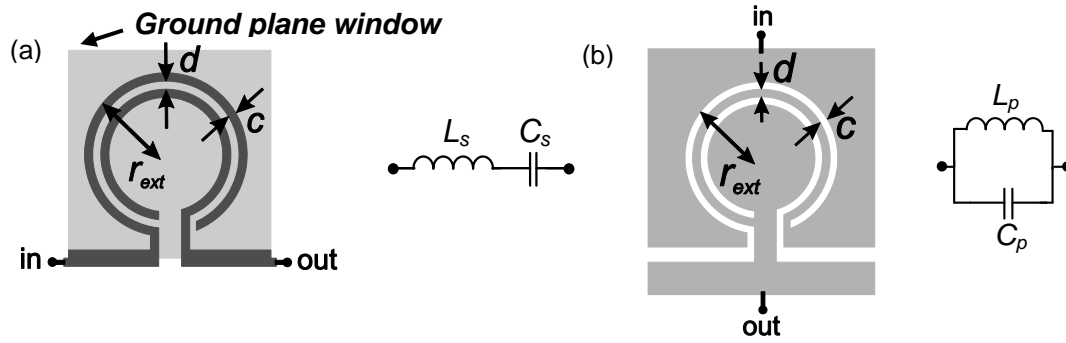
**Figure 3.1.** Topology and circuit model of the OSRR (a) and OCSRR (b).

On the other hand, L_p is four times the inductance of the CSRR, since it is the inductance of the metallic strip between the rings slots. Hence, given the same dimensions and substrate the OCSRR resonates at roughly half the frequency of the CSRR. For this reason, in view of the fact that both OSRRs and OCSRRs are twice as electrically small as their equivalent SRR and CSRR, respectively, the suitability of these particles to obtain compact microwave devices can already be envisaged, where the element values can be inferred according to the models reported in [53], [100] for the SRR and CSRR and their relation with the open particles [101], [102].

Since the OSRRs and OCSRRs are complementary particles, it is expected that their resonance frequencies will be roughly the same (provided identical dimensions and substrates are considered), as occurs with CSRRs and SRRs. With these latter particles, this aspect has been theoretically demonstrated and experimentally validated in [53]. Nonetheless, in the case of the open particles there is a higher degree of freedom on the dimensions, since the models do not account for the length of the connecting terminals of the resonators or the size of the ground plane window for the OSRR. Then, since these latter additional parameters do affect the frequency response, the duality between OSRR and OCSRR will not be as accurate as that between the SRR and CSRR. Additionally, although the presented models in Figure 3.1 describe the physical behavior of these particles to a good approximation, in order to accurately use these resonators in microwave applications, the parasitic effects when these particles are coupled to a host line must be taken into account.

In the following section, the topology and circuit models of OSRR- and OCSRR-loaded CPW and microstrip transmission lines will be studied. Moreover, a parameter extraction method to infer the element values of the CPW circuit model will be provided.

3.1.1 Circuit models of the open particles in CPW technology

Figure 3.2 shows the topology and electromagnetic simulation of the frequency response of an arbitrary series connected OSRR in a CPW host transmission line, where the asymmetry in width and length of the terminals is chosen in order to match the particle to the ports. As can be seen from the S-parameters, the resulting frequency response in magnitude is the characteristic response of a series *LC* resonator, with a resonance frequency close to 3 GHz in this case.
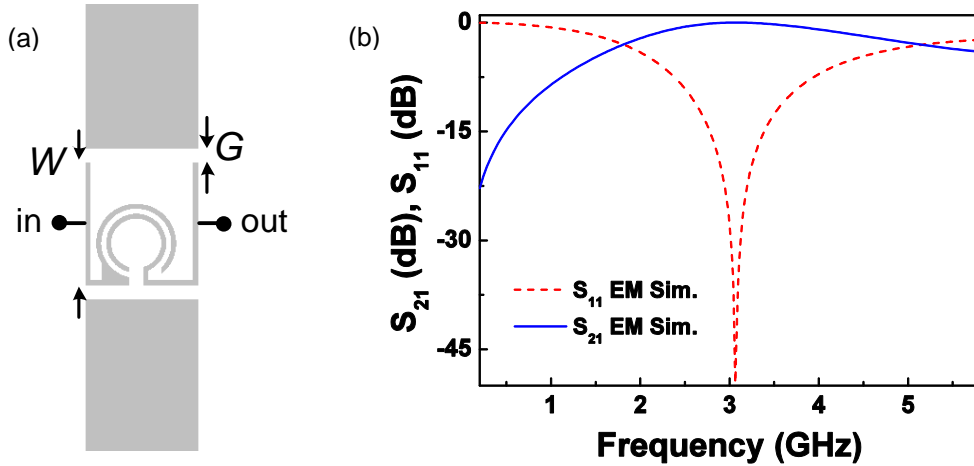
Figure 3.2. Topology (a) and electromagnetic simulation of the frequency response (magnitude) (b) of a series connected OSRR in a CPW transmission line. This structure has been implemented on the *Rogers RO3010* substrate with thickness h = 0.254 mm and measured dielectric constant ε_r = 11.2. The dimensions are: W = 5 mm, G = 0.55 mm, r_{ext} = 1.6 mm and c = d = 0.2 mm.

In order to study the phase variation, Figure 3.3 also shows the S_{11} in the Smith Chart, and the phase of S_{21} corresponding to the topology of Figure 3.2(a). The expected behavior of an ideal *LC* series resonator, with an S_{11} allocated in the unit resistance circle of the Smith Chart at all frequencies is not obtained, and the phase of S_{21} exhibits a shift of roughly 20º at resonance. Thus, this fact invalidates the possibility of considering a series OSRR in CPW technology merely as a series *LC* resonator. An easy procedure to deduce the circuit model that accurately describes the behavior of the resonator is by analyzing the series and shunt impedances of the equivalent *T-* or *π*-circuit model. These reactances can be obtained from simulation by means of the well-known S-parameters transformations [1]. The reactances of the *π*-model of the structure of Figure 3.2(a) are depicted in Figure 3.4.

Through this analysis, it can be deduced that the series reactance of the OSRR behaves as that of a pure series *LC* resonator in the region of interest. To prove this fact, a circuit simulation of a series *LC* tank has also been added in the figure, where a perfect fitting can be appreciated in the region of interest. Furthermore, an additional shunt capacitive effect is appreciated by inspection of the parallel reactance, where the symmetric condition is satisfied (X_{p1} = X_{p2}). The response perfectly fits the curve of a capacitor in the region of interest. Nonetheless, a small resonance can be appreciated in the parallel reactance below the resonance frequency, in this specific case being practically nil, but becoming very pronounced in certain cases. Specifically, the reactances X_{p1}, X_{p2} exhibit opposite resonances (one tends towards $-\infty$ whereas the other towards ∞).

Therefore, from the Foster theorem it can be deduced that since a negative reactance slope is present, the resulting circuit cannot be modeled with a *T-* or *π*-model by means of a combination of reactive elements. This is due to a series inductance at the terminals of the shunt capacitances, which prevents the possibility of obtaining an equivalent *T-* or *π*-model. Nonetheless, this effect has been experimentally proven to be negligible both in magnitude and in phase, even in the

cases where it is abruptly present in reactance. For this reason and for design purposes, these inductances will be neglected in CPW technology.

Consequently, the aforementioned results can be interpreted as if the particle under study were to behave as a series *LC* resonator with an additional phase shift. Thus, the resulting equivalent circuit is that shown in Figure 3.5(a), which can be simplified to that of Figure 3.5(b) [105]. One of the advantages of the equivalent circuit shown in Figure 3.5(b) is that it allows an easy parameter extraction method. This method, explained in Appendix A, enables the possibility of inferring the element values of the OSRR for an arbitrary topology with an electromagnetic lossless simulated response.
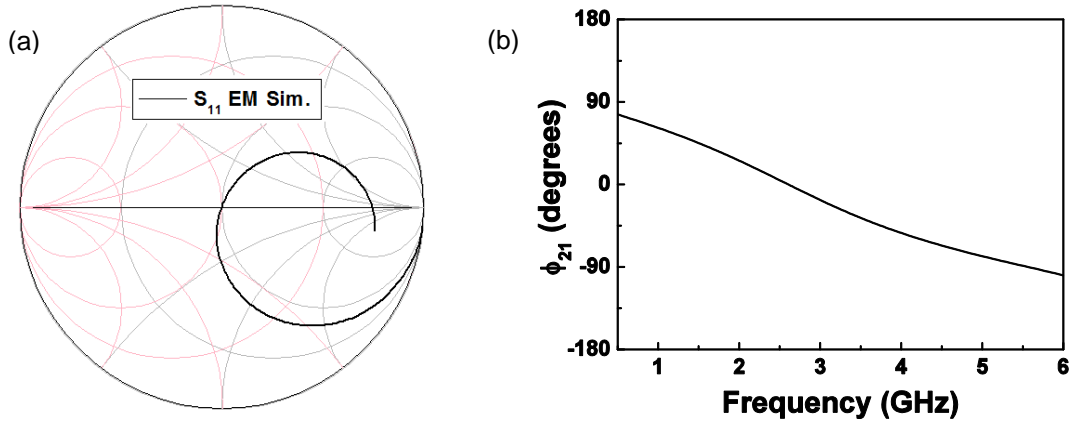
Figure 3.3. Representation of S_{11} in the Smith Chart (a) and phase of S_{21} (b) of the topology of Figure 3.2(a).
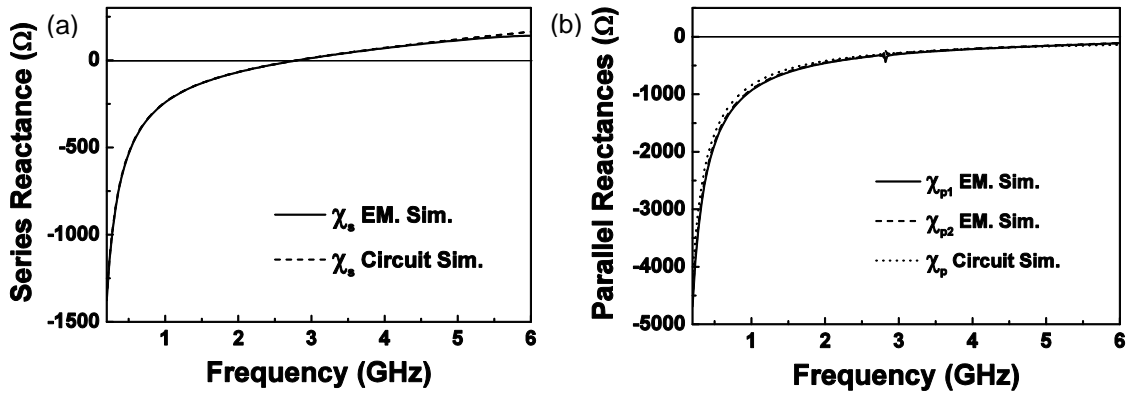
Figure 3.4. Series χ_s (a) and parallel χ_{p1}, χ_{p2} (b) reactances of the asymmetric π-model extracted through the S-parameters transformations of the electromagnetic and circuit simulation of the OSRR shown in Figure 3.2(a). The element values of the equivalent circuit in reference to Figure 3.5(b) are: $C = 0.189$ pF, $L'_s = 5.55$ nH and $C_s = 0.58$ pF.
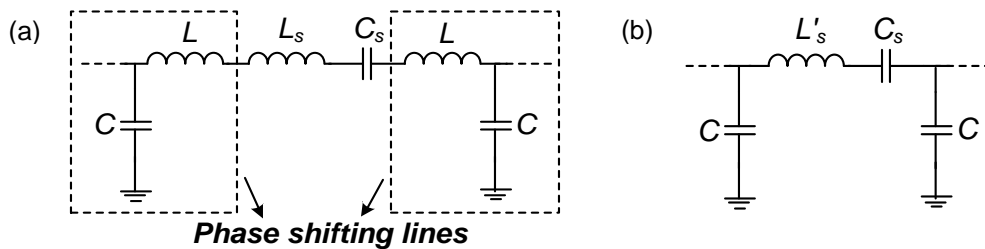
Figure 3.5. Circuit model of a series OSRR in CPW technology (a) and simplified model (b), where $L'_s = L_s + 2L$.
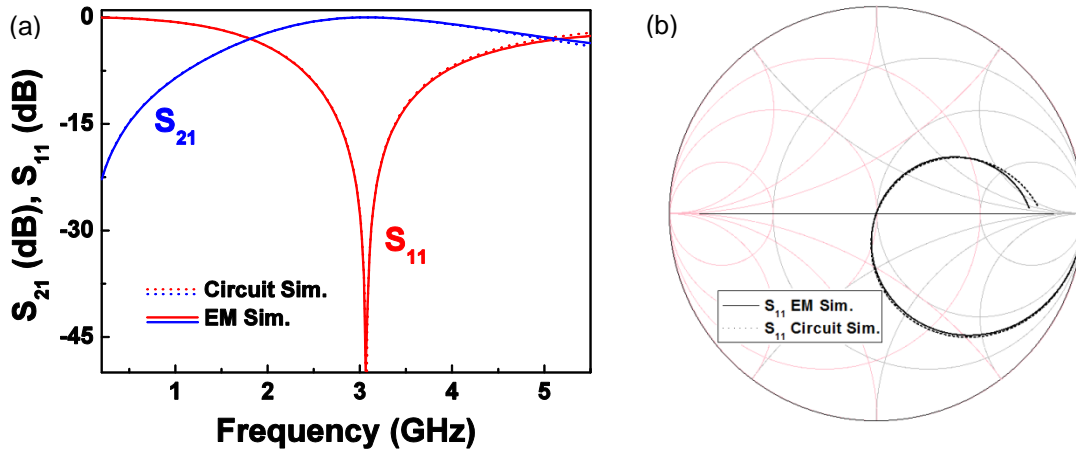
Figure 3.6. Electromagnetic and circuit simulation of the structure of Figure 3.2(a). Magnitude (a); Smith Chart (b). The element values of the equivalent circuit inferred by parameter extraction in reference to Figure 3.5(b) are: $C = 0.189$ pF, $L'_s = 5.55$ nH and $C_s = 0.58$ pF.

By way of example, Figure 3.6 shows the comparison between the electromagnetic and circuit simulation of the OSRR shown in Figure 3.2(a), where the element values have been inferred by this parameter extraction method. As can be appreciated from Figure 3.6, good agreement between circuit and electromagnetic simulation is obtained, thus validating the parameter extraction method, as well as the proposed circuit model.

A similar phenomenology arises if the same study is carried out with an OCSRR-loaded CPW transmission line, having to consider the phase shift to predict the frequency response of the structure. Figure 3.7 shows the topology of a pair of shunt connected OCSRRs, as well as the resulting equivalent circuit [105]. In order to prevent the slot mode, the different ground plane regions are connected through strips (etched in the ground plane) and vias. This forces the same potential between the different ground plane regions. An additional strip to connect the ground planes at both sides of the central strip could also be considered, with the additional effect of enhancing the shunt capacitance to ground, as shown in the topology of Figure 3.8(a).

As well as with the OSRR, a parameter extraction method for the OCSRR has also been deduced and reproduced in Appendix A. By means of the proposed equivalent circuit, as well as with this parameter extraction method, the comparison between electromagnetic and circuit simulation of an arbitrary OCSRR is shown in Figure 3.8, where the good agreement around the resonance frequency between the curves validates both the parameter extraction method and the circuit model. Nonetheless, a slight disagreement at lower frequencies and a more pronounced disagreement above the resonance frequency (above 4 GHz) are appreciated. This is due to the connection between the central strip of the CPW transmission line and the inner metallic region of the OCSRR, which generates an inductive effect in series with the shunt resonator. Hence, in order to consider this particle for applications where a prediction far below and beyond the resonance frequency is required, such as wideband devices, this additional inductive effect should be taken into account. Figure 3.9(a) shows the resulting wideband circuit model of an OCSRR-loaded CPW transmission line, where the approach of considering that the shunt capacitances C could still be absorbed by C'_p regardless of the presence of L_{sh} has been considered.
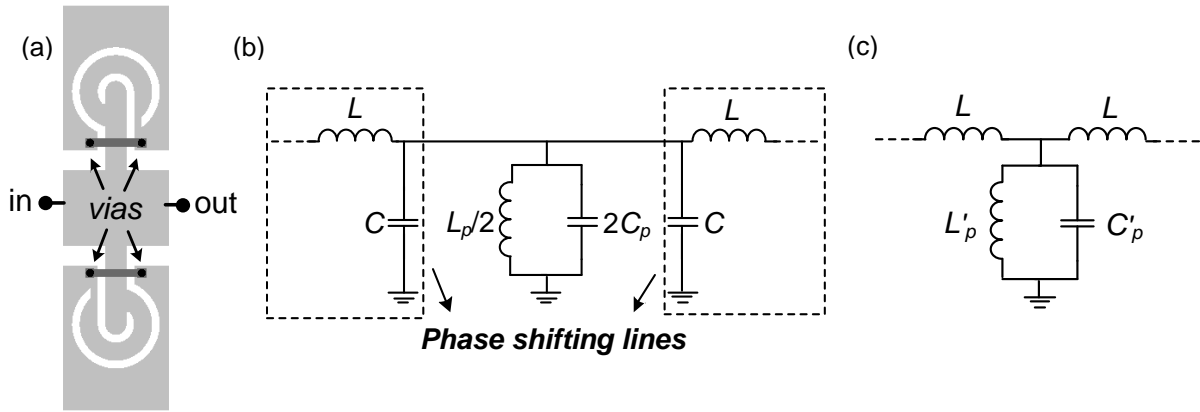
Figure 3.7. Topology (a), circuit model (b) and simplified circuit model (c) of a pair of shunt connected OCSRRs in a CPW transmission line, where $L'_p = L_p/2$, $C'_p = 2(C+C_p)$.
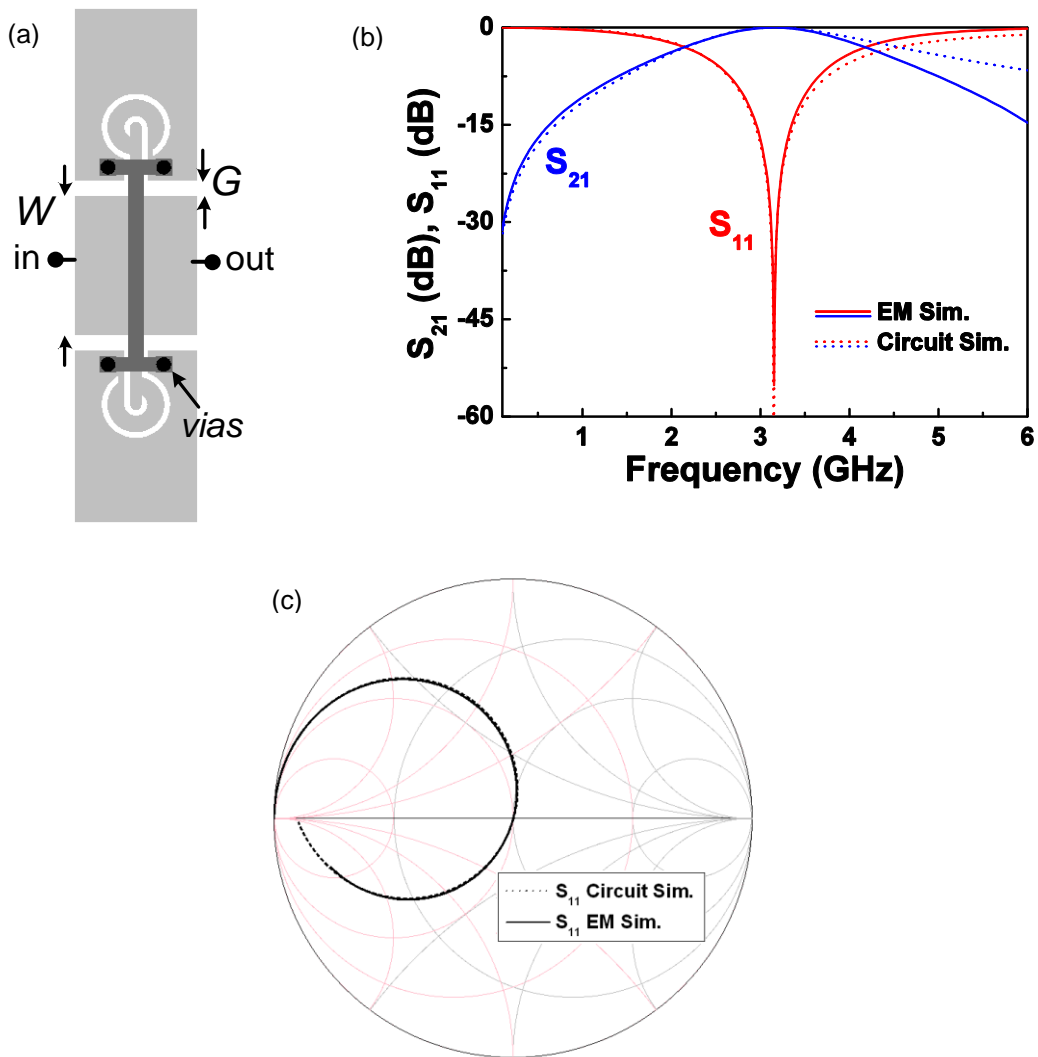
Figure 3.8. Topology (a), frequency response (magnitude) (b) and representation of the S_{11} in the Smith Chart (c) corresponding to a pair of shunt connected OCSRRs in a CPW transmission line with $r_{ext} = 1.2$ mm, $c = 0.2$ mm, $d = 0.6$ mm, $W = 5$ mm and $G = 0.55$ mm. The width of the strip connecting the different ground planes is 0.55 mm. The structure has been implemented on the *Rogers RO3010* substrate with thickness $h = 0.254$ mm and measured dielectric constant $\varepsilon_r = 11.2$. The element values inferred by the parameter extraction method in reference to Figure 3.7(c) are: $L = 0.32$ pF, $L'_p = 0.983$ nH and $C'_p = 2.85$ pF.
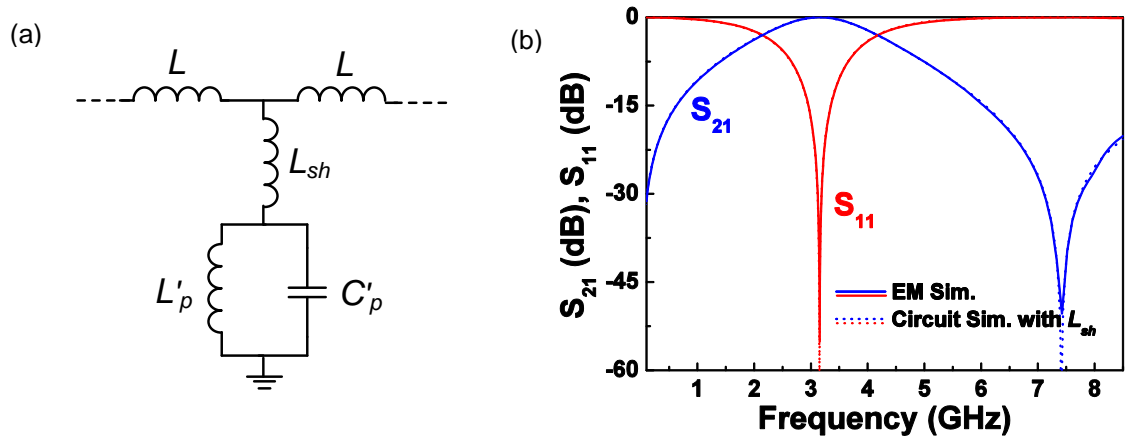
Figure 3.9. Wideband circuit model (a) and frequency response (magnitude) (b) of the pair of shunt connected OCSRRs shown in Figure 3.8(a). The element values inferred by the parameter extraction method are: $L = 0.345$ pF, $L'_p = 0.94$ nH, $C'_p = 2.98$ pF and $L_{sh} = 0.185$ nH.

Moreover, Figure 3.9(b) shows the comparison between electromagnetic and circuit simulation of the same topology of Figure 3.8(a) but considering this additional inductance L_{sh}, where a parameter extraction method that also considers this element has been considered and reported in Appendix A.

As can be observed, a more accurate agreement is achieved, predicting the position of the transmission zero due to the resonance of the complete shunt branch. Consequently, depending on the application and design requirements, this more accurate or wideband circuit model will be considered.

3.1.2 Circuit models of the open particles in microstrip technology

Figure 3.10(a) shows the topology of a series connected OSRR in microstrip technology. In this case, a ground plane window is required, in addition to the asymmetric access lines to match the resonator to the ports (as was also done in CPW technology).

In Figure 3.10(b)-(d) the magnitude and phase response of the structure is depicted. As can be appreciated, in microstrip technology the OSRR presents a second resonance frequency near the fundamental resonance. This resonance frequency can be moved farther away as the substrate gets thinner. Nonetheless, for substrates as thin as 0.254 mm (such as that corresponding to Figure 3.10), this resonance is still very close, which can be problematic both for the circuit model accurateness, as well as for its applications. Furthermore, by inspection of the Smith Chart it can be deduced that the response is asymmetric (this is also true if the terminals accessing the rings are symmetric), and with a S_{21} phase shift at the resonance frequency above 60º (in comparison with the 20º S_{21} phase shift of the OSRR in CPW technology). Consequently, in order to model the higher phase shift, additional elements will have to be considered.
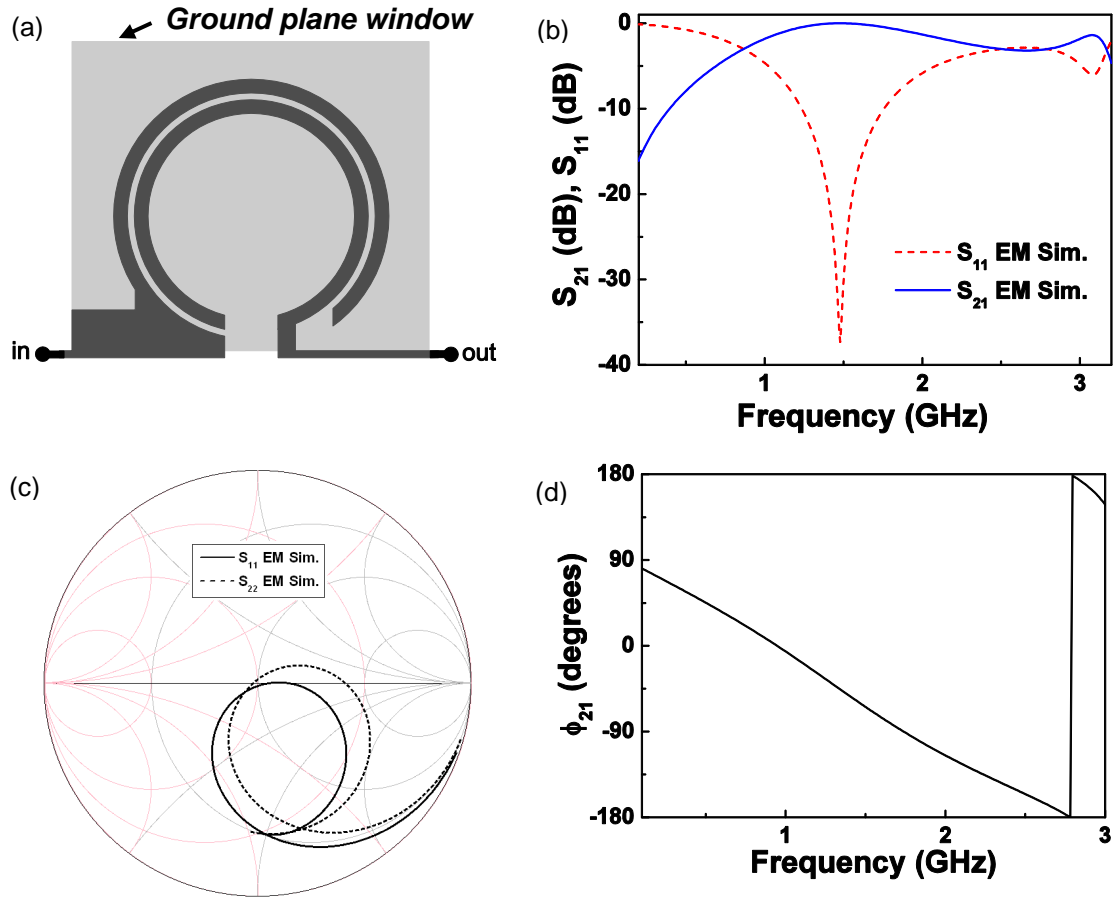
Figure 3.10. Topology (a), frequency response (magnitude) (b), representation of the S_{11} and S_{22} in the Smith Chart (c) and phase of S_{21} (d) obtained by electromagnetic simulation of a series connected OSRR in microstrip technology with $r_{ext} = 4$ mm, $c = 0.4$ mm and $d = 0.2$ mm. The considered substrate is the *Rogers RO3010* with thickness $h = 0.254$ mm and dielectric constant $\varepsilon_r = 10.2$.

By performing a similar process as that reported with CPW technology, analyzing the impedances, the circuit model of Figure 3.11 is obtained, where additional parameters in comparison with the series connected OSRR in a CPW transmission line are required [105]. In fact, the model of Figure 3.11 is also valid for CPW technology, but since the resonator in the latter case has a much smaller phase shift, the inductances at the terminals of the capacitance can be neglected and the shunt capacitances considered as equal ($C_1 = C_2$).

One of the disadvantages of this microstrip model is that the parameter extraction method presented for CPW technology cannot be considered, since it does not have an equivalent π-circuit model composed solely of reactive elements.
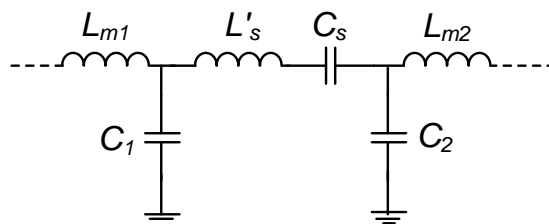
Figure 3.11. Circuit model of a series connected OSRR in microstrip technology.

45
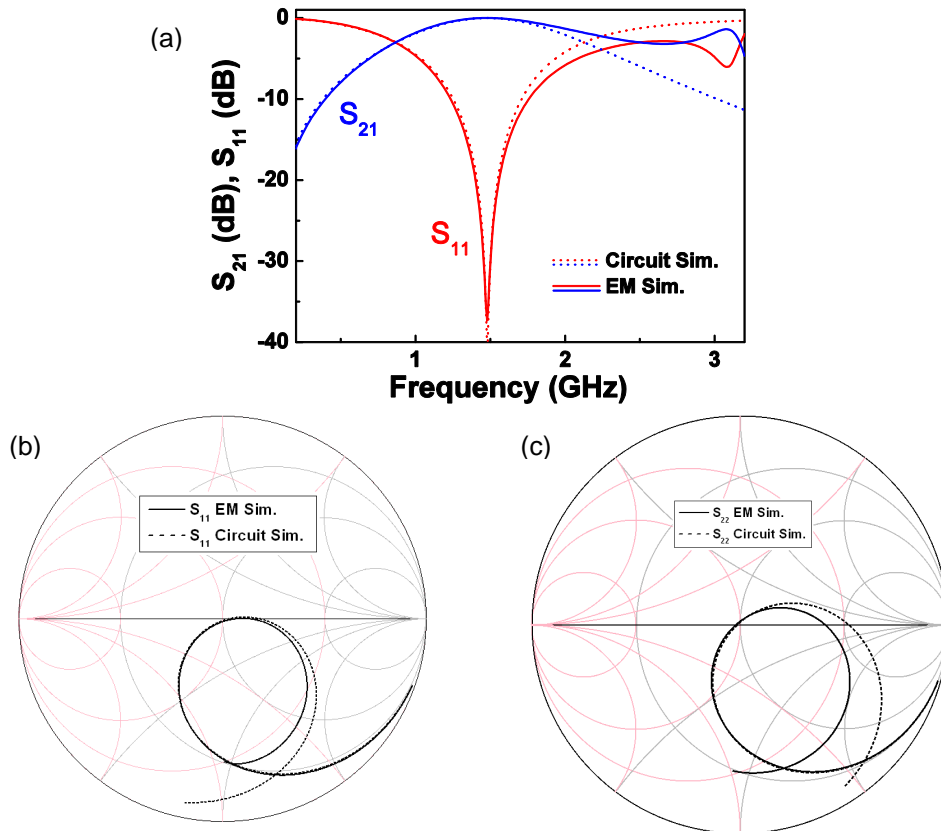
Figure 3.12. Electromagnetic and circuit simulation of the structure of Figure 3.10(a). Frequency response (magnitude) (a); Representation of the S_{11} in the Smith Chart (b); Representation of the S_{22} in the Smith Chart (c). The element values in reference to Figure 3.11 are: L'_s = 12.93 nH, C_s = 1.33 pF, C_1 = 1.38 pF, C_2 = 0.98 pF, L_{m1} = 0.8 nH and L_{m2} = 0 nH.

Additionally, the equivalent circuit has six unknowns, which complicates the possibility of obtaining a parameter extraction method. Thus, in order to design microwave components, a manual curve fitting will be required.

In Figure 3.12 a comparison between electromagnetic and circuit simulation of the topology of Figure 3.10(a) is shown, where the element values have been inferred by curve fitting both responses. Good agreement in magnitude and phase is obtained below and around the resonance frequency, failing the model at higher frequencies.

On the other hand, if an OCSRR is shunt connected in a microstrip line, the resulting equivalent circuit is simpler than its CPW counterpart. This can be deduced by inspection of the topology and the electromagnetic simulated response as shown in Figure 3.13. In this case, we have the characteristics of a pure parallel *LC* resonator, mostly due to the elimination of the terminals that connect the rings to the ports.

Thus, it is now possible to consider a pure parallel *LC* resonator as the equivalent circuit model for the shunt OCSRR in microstrip technology. In order to verify this assumption, in Figure 3.13 the circuit simulation of a shunt resonator has also been added, appreciating a good agreement throughout all the band of interest. In addition, the inductive effect in series with the shunt resonator is also present in this case, being again possible to obtain a wideband model by considering this additional element.
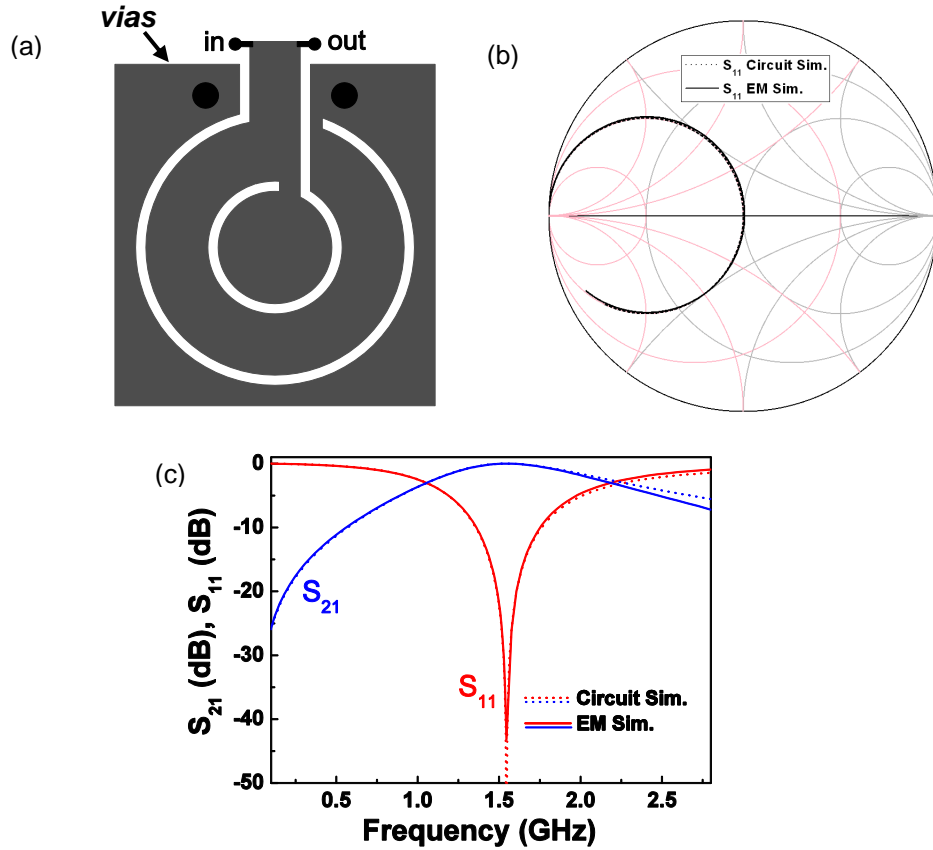
Figure 3.13. Topology (a), Smith Chart (b) and frequency response (magnitude) (c) of the electromagnetic and circuit simulation of a shunt OCSRR in microstrip technology with $r_{ext} = 2.7$ mm, $c = 0.2$ mm and $d = 1.2$ mm. The considered substrate is the *Rogers RO3010* with thickness $h = 0.254$ mm and dielectric constant $\varepsilon_r = 10.2$. The element values of the shunt resonator in reference of Figure 3.1(b) are: $L_p = 2.02$ nH and $C_p = 5.25$ pF.

3.2 Implementation and applications of CRLH lines with open resonators

In this section, the possibility of implementing CRLH lines by means of the combination of OSRRs and OCSRRs in CPW and microstrip technology will be examined. By means of these lines, microwave devices such as dual-band components or wideband band-pass filters will be implemented. Since in the previous section the drawbacks of microstrip technology have been predicted, special emphasis will be placed on CPW technology, dedicating only the last section demonstrating the possibilities of artificial lines implemented in microstrip technology.

3.2.1 Design and applications of CPW CRLH lines

Figure 3.14 shows the typical topologies to implement CRLH line unit cells based on the combination of series connected OSRRs and shunt connected OCSRRs in a CPW host line. In Figure 3.14(a), the canonical *T*-model unit cell of the CRLH line of Figure 2.11(a) is sought. Consequently, series connected OSRRs are hosted at the external stages and a pair of shunt connected OCSRRs are hosted in the central stage.

47
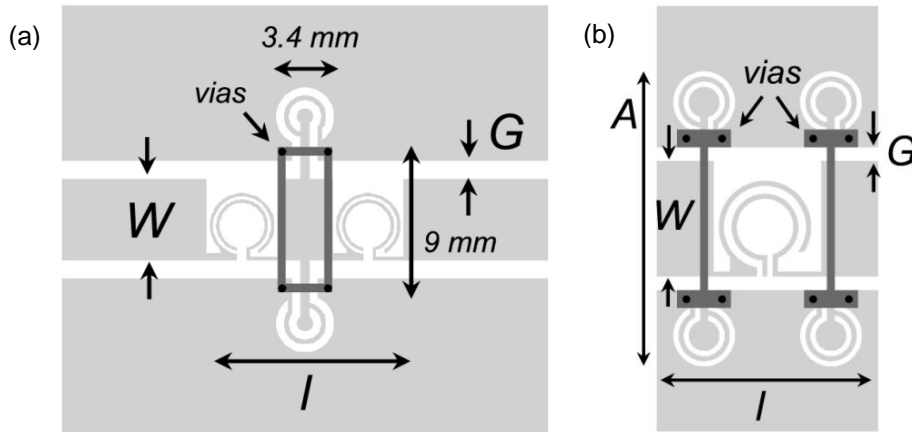
Figure 3.14. Typical CPW topologies to implement the T-(a) or π-(b) model unit cell of a CRLH transmission line based on a combination of OSRRs and OCSRRs. For the structure (a) with series connected OSRRs in the external stages and a pair of shunt connected OCSRRs in the central stage, the considered substrate is the *Rogers RO3010* with thickness h = 1.27 mm and measured dielectric constant ε_r = 11.25; For the structure (b) with OCSRRs shunt connected in the external stages and a series connected OSRR in the central stage, the considered substrate is the *Rogers RO3010* with thickness h = 0.254 mm and measured dielectric constant ε_r = 11.2; Dimensions are: (a): l = 12.4 mm, W = 5 mm and G = 1.16 mm. For OCSRR: r_{ext} = 1.8 mm, c = 0.5 mm and d = 0.3 mm. For OSRR: r_{ext} = 2 mm and c = d = 0.2 mm; (b): l = 7.4 mm, A = 11.5 mm, W = 4.5 mm and G = 0.52 mm. For the OCSRRs: r_{ext} = 1.2 mm, c = 0.2 mm and d = 0.2 mm. For the OSRRs: r_{ext} =1.8 mm, c = 0.2 mm and d = 0.3 mm.
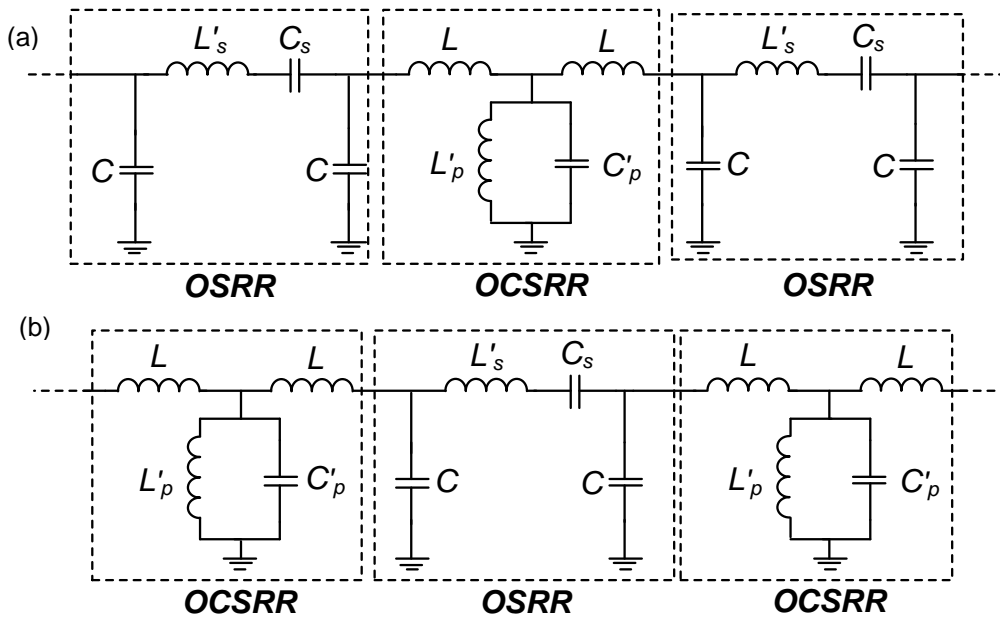
Figure 3.15. Circuit models of the unit cells of a CPW CRLH transmission line based on a combination of OSRRs and OCSRRs, considering the topology of Figure 3.14(a), (a), and the topology of Figure 3.14(b), (b).

On the other hand, the topology of Figure 3.14(b) considers the canonical π-model unit cell of the CRLH line based on Figure 2.11(b), resulting in a pair of shunt connected OCSRRs at the external stages and a series connected OSRR in the central stage. Figure 3.15 also shows the equivalent circuit models in both cases considering the circuit models obtained in section 3.1.1 (where the simple OCSRR model without the additional parameter L_{sh} is initially analyzed).
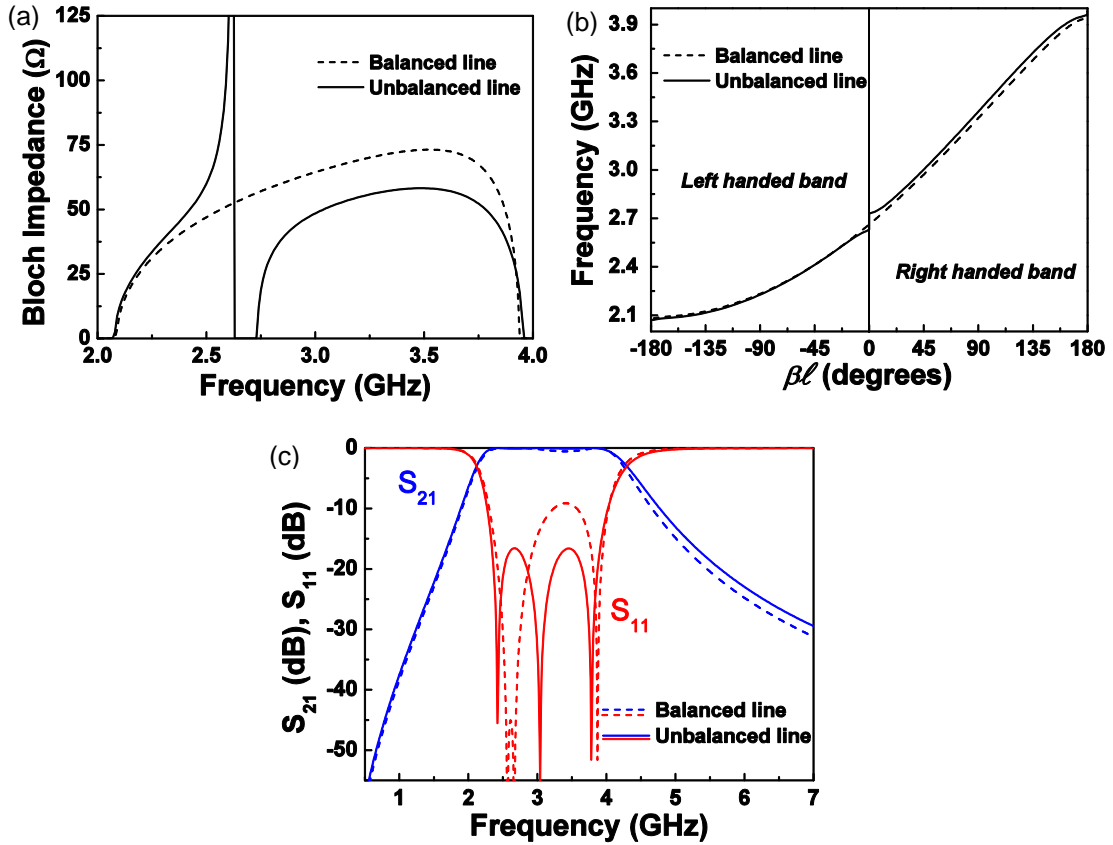
Figure 3.16. Bloch impedance (a), dispersion diagram (b) and S-parameters (c) of a balanced and unbalanced CRLH line composed of the circuit of Figure 3.15(b). The values of the equivalent circuit in reference to Figure 3.15(b) are: For the balanced line: C = 0.4 pF, L'_s = 5.55 nH, C_s = 0.598 pF, L = 0.4 nH, C'_p = 2.083 pF and L'_p = 0.94 nH. For the unbalanced line: C = 0.4 pF, L'_s = 4.944 nH, C_s = 0.632 pF, L = 0.4 nH, C'_p = 2.25 pF and L'_p = 0.94 nH.

As can be seen from Figure 3.15(a)-(b), the equivalent circuit tends towards the canonical circuit of a CRLH line as the parasitics L, C tend towards zero. If they are not negligible, a CRLH line behavior is still obtained, although these parameters will have to be taken into account in the design process.

One of the consequences of the presence of these parasitics is that in order to obtain a balanced CRLH line, the condition of an equal resonance frequency of the series and shunt resonator will not have to be satisfied. This is because if the latter case occurs, then at this resonance frequency, the parasitics will play a role, with the resulting non-zero phase shift. This can be observed from Figure 3.16, where arbitrary balanced and unbalanced lines formed by the circuit of Figure 3.15(b) with the same parasitics are compared. Although the balanced condition can still be satisfied both in the dispersion diagram and in the impedance with the proposed equivalent circuits, this leads to an asymmetric magnitude response. Therefore, to obtain an equal-ripple magnitude response, the impedance and dispersion diagram must be unbalanced.

Figure 3.17 shows the first realization of an arbitrary CRLH line based on open resonators [105]. The response corresponds to the topology of Figure 3.14(a), where its characteristic behavior can be appreciated, with a left- and right-handed propagation band.
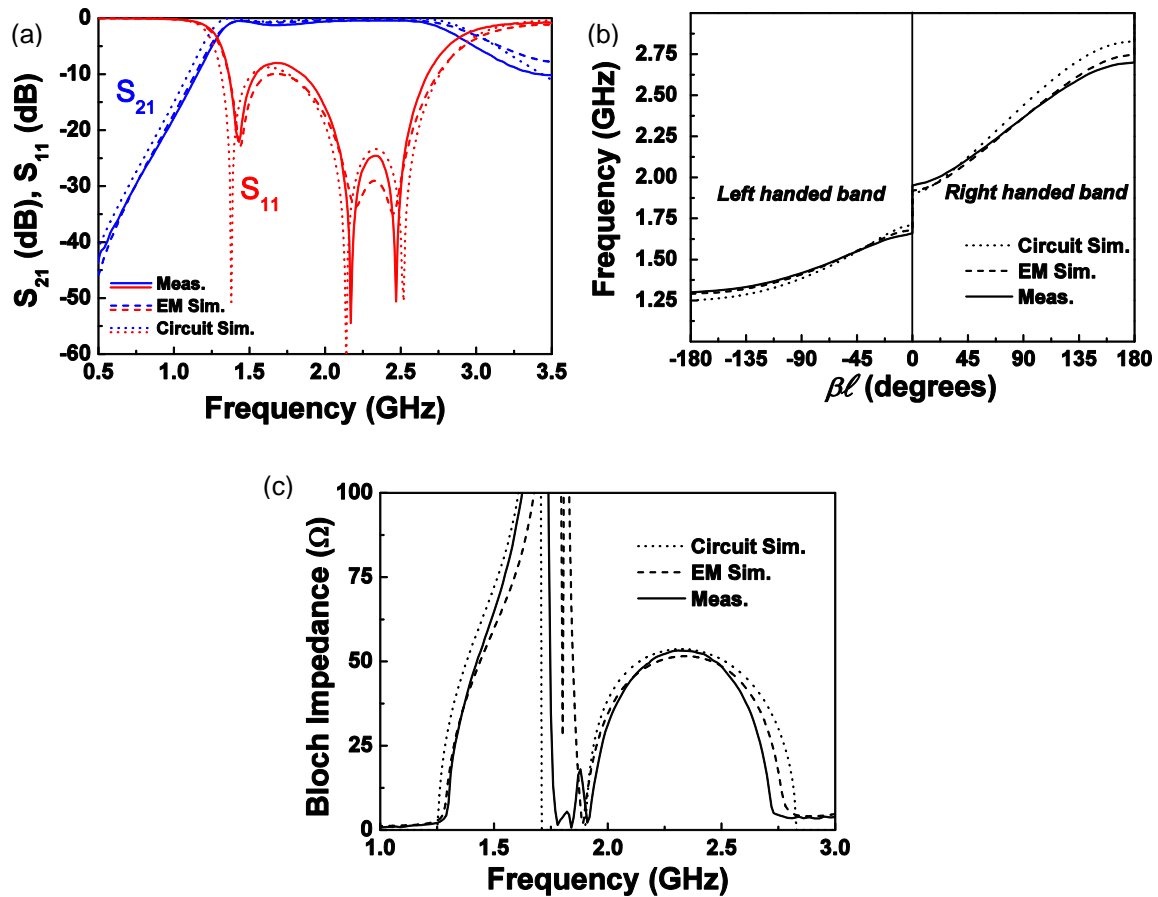
Figure 3.17. S-parameters (a), dispersion diagram (b) and Bloch impedance (c) of the structure of Figure 3.14(a). The values of the equivalent circuit in reference to Figure 3.15(a) are: $C = 0.24$ pF, $L'_s = 6.76$ nH, $C_s = 0.95$ pF, $L = 0.56$ nH, $C'_p = 2.44$ pF and $L'_p = 2.53$ nH.

Another aspect to highlight is the agreement between circuit simulation and electromagnetic simulation/measurement, which not only validates the parameter extraction method, but also demonstrates that the coupling between the resonators is negligible. Thus, for all the applications that will be shown, it will be possible to design and force the specifications directly to the isolated resonators.

Figure 3.18 shows a CRLH line with a flat band response, which could be applied to the design of band-pass filters [106]. By inspection of the dispersion diagram and Bloch impedance, it can be seen how although a flat response is obtained, the balanced condition is not actually satisfied, with a small gap due to the presence of parasitics (the smaller the parasitics, the smaller the gap will be).

Moreover, the parasitic effects can be drastically minimized if the terminals of the OCSRR are shortened in the topology of Figure 3.14(b) (with the equivalent circuit of Figure 3.15b). By means of this technique, the parasitic element L of the OCSRR vanishes, and therefore the structure tends towards the canonical CRLH line model, since the parasitic effect C of the OSRR is added to the shunt capacitance of the OCSRR. A similar phenomenology can be obtained with the topology of Figure 3.14(a) (with the equivalent circuit of Figure 3.15a), where if the gaps of the CPW line are expanded, the parasitic effect C tends towards zero and the parasitic element L is absorbed by the series resonator.
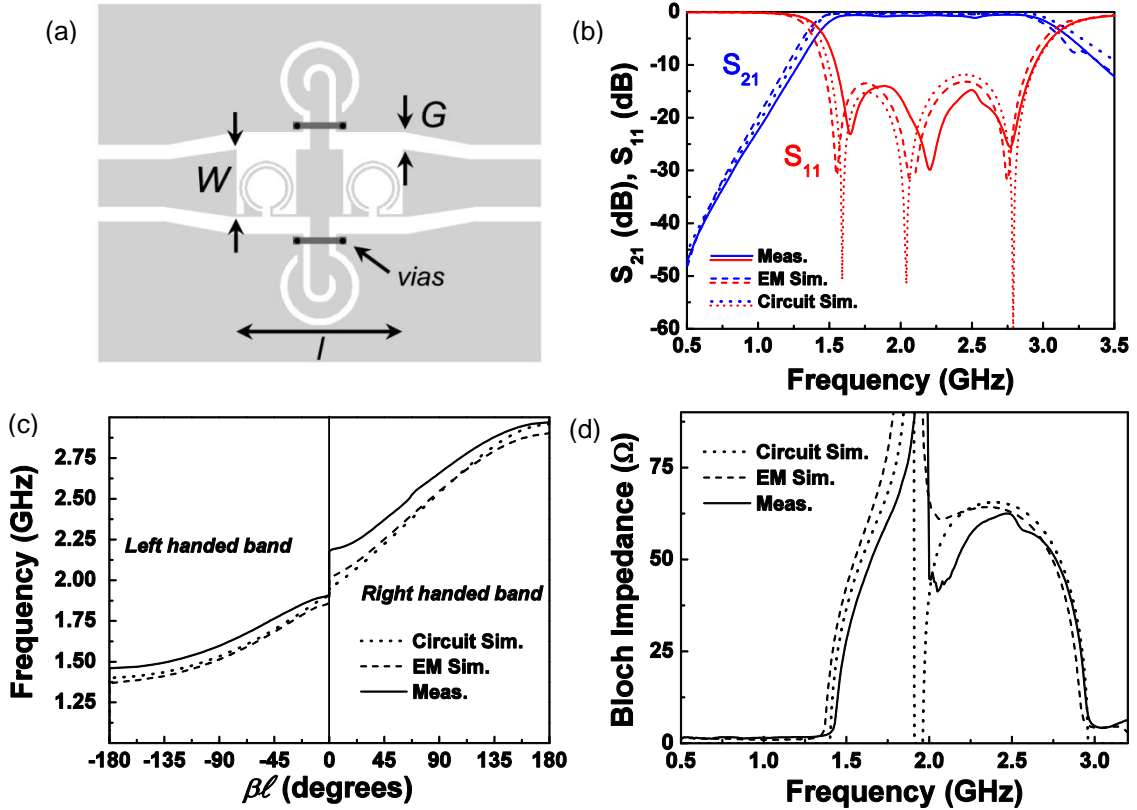
Figure 3.18. Topology (a), frequency response (b), dispersion diagram (c) and Bloch impedance (d) of the unit cell of a CPW quasi-balanced CRLH line based on open resonators. The considered substrate is the *Rogers RO3010* with thickness h = 1.27 mm and dielectric constant ε_r = 10.2. Dimensions are: l = 12.3 mm, W = 5 mm and G = 1.28 mm. For the OCSRR: r_{ext} = 2.9 mm, c = 0.5 mm and d = 1.2 mm. For the OSRRs: r_{ext} = 2 mm and $c = d$ = 0.2 mm.

This phenomenology has been studied with the layout of Figure 3.14(b) and applied as an example to obtain a third-order Chebyshev band-pass filter, with 0.07 dB ripple, central frequency f_0 = 2.8 GHz and fractional bandwidth *FBW* = 50% [107]. To this end, the models presented in [53], [100] for the SRR and CSRR and their relation with the open particles ([101], [102]) have been considered to obtain an initial layout of the OSRR and OCSRR. Afterwards, by means of the parameter extraction method the particles were optimized until they met the specifications (considering the capacitance *C* as part of the shunt capacitance of the band-pass prototype). Nonetheless, since the purpose of this design is to study the reduction of the parasitics' effects rather than to design a filter with a very good rejection, this latter aspect has not been optimized, leaving this issue to the filter section 3.2.1.2. Figure 3.19 shows the resulting dispersion diagram and frequency response (magnitude). Given that the length of the OCSRR CPW terminals has been minimized, a parasitic inductance of L = 0.05 nH is achieved, leading to an almost continuous transition between the left- and right-handed band. Moreover, a very good agreement between electromagnetic and circuit simulation in the band of interest is obtained, the model failing at higher frequencies since the wideband model of the OCSRR has not been considered, as already explained in section 3.1. Hence, by a proper design, it is also possible to obtain almost negligible effects of the parasitics in order to obtain a purely CRLH behavior if needed.
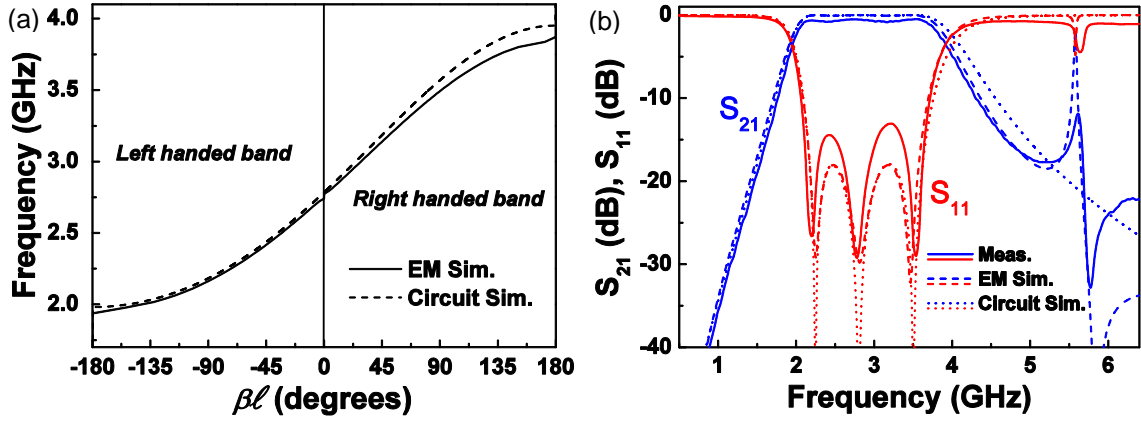
Figure 3.19. Dispersion diagram (a) and frequency response (b) of the CPW quasi-balanced CRLH line based on open resonators shown in Figure 3.14(b). The values of the equivalent circuit in reference to Figure 3.15(b) are: $C = 0.19$ pF, $L = 0.05$ nH, $C_s = 0.515$ pF, $L'_s = 6.16$ nH, $C'_p = 1.91$ pF and $L'_p = 1.55$ nH.

After the implementation of CRLH lines by means of open resonators has been validated, the potential applications of these lines will be studied in the following sections, examining in this thesis the design of dual-band components and wideband band-pass filters. Moreover, although it has been proven that given certain requirements it is possible to minimize the parasitics in order to become almost negligible, in the following sections the more general case with non-negligible parasitics will be considered.

3.2.1.1   Dual-band components

As discussed in section 2.3.2, one of the advantages of artificial lines is the possibility of forcing a phase and impedance condition at two arbitrary frequencies f_1 and f_2. The most common application of this is the implementation of dual-band impedance inverters, which are useful for designing many planar microwave devices such as power dividers or couplers. Therefore, the requirements in these cases force an electrical length for the artificial lines of $\beta l = \mp 90^\circ$ and impedance Z_a at two arbitrary frequencies. In [84], these requirements were obtained by forcing the above conditions through the propagation constant defined in (2.16) and the Bloch impedance given by equation (2.20), leading to

$$Z_s(\omega)|_{f_1} = -jZ_a \tag{3.1}$$

$$Z_s(\omega)|_{f_2} = +jZ_a \tag{3.2}$$

$$Z_p(\omega)\big|_{f_1} = +jZ_a \tag{3.3}$$

$$Z_p(\omega)\big|_{f_2} = -jZ_a \tag{3.4}$$

Therefore, knowing the series and shunt impedances of the CRLH line, the element values of the circuit model can be inferred. To this end, the impedances of the structure formed by the cascaded OSRR-OCSRR-OSRR stages such as that shown in Figure 3.15(a) are calculated by means of the [ABCD] matrices, resulting in

52

$$Z_s(\omega) = \frac{-j\left[(1 - \omega^2 L'_s C_s) + L\omega^2(CL'_s C_s \omega^2 - C - C_s)\right]}{\omega\left[C_s + C\omega^2\left(CL(\omega^2 L'_s C_s - 1) - 2C_s L - L'_s C_s + \frac{1}{\omega^2}\right)\right]} \tag{3.5}$$

$$Z_p(\omega) = \frac{-j\omega L'_p C_s{}^2}{\left(1 - \omega^2 L'_p C'_p\right)C_1{}^2 + C\omega^2 C_2(CL\omega^2 C_2 L_2 - 2C_1 L_1)} \tag{3.6}$$

with

$$C_1 = C_s + C\left(1 - \frac{\omega^2}{\omega_s{}^2}\right) \tag{3.7}$$

$$C_2 = 2C_s + C\left(1 - \frac{\omega^2}{\omega_s{}^2}\right) \tag{3.8}$$

$$L_1 = L'_p + L\left(1 - \frac{\omega^2}{\omega_p{}^2}\right) \tag{3.9}$$

$$L_2 = 2L'_p + L\left(1 - \frac{\omega^2}{\omega_p{}^2}\right) \tag{3.10}$$

$$\omega_s = \frac{1}{\sqrt{L'_s C_s}} \tag{3.11}$$

$$\omega_p = \frac{1}{\sqrt{L'_p C'_p}} \tag{3.12}$$

where OSRRs with identical element values C, L'_s and C_s, at the external stages have been considered. By forcing equations (3.5) - (3.6) to fulfill the above cited conditions of equations (3.1) - (3.4) at the operating frequencies of the dual-band impedance inverter, four conditions result. However, we have six unknowns. Hence, in a first step, the parasitic elements L and C will have to be estimated or considered null in order to obtain the other four elements (which are analytically determined).

Then, the initial layout of the OSRR and OCSRR can be obtained by means of the models reported in [53], [100] - [102], and later optimized with the parameter extraction method until the resonator element values are identical to those inferred in the first step. Afterwards, the parasitics obtained from this layout optimization are introduced to equations (3.1) - (3.6) again to obtain the final element values considering the parasitics. Lastly, the final layout is implemented in order to satisfy the four cited conditions.

Throughout this methodology, a dual-band impedance inverter with an electrical length $\beta l = \mp 90^o$ and impedance $Z_a = 35.35\ \Omega$ at the frequencies of $f_1 = 2.4$ GHz and $f_2 = 3.75$ GHz is designed [106]. With these conditions, the element values without considering the parasitics are initially calculated (in reference to Figure 3.15a): $C = 0$ pF, $L = 0$ nH, $C_s = 0.68$ pF, $L'_s = 4.17$ nH, $C'_p = 3.34$ pF and $L'_p = 0.84$ nH. Afterwards, the initial layout is obtained and the parasitics inferred by parameter extraction method.

With the consideration of these parasitics, the element values that satisfy the requirements are analytically recalculated, as: $C = 0.2$ pF, $L = 0.25$ nH, $C_s = 0.66$ pF, $L'_s = 3.74$ nH, $C'_p = 2.99$ pF and $L'_p = 0.83$ nH. Then, the final layout is obtained through an optimization process with the parameter extraction method.
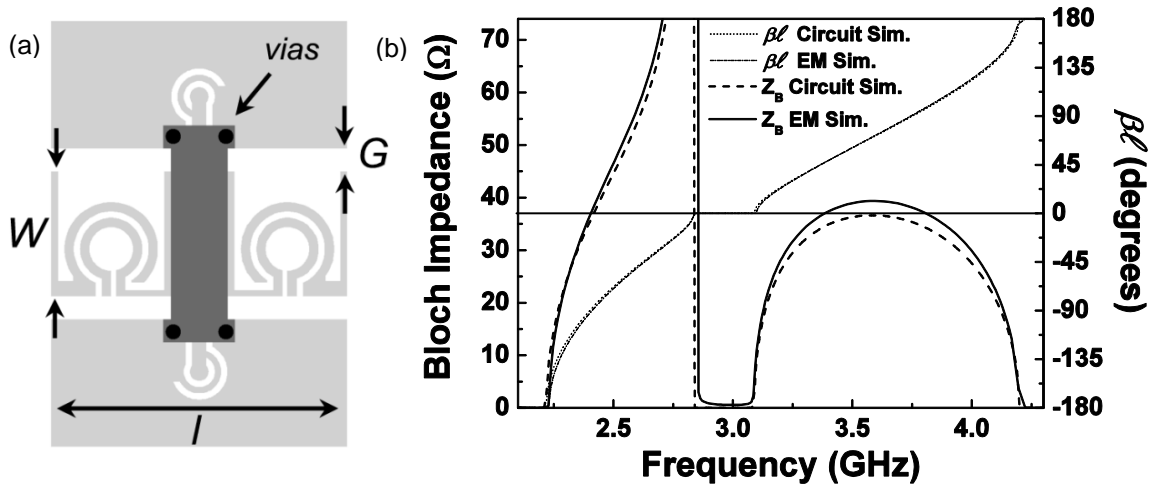
Figure 3.20. Layout (a) and simulated Bloch impedance and dispersion diagram (b) of the dual-band impedance inverter based on a combination of series OSRRs in the external stages and shunt OCSRRs in the central stage. The substrate is the *Rogers RO3010* with thickness $h = 0.635$ mm and dielectric constant $\varepsilon_r = 10.2$. Dimensions are: $l = 9$ mm, $W = 4$ mm and $G = 0.74$ mm. For the OCSRRs: $r_{ext} = 0.9$ mm, $c = 0.2$ mm and $d = 0.2$ mm. For the OSRRs: $r_{ext} = 1.5$ mm, $c = 0.3$ mm and $d = 0.2$ mm.
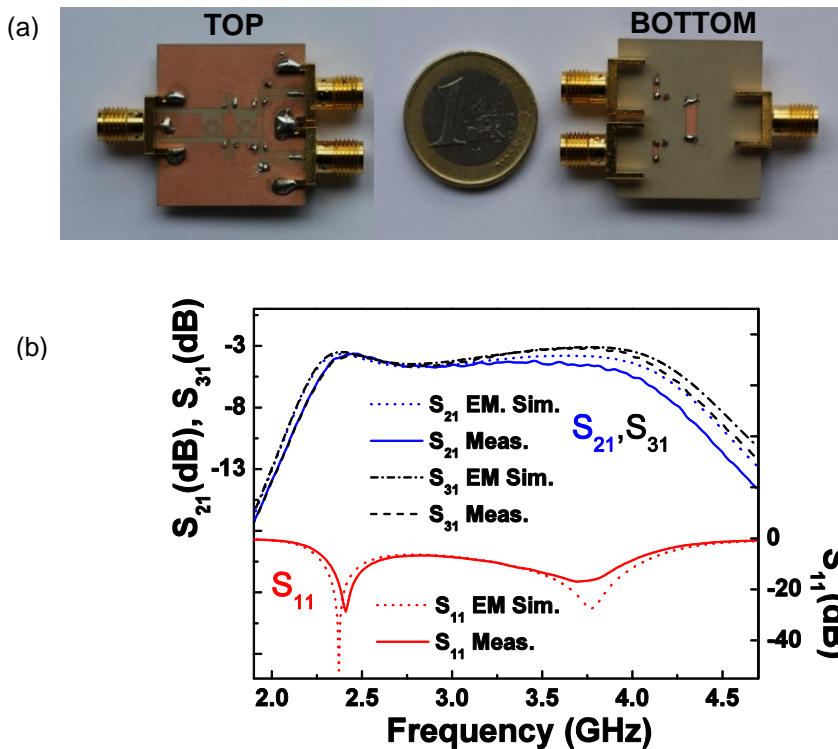
Figure 3.21. Photograph (a) and frequency response (b) of the dual-band power splitter based on the dual-band impedance inverter of Figure 3.20(a).

The resulting structure is shown in Figure 3.20(a). The wide metallic strip in the back substrate side has been added in order to enhance the shunt capacitance of the OCSRR stage, as required, to achieve the electrical characteristics of the device. In Figure 3.20(b) the circuit and electromagnetic simulation of the Bloch impedance and dispersion diagram are also shown. These results reveal that the required characteristics are satisfied. By cascading a 50 Ω input (access) line and two 50 Ω output lines, a dual-band power splitter results. The photograph of this device, as well as the simulated and measured power splitting and matching are depicted in Figure 3.21, where the required functionality at the two operating frequencies is achieved.

3.2.1.2 Wideband band-pass filters

Artificial lines based on open resonators can also be applied to the design of band-pass filters. For this purpose, periodicity can be sacrificed in order to obtain standard responses (Butterworth or Chebyshev). In this work, only the design of Chebyshev responses is considered, given its richer phenomenology and higher selectivity. Nonetheless, in order to obtain the desired response with the additional parasitics, some previous steps are required. To this end, different options arise. The first option consists of minimizing the effect of the parasitics and thus approaching the resulting circuit model to that of the band-pass prototype, as already shown in section 3.2.1. Nonetheless, this minimization is not always possible due to the specification requirements. In addition, if very wideband filters are designed, the consideration of an additional shunt inductance in series with the parallel *LC* tank is necessary (as explained in section 3.1), which invalidates the possibility of adding all the OSRR parasitic capacitances contributions to the capacitance of the shunt resonator. If the parasitics cannot be neglected, a similar procedure to that used for dual-band devices can be used. Hence, we first obtain the element values of the prototype Chebyshev filter. Afterwards, by means of the parameter extraction method and the models reported in [53], [100] - [102], we obtain the layout that satisfies the circuit conditions without considering the parasitics. At this point, a non-optimum response will be obtained due to interaction of the parasitics that directly affects the band-pass of the filter.

Thus, to obtain an optimum response, the layout parasitic values are inferred by the parameter extraction method, either with the simple or wideband model of the OCSRR depending on the bandwidth of the filter. Afterwards, the complete structure is tuned at the circuit level in order to find the circuit elements that satisfy the filter requirements with these additional elements. Finally, the layout satisfying the resulting circuit elements can be obtained with the help of the parameter extraction method. By means of this method, a third-order Chebyshev band-pass filter with central frequency $f_0 = $ 2.9 GHz, 0.02 dB ripple and 35% fractional bandwidth has been designed. The layout and photograph of the fabricated device are shown in Figure 3.22 [106]. This filter has been fabricated on the *Rogers RO3010* substrate with thickness $h = 0.254$ mm and measured dielectric constant $\varepsilon_r = 11.2$, where it has been found that by using thinner substrates the stop-band response is improved (i.e., the first spurious band due to the distributed resonances of the resonators is shifted to higher frequencies).
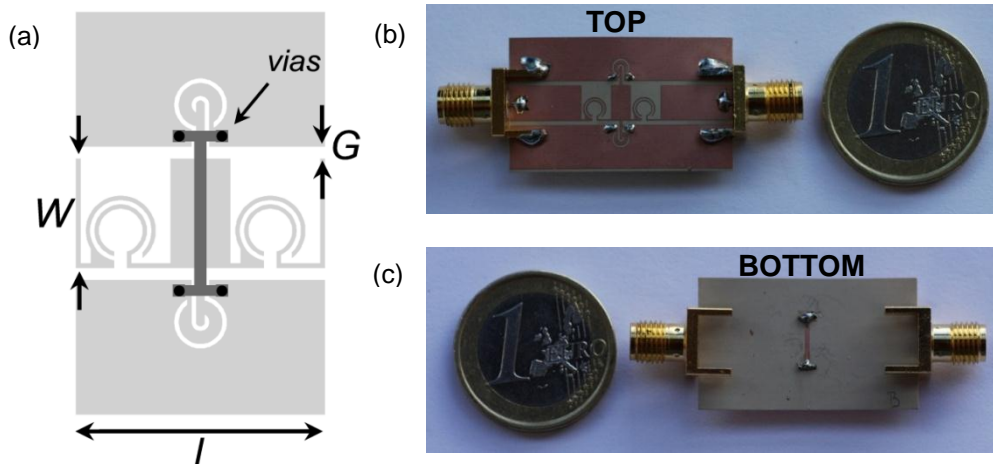
Figure 3.22. Layout (a) and top (b) - bottom (c) photograph of the CPW wideband band-pass filter based on a combination of series connected OSRRs in the external stages and a pair of shunt connected OCSRRs in the central stage. Dimensions are: l = 9 mm, W = 5 mm and G = 0.55 mm. For the OCSRR: r_{ext} = 1.2 mm, c = 0.2 mm and d = 0.6 mm. For the OSRR: r_{ext} = 1.6 mm and $c = d$ = 0.2 mm.
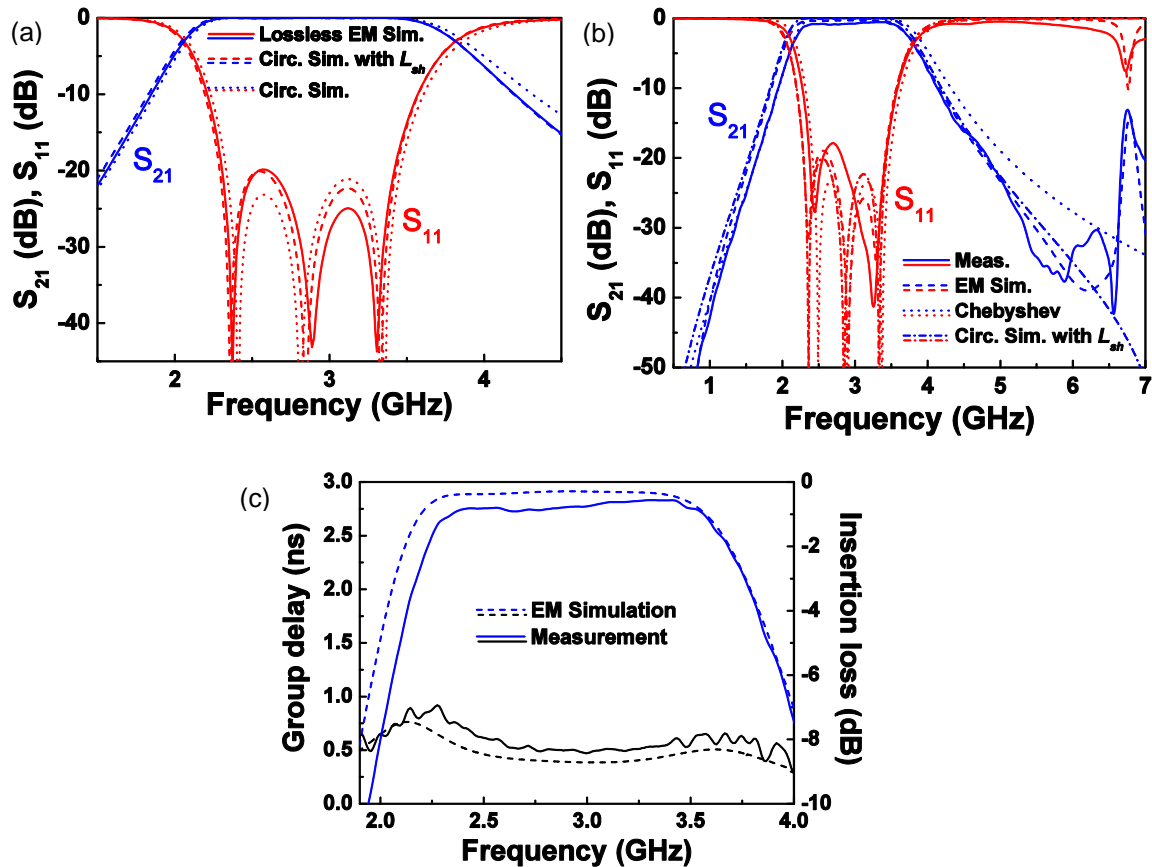
Figure 3.23. Frequency response simulation without losses (a); Wideband frequency response simulation with losses and measurement (b); Group delay and detail of the insertion loss of the circuit of Figure 3.22. The Chebyshev element values obtained from the band-pass prototype transformations, in reference to Figure 2.11(a), are: C_L = 0.27 pF, L_L = 0.93 nH, C_R = 3.3 pF and L_R = 11.52 nH. The values of the circuit simulation considering parasitics, inferred from parameter extraction method, are (in reference to Figure 3.15a): C = 0.19 pF, L = 0.4 nH, C_s = 0.58 pF, L'_s = 5.55 nH, C'_p = 3 pF and L'_p = 0.94 nH. The modified values of the OCSRR considering the wideband model with the additional parasitic element L_{sh} are (in reference to Figure 3.9a): L = 0.345 nH, C'_p = 2.98 pF, L'_p = 0.94 nH and L_{sh} = 0.19 nH.

Figure 3.23(a) shows the electromagnetic and circuit simulation of the filter without losses, considering for comparison purposes both the simple and wideband OCSRR model (i.e., considering the case with and without the additional parameter L_{sh} in reference of Figure 3.9a). As can be appreciated, since the fractional bandwidth of the filter is moderate, the simple OCSRR model can still predict the band, although it begins to fail at higher frequencies. Figure 3.23(b) also shows the wideband frequency response of the electromagnetic simulation considering dielectric, conductor and radiation losses, the circuit and ideal Chebyshev models, as well as the measurement of the fabricated device. The group delay and insertion loss of the electromagnetic simulation and measurement are also depicted in Figure 3.23(c). There is good agreement between all the curves in the region of interest, with the first spurious band at roughly 2.3 times the central filter frequency. Measured filter characteristics are good with insertion losses lower than 1dB between 2.3 GHz and 3.5 GHz, and measured return losses better than 18 dB between 2.36 GHz and 3.41 GHz. Furthermore, the circuit simulation considering the parasitic element L_{sh} predicts both the band-pass and the stop-band rejection, where due to this additional shunt inductance behavior, these types of filters will have the advantage of a more selective upper transition band compared to the Chebyshev responses, as well as an additional transmission zero above the band (present at higher frequencies than those depicted for the filter shown).

The dissipation effects of the filter have also been experimentally inferred through the Cohn formula [108] (also reported in more recent publications [26]). The average un-loaded Q-factor of the resonators resulting from this method is $Q_u = 108$, where the Chebyshev prototype elements and the approximation of an equal quality factor of the OSRRs and OCSRRs resonators have been considered.

The technique used to design this kind of filters has been proven to be simple for small order filters and/or small parasitic elements, since the element tuning to infer the optimum response considering parasitics is realized at the circuit level. Nonetheless, if either the order or the parasitic element values dramatically increase, the manual tuning of the whole structure can be a complex and time consuming task.

In these latter circumstances, an automatic optimization routine that forces the frequency positions at the N matching points of the Chebyshev response (i.e., where the input impedance is 50 Ω) can be implemented in a commercial simulator such as Agilent *ADS*, with N being the filter order. Hence, by predefining the frequency matching positions (which are given by the Chebyshev prototype response), the optimum circuit elements considering a set of fixed parasitics values can be automatically obtained for any filter order or any fixed parasitic value. As an example, this routine is applied to the already designed filter, where the final circuit elements inferred by the parameter extraction method are considered as a starting point and optimized to fulfill the initial filter requirements considering constant parasitics (since these are the only non-controllable parameters). Figure 3.24(a) shows the frequency response comparison between the circuit model and the Chebyshev response. As can be observed, if the simple OCSRR model is considered, a nearly perfect fit between both curves is obtained with this method, with a slight deviation only on the stop-band rejection at high frequencies.
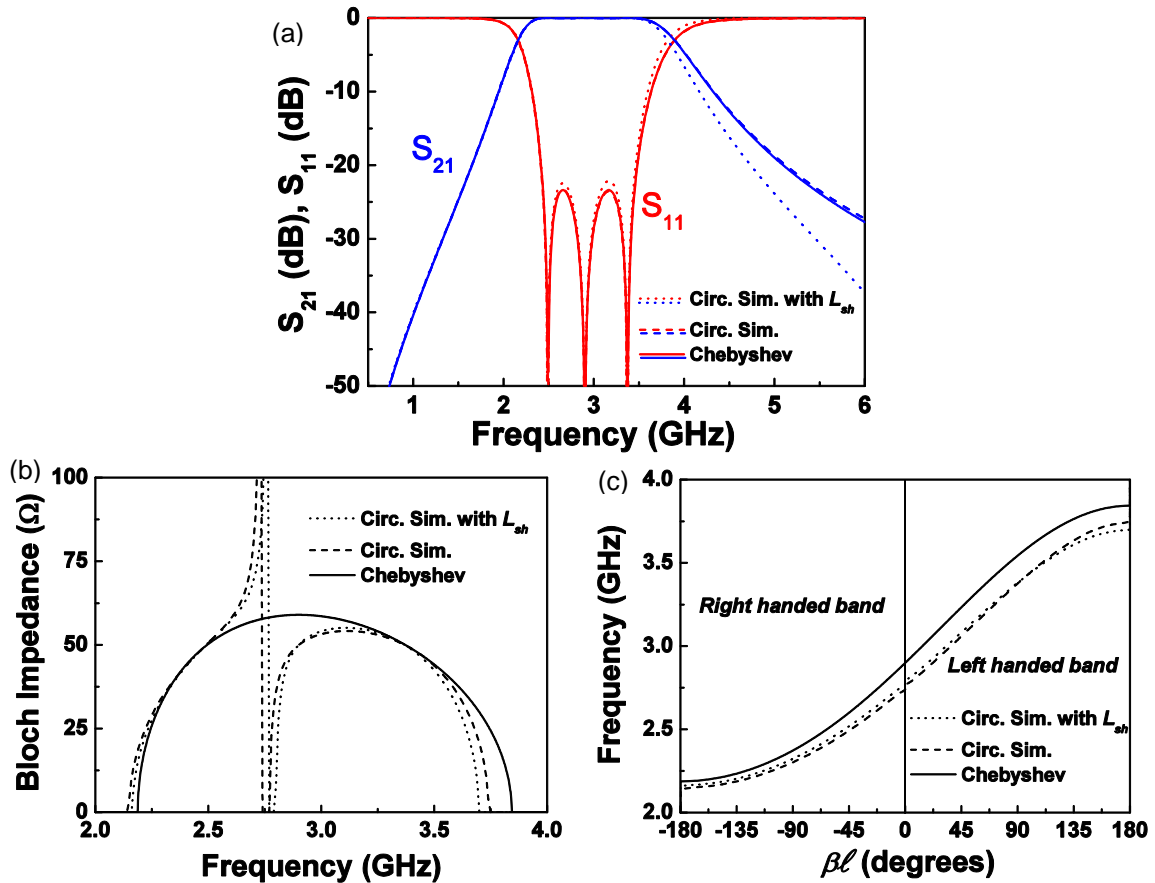
Figure 3.24. Frequency response (a), Bloch Impedance (b) and dispersion diagram (c) comparison between the ideal Chebyshev and circuit simulation obtained by automatic matching point optimization considering both the simple and wideband model of the OCSRR. The circuit values are: For the case of considering the simple OCSRR model (in reference to Figure 3.15a): $C = 0.19$ pF, $L = 0.4$ nH, $C_s = 0.55$ pF, $L'_s = 5.57$ nH, $C'_p = 3.17$ pF and $L'_p = 0.86$ nH. For the case of considering the wideband OCSRR model (in reference to Figure 3.5b and Figure 3.9a): $C = 0.19$ pF, $L = 0.4$ nH, $L_{sh} = 0.19$ nH, $C_s = 0.52$ pF, $L'_s = 5.76$ nH, $C'_p = 3.24$ pF and $L'_p = 0.8$ nH.

On the other hand, if the same method is considered with the wideband model of the OCSRR (i.e., considering the additional inductance L_{sh}) it can be seen how the same goals are achieved, but with a slight discrepancy in return loss, as well as a higher upper selectivity due to this factor. Moreover, in Figure 3.24(b)-(c) the Bloch impedance and dispersion diagram comparison (which still makes sense for a third-order structure) is also shown. As already mentioned, it can be appreciated how the unbalanced condition in the open resonators based CPW CRLH lines is required in order to obtain an equal-ripple magnitude response. Moreover, from these responses it can be verified that CRLH lines based on open resonators are useful to achieve wideband standard responses.

Once the design procedure has been established, the limitation of this approach is studied by designing different types of bandwidths and filter orders. In order to correctly compare the above presented filter with the forthcoming different ripple filters, the -3 dB fractional bandwidth parameter FBW_{-3dB} can be considered, related to the fractional bandwidth of a Chebyshev filter FBW as [109]

$$\frac{FBW_{-3dB}}{FBW} = cosh\left[\frac{1}{N}acosh\left(\frac{1}{\sqrt{10^{0.1ripple} - 1}}\right)\right] \tag{3.13}$$

where N is the order of the filter and the ripple is given in decibels. Therefore, if a Chebyshev response with 3 dB ripple is considered, the hyperbolic arccosine is zero and the ratio of fractional bandwidth reduces to unity as expected, since both fractional bandwidths are the same in this case. In a similar manner, the above designed filter with 35% *FBW* presents a *FBW$_{-3dB}$* = 60%. Additionally, two third-order filters with f_0 = 2 GHz, ripple of 0.15 dB and fractional bandwidth of 70% (*FBW$_{-3dB}$* = 93%) and 90% (*FBW$_{-3dB}$* = 119%), respectively, have been designed. The layouts and photographs of each filter are shown in Figure 3.25 [110], [111].
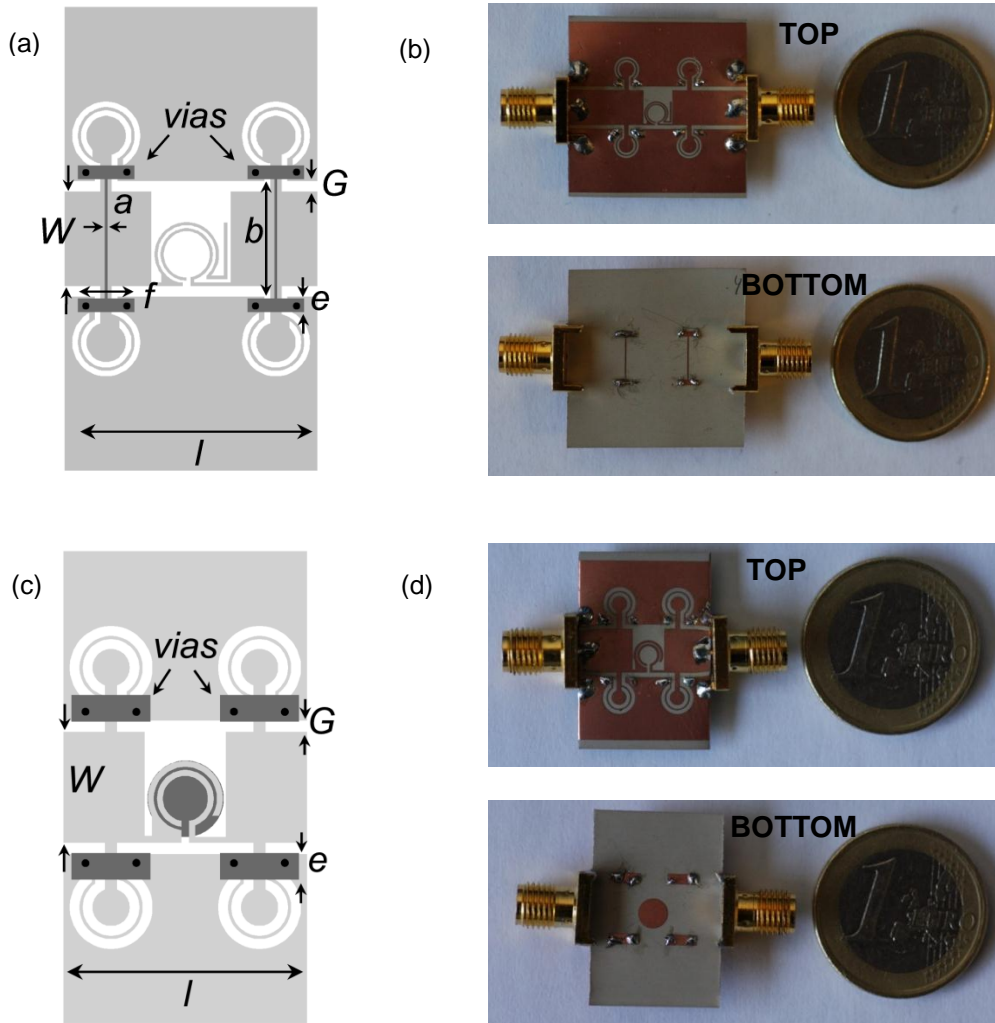
Figure 3.25. Topology (a), (c) and photograph (b), (d) of the designed third-order filter with 70% and 90% fractional bandwidth, respectively. The considered substrate is the *Rogers RO3010* with thickness h = 0.254 mm and measured dielectric constant ε_r = 11.2. Dimensions are: (a)-(b): l = 13.38 mm, W = 5 mm, G = 0.547 mm, a = 0.16 mm, b = 6.27 mm, e = 0.73 mm and f = 3 mm. For the OCSRR: r_{ext} = 1.8 mm, c = 0.3 mm and d = 0.16 mm. For the OSRR: r_{ext} = 1.7mm and c = d = 0.16mm. (c) - (d): l = 12.32 mm, W = 5.6 mm, G = 0.574 mm and e = 1.34 mm. For the OCSRR: r_{ext} = 2.1 mm, c = 0.5 mm and d = 0.16 mm. For the OSRR: r_{ext} = 1.9 mm, c = 0.3 mm and d = 0.16 mm.
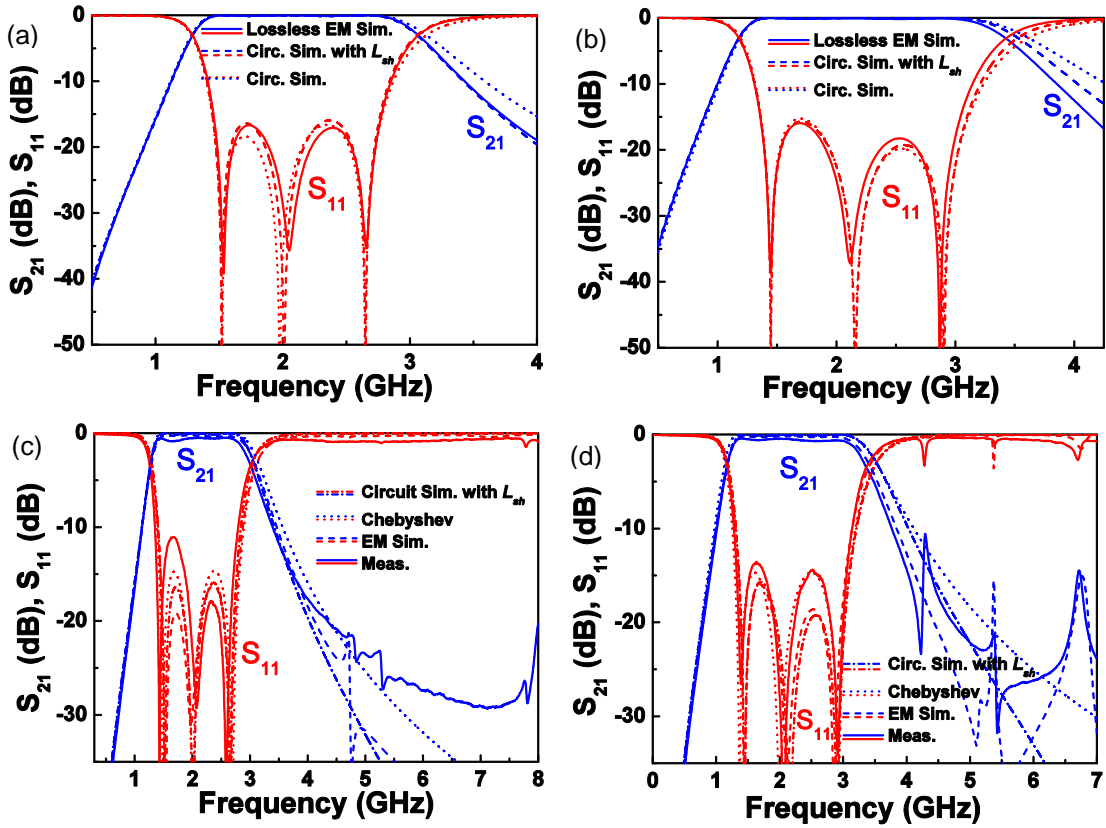
Figure 3.26. Frequency response without losses (a), (b) and wideband frequency response (c), (d) of the designed third-order filter with 70% and 90% fractional bandwidth, respectively. The values of the circuit simulation considering parasitics, inferred from parameter extraction method, are (in reference to Figure 3.15b): (a), (c): $C = 0.188$ pF, $L = 0.62$ nH, $C_s = 0.85$ pF, $L'_s = 6.3$ nH, $C'_p = 2.43$ pF and $L'_p = 2.7$ nH. (b), (d): $L = 0.384$ nH, $C'_p = 1.79$ pF and $L'_p = 3.2$ nH, $C_s = 1.08$ pF, $L'_s = 4.89$ nH and $C = 0.182$ pF. The modified values of the OCSRR considering the wideband model with the additional parasitic element L_{sh} are (in reference to Figure 3.9a): (a), (c): $L = 0.62$ nH, $C'_p = 2.54$ pF, $L'_p = 2.56$ nH and $L_{sh} = 0.15$ nH. (b), (d): $L = 0.384$ nH, $C'_p = 1.779$ pF, $L'_p = 3.216$ nH and $L_{sh} = 0.2$ nH.

In Figure 3.26(a)-(b) the lossless frequency response comparison of these filters is shown, including the electromagnetic simulation and the circuit simulation, considering the simple and wideband OCSRR model (i.e., with and without considering L_{sh}). In Figure 3.26(c)-(d) the wideband frequency response of these filters including measurement is depicted. As can be seen, the higher the bandwidth, the worse the model prediction of the upper transition band. Nonetheless, the wideband model of the OCSRR has been proven to be useful for filters with fractional bandwidths as high as 90%. For higher bandwidth requirements, the model will not accurately predict the upper transition band due to the limited range of operation of the lumped element equivalent circuit model. However, since the limitation to design wider band filters would come only from the model rather than from the layout, it would still be possible to consider this approach for wider band filters, where enhanced nominal bandwidths in the design could be considered to compensate the model inaccuracies. Good agreement between the measured frequency responses and the simulations is obtained. Wide stop-bands are achieved in both cases (the 70% fractional bandwidth filter is free of spurious bands in the depicted range, i.e., four times the central filter frequency).
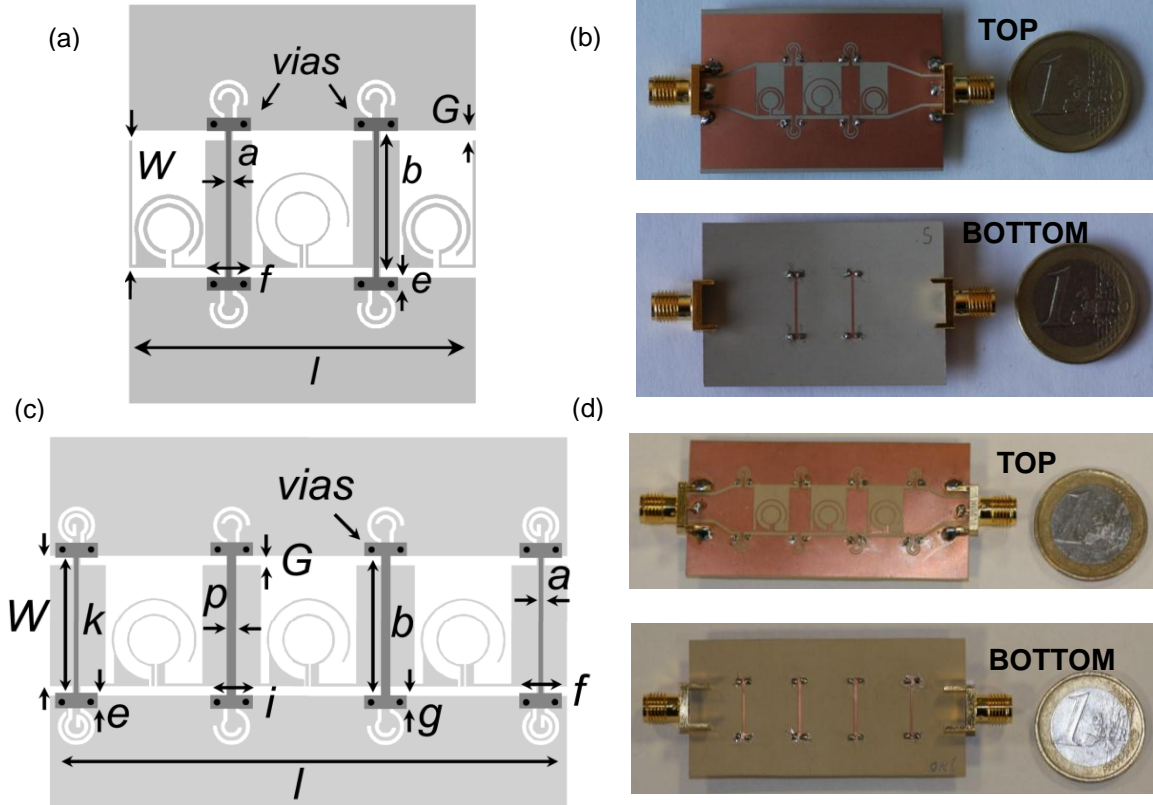
Figure 3.27. Topology (a), (c) and photograph (b), (d) of the designed fifth- and seventh-order filter, respectively. The considered substrate is the *Rogers RO3010* with thickness h = 0.254 mm and measured dielectric constant ε_r = 11.2. Dimensions are: (a), (b): l = 25 mm, W = 9.23 mm, G = 0.71 mm, a = 0.4 mm, b = 10.64 mm, e = 0.96 mm and f = 3.2 mm. For the external OSRRs: r_{ext} = 2.5 mm, c = 0.3 mm and d = 0.35 mm. For the central OSRR: r_{ext} = 3.4 mm, c = 0.16 mm and d = 1.24 mm. For the OCSRRs: r_{ext} = 1.4 mm and $c = d$ = 0.3 mm. (c), (d): l = 39.16 mm, W = 9.23 mm, G = 0.712 mm, a = 0.35 mm, b = 10.63 mm, e = 1.19 mm, f = l = 3.2 mm, g = 1 mm, k = 10.3 mm and p = 0.71 mm. For the OCSRRs of stages 1 and 7, r_{ext} = 1.4 mm, c = 0.3 mm and d = 0.2 mm; For the OCSRRs of stages 3 and 5, r_{ext} = 1.4 mm, c = 0.3 mm and d = 0.3mm; For the OSRRs of stages 2, 4 and 6, r_{ext} = 3.2 mm, c = 0.16 mm and d = 1.02 mm.

Filter size is as small as $0.13\lambda_g \times 0.15\lambda_g$ and $0.13\lambda_g \times 0.17\lambda_g$ for the 70% and 90% fractional bandwidth filter, respectively, where λ_g is the guided wavelength at the central filter frequency.

Higher order structures have also been studied [110], [111]. An order-5 Chebyshev filter with f_0 = 2 GHz, ripple of 0.05 dB and fractional bandwidth of 50% (FBW_{-3dB} = 59%) and an order-7 filter with f_0 = 1.87 GHz, ripple of 0.25 dB and fractional bandwidth of 53% (FBW_{-3dB} = 55%), have been designed. The layouts and photographs of these filters are shown in Figure 3.27 and the frequency response in Figure 3.28. From this analysis, it can be deduced that the parameter L_{sh} has to be also considered for high order filters although the bandwidth of the filter is relatively small compared to the cases analyzed before. This is because the small error of the simple OCSRR model is multiplied for each OCSRR stage, resulting in higher inaccuracies both below and above the band as the order increases (whereas for low order filters the simple OCSRR only results in inaccuracies above the band).
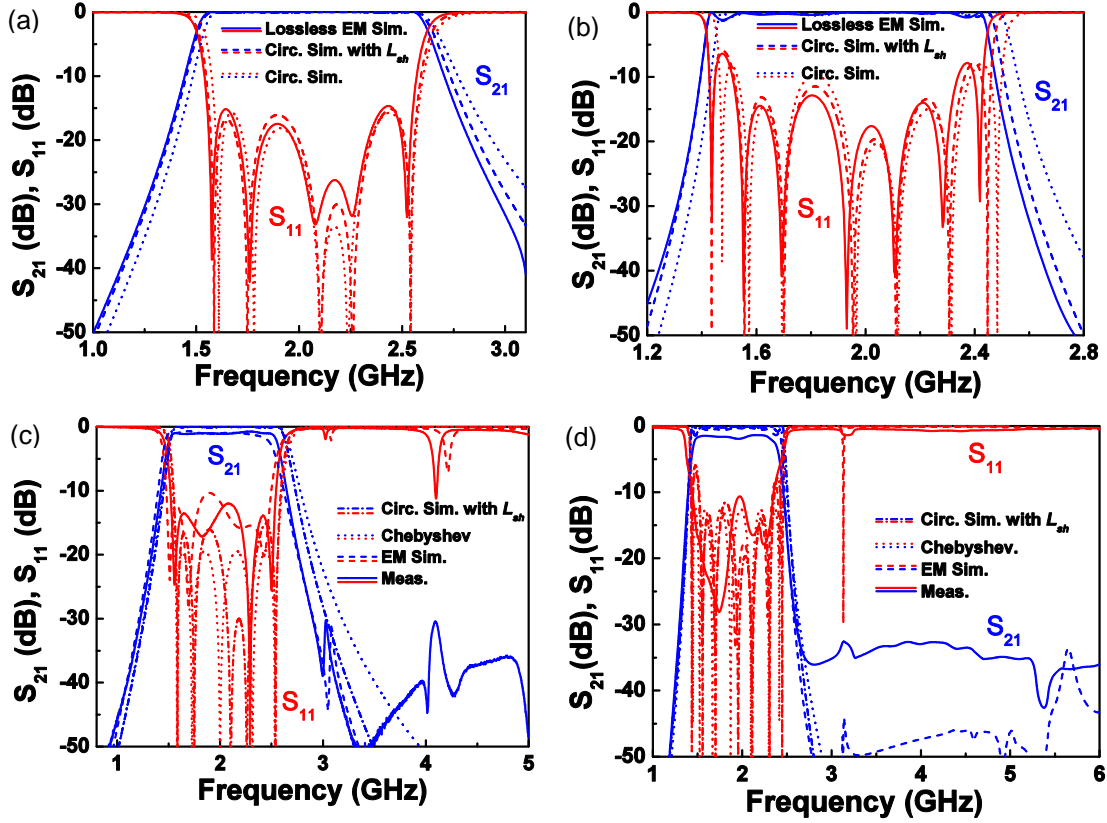
Figure 3.28. Frequency response without losses (a), (b) and wideband frequency response (c), (d) of the designed fifth- and seventh-order filter, respectively. The element values for the circuit simulation without considering L_{sh} are (in reference to Figure 3.15): (a), (c): For the external OSRRs: $C = 0.207$ pF, $C_s = 0.763$ pF and $L'_s = 8.501$ nH. For the central OSRR: $C = 0.274$ pF, $C_s = 0.436$ pF and $L'_s = 13.118$ nH. For the OCSRRs: $L = 0.474$ nH, $C'_p = 4.5$ pF and $L'_p = 1.224$ nH. (b), (d): For the OCSRRs of stages 1 and 7, $L'_p = 1.56$ nH, $C'_p = 4.34$ pF and $L = 0.47$ nH; For the OCSRRs of stages 3 and 5, $L'_p = 0.979$ nH, $C'_p = 6.46$ pF and $L = 0.501$ nH; For the OSRRs of stages 2, 4 and 6, $L'_s = 11$ nH, $C_s = 0.588$ pF and $C = 0.26$ pF. The modified values of the OCSRR considering the wideband model with the additional parasitic element L_{sh} are (in reference to Figure 3.9a): (a), (c) $L = 0.385$ nH, $C'_p = 4.4$ pF, $L'_p = 1.259$ nH and $L_{sh} = 0.35$ nH. (b), (d): For the OCSRRs of stages 1 and 7, $L'_p = 1.56$ nH, $C'_p = 4.35$ pF, $L = 0.48$ nH and $L_{sh} = 0.31$ nH; For the OCSRRs of stages 3 and 5, $L'_p = 1.009$ nH, $C'_p = 6.28$ pF, $L = 0.501$ nH and $L_{sh} = 0.33$ nH.

This phenomenon can be clearly appreciated in Figure 3.28(b), where the seventh-order filter presents a very good agreement between the circuit and electromagnetic response around the band-pass but tends to fail at the edges if the parameter L_{sh} is not considered. On the other hand, it is demonstrated that the design of high order filters is also possible with this approach if the wideband model of the OCSRR is considered, obtaining similar results in measurement (although higher losses are observed for the seventh-order filter due to the non-consideration of conductor losses and fabrication tolerances). In addition, a high selectivity is obtained, with a rejection level better than -30 dB for at least $2.5f_0$ and $3f_0$, with filter dimensions as small as $0.24\lambda_g \times 0.17\lambda_g$ and $0.37\lambda_g \times 0.17\lambda_g$ for the fifth- and seventh-order filter, respectively.

Finally, although it is difficult to briefly compare the presented filters with other planar implementations unless similar specifications are considered, the paper by Z-C. Hao and J-S. Hong [112] devoted to the state of the art of ultra-wideband filters can be

considered, where several recent implementations are highlighted. The combination of size and performance of this new approach can be considered to be competitive in comparison with the state of the art presented in [112].

3.2.2   Design and applications of microstrip CRLH lines

The study to combine both OSRRs and OCSRRs in microstrip technology has also been examined [106]. Nonetheless, since the microstrip OSRR model is much more complex than that in CPW technology, the parameter extraction method is no longer valid, and a more complex design is required. Hence, a similar methodology can be applied although with a manual curve fitting between the responses.

In order to demonstrate this possibility, a third-order Chebyshev band-pass filter with f_0 = 1.3 GHz, fractional bandwidth 50%, and ripple of 0.1 dB is designed. The layout of the final filter is depicted in Figure 3.29. The electromagnetic simulated and experimental frequency responses of this filter are depicted in Figure 3.30(a). The circuit simulation of the filter, as well as the ideal Chebyshev response, is also included in the figure. The group delay and insertion losses are also shown in Figure 3.30(b). Again, the different curves are in good agreement in the region of interest. Measured filter characteristics are good, with insertion losses lower than 0.56 dB between 1 GHz and 1.6 GHz, and return losses better than 16 dB between 1 GHz and 1.61 GHz. In this case, the average un-loaded Q-factor of the filter resonators has been found to be Q_u= 181 where the Chebyshev prototype elements and the approximation of an equal quality factor of the OSRRs and OCSRRs resonators have been considered.

Thus, the implementation of artificial lines implemented by the combination of OSRRs and OCSRRs in microstrip technology has also been demonstrated and applied to band-pass filters. Nonetheless, since the design is more complex, no further applications have been considered.
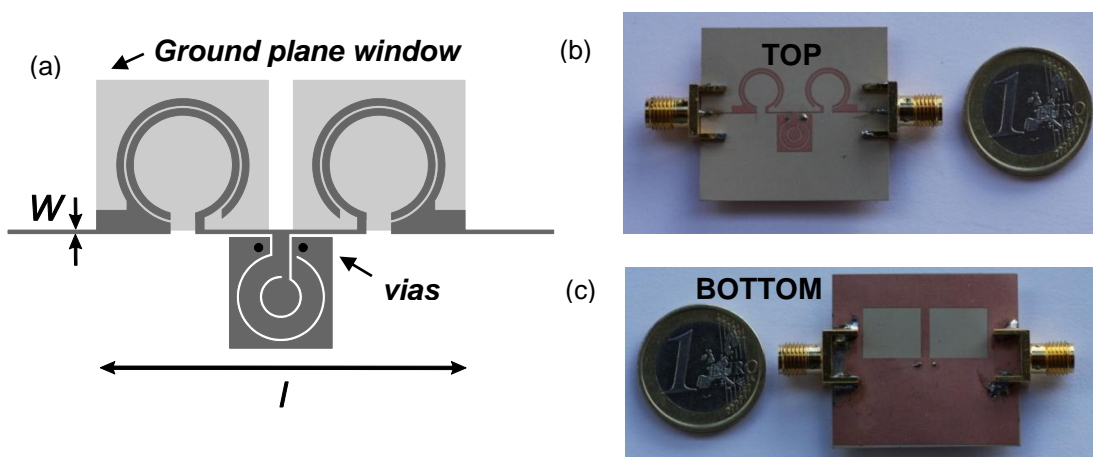
Figure 3.29. Layout (a) and top (b) - bottom (c) photograph of the microstrip wideband band-pass filter based on a combination of series connected OSRRs in the external stages and a pair of shunt connected OCSRRs in the central stage. The substrate is the *Rogers RO3010* with thickness h = 0.254 mm and measured dielectric constant ε_r = 11.2. Dimensions are: l = 22.3 mm and W = 0.21 mm. For the OCSRR: r_{ext} = 2.7 mm, c = 0.2 mm and d = 1.2 mm. For the OSRR: r_{ext} = 4 mm, c = 0.4 mm and d = 0.2 mm.
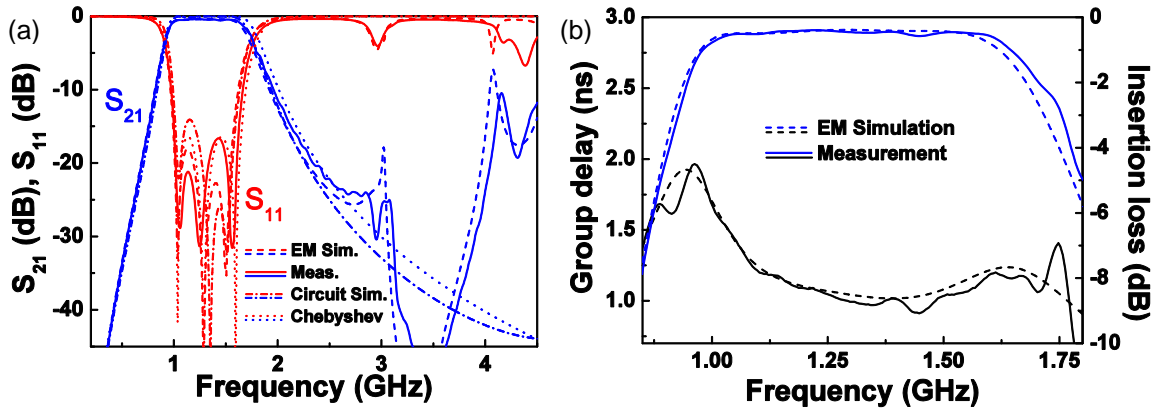
Figure 3.30. Frequency response (a), group delay and insertion loss (b) of the circuit of Figure 3.29. The element values obtained from the band-pass prototype transformations, in reference to Figure 2.11(a), are: C_L = 0.27 pF, L_L = 0.93 nH, C_R = 3.3 pF and L_R = 11.52 nH. The values of the circuit simulation considering parasitics, inferred from curve fitting are, in reference to Figure 3.1(b) and Figure 3.11: L_{m1} = 0.8 nH, L_{m2} = 0.4 nH, L'_s = 12.93 nH, C_s = 1.33 pF, C_1 = 1.28 pF, C_2 = 0.98 pF, L_p = 2 nH and C_p = 5.8 nH.

3.3 Implementation and applications of E-CRLH lines with open resonators

In this section, the possibility of extending the previous concepts to design fully-planar E-CRLH lines by means of open resonators will be studied. Since the circuit model of these artificial lines (shown in Figure 2.14b) is formed only by shunt and series resonators, it seems feasible to implement these lines by combining OSRRs and OCSRRs. Nonetheless, as will be seen later, depending on the element values required for the application, and the already mentioned OSRR limitation in microstrip technology, the substitution of some of these resonators with other semi-lumped elements will have to be considered.

In addition, unlike the conventional CRLH lines, both microstrip and CPW E-CRLH lines can be modeled with the same equivalent circuit which can predict the response at the different bands. For this purpose, the topology, accurate circuit model and synthesis of the E-CRLH line for both technologies will be presented, demonstrating its possible applications to the design of quad-band components or dual-band band-pass filters.

3.3.1 Topology and synthesis of the proposed E-CRLH line

Figure 3.31 shows the topology of the proposed CPW and microstrip E-CRLH line based on open particles [113], [114]. In CPW technology, the series and parallel LC resonators are implemented by means of OSRRs and OCSRRs, respectively, with the exception of the parallel resonator in the series branch, which is implemented by parallel connecting a capacitive patch and a meander inductor. The choice of this latter semi-lumped element instead of a series OCSRR is due to the required high ratio between inductance and capacitance which typically results when applying this unit cell

for the forthcoming applications. On the other hand, in microstrip technology the series connected OSRRs can no longer be described by a simple model, as already shown in section 3.1.2, and thus these resonators are also replaced for other semi-lumped elements composed of meander inductors, patch capacitances and interdigital capacitances, with an additional etching in the ground plane to avoid a high increase of the ground plane capacitance.

Consequently, for microstrip technology the shunt connected series resonator (L_{vs}, C_{vs}) is implemented by means of the central meander strip and a patch capacitance, the series resonator of the series branch (L_{hs}, C_{hs}) is implemented by means of an interdigital capacitor and a meander inductor and the physical realization of the parallel resonator of the series branch (L_{hp}, C_{hp}) is achieved by means of an additional meander inductor and a patch capacitance. The accurate circuit model that describes the presented CPW and microstrip E-CRLH lines is shown in Figure 3.32. It corresponds to the canonical E-CRLH line presented in Figure 2.14(b), though with three additional parameters due to the parasitics (C_1, C_2 and L).

Nonetheless, as occurred with the conventional CRLH lines implemented with open resonators, if these parasitics are considered in the design procedure, the desired multi-band functionality can still be obtained. To design quad-band components, the already explained theory of section 3.2.1.1 for dual-band devices can be considered although with the required expansion to obtain the quad-band functionality.
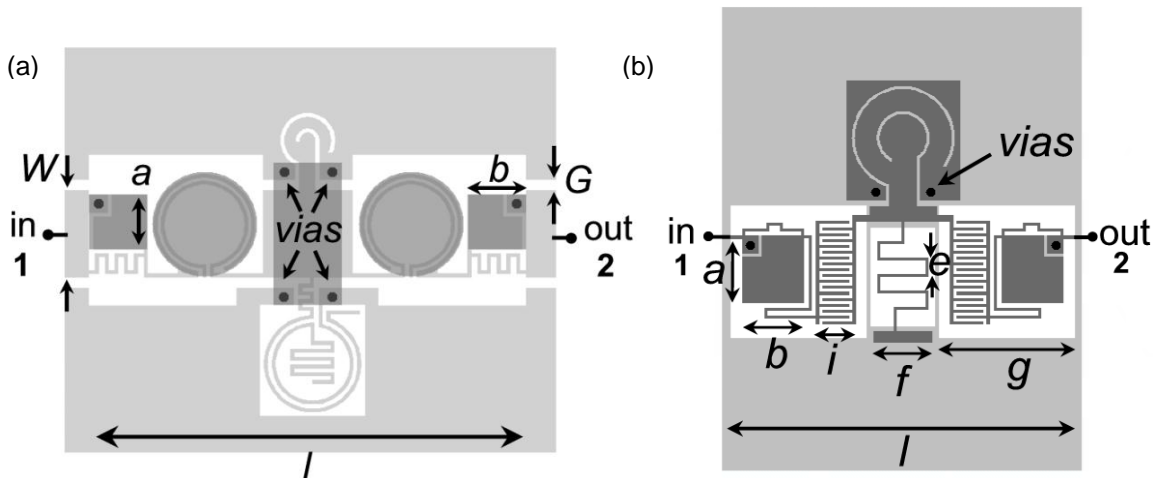
Figure 3.31. Topology of the proposed fully-planar CPW (a) and microstrip (b) E-CRLH line. The considered substrate is the *Rogers RO3010* with thickness h = 0.254 mm and measured dielectric constant of ε_r = 11.2 in CPW (a) and ε_r = 10.5 in microstrip (b). Dimensions are: For the CPW based E-CRLH line (a): W = 4.5 mm, G = 0.524 mm, a = 2.8 mm, b = 3 mm and l = 22.5 mm. The width and separation of all the meanders is 0.2 mm. For the series connected OSRRs, r_{ext} = 2.6 mm, c = 0. 2 mm and d = 0.15 mm; for the shunt connected OSRR, r_{ext} = 2.5 mm, c = 0.2 mm and d = 0.2 mm. For the OCSRR, r_{ext} = 1.4 mm, c = 0.2 mm and d = 0.6 mm. For the microstrip based E-CRLH line (b): a = 3.47 mm, b = 3.37 mm, e = 0.73 mm, f = 3.17 mm, g = 7.39 mm, i = 2.2 mm and l = 18.76 mm. For the OCSRR: r_{ext} = 2.8 mm, c = 0.16 mm and d = 1.2 mm. All the meanders have a width of 0.16 mm. The interdigital capacitors have a width and separation between fingers of 0.16 mm. The radius of the vias is 0.25 mm.
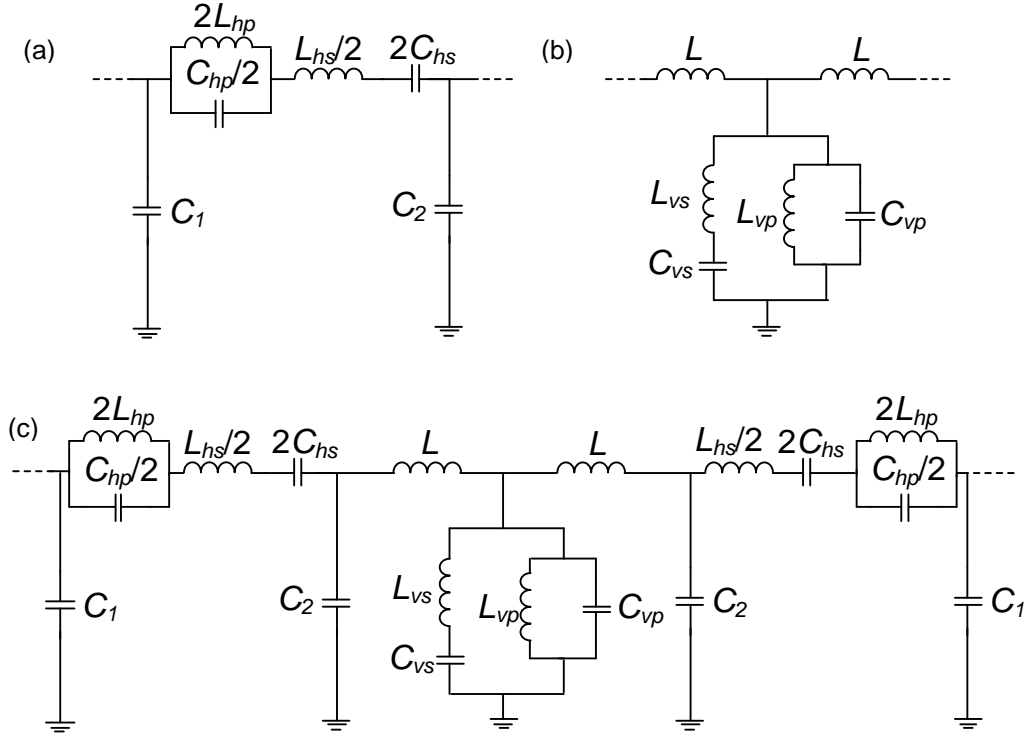
Figure 3.32. Accurate circuit model for the structures of Figure 3.31 divided in the series branch (a) and shunt branch (b). The complete model is thus obtained by cascading the two-port (a), (b) and (a), resulting in the circuit model of (c).

Focusing on impedance inverters (since it will be the building block for all the devices that will be shown), the electrical length has to be forced to $-90°$ at f_1 and f_3 (left-handed bands), and $+90°$ (right-handed bands) at f_2 and f_4, being $f_1 < f_2 < f_3 < f_4$. In addition, if the required impedance Z_a is also set at the four operation frequencies, from equations (2.16) and (2.20) it yields

$$\chi_s(\omega_n) = (-1)^n Z_a \tag{3.14}$$

$$\chi_p(\omega_n) = (-1)^{n+1} Z_a \tag{3.15}$$

where $n = 1, 2, 3, 4$ is the frequency index, and $\chi_s(\omega_n)$ and $\chi_p(\omega_n)$ are the reactances of the series and shunt branch of the T-circuit model, which for the case of the canonical E-CRLH line model of Figure 2.14(b) are given by

$$\chi_s(\omega_n) = \omega \frac{L_{hs}}{2} - \frac{1}{2\omega C_{hs}} + \frac{2\omega L_{hp}}{1 - \omega^2 L_{hp} C_{hs}} \tag{3.16}$$

$$\chi_p(\omega_n) = \frac{1}{\dfrac{1}{\omega L_{vs} - \dfrac{1}{\omega C_{vs}}} + \dfrac{1}{\omega L_{vp}} - \omega C_{vp}} \tag{3.17}$$

These reactances can also be calculated for the E-CRLH line model considering the parasitics. This can be done by obtaining the [ABCD] matrix of the circuit model of

Figure 3.32(c) and forcing it to be equal to the [ABCD] matrix of a *T*-circuit model. Nonetheless, if the parasitic values are unknown, then the system cannot be analytically solved. Thus, equations (3.16), (3.17) are initially considered in order to obtain a first tentative layout to infer the parasitic elements. This layout is obtained considering the reported models for the open particles [53], [100] - [102], the well-known parallel plate capacitor formula, as well as the straight-line inductor approximation [26]

$$L(\text{nH}) = 2 \cdot 10^{-4} l \left[ln\left(\frac{l}{W_s + t}\right) + 1.193 + 0.2235 \frac{W_s + t}{l} \right] K_g \qquad (3.18)$$

where W_s is the strip width, l the strip length, t the metal thickness (all given in μm) and $K_g = 0.57 - 0.145 \cdot ln(W_s/h)$. Afterwards, an optimization process through the curve fitting the reactances inferred from circuit and electromagnetic simulation is applied, where the complete circuit values of Figure 3.32 (including parasitics) are obtained. The next step is to analytically re-calculate the resonator elements considering the inferred parasitics so that the required values of impedance and phase at the operating frequencies are obtained. Consequently, equations (3.14), (3.15) are solved considering in this case the series and parallel reactances of the equivalent *T*-circuit model of the E- CRLH line model shown in Figure 3.32(c). Once all the element values are obtained, the topology of the different resonators at the layout level is modified in order to fit the electromagnetic simulation of each section of the structure to the circuit simulation (this does not substantially affect the parasitics). By these means, the layout of the whole structure which provides the required values of characteristic impedance and phase at the operating frequencies is obtained.

3.3.2   Quad-band applications

In this section, the unit cells of the type of Figure 3.31 with its circuit model of Figure 3.32(c) will be applied to the design of quad-band impedance inverters, power dividers and hybrid couplers.

3.3.2.1   Quad-band impedance inverters

The implementation of a quad-band impedance inverter operative at the commercial GSM (f_1 = 0.9 GHz, f_4 = 1.8 GHz) and the GPS (f_2 = 1.176 GHz, f_3 = 1.575 GHz) frequency bands is considered as case study [113], [114]. The characteristic impedance has been forced to be 35.35 Ω at these frequencies, in order to subsequently implement a quad-band Y-junction power divider as proof of a concept demonstrator. The element values of the ideal circuit (Figure 2.14b) that result by solving equations (3.14), (3.15) with $\chi_s(\omega_n)$ and $\chi_p(\omega_n)$ given by (3.16), (3.17) are L_{hs} = 22.46 nH, C_{hs} = 0.77 pF, L_{hp} = 0.88 nH, C_{hp} = 14.05 pF, L_{vs} = 8.78 nH, C_{vs} = 1.41 pF, L_{vp} = 1.91 nH and C_{vp} = 8.99 pF. The resulting topology following the methodology explained in the last subsection for the CPW and microstrip based E-CRLH lines are those shown in Figure 3.31, where the recalculated element values considering parasitics are for the CPW E-CRLH line of Figure 3.31(a): L_{hs} = 21 nH, C_{hs} = 0.775 pF,

L_{hp} = 0.88 nH, C_{hp} = 13.96 pF, L_{vs} = 8.8 nH, C_{vs} = 1.41 pF, L_{vp} = 1.95 nH, C_{vp} = 8.3 pF, C_1 = 0.41 pF, C_2 = 0.22 pF and L = 0.4 nH, whereas for the microstrip E-CRLH line of Figure 3.31(b) they are: L_{hs} = 20.89 nH, C_{hs} = 0.76 pF, L_{hp} = 0.89 nH, C_{hp} = 13.92 pF, L_{vs} = 8.6 nH, C_{vs} = 1.44 pF, L_{vp} = 1.87 nH, C_{vp} = 7.98 pF, C_1 = 0.37 pF, C_2 = 0.62 pF and L = 0.45 nH. The electromagnetic and circuit simulated transmission and reflection coefficients of these inverters, inferred by considering 35.35 Ω port impedances, are depicted in Figure 3.33.

For comparison purposes, the insertion and return losses, inferred from the circuit simulation of the accurate circuit model of Figure 3.32 are also depicted in the figure. Figure 3.33 reveals the good matching level of the ports at the design frequencies, also confirmed by the representation of the Bloch impedance in Figure 3.34. The dispersion diagram (shown in Figure 3.35) indicates that the required phase shift (±90°) is achieved at each design frequency. Another aspect to highlight is the small inverter size, i.e., for the CPW E-CRLH line 22.5 mm × 15.6 mm, which corresponds to λ_g/9.5 × λ_g/13.5 at the first frequency band and λ_g/4.7 × λ_g/6.7 at the fourth frequency band; for the microstrip E-CRLH line 18.76 mm × 14.27 mm, which corresponds to λ_g/7 × λ_g/9.2 at the first frequency band and λ_g/3.5 × λ_g/4.6 at the fourth frequency band, with λ_g being the guided wavelength. Therefore, quad-band functionality is obtained while maintaining electrical dimensions of roughly the order of the conventional mono-band impedance inverter for the most restrictive frequency.
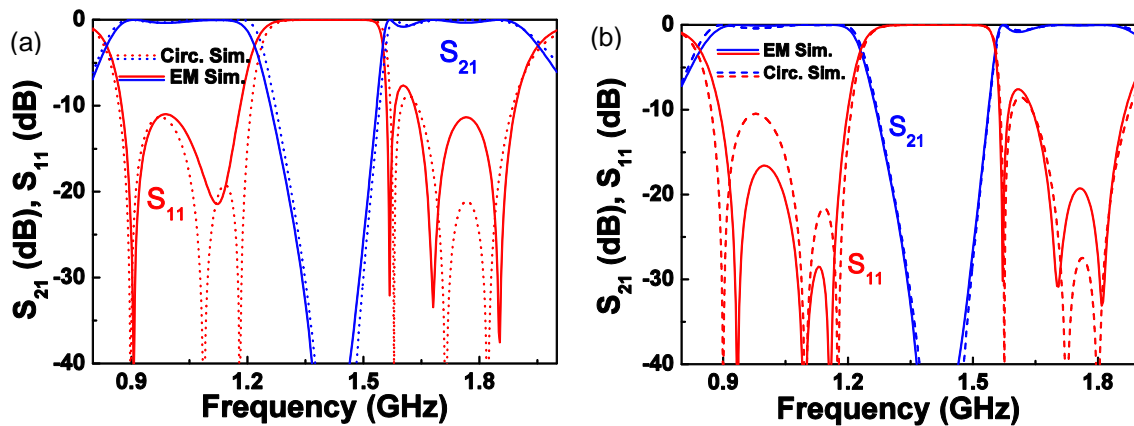
Figure 3.33. Simulated frequency response of the CPW (a) and microstrip (b) quad-band impedance inverters of Figure 3.31.
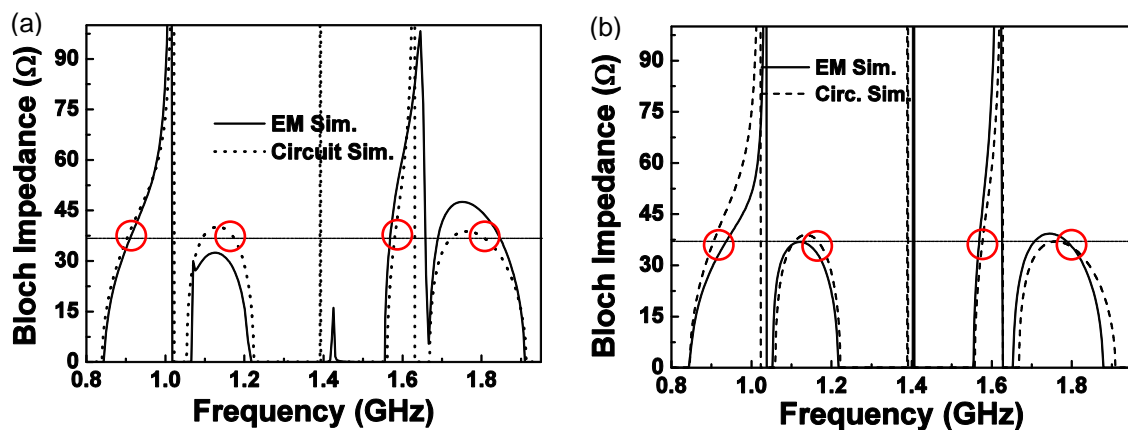
Figure 3.34. Simulated Bloch impedance of the CPW (a) and microstrip (b) quad-band impedance inverters of Figure 3.31.
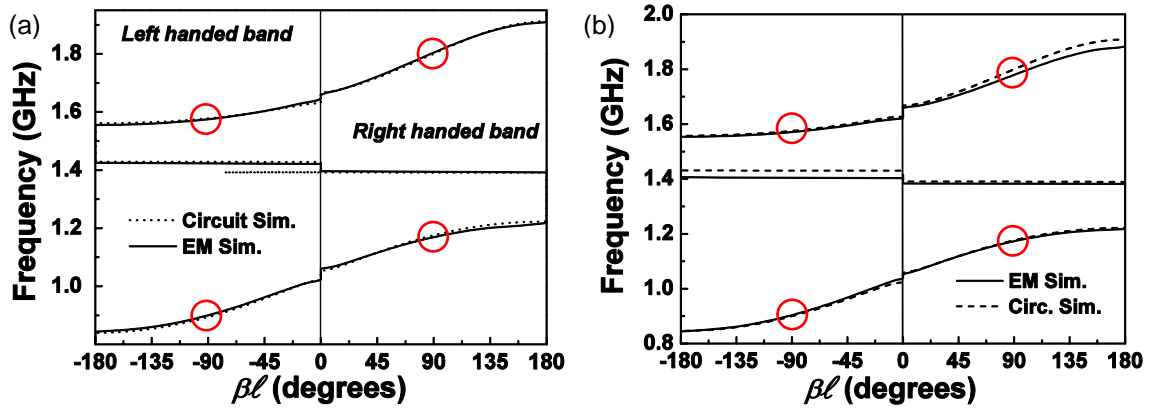
Figure 3.35. Simulated dispersion diagram of the CPW (a) and microstrip (b) quad-band impedance inverters of Figure 3.31.

3.3.2.2   Quad-band power splitters

The previous inverters have been used for the implementation of quad-band power splitters [113], [114]. To this end, two 50 Ω access lines have been added at the output. The photograph of the fabricated device is shown in Figure 3.36. The measured power splitting and matching are depicted in Figure 3.37, where for comparison purposes we have also included the results obtained from electromagnetic simulation. The agreement between experimental data and simulation is good, with measured return losses better than 10 dB for the four bands both in microstrip and CPW technology. The measured insertion losses (S_{21}) for the microstrip E-CRLH line are 4 dB, 5.9 dB, 6.3 dB and 4.6 dB, whereas for the CPW E-CRLH line they are 3.9 dB, 4.3 dB, 7.5 dB and 3.9 dB at the 1st, 2nd, 3rd and 4th bands, respectively (S_{31} roughly exhibits the same values). We would like to highlight that the quad-band power splitter has been fabricated from the previous inverter by merely cascading two access lines at the output port without any further optimization.
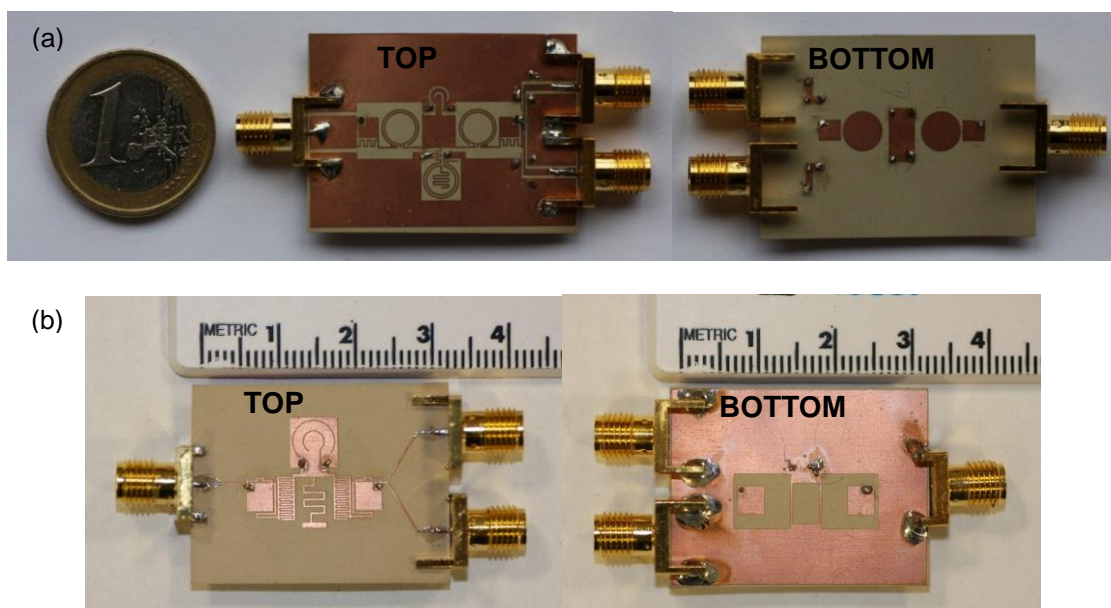
Figure 3.36. Photograph of the fabricated CPW (a) and microstrip (b) quad-band power splitter based on the quad-band impedance inverters of Figure 3.31.
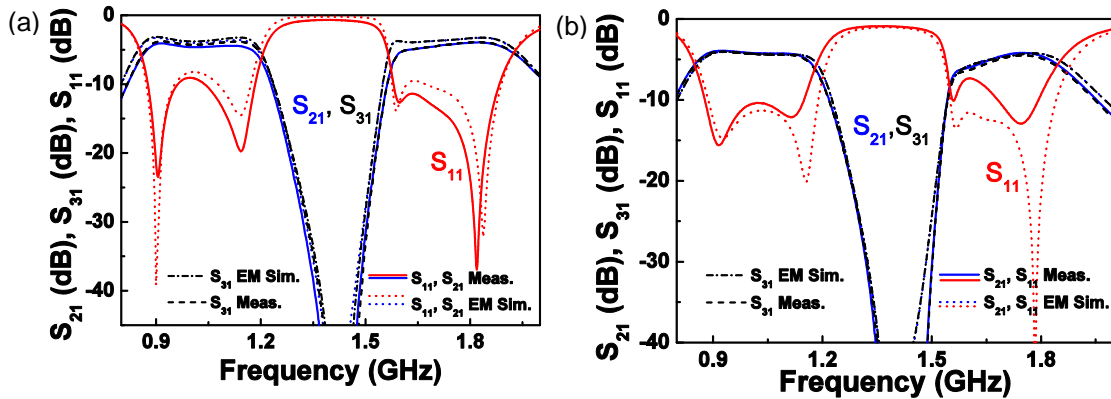
Figure 3.37. Simulated and measured frequency response of the CPW (a) and microstrip (b) quad-band power splitter of Figure 3.36.

Given that the quad-band condition is normally satisfied at the edges of the plateau, in order to increase the operational bandwidth at each band, as well as to avoid the shifting of the band to the stop-band region, band guards can be added to guarantee the functionality of the splitter for the GSM and GPS signals. To this end, we have slightly shifted down the frequencies f_1 and f_3 and shifted up f_2 and f_4, specifically 30 MHz and 20 MHz for the CPW and microstrip E-CRLH line, respectively. Nonetheless, it has to be taken into account that with this methodology the conditions of phase (±90°) as well as of impedance (35.35 Ω) are no longer achieved at the operation bands. However, since power dividers allow some flexibility in these values, the presented method still provides a good performance, though it has to be considered that for applications where these phase or impedance conditions are very strict, the aforementioned technique cannot be considered.
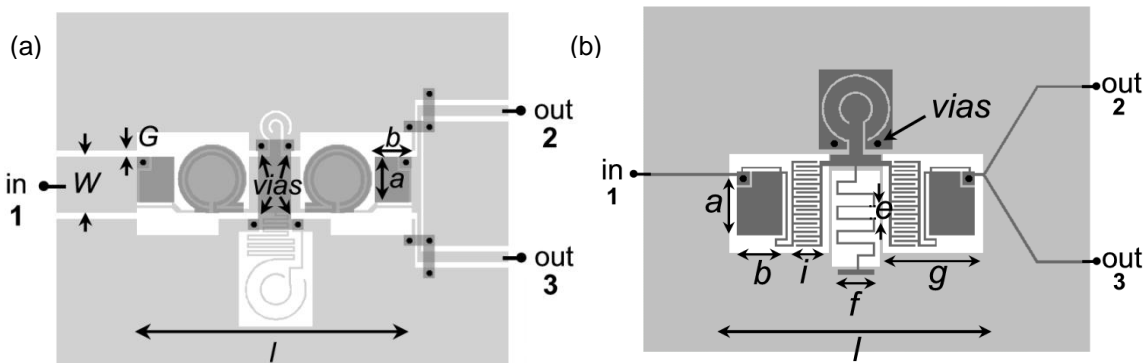
Figure 3.38. Layout of the quad-band CPW (a) and microstrip (b) power splitter with band guards. The considered substrate is the *Rogers RO3010* with thickness $h = 0.254$ mm and measured dielectric constant of $\varepsilon_r = 11.2$ in CPW (a) and $\varepsilon_r = 10.5$ in microstrip (b). Dimensions are: For the CPW power splitter: $W = 4.5$ mm, $G = 0.524$ mm, $a = 3.7$ mm, $b = 3$ mm and $l = 22.2$ mm. The width and separation of all the meanders is 0.16 mm. For the series connected OSRRs, $r_{ext} = 2.8$ mm, $c = 0.3$ mm and $d = 0.2$ mm; for the shunt connected OSRR, $r_{ext} = 2.5$ mm, $c = 0.16$ mm and $d = 1.04$ mm; for the OCSRR, $r_{ext} = 1.3$ mm, $c = 0.2$ mm and $d = 0.5$ mm. For the microstrip power splitter: $a = 4.33$ mm, $b = 3.34$ mm, $f = 2.67$ mm, $e = 0.73$ mm, $g = 7.3$ mm, $i = 2.29$ mm and $l = 18.57$ mm. The OCSRR dimensions are: $r_{ext} = 2.5$ mm, $c = 0.16$ mm and $d = 1.1$ mm. All the meanders have a width of 0.16 mm. The interdigital capacitors have a width and separation between fingers of 0.16 mm. The radius of the vias is 0.25 mm.
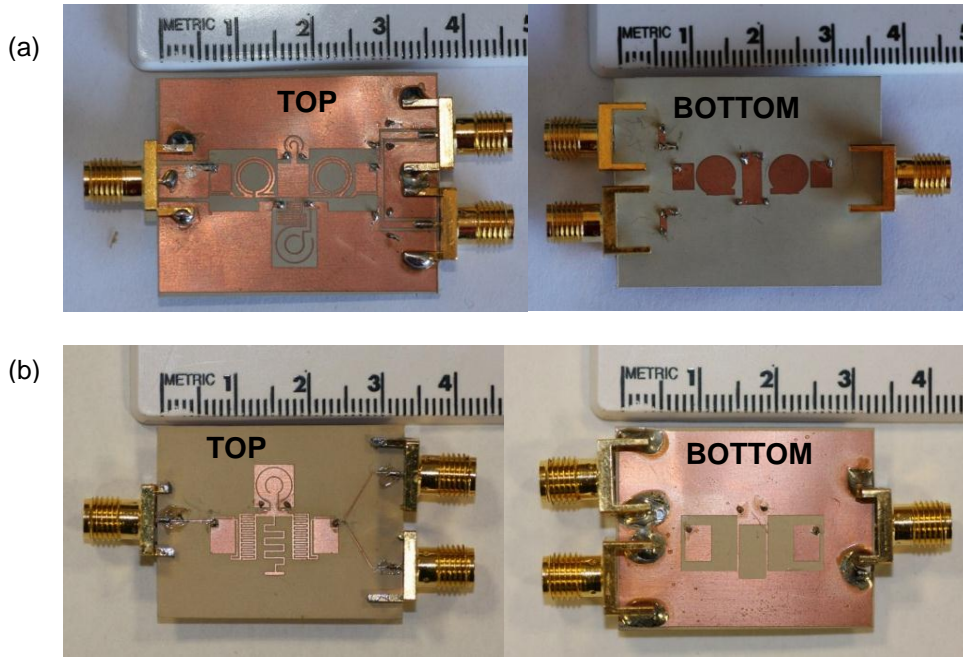
Figure 3.39. Photograph of the fabricated quad-band CPW (a) and microstrip (b) power splitter with band guards.
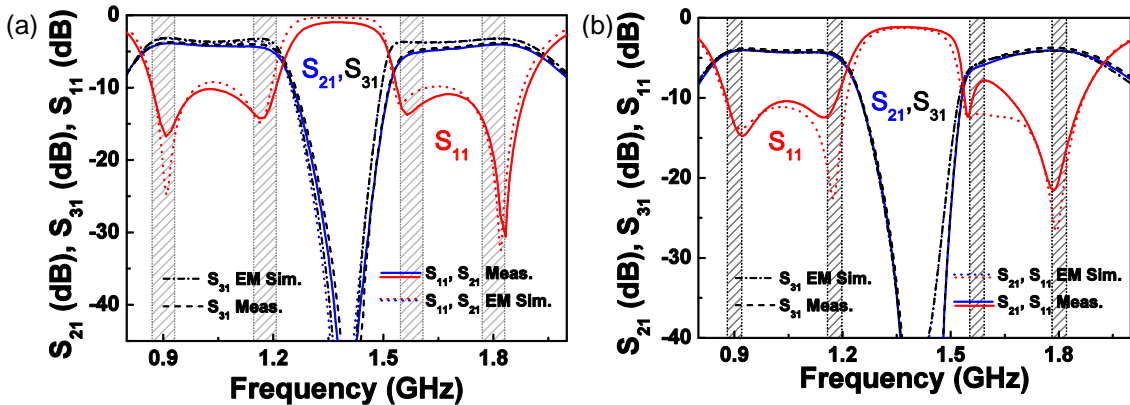
Figure 3.40. Simulated and measured frequency response of the CPW (a) and microstrip (b) power splitter of Figure 3.38. The band guards are indicated in the figure.

The layout and the photograph of the fabricated splitter with band guards are shown in Figure 3.38 and Figure 3.39, respectively, whereas the magnitude response is depicted in Figure 3.40, exhibiting an enhanced bandwidth maintaining a comparable performance to that of Figure 3.36 (where no band guards were present). Again, device dimensions are small, i.e., for the CPW E-CRLH line case 22.2 mm × 17.5 mm, which corresponds to $\lambda_g/9.6 \times \lambda_g/12.2$ whereas for the microstrip E-CRLH line case 18.87mm × 14.99 mm, which corresponds to $\lambda_g/7 \times \lambda_g/8$, with λ_g being the guided wavelength at the first band (900 MHz).

3.3.2.3   Quad-band branch line hybrid couplers

With the presented topologies, it is also possible to implement quad-band branch line hybrid couplers [114]. In this thesis, we will focus on microstrip technology, since it offers the easier implementation of such couplers. To this end, 50 Ω and 35.35 Ω quad-

band impedance inverters are designed, where the topology of the 35.35 Ω inverter of Figure 3.31(b) has been slightly modified in order to connect it in a square shaped geometry to the other impedance inverters of the branch line. The layout and dimensions of the 50 Ω and 35.35 Ω inverters are depicted in Figure 3.41. From these latter impedance inverters, we have implemented the quad-band branch line hybrid coupler depicted in Figure 3.42. The simulated and measured frequency response of the device is depicted in Figure 3.43. Matching in all bands is good, and power splitting (except in the 3rd band) is reasonable, taking into account the complexity of the device and the critical dimensions of some of its constitutive semi-lumped elements.
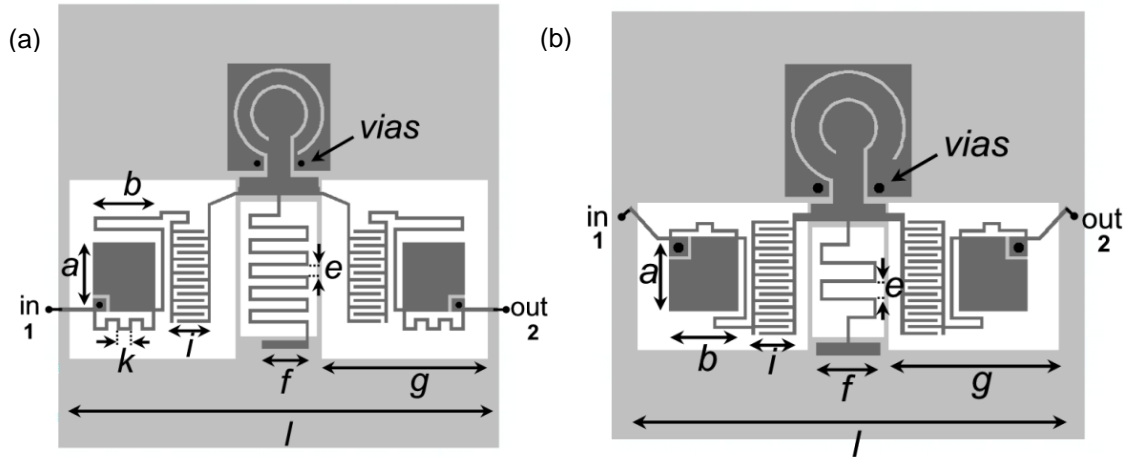
Figure 3.41. Layout of the 50 Ω (a) and 35.35 Ω (b) quad-band impedance inverter that will form the quad-band branch line hybrid coupler. The considered substrate is the *Rogers RO3010* with thickness $h = 0.254$ mm and measured dielectric constant of $\varepsilon_r = 10.5$. All the meanders have a width of 0.16 mm. The interdigital capacitors have a width and separation between fingers of 0.16 mm. Dimensions are: For the 50 Ω inverter (a): $a = 3.04$ mm, $b = 2.91$ mm, $f = 2.21$ mm, $e = 0.41$ mm, $g = 7.71$ mm, $i = 1.9$ mm, $k = 0.4$ mm and $l = 20.44$ mm. The OCSRR dimensions are: $r_{ext} = 2$ mm, $c = 0.16$ mm and $d = 0.6$ mm. The radius of the vias is 0.15 mm. For the 35.35 Ω inverter (b): $a = 3.47$ mm, $b = 3.37$ mm, $f = 3.17$ mm, $e = 0.73$ mm, $g = 8.34$ mm, $i = 2.2$ mm and $l = 21.64$ mm. The OCSRR dimensions are: $r_{ext} = 2.8$ mm, $c = 0.16$ mm and $d = 1.2$ mm. The radius of the vias is 0.25 mm.
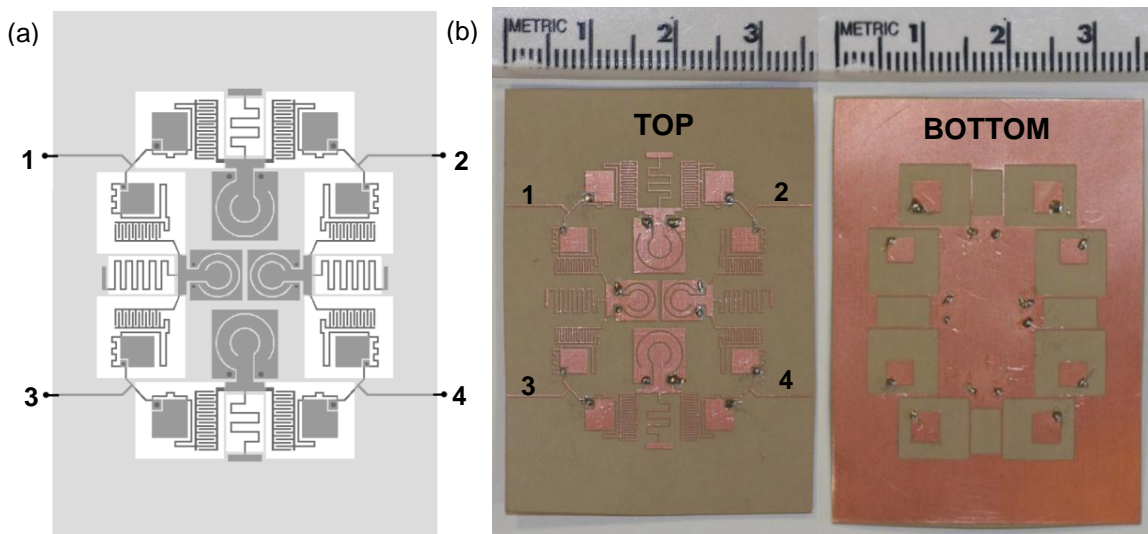
Figure 3.42. Layout (a) and photograph (b) of the fabricated quad-band branch line hybrid coupler based on the impedance inverters of Figure 3.41.
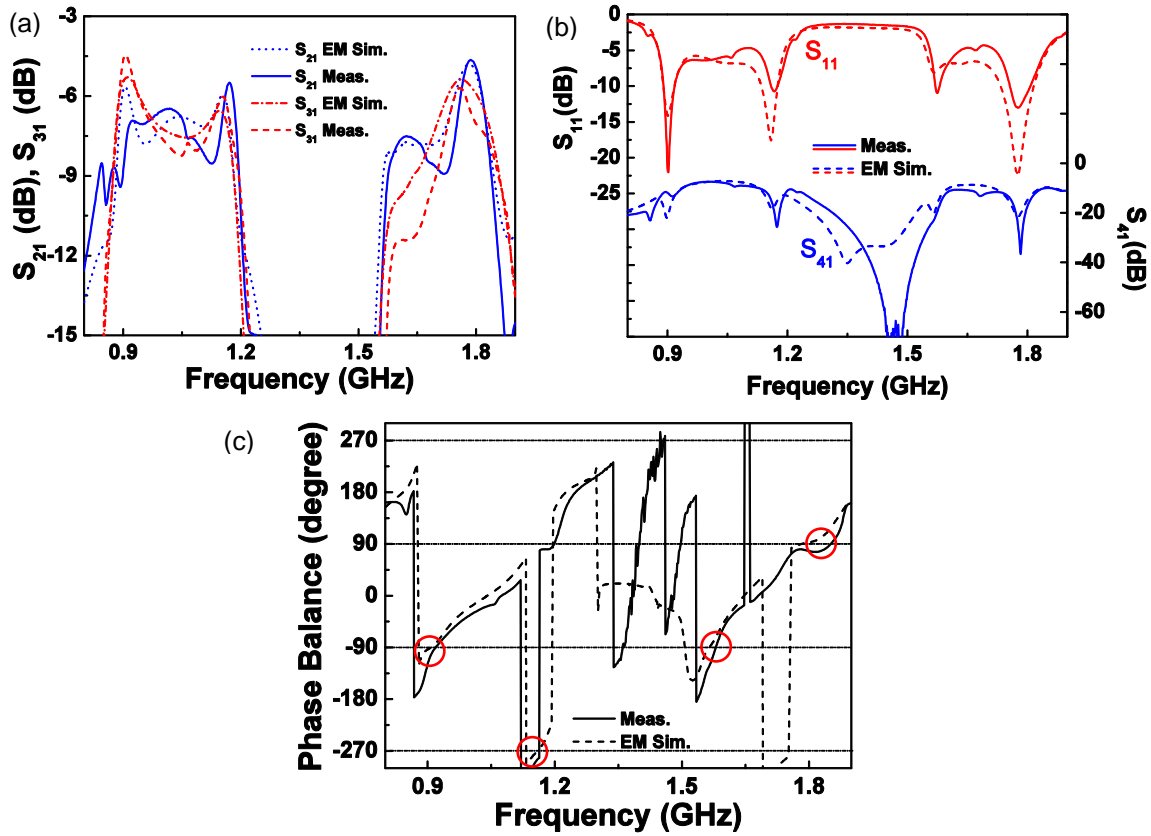
Figure 3.43. Measured and electromagnetic simulated frequency response of the quad-band branch line hybrid coupler of Figure 3.42. Power splitting (a); matching and isolation (b); phase balance (c).

The measured return losses are 22 dB, 10.7 dB, 11 dB and 13 dB for the first, second, third, and fourth bands, respectively. However, losses in the third band are not due to an improper design, as can be deduced from the electromagnetic simulation of the device with ohmic and dielectric losses excluded (shown in Figure 3.44 together with the circuit simulation of the quad-band branch line hybrid coupler). Indeed, losses can be mainly attributed to the finite conductivity of the metal, rather than to the effects of the dielectric (this has been verified by either switching off the ohmic or the dielectric losses in the simulations), which affects specially the third band since it is the narrowest. Further causes of device degradation can be variations of the actual device dimensions (due to fabrication related tolerances), as well as via metallization (the device contains 16 vias with soldered metallic pins).

The agreement between the lossless electromagnetic and circuit simulations is good for both the magnitude and the phase, in spite of the layout and circuit model complexity. It is remarkable that the measured phase balance of the output ports at the design frequencies is that corresponding to a quadrature hybrid coupler (see Figure 3.43c). This is expected on account of the phases of the transmission coefficients between the input and the output ports for the branch line coupler ($\pm 90^\circ$ for S_{21} and $\pm 180^\circ$ for S_{31}). Such phases, which have been inferred from electromagnetic simulation without access lines, are depicted in Figure 3.44(c), and are in good agreement with those inferred from circuit simulation. In addition, like in conventional branch line hybrid couplers, bandwidth is not a controllable parameter in the proposed couplers.
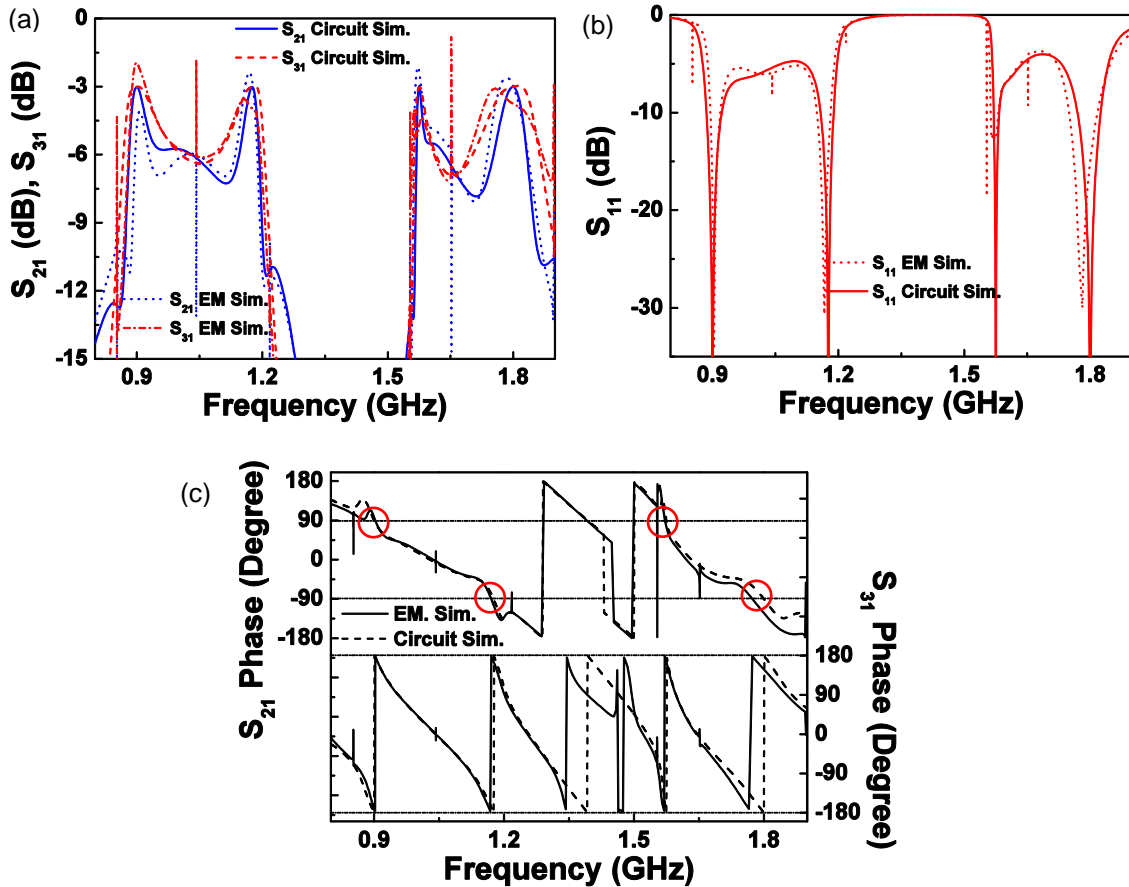
Figure 3.44. Electromagnetic simulation (with losses excluded) and circuit simulation of the quad-band branch line hybrid coupler of Figure 3.42. Power splitting (a); matching (b); phase response (c). The circuit elements corresponding to Figure 3.32 are for the 50 Ω impedance inverter: L_{hs} = 30.03 nH, C_{hs} = 0.54 pH, L_{hp} = 1.26 nH, C_{hp} = 9.87 pF, L_{vs} = 12.13 nH, C_{vs} = 1.02 pF, L_{vp} = 2.65 nH, C_{vp} = 5.31 pF, C_1 = 0.22 pF, C_2 = 0.61 pF and L = 0.45 nH. For the 35.35 Ω impedance inverter: L_{hs} = 20.89 nH, C_{hs} = 0.76 pF, L_{hp} = 0.89 nH, C_{hp} = 13.92 pF, L_{vs} = 8.6 nH, C_{vs} = 1.44 pF, L_{vp} = 1.87 nH, C_{vp} = 7.98 pF, C_1 = 0.37 pF, C_2 = 0.62 pF and L = 0.45 nH.

The reason for this is that the number of elements of the inverters is that required to achieve the characteristic impedance and phase at the four design frequencies. By implementing the impedance inverters with a higher number of unit cells, it would be potentially possible to enhance the bandwidth but at the penalty of a much larger size.

3.3.3   Dual-band band-pass filters

As already explained in section 2.3.2, E-CRLH lines also allow for the design of multi-band band-pass filters. If the purpose is to synthesize standard responses, such as the Chebyshev filter response, it is only possible to obtain dual-band behavior with the network of Figure 2.14(b) since more conditions are required, such as an equal-ripple and a fixed bandwidth at each band. This dual-band functionality can be obtained either from dispersion and impedance engineering [91], [92] or from the low-pass filter prototype through convenient transformations. The latter being considered, the mono-band band-pass filter response is firstly obtained from the well-known low-pass to band-pass transformation [25]

$$\frac{\Omega}{\Omega_c} = \frac{1}{FBW}\left(\frac{\omega}{\omega_0} - \frac{\omega_0}{\omega}\right) \tag{3.19}$$

with Ω and ω being the angular frequency of the low-pass and band-pass filter, respectively. *FBW* and ω_0 are the fractional bandwidth and central frequency of the band-pass filter and Ω_c is the angular cut-off frequency of the low-pass filter. Then, to obtain dual-band behavior, a second transformation is applied to the mono-band band-pass filter [43]

$$\omega = \frac{\omega_0}{w'}\left(\frac{\omega'}{\omega_0} - \frac{\omega_0}{\omega'}\right) \tag{3.20}$$

$$w' = \left(\frac{\omega_2 - \omega_1}{\omega_0}\right) \tag{3.21}$$

$$\omega_0 = \sqrt{\omega_1\omega_2} \tag{3.22}$$

with ω' being the angular frequency of the dual-band band-pass filter and ω_1, ω_2 the angular central frequencies of the first and second filter bands. Once these transformations are applied to the low-pass filter prototype, the circuit of Figure 2.14(b) is obtained, provided identical fractional bandwidths for the two bands ($FBW_1 = FBW_2 = FBW_{DB}$), as well as the narrow band approximation (i.e., a fractional bandwidth of each band FBW_{DB} less than 10%), are considered [43]. As reported in [43], the element values of the circuit of Figure 2.14(b) are obtained from a set of equations dependent on the low-pass filter prototype coefficients g_i, Ω_c and on the relevant design parameters, namely, the angular central frequencies ω_1, ω_2 and the FBW_{DB}

$$FBW_{DB} = FBW\left(\frac{\omega_2 - \omega_1}{\omega_2 + \omega_1}\right) \tag{3.23}$$

$$L_{hs} = \frac{2g_1\Omega_c Z_0}{g_0 FBW \cdot (\omega_2 - \omega_1)} \tag{3.24}$$

$$C_{hs} = \frac{1}{L_{hs}\omega_0^2} \tag{3.25}$$

$$L_{hp} = \frac{g_1\Omega_c Z_0(\omega_2 - \omega_1)}{2FBW g_0\omega_0^2} \tag{3.26}$$

$$C_{hp} = \frac{1}{L_{hp}\omega_0^2} \tag{3.27}$$

$$L_{vp} = \frac{FBW \cdot Z_0(\omega_2 - \omega_1)}{g_0 g_2\Omega_c\omega_0^2} \tag{3.28}$$

$$C_{vp} = \frac{1}{L_{vp}\omega_0^2} \tag{3.29}$$

$$L_{vs} = \frac{FBW \cdot Z_0}{g_0 g_2 \Omega_c (\omega_2 - \omega_1)} \tag{3.30}$$

$$C_{vs} = \frac{1}{L_{vs} \omega_0^2} \tag{3.31}$$

where the impedance scaling factor has already been considered in the above equations.

Using this procedure, a dual-band band-pass filter that covers the GSM (0.9 GHz - 1.8 GHz) and the *L1* (1.575 GHz) - *L5* (1.176 GHz) civil GPS frequency bands is designed [114], [115]. A third-order Chebyshev response with 0.01 dB ripple, central frequencies of $f_1 = 1.02$ GHz and $f_2 = 1.68$ GHz, and 20% fractional bandwidth (i.e., *FBW* = 0.2) has been considered. Even though the narrow band approximation is not satisfied, the filter response is in good agreement with the ideal mono-band Chebyshev response, where only small deviations in the transition bands are observed. From the above-mentioned filter specifications, the values of the circuit elements (Figure 2.14b) are: $L_{hs} = 18.51$ nH, $C_{hs} = 0.79$ pF, $L_{hp} = 1.16$ nH, $C_{hp} = 12.69$ pF, $L_{vs} = 10.29$ nH, $C_{vs} = 1.43$ pF, $L_{vp} = 2.58$ nH and $C_{vp} = 5.71$ pF.

Using the design methodology applied to quad-band impedance inverters, the filter layout both in CPW and microstrip technology has been obtained (depicted in Figure 3.45 together with the photograph of the fabricated prototype). In this case, filter optimization taking parasitics into account has been carried out by tuning the reactive elements at the circuit level. The changed values considering parasitics in reference to Figure 3.32 are for the CPW E-CRLH line: $L_{hs} = 18.8$ nH, $C_{hs} = 0.81$ pF, $L_{hp} = 1.14$ nH, $C_{hp} = 12.98$ pF, $L_{vs} = 10.43$ nH, $C_{vs} = 1.43$ pF, $L_{vp} = 2.56$ nH, $C_{vp} = 4.85$ pF, $C_1 = 0.24$ pF, $C_2 = 0.44$ pF and $L = 0.32$ nH, whereas for the microstrip E-CRLH line they are: $L_{hs} = 18.26$ nH, $C_{hs} = 0.8$ pF, $L_{hp} = 1.16$ nH, $C_{hp} = 12.69$ pF, $L_{vs} = 10.29$ nH, $C_{vs} = 1.43$ pF, $L_{vp} = 2.58$ nH, $C_{vp} = 4.4$ pF, $C_1 = 0.33$ pF, $C_2 = 0.51$ pF and $L = 0.45$ nH. The dual-band band-pass frequency response comparison between electromagnetic simulation, circuit simulation of the accurate circuit model of Figure 3.32 and the dual-band Chebyshev response (circuit of Figure 2.14b), are depicted in Figure 3.46(a)-(b), where good agreement between the different responses is obtained.

In Figure 3.46(c)-(f) the electromagnetic and measured wideband frequency response is depicted, as well as the group delay. Again, the measured response is predicted by the electromagnetic simulation, although the measured band-pass level of the CPW dual-band band-pass filter is slightly shifted due to the consideration of only dielectric losses in the electromagnetic simulation in this latter case. Measured return losses at both bands are better than 14 dB for the CPW case and 20 dB for the microstrip case, with the first spurious appearing at 3.82 GHz ($2.9f_0$) and 4.6 GHz ($3.5f_0$) for the CPW and microstrip case, respectively, f_0 given by expression (3.22). Moreover, the size of the filter is 20.9 mm $\times$ 17.5 mm and 19.5 mm $\times$ 13.5 mm, which corresponds to $\lambda_g/7 \times \lambda_g/8.4$, and $\lambda_g/4.5 \times \lambda_g/6.6$, for the CPW and microstrip case, respectively, with λ_g being the guided wavelength at f_0.
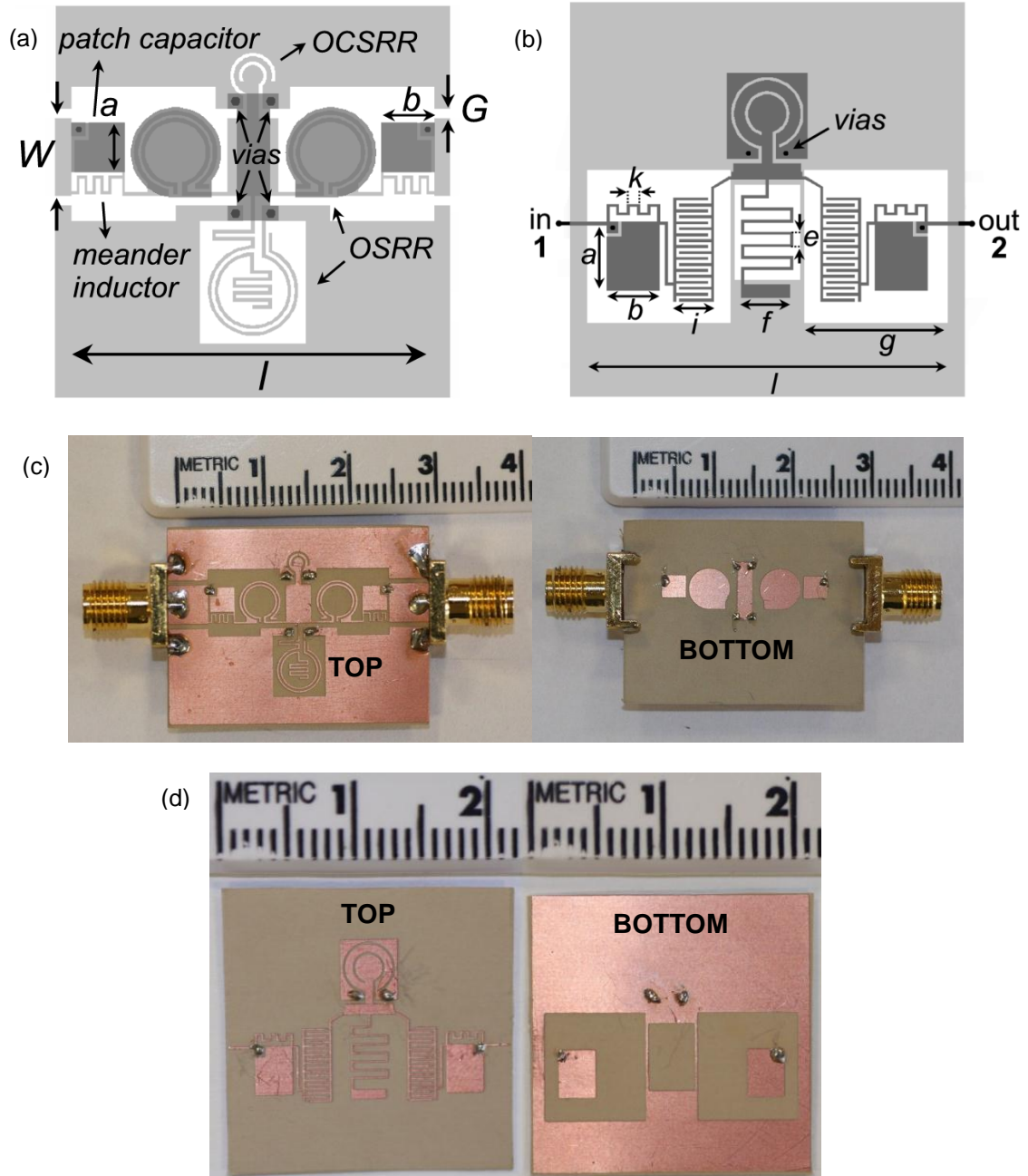
Figure 3.45. Topology and photograph of the designed dual-band CPW (a), (c) and microstrip (b), (d) dual-band band-pass filter. The considered substrate is the *Rogers RO3010* with thickness $h = 0.254$ mm and measured dielectric constant of $\varepsilon_r = 11.2$ in CPW (a), (c) and $\varepsilon_r = 10.5$ in microstrip (b), (d). The dimensions are: For the CPW dual-band filter: $W = 4.5$ mm, $G = 0.524$ mm, $a = 2.86$ mm, $b = 3$ mm and $l = 20.9$ mm. The width and separation of all the meanders is 0.16 mm for the semi-lumped elements and 0.2 mm for the shunt OSRR. For the series connected OSRRs, $r_{ext} = 2.4$ mm, $c = 0.2$ mm and $d = 0.15$ mm; for the shunt connected OSRR, $r_{ext} = 2.6$ mm and $c = d = 0.2$ mm; for the OCSRR, $r_{ext} = 1.3$ mm, $c = 0.2$ mm and $d = 0.3$ mm. For the microstrip dual-band filter: $a = 3.52$ mm, $b = 2.85$ mm, $f = 2.64$ mm, $e = 0.49$ mm, $g = 7.71$ mm, $i = 2.19$ mm and $l = 19.4$ mm. The OCSRR dimensions are: $r_{ext} = 1.95$ mm, $c = 0.16$ mm and $d = 0.6$ mm. All the meanders have a width of 0.16 mm. The interdigital capacitors have a width and separation between fingers of 0.16 mm. The radius of the vias is 0.15 mm.
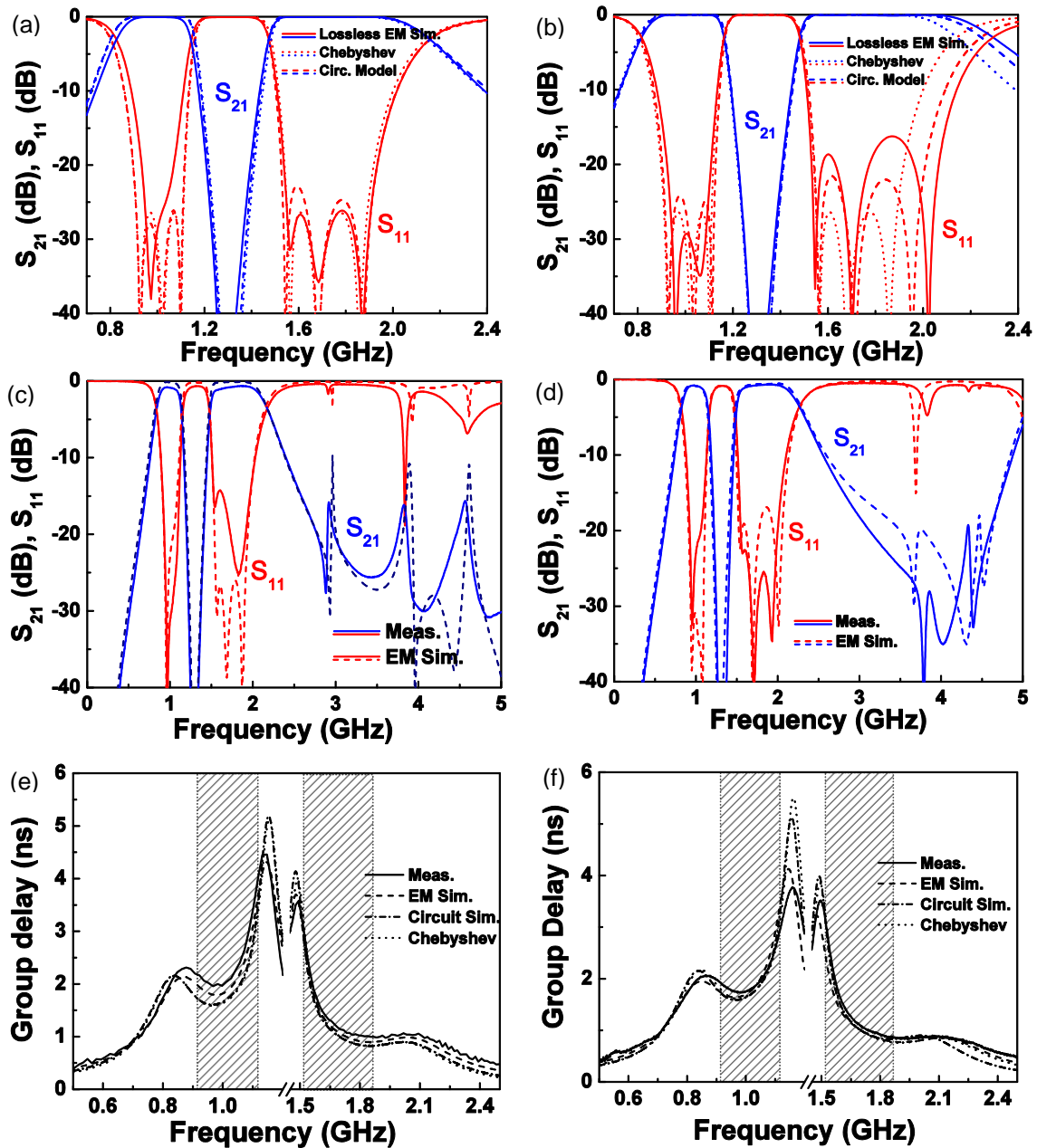
Figure 3.46. Frequency response simulation without losses (a), (b), wideband frequency response (c), (d) and group delay (e), (f) of the CPW and microstrip dual-band band-pass filter of Figure 3.45, respectively.

3.3.4   Study of the limitations

We have demonstrated the quad-band functionality of several components, fully implemented in planar technology either in microstrip or CPW technology at four commercial bands. The element values of the equivalent circuit model (Figure 3.32) have been found to be moderate for the different designed quad-band impedance inverters, and as a result it has been possible to implement the different circuits in planar technology. However, these elements depend on the relative values of the operating frequencies and, for certain designs, it may be difficult to implement these with semi-lumped components. Indeed, since the effects of the parasitics in the model

of Figure 3.32 are not very critical, we can use the simpler model of Figure 2.14(b) to estimate the values of the different elements as a function of the design frequencies and characteristic impedance. We have thus solved equations (3.14) - (3.17) analytically, and we have obtained the following results [114]

$$L_{hs}/2 = \frac{Z_a}{(\omega_4 - \omega_3) + (\omega_2 - \omega_1)} \tag{3.32}$$

$$C_{vp} = \frac{L_{hs}}{2Z_a^2} \tag{3.33}$$

$$L_{vp} = Z_a \left\{ \left(\frac{1}{\omega_1} - \frac{1}{\omega_2} \right) + \left(\frac{1}{\omega_3} - \frac{1}{\omega_4} \right) \right\} \tag{3.34}$$

$$C_{hs} = \frac{L_{vp}}{Z_a^2 2} \tag{3.35}$$

$$L_{vs} = \frac{-Z_a\{[(\omega_3 - \omega_4)\omega_2 + \omega_3\omega_4]\omega_1 - \omega_2\omega_3\omega_4\}(\omega_1 - \omega_2 + \omega_3 - \omega_4)^2}{(\omega_1 - \omega_2)(\omega_2 - \omega_3)(\omega_3 - \omega_4)(\omega_1 - \omega_4)(\omega_1 + \omega_3)(\omega_2 + \omega_4)} \tag{3.36}$$

$$C_{hp} = \frac{2L_{vs}}{Z_a^2} \tag{3.37}$$

$$C_{vs} = \frac{-(\omega_1 - \omega_2)(\omega_2 - \omega_3)(\omega_3 - \omega_4)(\omega_1 - \omega_4)(\omega_1 + \omega_3)(\omega_2 + \omega_4)}{Z_a\{[(\omega_3 - \omega_4)\omega_2 + \omega_3\omega_4]\omega_1 - \omega_2\omega_3\omega_4\}^2(\omega_1 - \omega_2 + \omega_3 - \omega_4)} \tag{3.38}$$

$$2L_{hp} = Z_a^2 C_{vs} \tag{3.39}$$

According to the previous expressions, to keep all the inductances small or moderate (large inductances limit device implementation in fully planar technology), it is necessary that any pair of consecutive operating frequencies presents a non-negligible frequency span (separation). On the contrary, some of the inductance values increase substantially and jeopardize the fully planar implementation of the device. To illustrate this, we have set f_1 = 0.9 GHz and f_4 = 1.8 GHz (the GSM frequencies considered in the reported prototype devices), and we have calculated the values of the inductances by varying the frequency difference between f_2 and f_3, considering that this frequency span is centered at $(f_1 + f_4)/2$, which means that $f_2 - f_1 = f_4 - f_3$. The different inductances of the model of Figure 2.14(b) are depicted in Figure 3.47 as a function of $f_{dif} = f_3 - f_2$ for the case of Z_a = 1 Ohm (so that the results are easily scalable with the inverter impedance). At the ends of the span, at least one of the inductances tends towards infinity. For this reason, we should avoid very close or very distant values of f_3 and f_2. Under the considered conditions (for the examples reported in the previous sections), the inductances that may limit the fully planar implementation are L_{vs} and L_{hs}. Although the considered frequencies in the reported examples do not exactly satisfy the conditions of Figure 3.47, f_3 and f_2 are roughly equidistant from $(f_1 + f_4)/2$ and close to the center of the span in Figure 3.47. This explains why we have been able to implement the reported devices by means of semi-lumped planar resonators.
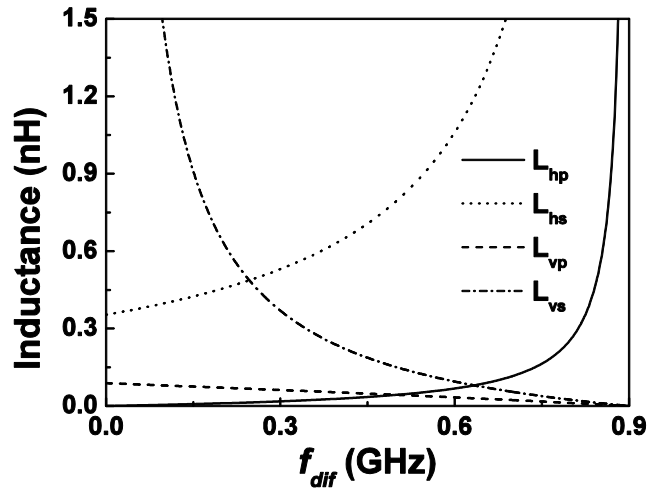
Figure 3.47. Variation of the inductances of the generalized model of Figure 2.14(b) as a function of f_{dif}.

Another limitation for the implementation of planar quad-band impedance inverters may come from the frequency difference between the upper (f_4) and lower (f_1) frequencies. If these frequencies are very distant, the validity of the model of Figure 3.32 (including parasitics) in the whole frequency span cannot be guaranteed, and hence the proposed design approach may be no longer valid. It is difficult to establish a maximum difference between f_1 and f_4 since the wideband behavior of the lumped model of Figure 3.32 depends on the considered substrate and element values. However, for most substrates and device specifications our experience dictates that it is possible to achieve fully planar devices with f_4/f_1 ratios up to 2 - 3 (being difficult to establish an accurate limit within this interval).

Therefore, according to this discussion, it is not always possible to implement quad-band devices in fully planar technology. Nevertheless, we have given the conditions (concerning the relative positions of the design frequencies) that must be fulfilled for the viability of the fully planar implementation, and these conditions have been validated by means of the proposed examples. Obviously, it is not possible to establish clear limits (as has been mentioned), though the contents of this discussion can be useful as guidelines for those designers willing to implement planar multi-band components based on impedance inverters.

In **summary**, the open resonant particles OSRRs and OCSRRs have been introduced in this chapter. The accurate circuit models of these resonators loading a CPW or a microstrip line including parasitics, have been provided. It has been demonstrated that OSRRs and OCSRRs can be combined to implement CRLH lines. These lines have been used for the design of compact dual-band components and filters, with wideband response and different orders. Finally, the open resonators combined with different semi-lumped elements have been used for the design of fully planar quad-band components and dual-band band-pass filters on the basis of the E-CRLH line concept.

CHAPTER 4

Tunable artificial lines based on open resonators

Tunable components provide the possibility of adapting themselves and operating at different frequency bands under electronic control, hence granting the device an equivalent multi-band functionality. In addition, if combined with artificial lines, further advantages such as the previously mentioned impedance and phase control are obtained.

This chapter is devoted to the analysis of the tunability of the CRLH lines proposed in chapter 3. The tunability is achieved by means of ferroelectric materials, specifically Barium-Strontium-Titanate (BST) thick-films, which change the electrical properties of the structure through the application of a static electric field. As will be seen, the size, the controllability of the different elements, and the simplicity of the biasing scheme (a single voltage can be used to tune the whole structure) are the main advantages of this approach.

In section 4.1, the state of the art on tunable artificial lines is reviewed, focusing mainly on the resonant-type approach. In section 4.2, an arbitrary tunable CRLH line based on open resonators and BST thick-films is designed and fabricated as a proof-of concept demonstrator. Once the approach is experimentally validated, in section 4.3 some of its potential applications are shown by presenting the design methodology of phase shifters, tunable wideband band-pass filters and dual-band components.

4.1 State of the art on tunable artificial lines

Various authors have worked with the aim of obtaining tunable artificial transmission lines. Regarding the *CL*-loaded approach, in [116] a tunable artificial line was presented to control the radiation angle and beam width of leaky-wave antennas through diode varactors. In [117], a tunable left-handed artificial line was implemented with ferroelectric capacitors and applied to phase shifters, with the result of size reduction and enhanced tunability, in comparison with conventional phase shifters. In addition, in [69], [118], tunable artificial lines were designed with diode varactors with the ability to control both the propagation constant and the line impedance for the different tuning states, applying these concepts to phase shifters and impedance matching networks.

Focusing on the resonant-type approach, SRRs and CSRRs have also been tuned and applied to different purposes. In [119], varactor-loaded split ring resonators (VLSRRs) were coupled to a microstrip line to obtain tunable notch filters by varying the DC voltage of the varactors and hence the effective capacitance of the VLSRR. Afterwards, in [120] these same resonators were considered to implement tunable left-handed lines through the inclusion of metallic vias and series gaps. Figure 4.1 shows both the layout and response of this latter topology. A similar methodology was carried out with the CSRR and diode varactors (VLCSRR), having demonstrated the possibility of obtaining tunable notch filters and left-handed lines, as shown in Figure 4.2 [121], [122].
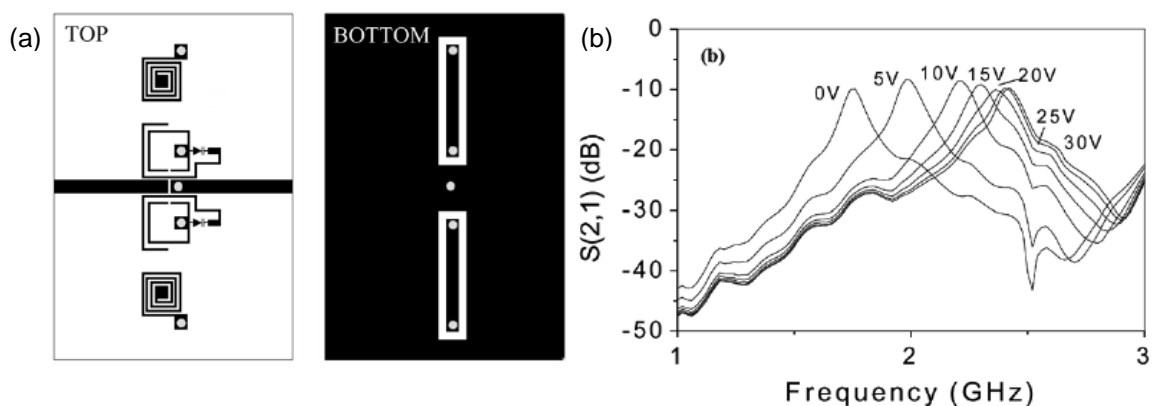
Figure 4.1. Layout (a) and measured response (b) of a tunable left-handed line implemented with a pair of VLSRRs coupled to a microstrip line with metallic vias and series gaps. Extracted from [120].

Although varactor diodes have been proven to be useful for the low region of the microwave spectrum, their low performance at high frequencies limits their possible application. In such cases, MEMS are a good alternative to overcome these drawbacks. In [123], MEMS switchable capacitors were combined with CSRR coupled to a CPW host line to implement tunable stop-band filters at Q-band, obtaining a 20% frequency tuning range. In Figure 4.3, the layout and topology of such configuration is shown, where the MEMS bridges actuates in switch-mode (i.e., only on-off states are considered). In [124], capacitive cantilever-type MEMS switches were integrated between the inner and outer rings of SRRs in microstrip technology to implement stop-band filters. By these means, a 4-pole reconfigurable band-stop filter was designed cascading four cells formed by an SRR coupled on each side of the microstrip line. Figure 4.4 shows the layout and frequency response. Through this method, the bandwidth of the stop-band response can be controlled (or even suppressed) by shifting the resonance frequency of the SRR through the up and down states of each switch actuator. In [125], similar stop-band responses were obtained by considering the MEMS as part of the SRR. Specifically, the tuning was achieved by suspending a part of the SRR, acting as up-curved cantilevers, as can be appreciated from the non-actuated SRR photograph of Figure 4.5. In Figure 4.5 the layouts of a two section stop-band filter with short and long cantilever-type SRRs are also depicted, as well as their frequency response. The tuning range is dramatically enhanced as the movable part increases, with tuning ranges of 12% and 42% for the short and long cantilever-type SRR, respectively.
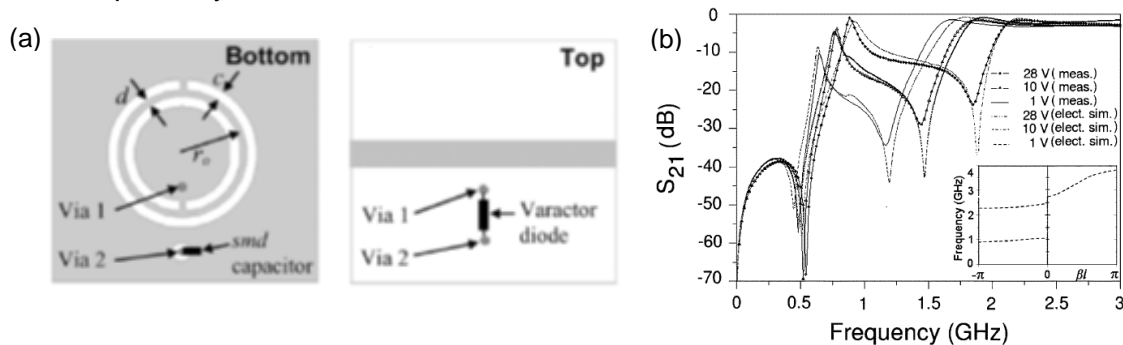
Figure 4.2. Layout of a VLCSRR coupled to a microstrip line (a) and frequency response and dispersion diagram with the additional inclusion of series gaps (b). Extracted from [121].
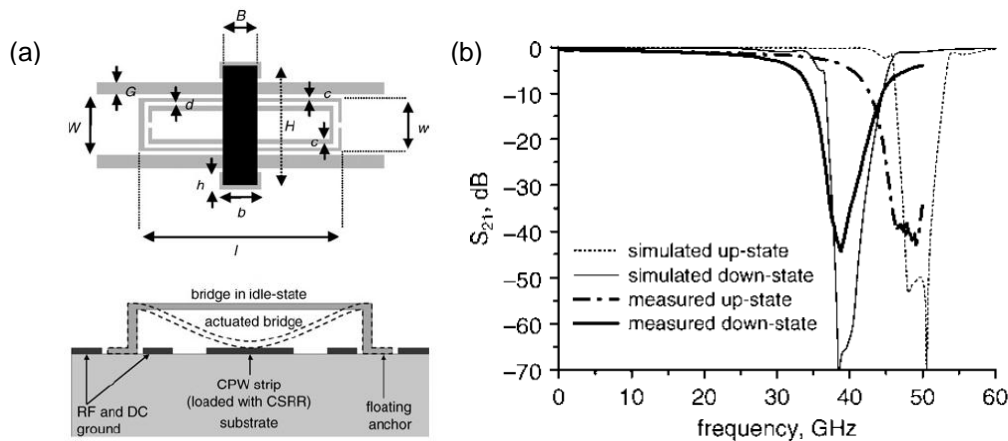
Figure 4.3. Unit cell and cross section of a CSRR loaded in a CPW transmission line with MEMS (a) and simulated and measured insertion losses (b). Extracted from [123].
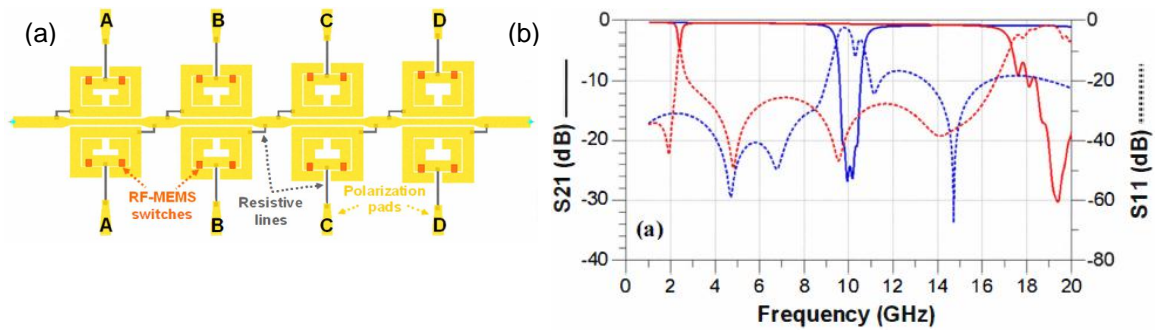
Figure 4.4. Layout of the 4-pole reconfigurable band stop filter based on MEMS-loaded SRR in microstrip technology (a) and frequency response when all MEMS are at up-state (blue) and all MEMS are at down state (red) (b). Extracted from [124].
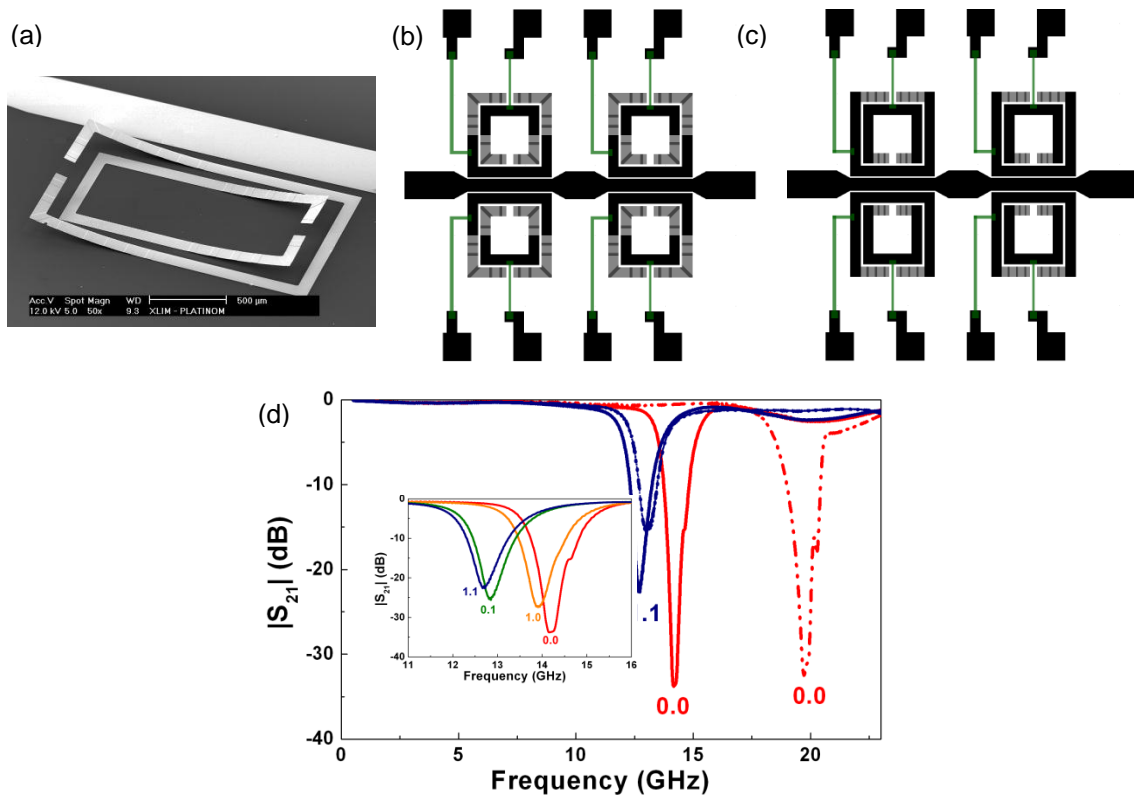
Figure 4.5. Photograph of a non-actuated cantilever-based SRR (a), layout of tunable stop-band filters based on square-shaped short (b) and long (c) cantilever-type SRR and its measured wideband frequency response for the extreme switching states (d). Solid lines correspond to the filter of Figure 4.5(b), whereas dash-dotted lines correspond to the filter of Figure 4.5(c). Actuation voltage is 30 V. Extracted from [125].

Finally, BST thick-films constitute another well-known technology to add tunability to microwave devices. Their main advantages are high power handling capabilities, fast switching speed and low cost production [126], [127]. This re-configurability can be obtained by screen printing a few microns thick BST thick-film under the metallization layer of a carrier substrate, which due to its high permittivity (the dielectric constant may typically vary between $\varepsilon_r \sim 200 - 700$) results in reasonable values of effective permittivity and tunability without the need for structures with critical dimensions [128]. By these means, tunable microstrip SRRs and OCSRRs have been presented in [129], [130]. The layout of these tunable cells is shown in Figure 4.6. The SRR coupled to a microstrip line can be tuned directly by applying a voltage between the inner and outer

rings, without the need of biasing lines. On the other hand, since in the OCSRR the two rings are electrically connected, additional biasing lines are added through the gaps of the resonator in order to obtain the required potential.

In Figure 4.7, the frequency response of a cascade of three SRRs and OCSRRs based on the unit cells of Figure 4.6 is shown. The frequency tunability is defined as

$$\tau = \frac{f_{max} - f_{min}}{f_{min}} \tag{4.1}$$

where f_{min} and f_{max} are the minimum and maximum tuning frequencies, respectively. Therefore, a tunability of 12.6% and 12% is obtained for the tunable SRR- and OCSRR-based structures, respectively, by applying a DC voltage from 0 V (untuned state) up to 140 V (tuned state). A tunable band-stop behavior is observed for the tunable SRR structure, whereas for the OCSRR structure, a tunable low-pass response is obtained (given that its equivalent circuit is mainly the canonical circuit of an elliptic low-pass filter, i.e., a series connected parallel LC tank and shunt-connected capacitances to ground).
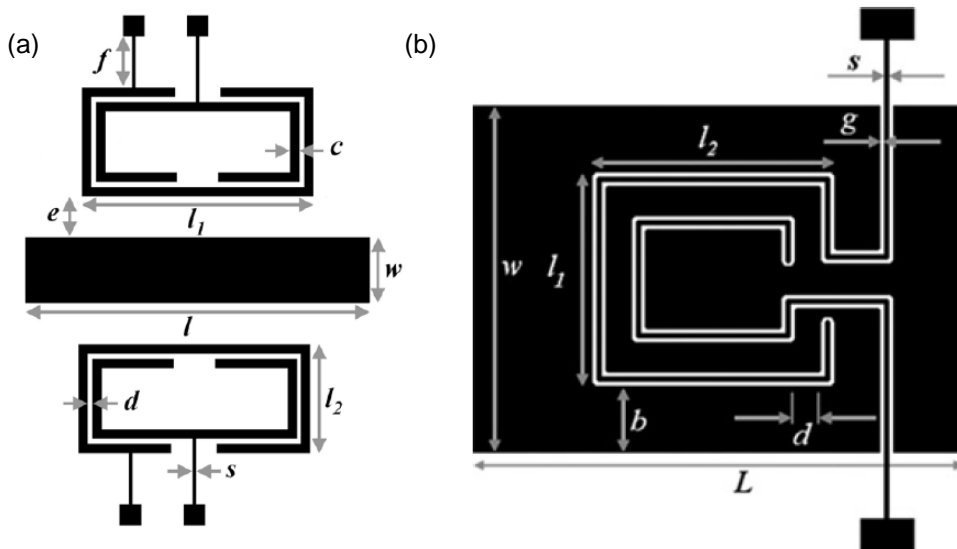
Figure 4.6. Layout of the tunable SRR (a) and OCSRR (b) based on BST thick-films. Extracted from [130].
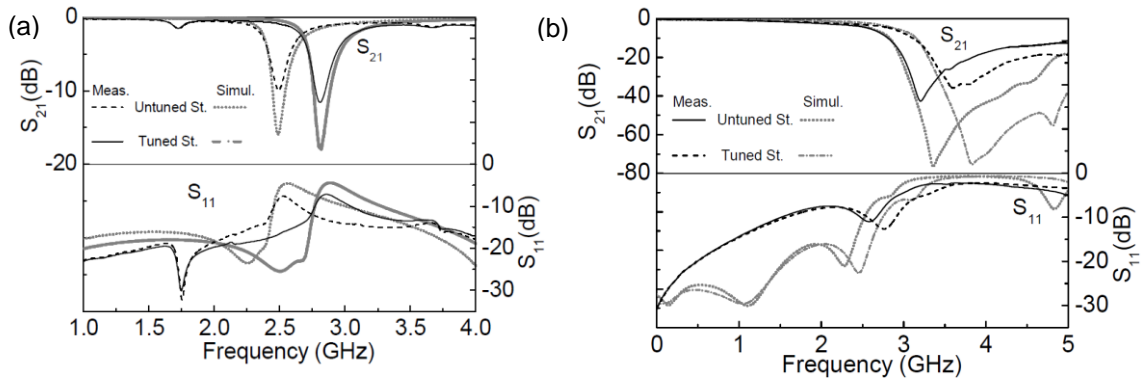
Figure 4.7. Frequency response of the cascade of three SRR- (a) and OCSRR- (b) stages based on the unit cells of Figure 4.6. Extracted from [130].

4.2 Tunable CRLH lines based on open resonators and BST thick-films

In this section, the possibility of obtaining a tunable CRLH line by means of the unit cells proposed in chapter 3 and BST thick-films is analyzed. To this end, the substrate shown in Figure 4.8(a) is considered. It is composed of a low-loss Al_2O_3 ceramic carrier substrate with permittivity ε_r = 9.8 and height of 650 µm, covered with a $Ba_{0.6}Sr_{0.4}TiO_3$ thick-film of a few microns created through a screen printing and sintering a BST powder-based paste [131]. On top of the BST layer, thin adhesive chrome and seed gold layers are thermally evaporated. The loss tangent of the BST thick-film is $tan\delta$ = 0.016 at 3 GHz, with an untuned permittivity of ε_r = 490, which can be reduced to ε_r = 220 by applying a DC voltage, representing a material tunability of 55%.

In order to design the desired planar structures, the geometry of the metallization is defined through a lithography step, with the subsequent gold electroplating process to increase the thickness of the seed gold layer to the required value (see Figure 4.8b). Finally, an additional lithography process is considered to exploit the adhesive chrome layer for the biasing network (see Figure 4.8c), which since its measured resistivity is about 50 kΩ/mm, will minimize or avoid its influence on the RF signals.

Considering the aforementioned substrate with a BST thick-film thickness of 7.5 µm, a tunable CPW CRLH transmission line formed by open resonators has been designed [132]. In Figure 4.9, the layout, the photograph and the equivalent circuit of the whole structure is shown, taking parasitic effects and the OCSRR wideband model into account. In this case, rather than pursuing a tunable CRLH line with specific functionality, the main aim is to study the capabilities of these OSRR and OCSRR lines as tunable structures based on BST thick-films. We have thus designed a line that exhibits a characteristic impedance of 50 Ω at 0.7 GHz for the untuned state. Square-shaped OCSRRs with meandered sections have been used to reduce the electrical size of the particle.

The OSRRs are tuned by applying a voltage between the rings, through the feeding ports and the ground plane. This is achieved since the central strip and the ground plane of the CPW are electrically connected through the OCSRR (this can also be deduced from the inductive path in Figure 4.9d).
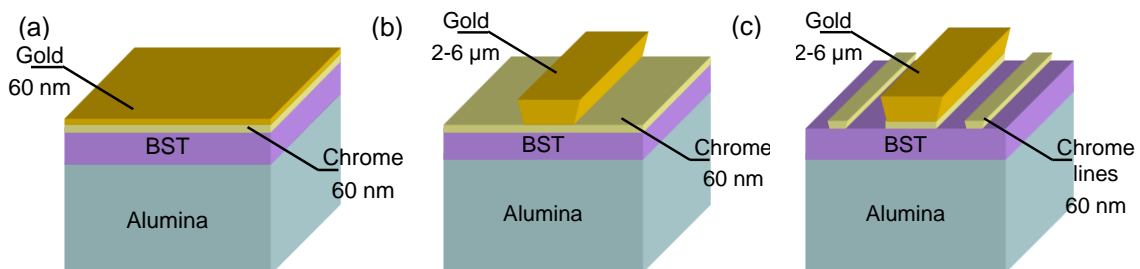
Figure 4.8. Fabrication process of the considered BST thick-film based substrate. Substrate after screen printing and sintering a BST thick-film and thermally evaporating an adhesive chrome layer and seed gold metallization (a). Substrate after the photolithography to define the metallization and the electroplating to grow the gold layer (b). Substrate after the additional photolithography to define the chrome lines for biasing purposes (c).
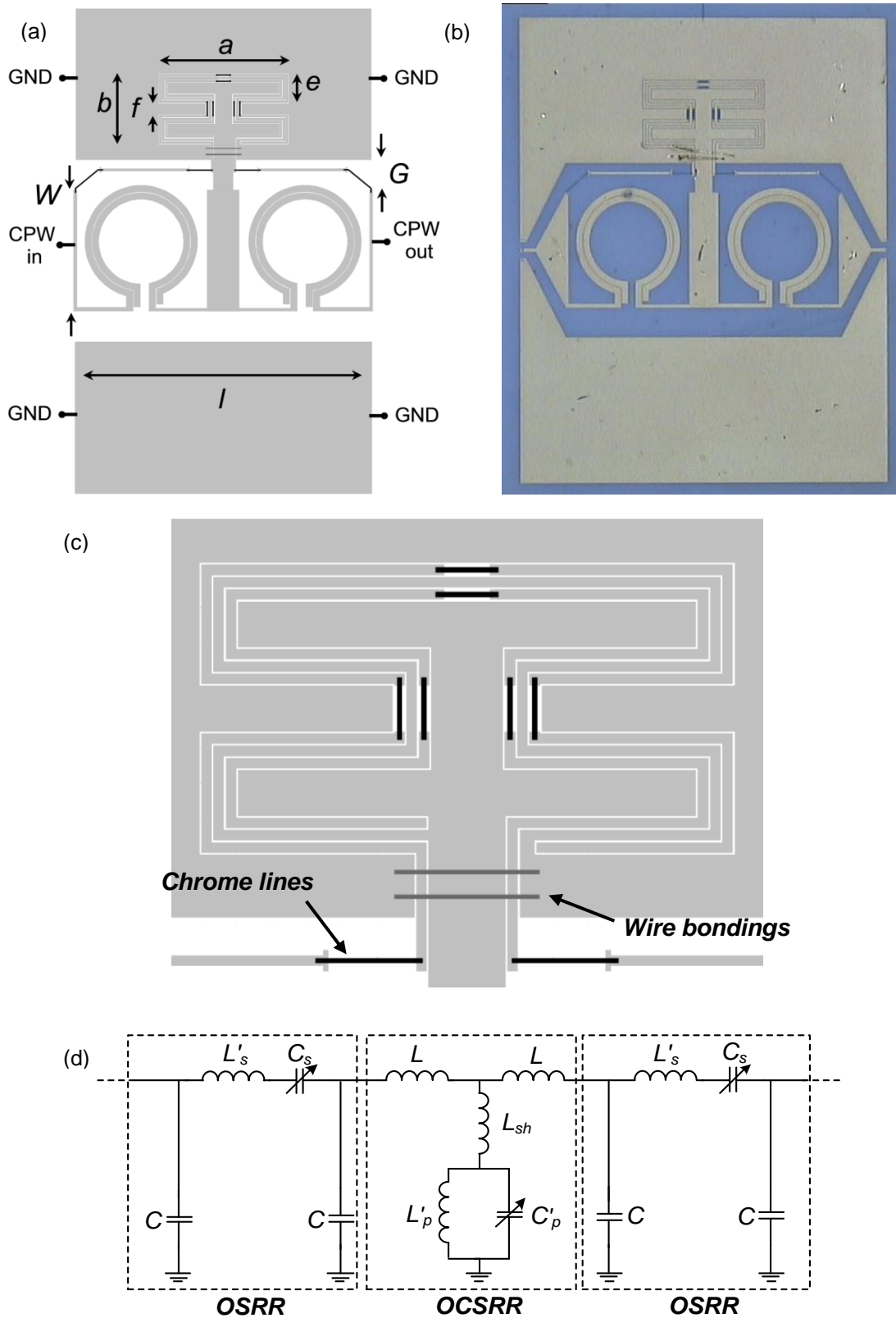
Figure 4.9. Layout (a) and photograph (b) of the tunable CRLH line, zoom of the OCSRR region (c) and equivalent circuit of the whole tunable structure (d). The chrome lines are depicted in black. Wire bondings connecting the ground planes of the OCSRR are also needed to avoid slot modes (depicted in dark gray). Dimensions are: $l = 6.9$ mm, $W = 2.8$ mm and $G = 0.72$ mm. For the OCSRR: $a = 3.05$ mm, $b = 1.66$ mm, $e = 0.7$ mm, $f = 0.26$ mm, $d = s = 60$ μm and $c = 10$ μm, s being the width of the biasing networks between the rings of the OCSRR. For the OSRR: $r_{ext} = 1.3$ mm, $d = 10$ μm and $c = 0.16$ mm.
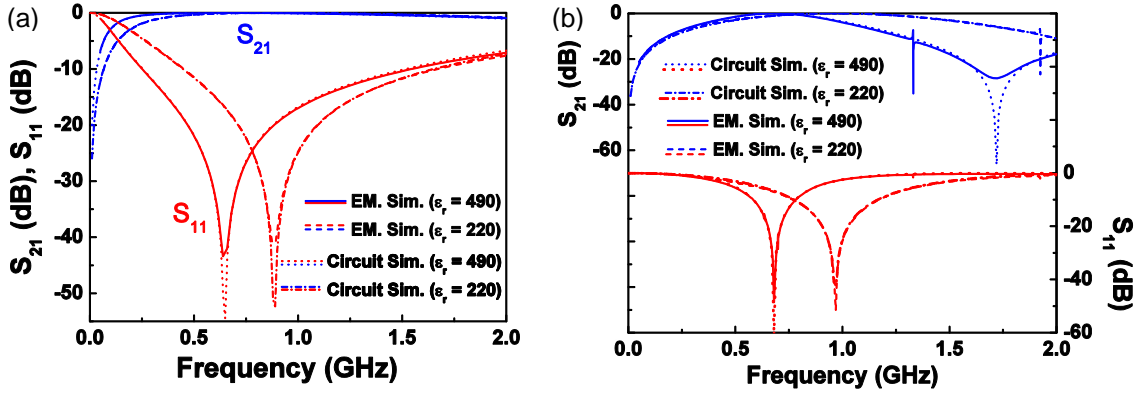
Figure 4.10. S-parameters for the untuned and maximum tuning states for the isolated OSRR (a) and OCSRR (b) of Figure 4.9(a). The extracted circuit values are in (reference to Figure 4.9d): For the untuned state: OSRR: C = 0.56 pF, L'_s = 6.57 nH and C_s = 15.94 pF. For the OCSRR: L = 0.18 nH, L'_p = 5.2 nH, C'_p = 10.67 pF and L_{sh} = 0.95 nH. For the tuned state: OSRR: C = 0.52 pF, L'_s = 6.57 nH and C_s = 8.03 pF. For the OCSRR: L = 0.18 nH, L'_p = 5.2 nH, C'_p = 5.37 pF and L_{sh} = 0.95 nH.

The tuning of the OCSRR requires two additional biasing lines inserted through the gaps of the rings since both rings are electrically connected, as already deduced in [130]. This biasing network is composed both of gold and chrome lines to avoid its RF influence on the biasing network, which could affect the band or the spurious response. The main advantage of this approach is that the biasing networks of the OCSRRs can be connected to the feeding ports and hence the tuning of the whole artificial line can be achieved by applying only a single voltage between the feeding ports and the ground plane (which can be done directly from the probes).

The electromagnetic simulation of the isolated OSRR and OCSRR of Figure 4.9(a), for the untuned and maximum tuning states of the BST-based substrate, is depicted in Figure 4.10. For these simulations, the chrome lines have not been considered due to the simulator software (Agilent *ADS*/Momentum) limitations, which cannot define different metal properties in the same layer. Nonetheless, since the resistivity of the chrome lines is about 50 kΩ/mm, the effect of these lines is expected to be negligible. In Figure 4.10 the circuit simulation at both states is also included, indicating in the same caption the element values inferred through the parameter extraction method explained in Appendix A. It is worth noting that the parasitics remain almost constant, even for the capacitance C of the OSRR, since the effect of the BST thick-film is mainly present only on the small gap regions of the resonators. The good agreement between circuit and electromagnetic simulation is also remarkable.

The tuning of the isolated OSRR and OCSRR is 37.1% and 42.3%, respectively. In Figure 4.11 the comparison between the electromagnetic simulation and circuit simulation for the whole structure is shown for the untuned state (lossless case), where a readjustment of the equivalent circuit values is needed because of the influence of the square OCSRR on the OSRR. In the same figure, the electromagnetic simulation for the maximum tuning state (ε_r = 220) is also shown. In view of the figure, it is apparent that significant tuning can be achieved through the proposed approach.
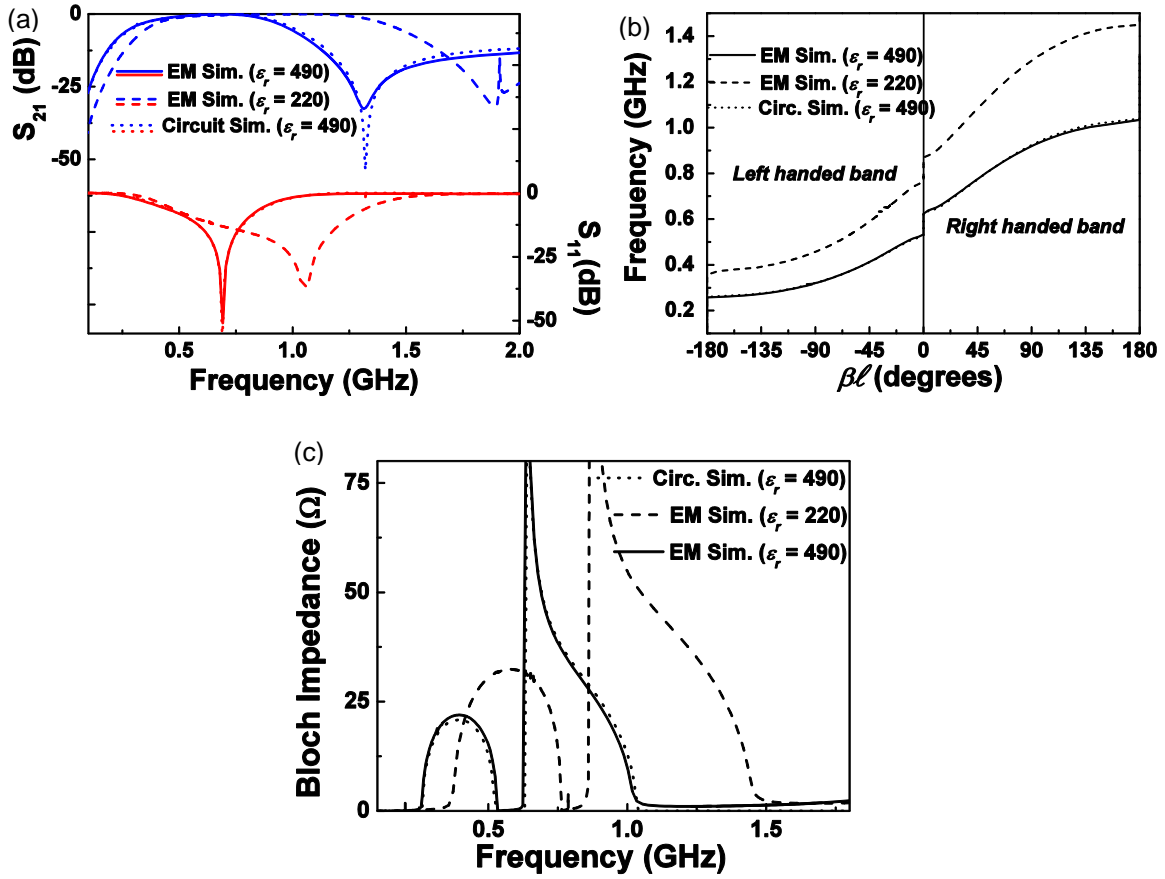
Figure 4.11. Lossless electromagnetic simulated S-parameters (a), dispersion diagram (b) and characteristic impedance (c) of the structure of Figure 4.9(a) for the untuned and maximum tuning states. The circuit simulation for the untuned state is also depicted. The equivalent circuit values are (in reference to Figure 4.9d): For the OSRR: $C = 0.44$ pF, $L'_s = 5.25$ nH and $C_s = 16.87$ pF. For the OCSRR: $L = 0.27$ nH, $L'_p = 5.25$ nH, $C'_p = 10.27$ pF and $L_{sh} = 1.93$ nH. The considered BST thick-film has a thickness of 7.5 μm and a permittivity of $\varepsilon_r = 490$ and $\varepsilon_r = 220$ for the untuned and maximum tuning states.

Figure 4.12(a) shows the measured S-parameters of the fabricated structure (layout of Figure 4.9a) for different applied voltages, where the electromagnetic simulation of the untuned and maximum tuning states taking losses into account are also included. Good agreement between measurement and electromagnetic simulation is obtained, with insertion losses of 2 dB and 1.4 dB at the central frequency for the untuned and maximum tuning state, respectively. Moreover, a frequency tunability of 36.6% is achieved.

One potential application of this artificial line is to be applied to band-pass filters, since the upper transmission zero gives a sharp transition band, and good out-of-band rejection is achieved, the first spurious appearing at $4.4f_0$ for the worst case (i.e., for the maximum tuning state).

Another possible application could be as phase shifter. As already pointed out in [47], [49], phase shifter implementation by means of artificial lines may result in compact size and flatter responses since the phase shift is no longer proportional to the length of the line.
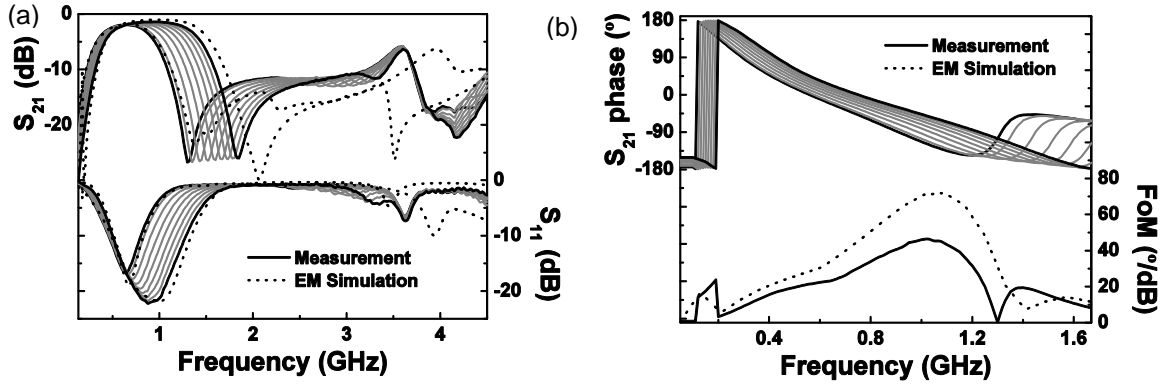
Figure 4.12. Measured S-parameters (a) and *FoM* (b) for the untuned ($\varepsilon_r = 490$) and maximum ($\varepsilon_r = 220$) tuning states of the structure of Figure 4.9(a). The tuning voltage is increased from 0 V up to 160 V in 8 steps. The electromagnetic simulations, including losses, for the maximum and untuned states are also depicted.

Additionally, these lines also present the advantage of allowing both negative, positive, or even zero degree phase shift. In Figure 4.12(b), the phase shift is shown, as well as the commonly used figure-of-merit (*FoM*) of phase shifters, which for BST thick-films (where ε_r is the variable parameter) can be defined as

$$FoM = \frac{\emptyset_{21}|_{\varepsilon_{r\,max}} - \emptyset_{21}|_{\varepsilon_{rmin}}}{min(|S_{21}[\mathrm{dB}]|)} \qquad (4.2)$$

A phase difference between the untuned and maximum tuning states of 67º and a maximum *FoM* of 45º/dB is achieved at 1.02 GHz, which is a reasonable value if compared to different phase shifters of the state of the art [133], [134]. The additional advantage of this approach is the controllability of the electric and physical parameters, as well as the size and the ultra-wideband response.

4.3 Applications

In this section, the presented tunable artificial lines will be applied to phase shifters, band-pass filters and dual-band components, analyzing for each case the strategies to enhance the tuning control as well as its limitations. All the devices that are presented here are being fabricated at the time of finalizing this thesis. For this reason, only the comparison between electromagnetic and circuit simulations will be shown.

4.3.1 Tunable band-pass filters and phase shifters

The design of phase shifters based on CRLH lines can be carried out either with metamaterial concepts or with the prototype band-pass filter theory, since both methods allow an easy control of the bandwidth and flatness of the band-pass where the phase shift is required. For this reason, in this subsection, both phase shifters and filters will be considered by means of a similar methodology.
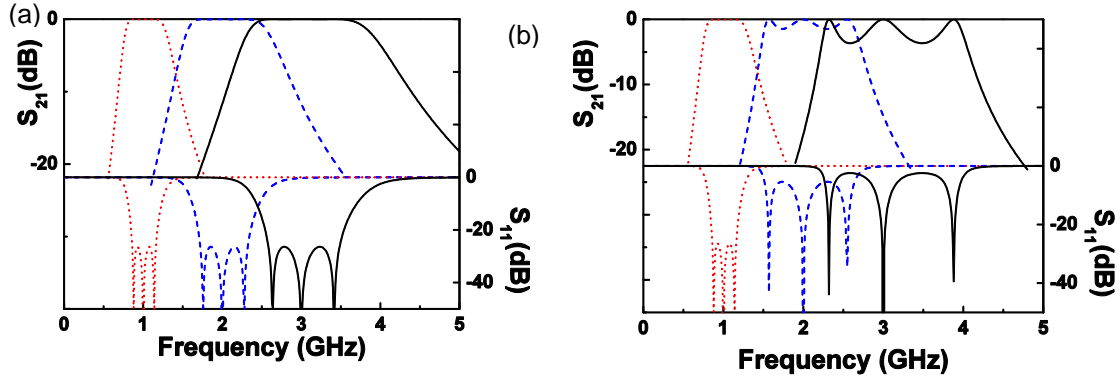
Figure 4.13. Frequency response of a tunable filter considering tunable capacitors with variable (a) and constant (b) inductors.

Focusing on the filter approach, assuming an ideal third-order Chebyshev band-pass filter (with the same equivalent circuit model of the unit cell of a CRLH line as Figure 2.11), the circuit element values (L_R, C_R, L_L and C_L) are univocally determined considering the low-pass prototype given the central frequency, bandwidth, order and ripple of the filter. Hence, to obtain a tunable filter or phase shifter with constant bandwidth and ripple, the four circuit elements should also be ideally tuned, resulting in a typical frequency response such as that shown in Figure 4.13(a), where a tunable filter with a central frequency f_0 from 1 GHz to 3 GHz with constant fractional bandwidth of 30% and ripple of 0.01 dB is considered.

On the other hand, if the inductances are kept constant and only capacitors are tuned, as is the case with most state of the art tunable components, to still obtain an optimum response considering the equivalent circuit model of Figure 2.11, some conditions must be relaxed. Since the filter order is fixed and the central frequency is given by the tuning state, the relaxed conditions are the bandwidth and ripple. In Figure 4.13(b) a response of a tunable filter with same requirement as in Figure 4.13(a) at $f_0 =$ 1 GHz is shown, but with constant inductances. As can be seen, as the frequency increases, so does the fractional bandwidth and ripple. For the considered case with a frequency tunability of $\tau = 200\%$, the bandwidth increases by a factor of 2, whereas the ripple increases from 0.01 dB up to 3.66 dB. In addition, since the resonance of the series and shunt branch still have to be equal at each tuning state in order to obtain an optimum filter, i.e.

$$\omega_0{}^2 = \frac{1}{C_R L_L} = \frac{1}{C_L L_R} \tag{4.3}$$

both series and shunt capacitances must be equally tuned if the inductances are constant.

The above conclusions can also be deduced with the metamaterial concepts, since the same circuit elements can be inferred setting the balanced condition at the central frequency, the impedance value at this central frequency (which will set the ripple), and the impedance at two frequencies below and above the central frequency (which will control the bandwidth). In addition, a Butterworth- or Chebyshev-type response can be obtained controlling the impedance at the central frequency. If this impedance is set

below the impedance of the ports, a single reflection zero will be present due to the phase matching condition (that is, both series and shunt branch resonates with the resulting total transmission). On the other hand, if the same impedance value is set above the ports impedance, two additional reflection zeros will be present owing to the impedance matching conditions below and above the central frequency, being able to control the ripple by the impedance value at the central frequency. Thus, considering a tunable filter for this latter case, if only capacitances are tunable, given that the impedance at the central frequency expressed by equation (2.26) is inversely proportional to the square root of the capacitances, it leads to an increasing ripple behavior as the central frequency increases. Moreover, the impedance condition at the cut-off frequencies also has to be relaxed to analytically solve the system, which will also result in the bandwidth variation predicted from the filter approach analysis.

Although several works have dealt with obtaining tunable responses with constant ripple and/or bandwidth and tunable capacitances [135], [136], in this work we will focus on the more general case where this increasing ripple and bandwidth does not entail a requirement issue, since the tunability ranges of the proposed structures (below 40%) will represent a variation of the fractional bandwidth and ripple that can be considered small.
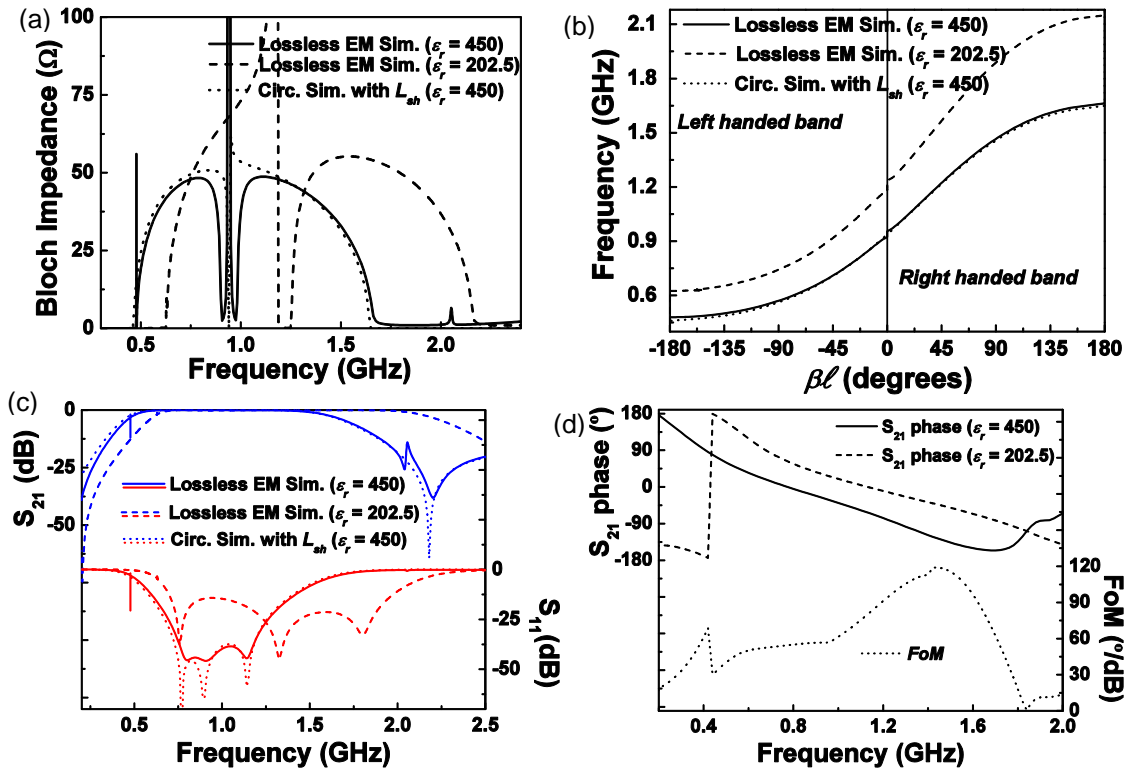
Figure 4.14. Electromagnetic simulated Bloch impedance (a), dispersion diagram (b), S-Parameters (c), and S_{21} phase and *FoM* (d) of the structure of Figure 4.9(a) for the untuned and maximum tuning states with modified BST thick-film properties. The circuit simulation for the untuned state is also depicted. The equivalent circuit values are in reference to Figure 4.9(d): for the OSRR: C = 0.23 pF, L'_s = 5.9 nH and C_s = 4.74 pF. For the OCSRR: L = 0.19 nH, L'_p = 5.8 nH, C'_p = 3.96 pF and L_{sh} = 1.75 nH. The considered BST thick-film has a thickness of 3.5 μm and a permittivity of ε_r = 450 and ε_r = 202.5 for the untuned and maximum tuning states.

In the topology based on open resonators, the above-mentioned conditions force both the OSRR and OCSRR to exhibit the same frequency tunability to maintain the optimum filter condition, where the presence of the parasitics has been found to not alter the previous assumptions. This situation was roughly satisfied in the already presented tunable CRLH line of Figure 4.9(a), where the OSRR and OCSRR exhibit a tunability of 37.1% and 42.3%, respectively. If the same structure is considered but with a BST thick-film layer with lower thickness and permittivity states (both parameters decreasing the effective permittivity), the obtained Bloch impedance can be increased and thus three reflection zeros can be obtained due to the phase and impedance matching conditions. In Figure 4.14(a)-(c) the Bloch impedance, dispersion diagram and S-parameters of the same structure as Figure 4.9(a) are shown but considering a BST thick-film thickness of 3.5 μm with untuned and maximum tuned permittivity states of $\varepsilon_r = 450$ and $\varepsilon_r = 202.5$, which could be useful for phase shifter applications. In such cases, a quasi-balanced line (the complete balanced condition would lead to non-flat responses due to the parasitics) is obtained. In addition, the tunabilities of the OSRR and OCSRR resonators are 31% and 30.9%, thus maintaining the equal-ripple response, although the ripple level and bandwidth increase by increasing the tuning (as already mentioned). The tunability of the central frequency of this structure has been found to be 30.1%.

Finally, in Figure 4.14(d) the electromagnetic simulation (considering losses) of the S_{21} phase and the *FoM* of phase shifters (derived from equation (4.2)) are also shown. Compared to the arbitrary CRLH line response of Figure 4.11 and Figure 4.12, when properly designed, the *FoM* can be of the order of 120º/dB (the initially proposed CRLH line exhibits a maximum simulated *FoM* of 70º/dB), hence confirming its suitability for phase shifting applications.

4.3.1.1 Independent resonator tuning

The topology presented up to this point allows the tunability of the whole band by means of a single voltage since both resonators exhibit the same frequency tunability. Nonetheless, this frequency tunability depends on the geometry of the resonators, the latter depending on the application requirements as well. Therefore, the equal tunability of the resonators will not always be possible. In addition, other applications such as multi-band components could require the independent control of the resonators to achieve their goals. Hence, an alternative topology to independently control the different resonators is required. In Figure 4.15 a possible solution that enables this control is shown. Interdigital capacitors have been added at the ground planes in order to decouple the DC and RF ground. With a voltage source controlling each resonator (one for the OCSRR and another for the external OSRRs), the independent control can be achieved while maintaining the initially proposed equivalent circuit model and methodology. The first voltage source will apply a potential between the input/output ports and the central ground plane, whereas the second voltage source will apply a potential between the ground plane of the external stages and the central ground plane (both voltage sources sharing the central ground plane as a zero reference to maintain the independent tuning).
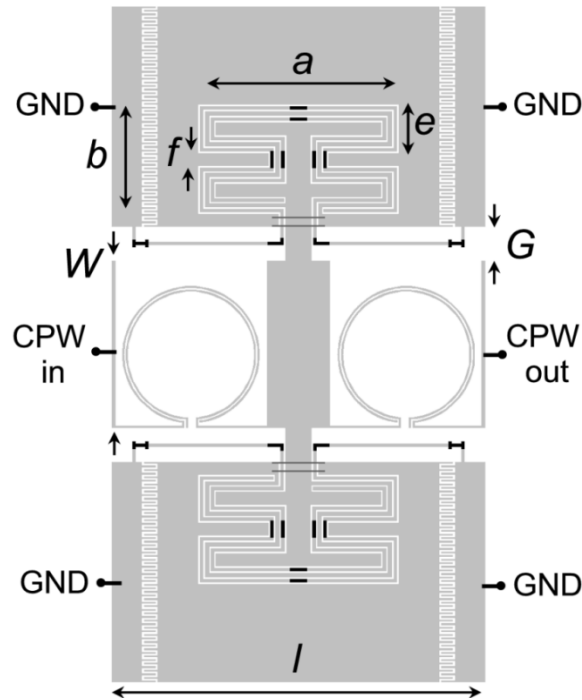
Figure 4.15. Layout of a tunable CPW wideband band-pass filter with independent tuning based on open resonators. Dimensions are: l = 6.24 mm, W = 2.8 mm and G = 0.57 mm. For the OCSRR: a = 3.36 mm, b = 1.83 mm, e = 0.81 mm, f = 0.22 mm, s = 60 μm, c = 75 μm and d = 25 μm. For the OSRR: r_{ext} = 1.15 mm, c = 25 μm and d = 35 μm. The considered BST thick-film has a thickness of 3.5 μm and a permittivity of ε_r = 450 and ε_r = 202.5 for the untuned and maximum tuning states.

To demonstrate its functionality, the proposed topology of Figure 4.15 has been designed to satisfy the requirements of a band-pass filter with central frequency f_0 = 1.18 GHz, a ripple of 0.002 dB and a fractional bandwidth of 42.4% (FBW_{3dB} = 100%) at the untuned state with the methodology explained in section 3.2.1.2. A low ripple level (0.002 dB) at the untuned state has been considered in order to obtain an acceptable ripple at the maximum tuning state (analytically predicted to be of 0.15 dB considering the 30% frequency tunability of the previous CRLH line).

The comparison between the ideal Chebyshev response, the circuit simulation considering parasitics and the electromagnetic response at the untuned state (ε_r = 450) is depicted in Figure 4.16(a). Good agreement between all the curves can be appreciated. The resonance frequency tunability of the isolated resonators is τ = 34.6% for the OSRR and τ = 27.7% for the OCSRR, considering a 3.5 μm BST thick-film with untuned and maximum tuning states of ε_r = 450 and ε_r = 202.5, respectively. Given that in the analyzed band-pass filters topology the capacitances must be equally tuned to obtain an equal-ripple optimum response, this will also mean that both OSRRs and OCSRRs should be equally tuned. Therefore, the optimal maximum tuning state will be restricted by the minimum tunability of the OSRR or OCSRR. Since in this case the minimum tunability is that of the OCSRR, the maximum optimum tuning will arise when both resonators exhibit a tunability of 27.7%. This latter condition is satisfied when the BST thick-film permittivity in the region of the OCSRR and the OSRR are $\varepsilon_{r\,OCSRR}$ = 202.5 and $\varepsilon_{r\,OSRR}$ = 235, respectively.
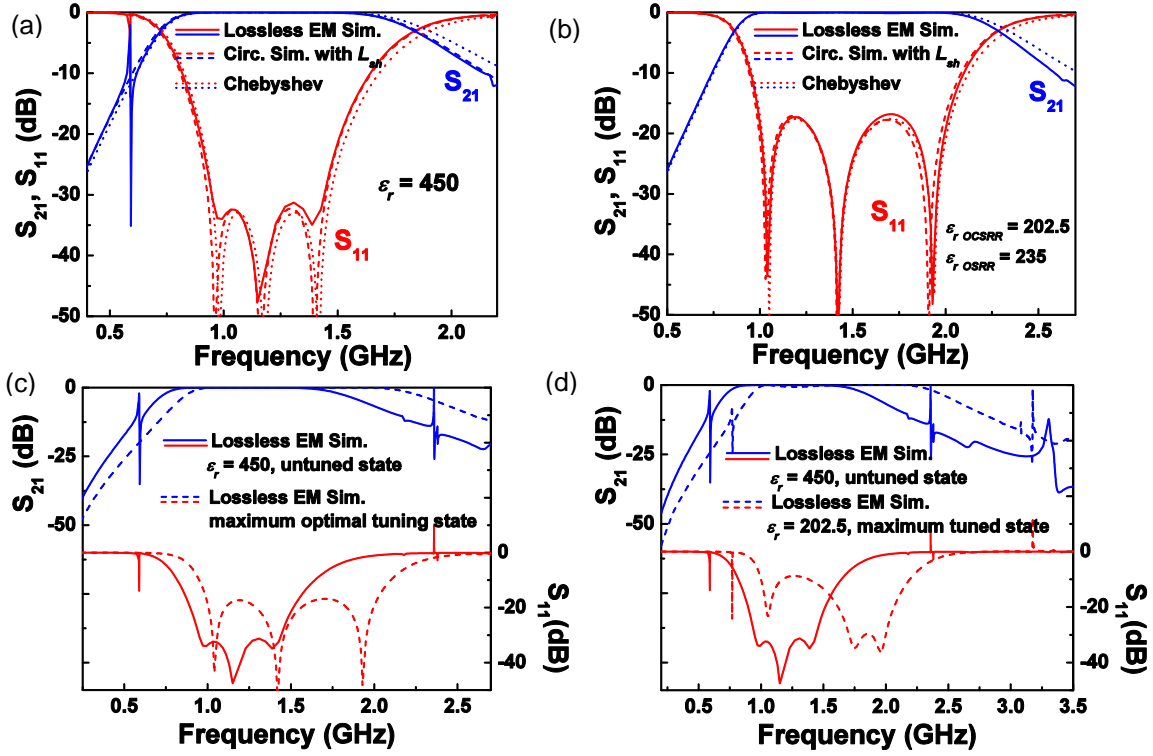
Figure 4.16. Frequency response (a), (b) and wideband frequency responses (c), (d) of the topology of Figure 4.15 for different tuning states. (a): Untuned state (ε_r = 450); (b): Maximum optimal tuning state; (c): Untuned (ε_r = 450) and maximum optimal tuning state ($\varepsilon_{r\,OCSRR}$ = 202.5, $\varepsilon_{r\,OSRR}$ = 235). (d): Untuned (ε_r = 450) and maximum (ε_r = 202.5) tuning state; The Chebyshev element values obtained from the band-pass prototype transformations, in reference to Figure 2.11(a), are for the untuned state (ε_r = 450): C_L = 1.21 pF, L_L = 3.53 nH, C_R = 5.15 pF and L_R = 15.03 nH. For the maximum optimum tuning state ($\varepsilon_{r\,OCSRR}$ = 202.5, $\varepsilon_{r\,OSRR}$ = 235), the modified capacitances are: C_L = 0.83 pF and C_R = 3.53 pF. The values of the circuit simulation considering parasitics are in reference to Figure 4.9(d): for the untuned state (ε_r = 450): C = 0.19 pF, L = 0.26 nH, C_s = 2.47 pF, L'_s = 7.68 nH, C'_p = 4.83 pF, L'_p = 3.53 nH and L_{sh} = 0.3 nH. The modified capacitances for the maximum optimum tuned state ($\varepsilon_{r\,OCSRR}$ = 202.5, $\varepsilon_{r\,OSRR}$ = 235) are: C_s = 1.68 pF and C'_p = 3.23 pF.

The maximum optimal tuned central frequency of the filter has been found to be (both from analytical equations or by electromagnetic/circuit simulations) of 1.425 GHz, with a ripple of 0.076 dB and fractional bandwidth of 72% (FBW_{-3dB} = 103.4%). In Figure 4.16(b) the resulting electromagnetic and circuit frequency response is depicted. Given that the available simulator software (*Agilent ADS*/Momentum) only allows the substrate definition with equal permittivity throughout the layer, the represented electromagnetic response is the result of cascading the isolated OSRR and OCSRR electromagnetic simulations, presenting the drawback of not taking into account the couplings between resonators (though it has been proven to only slightly affect the response with the meandered rectangular shaped OCSRR). There is good agreement between all the curves, where the prediction of the filter response for the untuned and maximum tuning states is validated. In Figure 4.16(c) the wideband frequency response for the untuned and maximum optimal tuning range is also shown, where the expected central frequency tunability of 20.7% is obtained. This tunability is decreased compared to the previous CRLH lines since the gaps of the resonators, which are strongly dependent on the BST thick-film tunability, have been increased in order to

satisfy the filter requirements. In addition, in this case the OSRR is not tuned to the maximum case to achieve an optimal equal-ripple response. In Figure 4.16(d) the comparison for the untuned and maximum tuning state (i.e., $\varepsilon_{r\,OCSRR} = \varepsilon_{r\,OSRR} = 202.5$ and hence non-equal tunability of the capacitances arise) is shown, where the unequal ripple and degraded performance can be appreciated since the design conditions are not satisfied.

4.3.2 Tunable dual-band components

The methodology developed in section 3.2.1.1 can also be applied to obtain tunable dual-band components by means of BST thick-films. For a dual-band impedance inverter, the conditions of phase $\beta l_1 = -90°$, $\beta l_2 = 90°$ and impedance $Z_{a1} = Z_{a2} = Z_a$ at two arbitrary frequencies ω_1 and ω_2 leads to equations (3.1) - (3.4), which, assuming the canonical CRLH line of Figure 2.11, result in the following circuit elements [8]

$$L_s = \frac{Z_a}{\omega_2 - \omega_1} \tag{4.4}$$

$$L_p = \frac{Z_a(\omega_2 - \omega_1)}{\omega_1\omega_2} \tag{4.5}$$

$$C_p = \frac{1}{Z_a(\omega_2 - \omega_1)} \tag{4.6}$$

$$C_s = \frac{\omega_2 - \omega_1}{Z_a\omega_1\omega_2} \tag{4.7}$$

If these operation frequencies ω_1 and ω_2 are arbitrarily tuned to a state of $\alpha\omega_1$ and $\gamma\omega_2$, then the condition of constant inductances inherent to BST thick-film materials yields

$$\gamma = \frac{1}{\alpha} \tag{4.8}$$

$$\alpha\omega_1 = -\omega_2 \tag{4.9}$$

which results in no physical solution. This means that in order to obtain a tunable dual-band impedance inverter with constant phase $\beta l = \mp90°$ and constant impedance Z_a at two arbitrary frequencies ω_1 and ω_2, both inductances and capacitances should ideally be tuned. To solve the system for the case of constant inductances, L_s, L_p, two of the four conditions βl_1, βl_2, Z_{a1}, Z_{a2} must be relaxed at the different tuning states. If we consider the impedances as unknowns (hence allowing the possibility of presenting different impedance values Z_{a1} and Z_{a2} for the different tuning states) and force the conditions $\beta l_1 = -90°$, $\beta l_2 = 90°$, then the series and shunt impedances are [9]

---

[8] In this section, the element values of Figure 2.11 are renamed for simplicity as $L_s = L_R/2$, $C_s = 2C_L$, $L_p = L_L$, $C_p = C_R$.
[9] Note that the unknown impedance, as well as the different Z_{a1}, Z_{a2} conditions are not necessarily required at the initial state where the layout is generated, given that the inductances are still a design parameter.

$$Z_s(\omega)|_{f_1} = -jZ_{a1} \tag{4.10}$$

$$Z_s(\omega)|_{f_2} = +jZ_{a2} \tag{4.11}$$

$$Z_p(\omega)|_{f_1} = +jZ_{a1} \tag{4.12}$$

$$Z_p(\omega)|_{f_2} = -jZ_{a2} \tag{4.13}$$

which for the case of the conventional CRLH lines results in the following circuit element values

$$L_s = \frac{Z_{a1}\omega_1 + Z_{a2}\omega_2}{\omega_2^2 - \omega_1^2} \tag{4.14}$$

$$L_p = \frac{Z_{a1}Z_{a2}(\omega_2^2 - \omega_1^2)}{\omega_1\omega_2(Z_{a1}\omega_1 + Z_{a2}\omega_2)} \tag{4.15}$$

$$C_p = \frac{Z_{a1}\omega_2 + Z_{a2}\omega_1}{Z_{a1}Z_{a2}(\omega_2^2 - \omega_1^2)} \tag{4.16}$$

$$C_s = \frac{\omega_2^2 - \omega_1^2}{\omega_1\omega_2(Z_{a2}\omega_1 + Z_{a1}\omega_2)} \tag{4.17}$$

Given that the inductances will be constant and fixed by the initial state, equations (4.14) - (4.17) can be rewritten to infer the value of the unknown impedances and required capacitances at each tuning state as

$$Z_{a1} = \frac{L_s(\omega_2^2 - \omega_1^2) - \sqrt{L_s\left(L_s(\omega_1^2 - \omega_2^2)^2 - 4\omega_1^2\omega_2^2 L_p\right)}}{2\omega_1} \tag{4.18}$$

$$Z_{a2} = \frac{L_s(\omega_2^2 - \omega_1^2) + \sqrt{L_s\left(L_s(\omega_1^2 - \omega_2^2)^2 - 4\omega_1^2\omega_2^2 L_p\right)}}{2\omega_2} \tag{4.19}$$

$$C_p = \frac{(\omega_2^2 - \omega_1^2)\sqrt{L_s\left(L_s(\omega_1^2 - \omega_2^2)^2 - 4\omega_1^2\omega_2^2 L_p\right)} + L_s(\omega_1^4 - \omega_2^4)}{2\omega_1^2\omega_2^2 L_p L_s(\omega_1^2 - \omega_2^2)} \tag{4.20}$$

$$C_s = \frac{2(\omega_2^2 - \omega_1^2)}{(\omega_1^2 - \omega_2^2)\sqrt{L_s\left(L_s(\omega_1^2 - \omega_2^2)^2 - 4\omega_1^2\omega_2^2 L_p\right)} + L_s(\omega_2^4 - \omega_1^4)} \tag{4.21}$$

where the impedances and capacitances will be real as long as the following condition is satisfied

$$\frac{\delta(\omega_1^2 - \omega_2^2)^2}{\omega_1^2\omega_2^2} \geq 1 \tag{4.22}$$

where

97

$$\delta = \frac{L_s}{4L_p} \tag{4.23}$$

with δ being constant for all tuning states. Hence, the inequality (4.22) defines the possible tunability regions where physical capacitance solutions arise. If the frequencies ω_1, ω_2 are considered to be those of the initial state, then the inequality at an arbitrary tuned state with frequencies $\alpha\omega_1$, $\gamma\omega_2$ can be expressed as

$$\frac{\delta(\alpha^2\omega_1{}^2 - \gamma^2\omega_2{}^2)^2}{\gamma^2\alpha^2\omega_1{}^2\omega_2{}^2} \geq 1 \tag{4.24}$$

Considering that the initial state (where there is still control of both inductances and capacitances) does satisfy equation (4.22), then the inequality (4.24) will also be satisfied if

$$\frac{\delta(\alpha^2\omega_1{}^2 - \gamma^2\omega_2{}^2)^2}{\gamma^2\alpha^2\omega_1{}^2\omega_2{}^2} \geq \frac{\delta(\omega_1{}^2 - \omega_2{}^2)^2}{\omega_1{}^2\omega_2{}^2} \tag{4.25}$$

which can be rewritten as

$$\frac{(\omega_1{}^2 - \omega_2{}^2)^2}{\left(\frac{\alpha}{\gamma}\omega_1{}^2 - \frac{\gamma}{\alpha}\omega_2{}^2\right)^2} \leq 1 \tag{4.26}$$

From this point on, if the two frequency bands ω_1, ω_2 are equally tuned (i.e., if $\alpha = \gamma$), then inequality (4.26) is still satisfied for all values of $\alpha \in \Re$, with the consequent real impedances and capacitances. In addition, from equations (4.18) - (4.21), the impedance and capacitance values at these tuned frequencies $\alpha\omega_1$, $\alpha\omega_2$ can be expressed as

$$Z_{a1,2}\big|_{tuned} = \alpha Z_{a1,2}\big|_{untuned} \tag{4.27}$$

$$C_{s,p}\big|_{tuned} = \frac{C_{s,p}\big|_{untuned}}{\alpha^2} \tag{4.28}$$

That is, an equally linear dependence of the impedances Z_{a1}, Z_{a2} is obtained if equal tuning is applied at both bands. On the other hand, both capacitances are also equally decreased, although in this case being inversely proportional to the square of the tuning. Thus, if the initial state is designed with real impedances and forcing the $Z_{a1} = Z_{a2}$ condition, then this latter condition will be satisfied for all tuning states, although with an increasing real value as the operating frequencies get higher.

The nature of the impedances and capacitances for the case of an independent tuning of the frequency bands ω_1, ω_2 can also be analyzed. From (4.26), it follows that for all values of $0 < \alpha \leq 1$ and $\gamma \geq 1$ (i.e., if the bands ω_1, ω_2 are simultaneously or independently separated from each other), the inequality is satisfied. In these situations, from equations (4.18) and (4.19) it can be deduced that the impedances Z_{a1}, Z_{a2} result in different values and opposite tendencies. This can be graphically

appreciated in Figure 4.17, where a dual-band impedance inverter with $f_1 = 0.75$ GHz and $f_2 = 1.5$ GHz and impedance $Z_{a1} = Z_{a2} = 29$ Ω has been considered as the initial state and tuned with the above-mentioned conditions, where $Z_{a1} = Z_{a2}$ is only satisfied at α = γ = 1 (i.e., the untuned state). In Figure 4.18 the capacitance evolution considering these impedances is also shown, where the parameter α is delimited from 0.6 to 1 for better understanding given that at α = 0 the series and shunt capacitances tend towards zero and infinity, respectively. From this representation, an opposite tendency of the capacitances C_s, C_p can be appreciated when either the first or the second band is tuned. This means that to satisfy an unequal tuning with real impedances as a solution the tunable component should allow both the increasing and decreasing of the capacitances. Nonetheless, this not possible either at the untuned or maximum material tuning states.
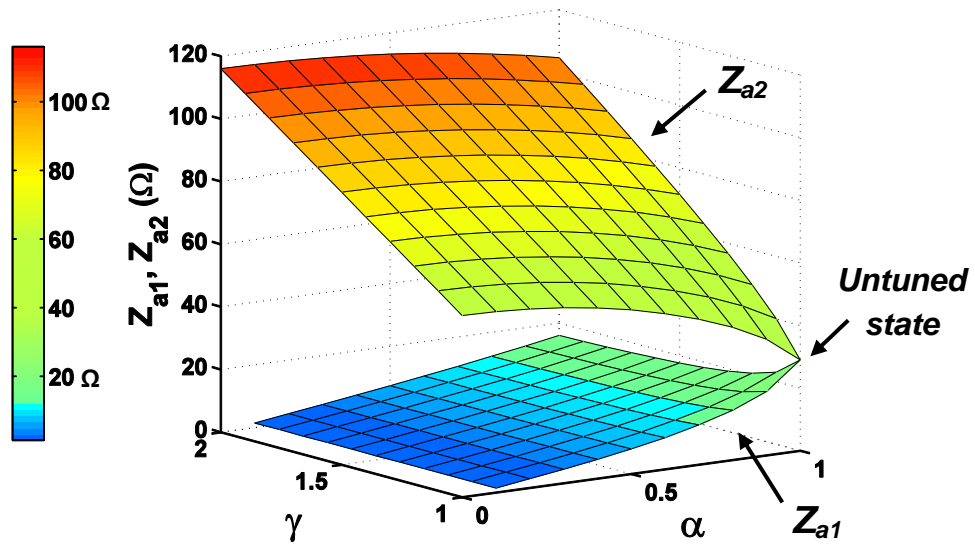
Figure 4.17. Tuning evolution of the Z_{a1}, Z_{a2} impedances considering an initial untuned state (α = γ = 1) of $f_1 = 0.75$ GHz and $f_2 = 1.5$ GHz and impedance $Z_{a1} = Z_{a2} = 29$ Ω.
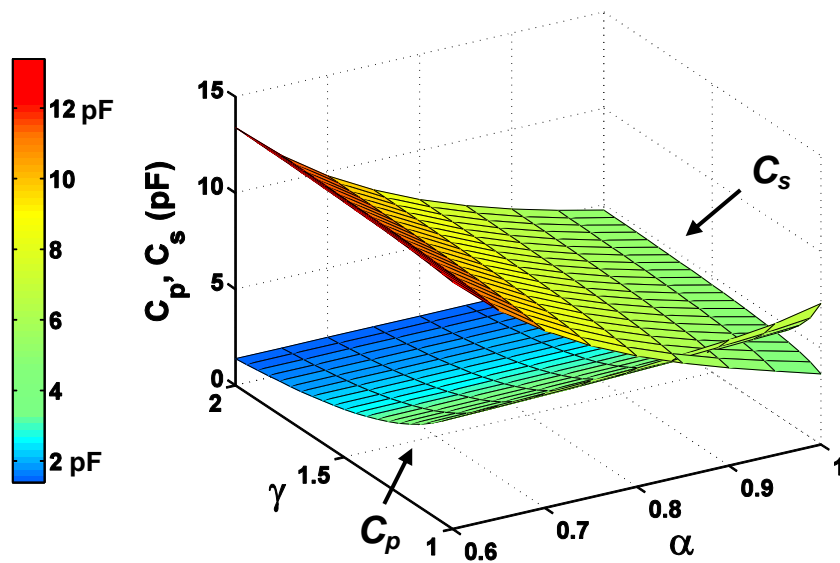
Figure 4.18. Tuning evolution of the capacitances C_s, C_p considering an initial untuned state (α = γ = 1) of $f_1 = 0.75$ GHz and $f_2 = 1.5$ GHz and impedance $Z_{a1} = Z_{a2} = 29$ Ω.

Hence, if an independent frequency band tuning is required, the initial design from which the re-configurability would be applied must be set at an intermediate tuned state in order to be able to independently tune the capacitances with opposite tendencies.

Finally, if the frequencies ω_1 and ω_2 are tuned close to each other (either independently or simultaneously), the inequality (4.26) does not necessarily satisfy. Hence, depending on the frequency positions and initial inductance values, no physical solution will be obtained in these latter cases since complex capacitances and impedances result.

It is also important to consider that although in this work a tunable dual-band impedance inverter with a variable characteristic impedance and constant phase with the tuning (±90º at each frequency) has been analyzed, a similar procedure could be applied to obtain a variable phase but with a constant impedance tunable dual-band impedance inverter. In addition, although all the aforementioned assumptions do not consider the parasitics present in the CRLH lines based on open resonators, it has been numerically and experimentally deduced that the same tendencies as those of the canonical CRLH line are obtained, though the analytical verification becomes much more complex. Nonetheless, for a structure considering parasitics with the same impedance $Z_{a1} = Z_{a2}$ at the initial untuned state, if an equal tuning is applied at the two frequency bands, then the condition of equal value at both bands does not satisfy, still obtaining an increasingly real solution for all values although with a slight discrepancy between both impedances Z_{a1}, Z_{a2} (becoming more pronounced as the tuning increases). However, given the tunabilities of the available technology, the resulting impedances at the maximum state can still be considered as almost constant, hence maintaining the same goal designs as those explained for the ideal CRLH line.

From the exposed analysis, it follows that depending on the tuning required, different impedance strategies will have to be considered. In this work, the performance will be optimized for an equal tuning of both frequencies considering $Z_{a1} = Z_{a2}$ at the untuned state. Thus, due to the linear increasing impedance tendency with the tuning in such cases (see equation (4.27)), a lower initial value than the desired impedance is chosen[10]. Specifically, if the dual-band component is equally tuned as $\alpha\omega_1$ and $\alpha\omega_2$, then the optimal impedance value required $Z_{a\,opt}$ to minimize the performance degradation as the tuning increases, is

$$Z_{a\,opt} = Z_a \left(\frac{2}{\tau + 2} \right) \qquad (4.29)$$

with Z_a being the desired impedance of the application and τ the frequency tunability defined in (4.1).

By considering this, a dual-band impedance inverter of $\beta l = \mp 90º$, and $Z_a = 35.35\ \Omega$ at the frequencies $f_1 = 0.75$ GHz and $f_2 = 1.5$ GHz is designed. This leads to a required impedance at the untuned state of $Z_{a\,opt} = 30\ \Omega$ if a tunability of 30% is considered. To

---

[10] Note that in order to optimize the independent tuning of the bands, a higher Z_{a1} and lower Z_{a2} should be chosen and forced at an intermediate tuned state to compensate the opposite tendencies shown in Figure 4.17 and Figure 4.18.

infer the layout of the dual-band impedance inverter at the untuned state forcing impedance $Z_{a\ opt}$, the design methodology proposed in section 3.2.1.1 can be considered. This methodology neglects the inductive effect L_{sh}, but as will be proven, this approximation is still valid since the upper band is not of interest in the dual-band applications presented herein. Once this design is obtained, the values of the capacitances required to obtain the desired frequency tuned position and the resulting increased impedance values can be inferred through similar equations of (4.14) - (4.19) but considering parasitics.

The layout obtained from this methodology is shown in Figure 4.19(a), where the topology with independent OSRR and OCSRR control has been chosen to analyze the independent tuning of the bands as well as to relax the condition of equal permittivity dependent tunability of the different resonators (since this tunability will depend on the geometry which is fixed by the requirements). The OSRR and OCSRR tunability has been found to be for these structures of $\tau = 31.8\%$ and $\tau = 33.9\%$, respectively. In Figure 4.20 the Bloch impedance and dispersion diagram is shown for the untuned and maximum tuning states (i.e., $\varepsilon_r = 450$ and $\varepsilon_r = 202.5$, respectively) for the designed dual-band impedance inverter. Due to the simulator software limitations, a homogeneous permittivity is considered through the entire BST thick-film layer, although since both OSRR and OCSRR present almost equal tunability, only slight discrepancies are expected if compared to the case where independent tuning could be considered.
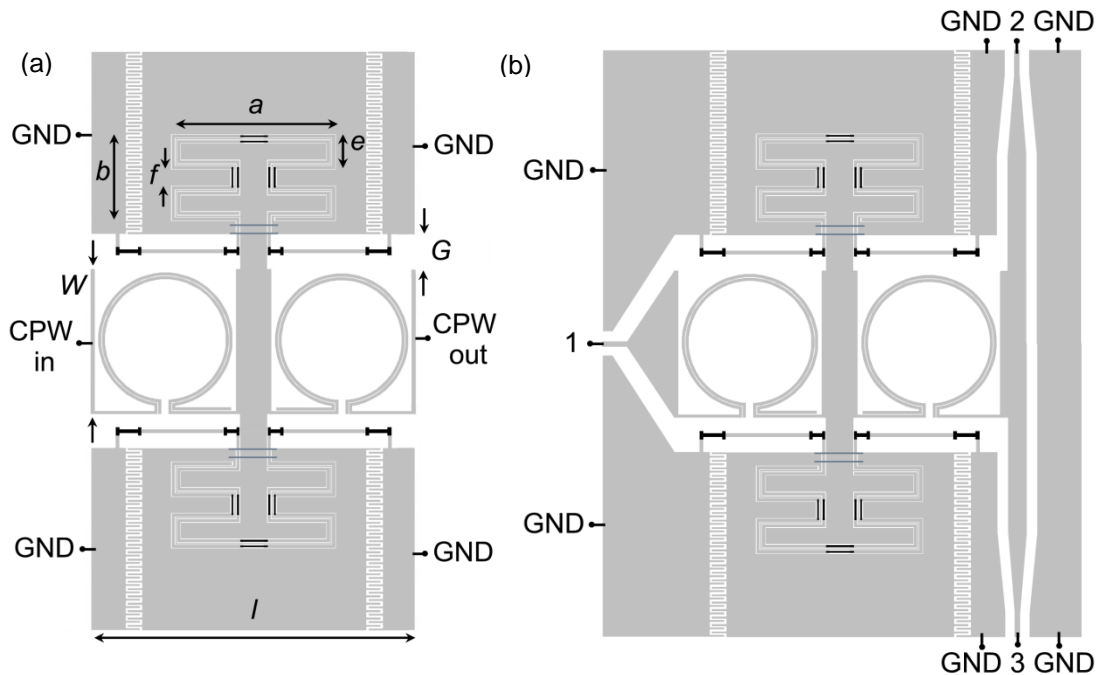
Figure 4.19. Topology of a tunable dual-band impedance inverter with independent control of the OSRR and OCSRR (a). The resulting dual-band power divider obtained by cascading two 50 Ω ports at the output and a 50 Ω port at the input is also depicted in (b). The considered BST thick-film has a thickness of 3.5 μm and a permittivity of $\varepsilon_r = 450$ and $\varepsilon_r = 202.5$ for the untuned and maximum tuning states. Dimensions are: $l = 5.25$ mm, $W = 2.35$ mm and $G = 0.57$ mm. For the OCSRR: $a = 2.67$ mm, $b = 1.42$ mm, $e = 0.58$ mm, $f = 0.26$ mm, $s = 50$ μm, $c = 20$ μm and $d = 10$ μm. For the OSRR: $r_{ext} = 1.15$ mm, $c = 10$ μm and $d = 50$ μm.
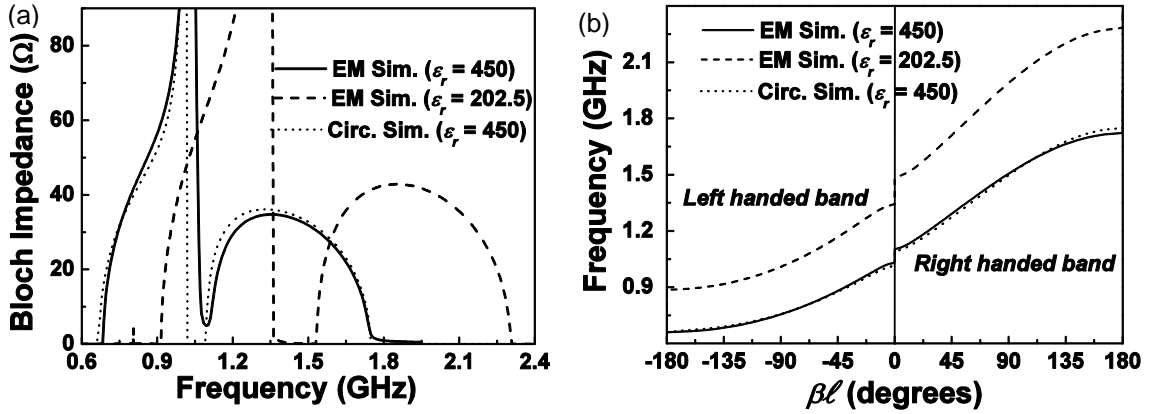
Figure 4.20. Lossless electromagnetic simulated Bloch impedance (a) and dispersion diagram (b) of the tunable dual-band impedance inverter of Figure 4.19(a) for the untuned (ε_r = 450) and maximum (ε_r = 202.5) tuning states. The circuit simulation for the untuned state is also depicted. The equivalent circuit values are in reference to Figure 4.9(d): For the OSRR: C = 0.35 pF, L'_s = 6.57 nH and C_s = 3.14 pF. For the OCSRR: L = 0.17 nH, L'_p = 3.43 nH, C'_p = 5.82 pF and L_{sh} = 0 nH.
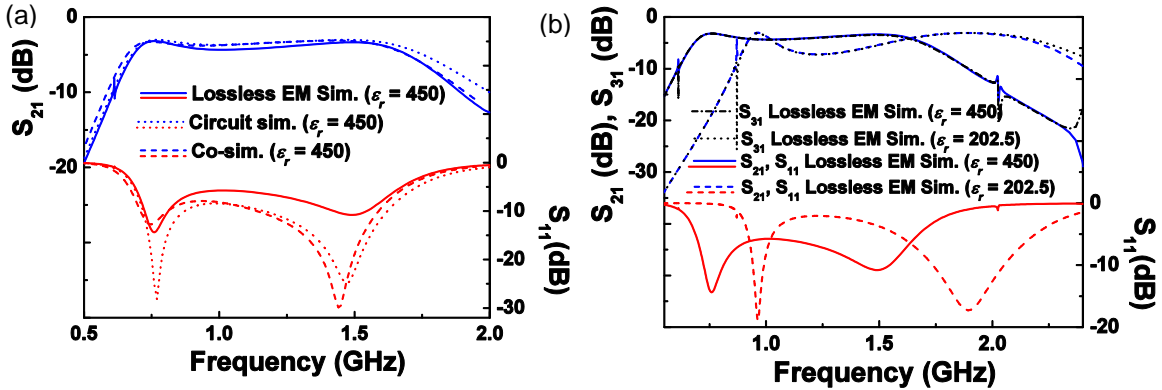
Figure 4.21. Lossless electromagnetic simulated S-parameters of the tunable dual-band power divider of Figure 4.19(b). (a): Comparison of the circuit, co-simulation and electromagnetic simulation for the untuned state. (b): Comparison of the electromagnetic simulation for the untuned and maximum tuning states.

As can be seen from Figure 4.20 (b), an increasing Bloch impedance is obtained with the tuning, leading to a maximum impedance of 46 Ω and 40.8 Ω at the maximum tuned state for the first and second frequency band, respectively (i.e., where the condition βl = ∓90º is satisfied). This unequal impedance is attributed to the slightly different tunabilities of the OSRR and OCSRR resonators, as well as to the presence of the parasitics (as already explained at the beginning of this subsection). By adding a 50 Ω port at the input and two 50 Ω ports at the output, a dual-band power divider is obtained, showing the layout in Figure 4.19(b), where no additional optimization has been carried out.

In Figure 4.21(a) the S-parameters for the untuned state of the power divider of Figure 4.19(b) are depicted. In this figure, the electromagnetic simulation of the whole structure of Figure 4.19(b), the co-simulation of the inverter of Figure 4.19(a) cascading two 50 Ω ports at the output and a 50 Ω port at the input (these connections made at the circuit level), and the circuit simulation of the equivalent circuit of Figure 4.9(d) with

the circuit elements of the caption of Figure 4.20, considering the latter mentioned port connections are compared. For clarity purposes, only the S_{21} is shown (both S_{31} and S_{21} curves have been found to be in perfect agreement for the circuit and co-simulation, only differing in the complete electromagnetic simulation above the upper band). From these results, it can be seen that the circuit model can predict the power divider's dual-band behavior, where the impact of the layout connections of the different ports and the tapper at the input degrades the matching levels but do not affect the operation frequency position. This would also allow the study of the independent tuning of the resonators, where given the limitation of our simulation tools it would require the co-simulation of the cascaded OSRR and OCSRR sections.

In Figure 4.21(b), the electromagnetic simulation comparison of the untuned and maximum tuning states of the tunable dual-band power divider is also shown. A tunability of 27.2% and 26.7% for the first and second band is obtained if both resonators are equally tuned (which has been approximated by considering a homogeneous permittivity thick-film BST layer). This also demonstrates that if only equal tuning of the different bands is required, for certain specifications where both resonators inherently present a similar tunability (as in the case shown), the interdigital capacitors at the ground planes could be omitted and the whole structure controlled by a single voltage source, thus simplifying the structure and biasing network.

Independent tuning of the two frequency bands ω_1, ω_2 could also be applied to the designed structure by considering different permittivities for the OSRR and OCSRR (which is equivalent to applying different voltages to the fabricated devices). Nonetheless, as has already been observed at the beginning of this section, to obtain an optimum response this would require unequal impedances and a decrease of the capacitance with the tuning, with neither of these conditions being satisfied at the initially untuned state. Nonetheless, a suboptimum response could be obtained if the structure is initially equally tuned to an intermediate state (which results in an enhanced impedance) and afterwards a decreasing or increasing of the OSRR and OCSRR capacitances are applied (with the resulting opposite impedance values tendency).

In **summary**, it has been demonstrated that CRLH lines based on open resonators can be tuned by means of BST thick-films and applied to band-pass filters, phase shifters, dual-band impedance inverters and dual-band power dividers, where the independent or simultaneous tuning of the different resonators can be considered depending on the application.

CHAPTER 5

Filter miniaturization based on stepped impedance resonators

Ultra compact and highly selective planar filters are in demand in modern communication systems. To simultaneously achieve small dimensions and sharp cut-off responses, transmission zeros close to the transmission band are required. Thus, filters providing an elliptic-type function response are of primary interest. Various works have dealt with these responses either for low-pass, high-pass or band-pass filters [95], [137] - [159].

Although the wideband band-pass filters based on open resonators presented in chapter 3 exhibit a transmission zero above the pass-band, the controllability of this transmission zero is restricted by the geometry requirements of the resonators (which are given by the prototype coefficients). For this reason, a different alternative can be considered in order to obtain a better control and filter selectivity. In this chapter, SIRs will be studied to design elliptic-function filters in CPW technology. The CPW SIRs will be implemented by etching narrow and wide metallic strips in the back substrate side, resulting in a high degree of compactness with an easy fabrication process since vias

are not needed. To this end, in section 5.1 the study of the behavior of the CPW SIR will be analyzed, extracting its circuit model including parasitic effects to predict the filter response in a broadband frequency span. Afterwards, by means of this model and semi-lumped inductors or capacitors, these resonators will be applied to the design of elliptic-function low-pass and high-pass filters, as well as band-pass filters with controllable transmission zeros in section 5.2, 5.3 and 5.4, respectively.

The electromagnetic and circuit simulation of all the devices that will be presented are obtained by means of the commercial software *Agilent ADS/Momentum.* The fabrication process of all these devices is based on standard photo/mask etching techniques. The measurement is obtained by means of the *Agilent E8364B* vector network analyzer.

5.1 Study and analysis of the CPW SIR

Figure 5.1 shows the topology and first order circuit model of the asymmetric and symmetric SIR etched in the back side of the substrate of a CPW transmission line, making use of the two metal levels of the CPW structure [160], [161]. The resonator is composed of a metallic patch in the central strip coupled to the bottom substrate, which is connected with an inductive line to a capacitive patch coupled to the ground plane. Hence, this resonator behaves essentially as a shunt connected series resonator.

The choice between an asymmetric or symmetric resonator will depend on the element values needed for the application, since due to its topology the asymmetric SIR has twice the inductance of the symmetric SIR but half the capacitance, as shown in the models of Figure 5.1(b), (d). Thus, in the following sections, different topologies will be used to satisfy the different needs of the applications. To further miniaturize this resonator, vias could be used either at the central strip or at the ground planes to avoid the two series connected capacitances of the resonator. Nonetheless, the fabrication process would be more complex, and for this reason only the case without vias will be analyzed.
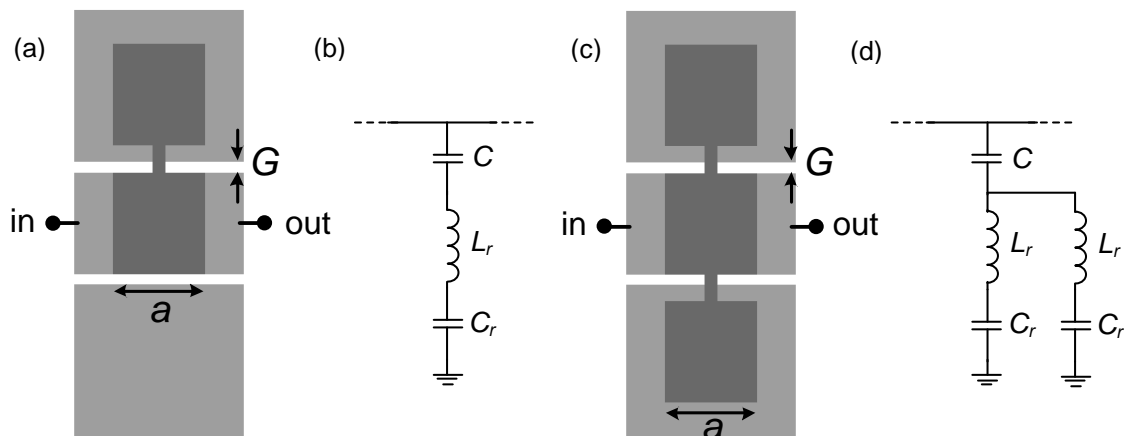
Figure 5.1. Layout (a), (c) and first order circuit model (b), (d) of an asymmetric and symmetric SIR in CPW technology.
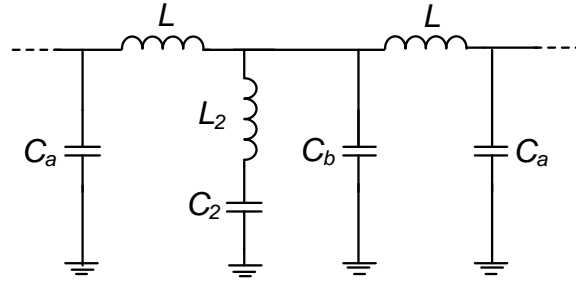
Figure 5.2. Accurate equivalent circuit model of the SIR in CPW technology. The relation between this model and that of Figure 5.1(b) is: $L_2 = L_r$; $C_2 = (C \cdot C_r)/(C + C_r)$, whereas for the model of Figure 5.1(d) is: $L_2 = L_r/2$, $C_2 = (C \cdot 2C_r)/(C + 2C_r)$.

To accurately predict the response of the whole structure, the parasitic behavior of the host line has to be taken into account. Hence, the accurate equivalent circuit of the resonator is that shown in Figure 5.2, where L and C_a - C_b are the inductance and capacitance of the host line and L_2 - C_2 are the inductance and capacitance of the resonator. The inductance of the SIR, L_2, and of the line, L, are determined by the length and width of the narrow strip of the inclusion and of the host line, respectively, which can be inferred by considering the straight-line inductor approximation of equation (3.18). On the other hand, the capacitance of the SIR, C_2, is determined by the area of the metallic rectangles, which are electrically coupled (face-to-face) to the central strip and ground plane of the CPW, which can be inferred from the parallel plate capacitance equations. Additional parameters could be taken into account, such as the small parasitic inductive effect of the central strip, but as will be corroborated later, the presented model predicts roughly enough the response and enables an easy design methodology.

In the following sections, the design of different elliptic-type or quasi-elliptic type responses will be presented based on the topologies of Figure 5.1 and its circuit model of Figure 5.2, where the required transmission zeros of the elliptic-function response will be provided by the shunt connected SIRs. In addition, depending on the application, the simplification or inclusion of additional elements with regard to those shown in Figure 5.1 will be considered. For instance, it will be observed how, since the parasitics play an important role at higher frequencies, for the design of low-pass filters these parasitics may be neglected without losing accuracy on the pass-band, whereas for band-pass or high-pass filters, they will have to be taken into account in order to correctly model the pass-band of these latter filters.

5.2 Design of compact elliptic low-pass filters

The two commonly used network structures for elliptic-function low-pass prototype filters are depicted in Figure 5.3. Focusing on CPW technology, two different realizations corresponding to the network of Figure 5.3(a) have been recently presented. In one of them [144], the low-pass elliptic-function was achieved by etching interdigital capacitances in the central strip of the CPW with an electrical short in one of the fingers in order to implement the series connected parallel resonators of the

network of Figure 5.3(a). In the other [145], the series connected parallel resonators were implemented by means of OCSRRs.

In this thesis, elliptic low-pass filters based on the network of Figure 5.3(b) and CPW SIRs have been implemented. Since in this case high series and shunt inductances are required, the asymmetric SIR and the narrowing and meandering of the central strip will be considered to maximize the shunt and series inductance, respectively. Thus, the typical topology for the proposed design will be that depicted in Figure 5.4(a), where an additional capacitance C_s associated with the meander is mandatory to accurately predict the broadband response, as shown in Figure 5.4(b) [162], [163].

To validate this model, Figure 5.5 shows the series, χ_s, and parallel, χ_p, reactance of the equivalent T-circuit model of the layout of Figure 5.4(a) (inferred from the simulated S-parameters) and also the reactances of the equivalent T-circuit models of those circuits shown in Figure 5.3(b) (for a third-order filter) and Figure 5.4(b). Note that χ_s and χ_p are not subjected to obey the Foster's reactance theorem since they result from T-circuit equivalence. The frequency response comparison between the electromagnetic and circuit simulations is also shown in Figure 5.6. As can be seen from Figure 5.5 and Figure 5.6, the electrical simulation of the equivalent circuit of Figure 5.4(b) is in good agreement with the electromagnetic simulation throughout the entire range shown.
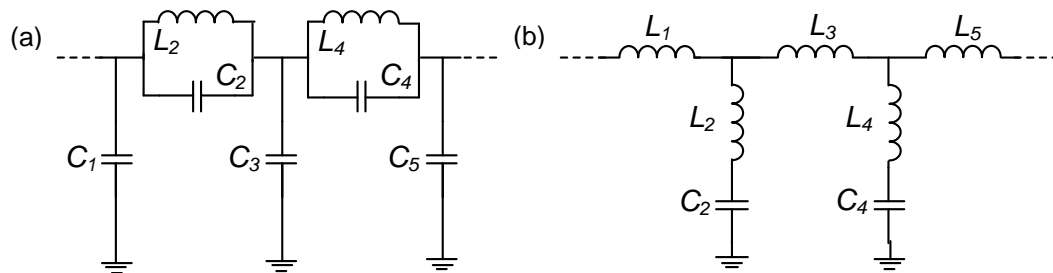
Figure 5.3. Low-pass elliptic-function prototype filters with (a) series connected parallel resonators and (b) shunt connected series resonators. The models correspond to a fifth-order prototype.
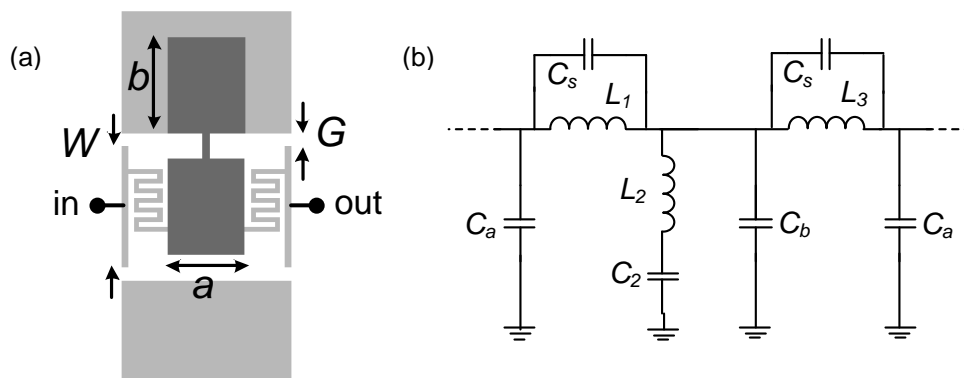
Figure 5.4. Topology of the SIR-based elliptic low-pass filters (a), and equivalent circuit model (b). Dimensions are: $W = 5$ mm, $G = 0.55$ mm, $a = 3.24$ mm and $b = 3.99$ mm. Back side metal is indicated in black color. The considered substrate thickness and dielectric constant are $h = 254$ μm and $\varepsilon_r = 11.2$, respectively.
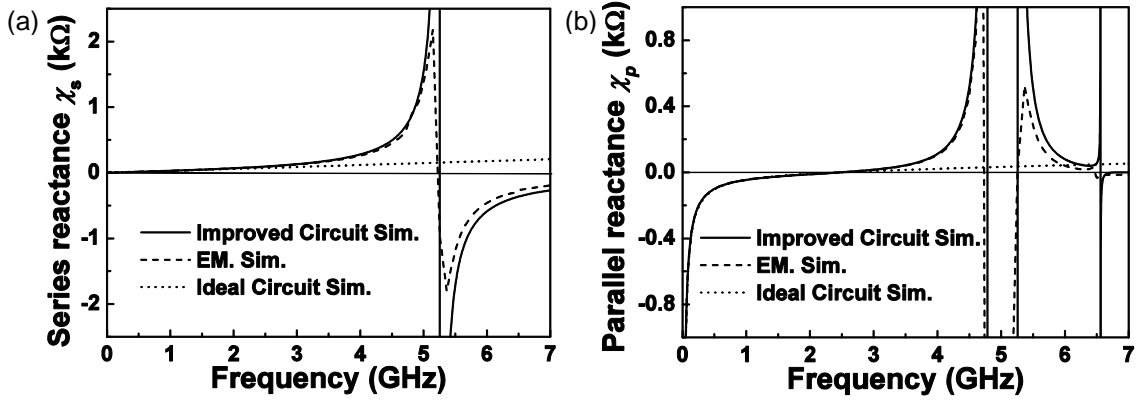
Figure 5.5. Series, χ_s, (a), and parallel, χ_p, (b) reactance of the layout shown in Figure 5.4(a) and the circuit models of Figure 5.3(b) and Figure 5.4(b). The element values of the ideal circuit in reference to Figure 5.3(b) are: $L_1 = L_3 = 4.7$ nH, $L_2 = 1.38$ nH and $C_2 = 2.98$ pF. The element values of the complete circuit model in reference to Figure 5.4(b) are: $L_1 = L_3 = 4.7$ nH, $L_2 = 1.65$ nH, $C_2 = 2.5$ pF, $C_a = 0.08$ pF, $C_b = 0.44$ pF and $C_s = 0.115$ pF.
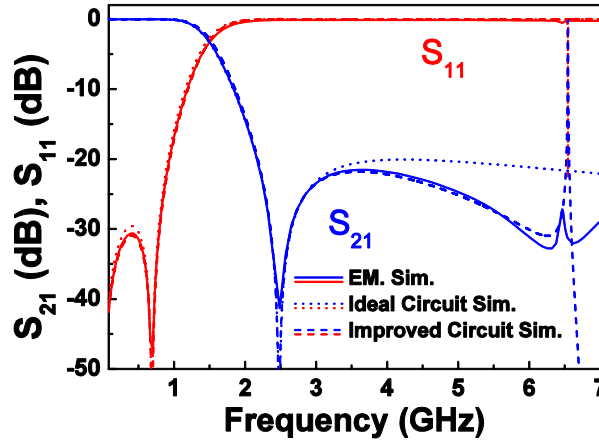
Figure 5.6. Electromagnetic, ideal circuit and improved circuit frequency response simulation of Figure 5.4(a), Figure 5.3(b) and Figure 5.4(b), respectively.

The peak at 6.5 GHz is mostly caused by the parasitic capacitance to the ground plane C_b. Given that the ideal circuit is able to describe the pass-band region of the filter and the position of the transmission zero to a good approximation, it is possible to approximate the structure of Figure 5.4(a) with the ideal equivalent circuit of Figure 5.3(b) to simplify the design process.

To demonstrate the possibility of designing standard elliptic low-pass filter responses, a third-order elliptic-function low-pass filter with a pass-band ripple of $L_{Ar} = 0.1$ dB, a cut-off frequency of $f_0 = 1$ GHz and a stop-band attenuation of $L_{As} = 30.52$ dB with the equal-ripple stop-band starting normalized frequency $\Omega_s = 2.5$ is designed. The element values corresponding to this elliptic filter response are (referred to the circuit of Figure 5.3b): $L_1 = L_3 = 7.54$ nH, $C_2 = 3.24$ pF and $L_2 = 0.96$ nH. The layout that satisfies the aforementioned values can be inferred by the parallel plate equation for the capacitances and equation (3.18) for the inductance, with the subsequent optimization process by curve fitting the series and parallel reactances of the simulated electromagnetic response to that of the circuit model.

The final layout and the photograph of the fabricated filter are both depicted in Figure 5.7, where tapered access lines have been added to measure the device. The simulated and measured frequency responses and group delay of the device are shown in Figure 5.8(a). The circuit simulation of the model of Figure 5.3(b) is also depicted in Figure 5.8(a).

The presence of the additional transmission zero at approximately 4.5 GHz, the first spurious present at 6.9 GHz, and the better matching level at the band-pass of the simulated electromagnetic response are mostly due to the series capacitance C_s and to the line to ground capacitances C_b - C_a. The agreement between experimental data and the elliptic-function response is good up to approximately 3.5 GHz. Nonetheless, the performance of the electromagnetic simulation at the band-pass is poorer than that obtained from measurement. This phenomenon is thought to be caused by a simulation inaccuracy. To validate this latter statement, Figure 5.8(b) shows the comparison between measurement, the already shown electromagnetic response where a finite upper conductor is considered (renaming such cases as "positive simulations", since only the upper strip metal that is used is drawn), as well as the same simulation considering the upper conductor as a slot (i.e., instead of defining the strip conductor, the slot of the metal is defined, and so, calling these simulations "negative simulations"). With the negative simulations we are able to better predict the measurement response (in-band return losses), although these results are in certain disagreement with the circuit simulations (pass-band region) since the design was inferred considering the positive simulations.

Measured insertion and return losses in the pass-band are good ($|IL| < 0.36$ dB, $|RL| > 24$ dB) and a sharp cut-off is obtained, with a stop-band rejection better than 30 dB between 2.5 GHz and 6.4 GHz. It is also remarkable that filter dimensions are small (i.e., 0.66 cm long and 0.92 cm wide), which correspond to $0.034\lambda_g \times 0.047\lambda_g$, where λ_g is the guided wavelength at the filter cut-off frequency.
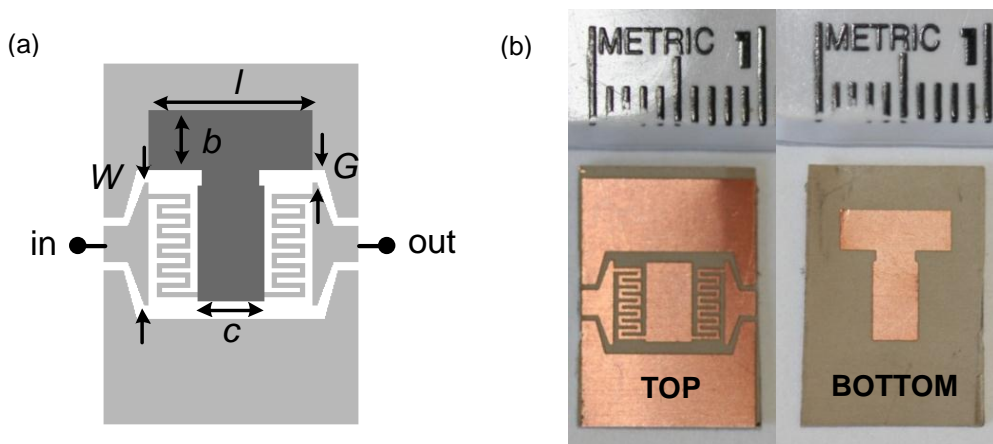
Figure 5.7. Layout (a) and photograph (b) of the fabricated third-order elliptic-function low-pass filter. Dimensions are: $W = 5$ mm, $G = 0.55$ mm, $l = 6.6$ mm, $b = 2.42$ mm and $c = 2.7$ mm. The strips of the meander lines are 0.2 mm width. The device has been fabricated on the *Rogers RO3010* substrate with measured dielectric constant $\varepsilon_r = 11.2$ and thickness $h = 254$ μm.
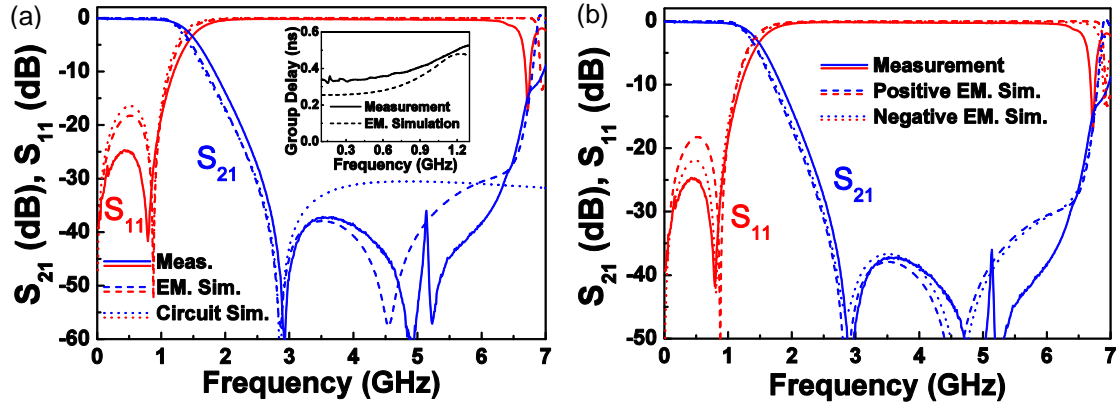
Figure 5.8. Ideal elliptic-function, electromagnetic and measured frequency response of the fabricated third-order elliptic-function low-pass filter of Figure 5.7(a); Comparison between the measured, positive and negative simulated frequency response (b).

In order to study the limitations of this approach, a fifth-order elliptic-function low-pass filter has also been designed with the following characteristics: a pass-band ripple of L_{Ar} = 0.1 dB, a cut-off frequency of f_0 = 1 GHz and a stop-band attenuation of L_{As} = 31.49 dB with equal-ripple stop-band starting normalized frequency Ω_s = 1.25. The element values (referred to the circuit of Figure 5.3b) are in this case: L_1 = 7.52 nH, C_2 = 3.52 pF, L_2 = 2.14 nH, L_3 = 11.47 nH, C_4 = 2.17 pF, L_4 = 7.02 nH and L_5 = 4.8 nH. Since the inductances of the series resonators are relatively high, the back side metallic patterns are slightly modified compared to the topology shown in Figure 5.4(a), that is, the strip connecting the two patch capacitances is also meandered. Nevertheless, the design procedure is identical to that of the previous filter. Furthermore, because of the higher electrical and physical length, as well as a more complex filter (in comparison with that of Figure 5.7), the possibility of including an electrical connection between the ground plane regions by means of two vias and a back side strip in order to avoid the appearance of the slot mode has been considered. The consequences of this additional connection will be discussed later.

The layout and photograph of this filter are both depicted in Figure 5.9. The simulated and measured frequency responses are shown in Figure 5.10(a), as well as the electromagnetic simulated filter response without the back side strip and the vias. The back side strip and vias improve the rejection level between the two transmission zeros and slightly the in-band return losses, albeit with the drawback of a degraded stop-band characteristic above the second transmission zero (which is thought to be due to the enhancement of the capacitance to ground where these elements are present). Hence, a trade-off between the performance up to the transmission zeros and that of the stop-band arise, where the choice of including the additional vias will depend on the filter requirements. In addition, the same simulation inaccuracies appreciated in the third-order filter are also present for the fifth-order filter, showing in Figure 5.10(b) the comparison between measurement, positive and negative electromagnetic simulation. A much better agreement between the simulation and the measurement can be appreciated at the pass-band if the negative simulation is considered, though the stop-band performance is better predicted by the positive simulations. Finally, the small filter dimensions, 12.1 mm × 13 mm ($0.062\lambda_g$ × $0.067\lambda_g$) are also remarkable.
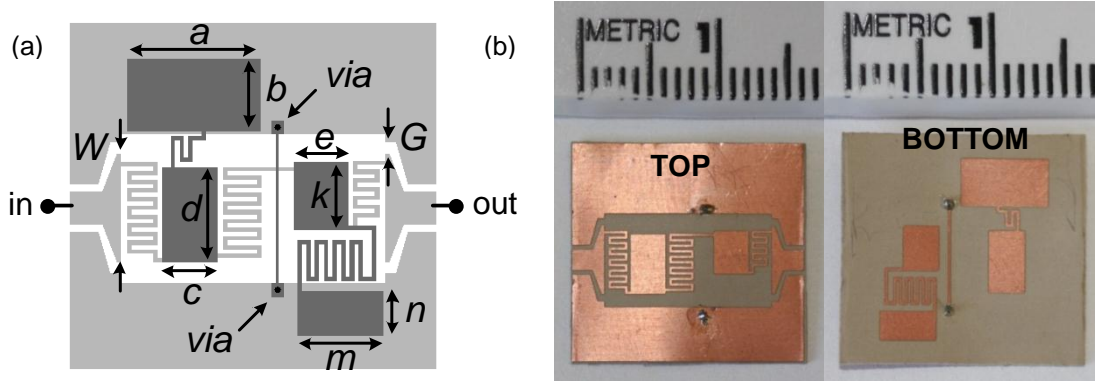
Figure 5.9. Layout (a) and photograph (b) of the fabricated fifth-order elliptic-function low-pass filter. Dimensions are: W = 5 mm, G = 0.55 mm, a = 6.12 mm, b = 3.32 mm, c = 2.54 mm, d = 4.34 mm, e = 2.54 mm, k = 3.14 mm, m = 3.96 mm and n = 2 mm. The strips of the meander lines are 0.2 mm width. The device has been fabricated on the *Rogers RO3010* substrate with measured dielectric constant ε_r = 11.2 and thickness h = 254 μm.
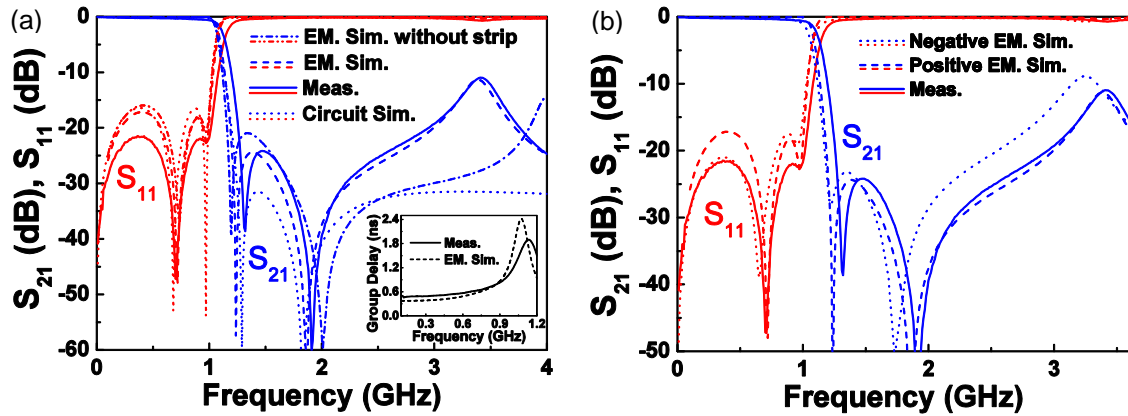
Figure 5.10. Ideal elliptic-function, electromagnetic and measured frequency response of the fabricated fifth-order elliptic-function low-pass filter of Figure 5.9, (a); Comparison between measurement, positive and negative simulated frequency response (b).

Reference	n	L_{ar} (dB)	L_{as} (dB)	Ω_s	Size	Ω_{-20dB}
[140]	3	0.1	35	2.921	$0.15\lambda_g \times 0.27\lambda_g$	1.6
[141]	3	0.1	30.52	2.5	$0.153\lambda_g \times 0.116\lambda_g$	3.7
[144]	3	0.1	18.86	1.7	$0.1\lambda_g \times 0.04\lambda_g$	2.2
This work	**3**	**0.1**	**30.52**	**2.5**	**$0.034\lambda_g \times 0.047\lambda_g$**	**6.7**
[141]	5	0.1	54	1.8	$0.172\lambda_g \times 0.093\lambda_g$	3.6
[143]	5	0.05	30	1.375	$0.25\lambda_g \times 0.19\lambda_g$	3.3
[145]	5	0.1	39.59	1.4	$0.13\lambda_g \times 0.086\lambda_g$	5
This work	**5**	**0.1**	**31.5**	**1.25**	**$0.062\lambda_g \times 0.067\lambda_g$**	**3**

Table 5.1: Size and performance comparison of various elliptic low-pass filters

In table 5.1, a comparison of the electrical size of the filters reported herein with those of various references is shown, where *n* is the order of the filter. We have also compared the stop-band performance by providing the frequency range where the stop-band rejection is better than -20 dB (this has been done through the normalized frequency, Ω_{-20dB}, defined as the ratio of the frequency where S_{21} = -20 dB and the cut-off frequency). This size comparison with other elliptic low-pass filters is indicative of the potentiality for size reduction of the proposed approach while maintaining a good performance and stop-band rejection.

5.3 Design of compact elliptic high-pass filters

Several works have aimed to implement elliptic-function high-pass filters. A possible method consists on considering the CRLH lines loaded with CSRRs, presented in section 2.2.4.2, and balance the structure in order to obtain the required wide band response [146] - [148]. Other approaches make use of different resonators etched in the ground plane or hybrid microstrip/CPW techniques, among others, obtaining similar results [149] - [151].

One possible network that synthesizes the ideal elliptic-function high-pass response is depicted in Figure 5.11, considering (without loss of generality) the case of a third-order filter since this is the case considered in the example reported later. The circuit consists of a cascade of series capacitances and shunt connected series resonators. At the resonance frequency of the series resonators, the corresponding shunt branch is short-circuited to ground, and the injected power is reflected back to the source (producing a transmission zero). Considering the model of the capacitive coupled CPW SIR proposed in Figure 5.2, if the effects of the parasitics of the line are minimized and a capacitance (by means of interdigital capacitors) is added in series with the resonator, the equivalent circuit of Figure 5.11 results. Therefore, elliptic-function high-pass responses can also be obtained with the proposed SIR topology. As occurred with the low-pass elliptic-function response, in order to obtain the required high inductance (L_2), asymmetric SIRs are considered, as well as the eventual meandering of the inductive strip. Thus, the resulting topology and equivalent circuit model is that shown in Figure 5.12, where the capacitance C_a (see Figure 5.4b) have been neglected since, as will be proven later, they have a negligible impact on the magnitude response of the high-pass filter.

In addition, unlike in the case of low-pass filters, where the ideal circuit model could be considered in the design process since the band of interest was allocated below the resonance frequency of the resonator (where the effect of the parasitics were small), the structure will be electrically bigger in the region of interest, since in high-pass filters the transmission band is allocated above the resonance frequency of the resonator, and hence the effect of the parasitics will be much more acute. Thus, the accurate circuit model will be mandatory in order to predict the electromagnetic behavior. The design methodology is based on the elliptic-function low-pass prototype filters, where the well-known low-pass to high-pass transformation equations are applied [26].
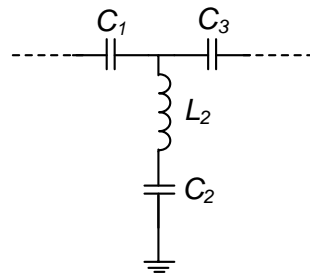
Figure 5.11. Third-order high-pass elliptic-function prototype filter.
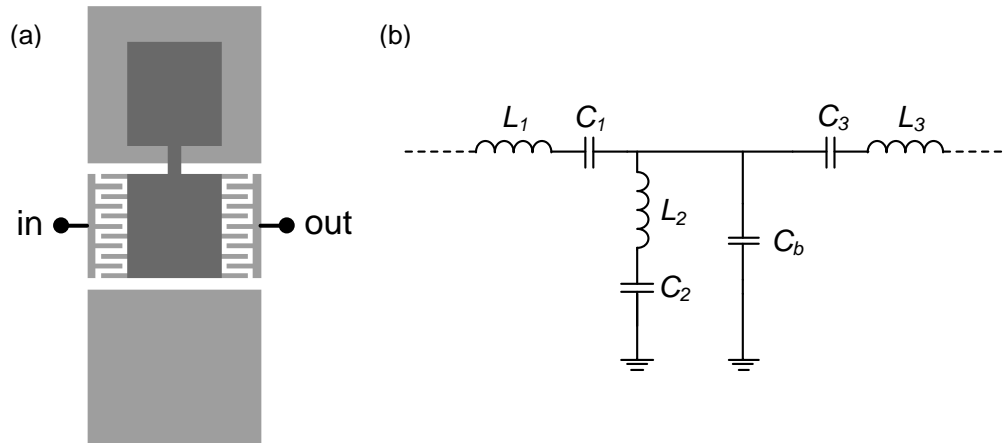
Figure 5.12. Typical topology of the proposed SIR-based elliptic-function high-pass filter (a) and circuit model including parasitics (b). The dark color represents the SIR, etched in the back substrate side.

To demonstrate the possibility of implementing elliptic-function high-pass filters with the proposed SIR-based structures in CPW technology, a third-order high-pass filter with a pass-band ripple of 0.1 dB, a minimum stop-band insertion loss of L_{as} = 18.85 dB, a cut-off frequency of 3 GHz and an equal-ripple stop-band starting frequency factor of Ω_{SB} = 1.69 is designed and fabricated. The element values corresponding to this elliptic-function response, referred to the circuit of Figure 5.11, are $C_1 = C_3 =$ 1.273 pF, C_2 = 3.263 pF, and L_2 = 3.143 nH. The layout generation has been carried out by means of a similar process to that of the low-pass filters, i.e., curve fitting the series and shunt reactances of the circuit and electromagnetic simulation.

After final optimization, the filter layout has been obtained (see Figure 5.13a). The series and shunt reactances of the equivalent *T*-circuit model of the structure of Figure 5.13(a) are depicted in Figure 5.14. These reactances were obtained from the full wave electromagnetic simulation of the structure. Since the structure is not exactly symmetric (with respect to the intermediate plane between the ports), the two series reactances can be, in principle, different and for this reason we obtained them independently. However, in practice, both reactances are almost undistinguishable. We have also included in Figure 5.14 the series and shunt reactances of the model of Figure 5.12(b), with the values indicated in the caption. As can be seen, the behavior of the structure is accurately predicted by the proposed equivalent circuit up to frequencies far beyond the transmission zero. However, a non-Foster behavior (negative slope) appears

around 4 GHz. This effect is due to the small parasitic inductance of the central patch between the capacitances C_1 and C_3, not taken into account in the circuit model of Figure 5.12(b). This series inductance is distributed between the SIR and the series capacitances and makes it impossible to obtain an equivalent *T*-circuit model composed of reactive elements, thereby not satisfying the Foster theorem in the whole range.
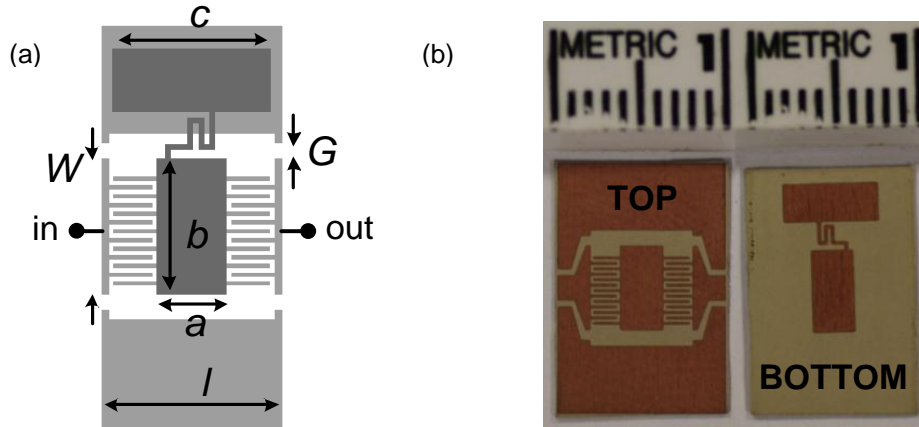
Figure 5.13. Layout (a) and photograph (b) of the fabricated elliptic-function high-pass filter. Dimensions are: W = 5 mm, G = 0.55 mm, l = 5.98 mm, a = 2.54 mm, b = 5 mm, c = 5.73 mm and d = 2.3 mm. The interdigital capacitors have a width and separation between fingers of 0.16 mm. The width and separation of the inductive strips of the SIR-based structure is 0.2 mm. The device has been fabricated on the *Rogers RO3010* substrate with thickness h = 254 μm and measured dielectric constant ε_r = 11.2.
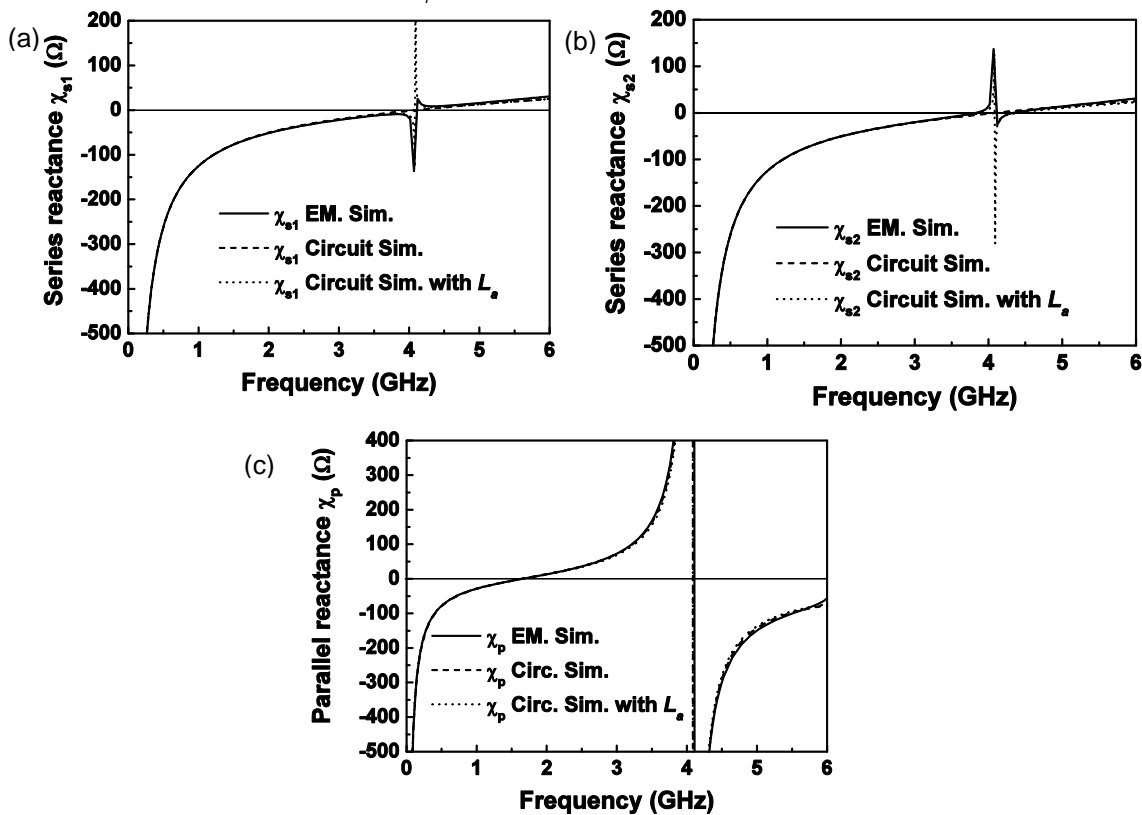
Figure 5.14. Series (a)-(b) and parallel (c) reactances of the equivalent *T*-circuit model of the layout of Figure 5.13(a) (electromagnetic simulation) and the circuit model of Figure 5.12(b). The values of the circuit model are: $L_1 = L_3$ = 1.26 nH, C_b = 0.6 pF, L_2 = 3.02 nH, C_2 = 3.11 pF and $C_1 = C_3$ = 1.2 pF.
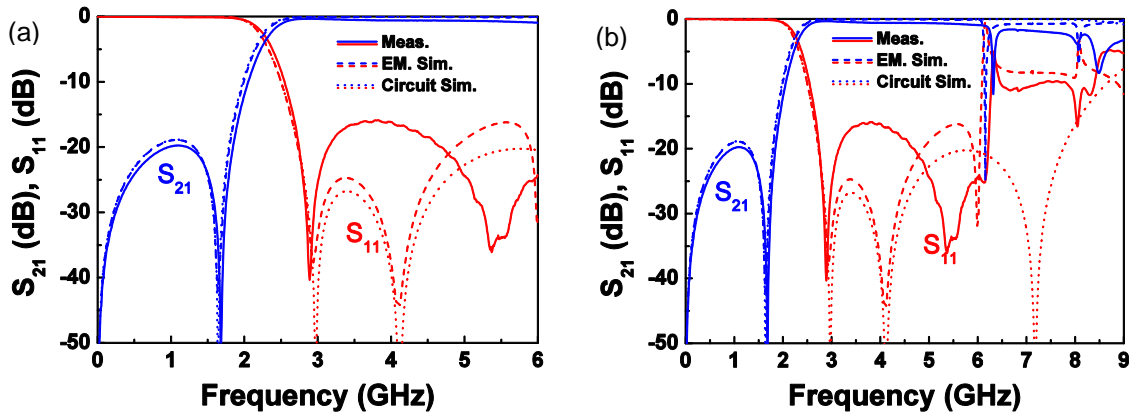
Figure 5.15. Narrow (a) and wideband (b) frequency response of the elliptic-function high-pass filter of Figure 5.13. The values of the circuit model are those indicated in the caption of Figure 5.14.
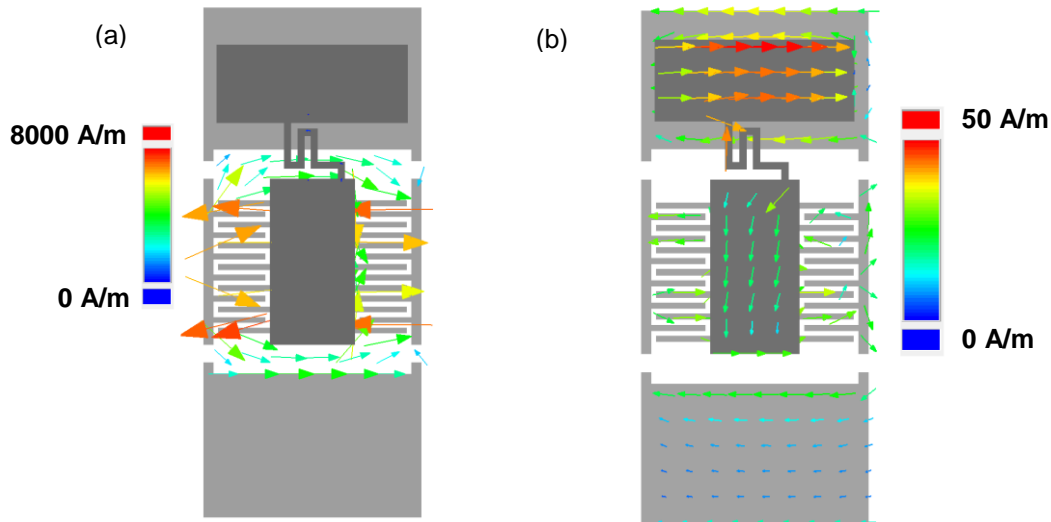
Figure 5.16. Magnetic (a) and electric (b) current distribution at the frequencies of the first (a) and second (b) spurious resonance of the layout of Figure 5.14.

However, the impact of this inductance on the frequency magnitude response of the filter is very small (the inductance value is $L_a = 0.02$ nH), only slightly reducing the matching levels at the band. Thus, although the previous effect could have been predicted in the circuit model, it has been neglected for design purposes. Nevertheless, the series and shunt reactances by including this parasitic inductance are also depicted in Figure 5.14, where it can be seen that the negative slope regions are correctly predicted.

The photograph of the designed filter is depicted in Figure 5.13(b), where tapered access lines are included for measuring purposes. The frequency response of the filter is shown in Figure 5.15, where good agreement between the circuit and electromagnetic simulation is observed. If the wideband response is considered (Figure 5.15b), additional resonances can be seen in the electromagnetic simulation and measurement around 6 GHz and 8 GHz, which are caused by a slot mode (because of the strong asymmetry of the SIR-based structure) and the distributed nature of the upper patch (as can also be verified by simulating this isolated patch), respectively. To

demonstrate this fact, in Figure 5.16 the electromagnetic simulated current distribution of the structure at these two frequencies is shown, where from the magnetic currents of Figure 5.16(a) and the electric currents of Figure 5.16(b) a slot mode and a distributed resonance of the upper patch can be appreciated, respectively.

The measured response is also reasonably consistent with the electromagnetic and circuit simulation up to 3 GHz. From that frequency forth, the return losses are slightly degraded compared to the simulations. This is attributed to fabrication tolerances and the connectors used. Moreover, due to the (although small) inductive effect of the line, the response slightly lessens with frequency (an effect not present in the ideal circuit of Figure 5.11). The fabricated filter is very small (5.98 mm $\times$ 12 mm), with an electrical size of $0.092\lambda_g \times 0.185\lambda_g$, with λ_g being the guided wavelength at the cut-off frequency.

In table 5.2, a comparison of the electrical size of the filter herein reported with those of several references is shown, where only elliptic-function high-pass filters composed of equivalent third-order responses are considered (and therefore only one transmission zero below the band is present). Given that elliptic ultra wideband filters can have an equivalent performance as elliptic high-pass filters (since the latter presents an upper cut-off frequency at which it no longer acts as a high-pass filter), some ultra wideband filters have also been added in the table.

The stop-band performance is also compared by providing the minimum stop-band rejection L_{as} and the equal-ripple stop-band starting frequency factor Ω_{SB} (i. e., the ratio between the cut-off frequency and the maximum frequency at which the required minimum stop-band rejection L_{as} is satisfied). In addition, the ratio between the frequency at which the filter ceases to present a high-pass response (or the response is not further shown) and the cut-off frequency is also considered, and denoted as Ω_{max}. This comparison with other elliptic high-pass filters demonstrates that the here presented approach can exhibit similar or even better performance and/or size reduction.

Reference	L_{as} (dB)	Ω_{SB}	Size	Ω_{max}
[149]	18.85	2.7	$0.29\lambda_g \times 0.12\lambda_g$	1.6
[147]	17	2	$0.126\lambda_g \times 0.126\lambda_g$	4
[150]	28	1.8	$0.102\lambda_g \times 0.146\lambda_g$	4
[148]	10	1.1	$0.093\lambda_g \times 0.066\lambda_g$	2
[151]	38	2.2	$0.058\lambda_g \times 0.183\lambda_g$	2.3
This work	**18.85**	**1.69**	**$0.092\lambda_g \times 0.185\lambda_g$**	**2**

Table 5.2: Size and performance comparison of various elliptic high-pass filters

5.4 Design of compact band-pass filters with transmission zeros

There are many different strategies to create transmission zeros in band-pass filters. For instance, through the introduction of cross coupling between nonadjacent resonators [152], [153] by providing more than one main path for the signal between the input and the output ports [154], [155] by introducing quarter wavelength open stubs [156], by properly positioning the tapping feed lines of the ports in coupled resonator filters [157], [158] or by providing signal paths to ground by means of shunt resonators [95], [159] among others. This latter category can be implementer with the presented SIR structures. Specifically, if we consider the topology used for elliptic high-pass filters and increase the parasitic behavior of the host line, band-pass filters with conventional Chebyshev responses and improved selectivity can be obtained. Within these conditions, we are able to obtain band-pass responses with an additional controllable transmission zero below the band arising from the additional C_2 capacitance present in the circuit of Figure 5.12(b). Moreover, although not predicted by the proposed model, the SIR exhibits additional resonances that can be useful to improve the upper transition band of the filter, since the position of such resonances can be controlled by means of SIR dimensions, as will be shown later.

The design procedure in this case consists of obtaining the g_i coefficients of the band-pass prototype that satisfy the specifications, and forcing the resulting ideal parallel shunt resonator to behave like the shunt impedance shown in Figure 5.12(b). To this end, we force both susceptances to be equal at the band edges, as well as forcing the frequency position of the transmission zero below the band. Forcing these conditions on a third-order filter, the following equations for the shunt branch result

$$L_2 = \frac{\omega_2 \omega_1 Z_0 (\omega_2 - \omega_1)}{g_2 (\omega_2{}^2 - \omega_Z{}^2)(\omega_1{}^2 - \omega_Z{}^2)} \tag{5.1}$$

$$C_2 = \frac{1}{L_2 \omega_Z{}^2} \tag{5.2}$$

$$C_b = \frac{(\omega_1 \omega_2 - \omega_Z{}^2)}{\omega_1 \omega_2 Z_0 (\omega_2 - \omega_1)} \tag{5.3}$$

with g_i being the coefficients of the low-pass prototype, Z_0 the characteristic impedance of the filter and ω_z, ω_1, ω_2 being the transmission zero, the lower and the upper cut-off frequencies, respectively. Moreover, since the series impedance of Figure 5.12(b) is the same as the ideal prototype Chebyshev filters, the equations of these reactive elements are obtained by the classic approach [26]

$$L_{1,3} = \frac{g_{1,3} Z_0 \omega_o}{(\omega_2 - \omega_1)} \tag{5.4}$$

$$C_{1,3} = \frac{1}{L_{1,3}\omega_o{}^2} \qquad\qquad (5.5)$$

Following this procedure, a third-order band-pass filter with a pass-band ripple of 0.035 dB, a central frequency of $f_0 = 6.26$ GHz, cut-off frequencies of 5.15 GHz and 7.6 GHz, and a transmission zero at 2.85 GHz is designed.

The g_i coefficients of the ideal Chebyshev band-pass filter are: $g_1 = g_3 = 0.814$ and $g_2 = 1.087$. With these coefficients, equations (5.1) - (5.5) are applied and the following element values are obtained: $L_1 = L_3 = 2.65$ nH, $C_1 = C_3 = 0.25$ pF, $L_2 = 0.77$ nH, $C_2 = 4.06$ pF and $C_b = 1.11$ pF. The design procedure to obtain the physical dimensions of the layout is the same as the elliptic-function high-pass filter, curve fitting the reactances of the electromagnetic response with the circuit simulation. Nonetheless, in this case a symmetric SIR has been used due to the low value of inductance needed, as well as to try to avoid the slot mode resonance. Using this procedure, the filter of Figure 5.17(a) is obtained. Figure 5.18 shows the series and parallel reactances, depicting only a series reactance χ_s since both reactances χ_{s1} and χ_{s2} have been found to be equal. The agreement between electromagnetic and circuit simulation is very good except above the pass-band, where the lumped element equivalent circuit model is no longer valid owing to the distributed nature of the second resonance of the SIR. Nevertheless, thanks to this second resonance, a transmission zero, improving the frequency selectivity above the filter pass-band, can be obtained.

The position of both SIR resonances (transmission zeros) can be controlled independently (to some extent) by means of the SIR dimensions [164]. Figure 5.19(d) depicts the response of the isolated SIR considered coupled to a 50 Ω CPW transmission line (reproduced in Figure 5.19a), where it can be seen the presence of the first transmission zero at the required frequency position (2.85 GHz), as well as a second resonance.
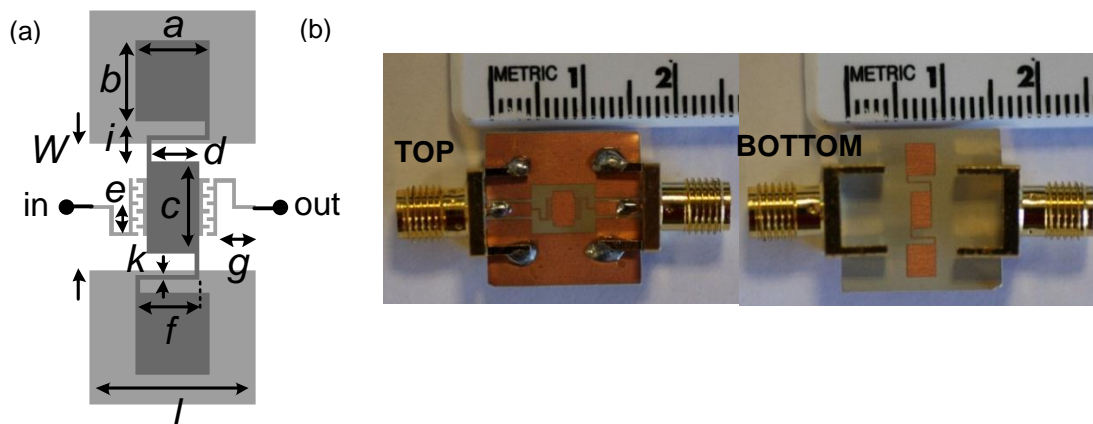
Figure 5.17. Layout (a) and photograph (b) of the designed band-pass filter. Dimensions are: $W = 5.3$ mm, $c = 3.85$ mm, $d = 2.21$ mm, $l = 6.93$ mm, $a = 3.1$ mm, $b = 3.4$ mm, $e = 1.12$ mm, $f = 2.66$ mm and $g = 1.62$ mm. The interdigital capacitors have a width and separation between fingers of 0.16 mm. The width of the SIR inductive strips are $k = 0.2$ mm and the width of the upper strip corresponding to the series inductance is 0.16mm. The device has been fabricated on the *Rogers RO3010* substrate with thickness $h = 254$ μm and dielectric constant $\varepsilon_r = 10.2$.
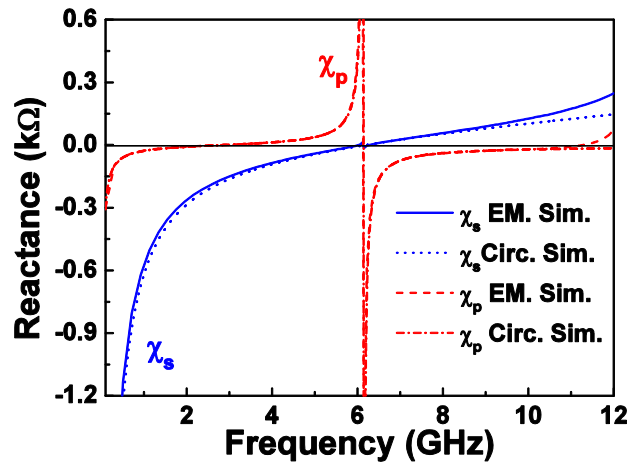
Figure 5.18. Series χ_s and parallel χ_p reactances of the equivalent T-circuit model of the layout of Figure 5.17(a) (electromagnetic simulation) and the circuit model of Figure 5.12(b). The values of the circuit model are: $L_1 = L_3 = 2.65$ nH, $C_1 = C_3 = 0.25$ pF, $L_2 = 0.77$ nH, $C_2 = 4.06$ pF and $C_b = 1.11$ pF.
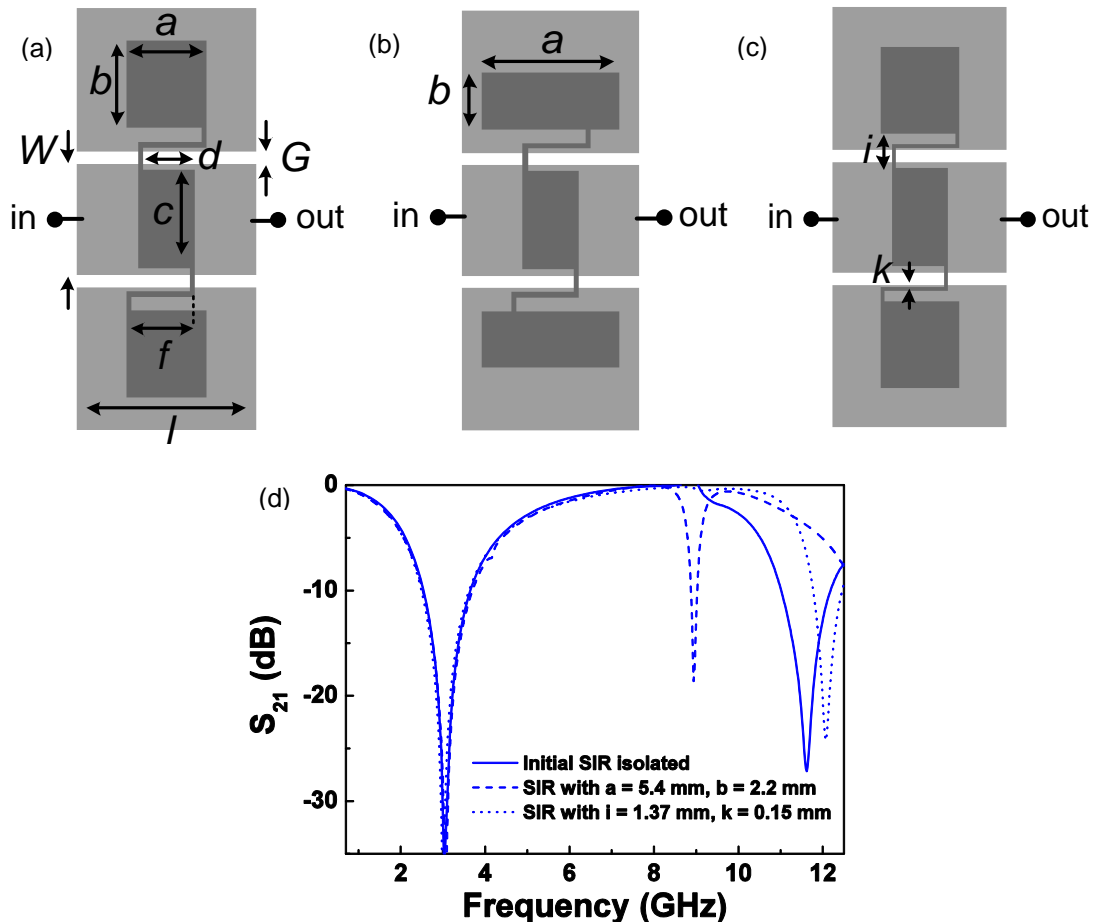
Figure 5.19. Topologies (a)-(c) and frequency responses (d) of different isolated SIRs loading the CPW structure of the fabricated filter. The dimensions of the topology of Figure 5.19(a) are those indicated in the caption of Figure 5.17. The modified dimensions of the topology of Figure 5.19(b) are: $a = 5.4$ mm and $b = 2.2$ mm. The modified dimensions of the topology of Figure 5.19(c) are: $i = 1.37$ mm and $k = 0.15$ mm.
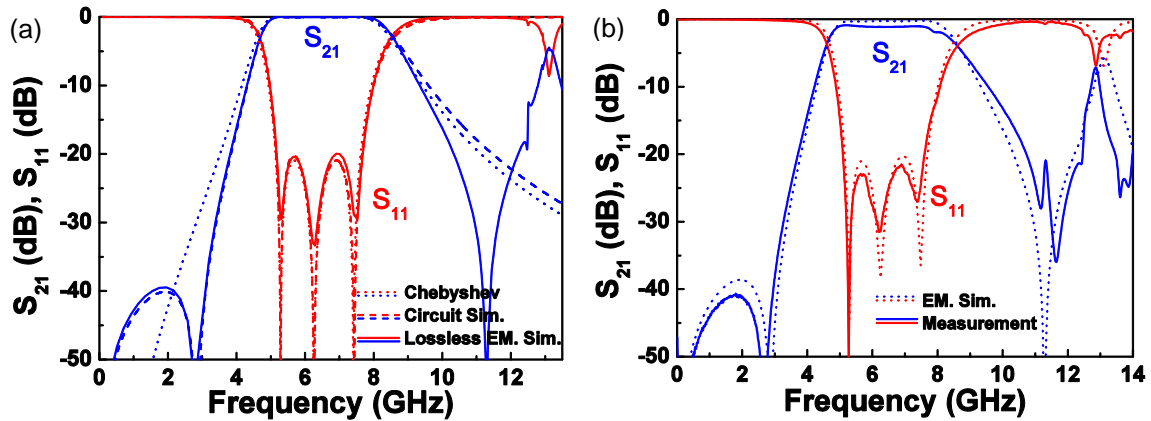
Figure 5.20. Simulated (a) and measured (b) frequency response of the band-pass filter of Figure 5.17.

In the same figure, additional SIR responses are shown controlling the second transmission zero while maintaining the same first resonance (and the L_2 and C_2 values). These responses have been generated by modifying the different metal patch (Figure 5.19b) or meander (Figure 5.19c) aspect ratios of the initial SIR topology. These results point out the flexibility of the SIR to tailor the second transmission zero while maintaining the characteristics of the first resonance. Figure 5.20(a) shows the frequency response of the layout of Figure 5.17(a), considering the circuit simulation of Figure 5.12(b) as well as the ideal Chebyshev response. The agreement between the circuit and electromagnetic simulation is remarkable up to roughly 10 GHz. Above that frequency, the filter experiences an improved fall-off (as compared to the circuit simulation) due to the second SIR resonance. The ideal Chebyshev response also indicates that standard responses can be obtained in the pass-band region improving both band edges by the introduction of transmission zeros. An additional distributed resonance appears at roughly $2f_0$, due mostly to the resonance of the patches. Hence, the squarer the patches, the farther this resonance appear. Another alternative to obtain an even higher second harmonic is to use radial stubs instead of rectangular patches [165].

In Figure 5.20(b) the comparison between the measured frequency response of the fabricated band-pass filter and the electromagnetic simulation considering losses is shown, where good agreement between both curves can be appreciated. The measured in-band return losses are better than 21.6 dB, and insertion losses are lower than 1.1 dB between 4.9 GHz and 7.6 GHz. In Figure 5.17(b) the photograph of the filter is also shown. The final layout has dimensions of 6.93 mm $\times$ 13.97 mm, which correspond to 0.22 λ_g $\times$ 0.45 λ_g, with λ_g being the guided wavelength at the central frequency of the filter. It is worth noting that this filter is electrically bigger than the elliptic-function high-pass filter due to the fact that the electrical size of the band-pass filter is calculated at the central frequency, whereas in the elliptic-function high-pass filter it is calculated at the cut-off frequency.

In **summary**, SIRs coupled to CPW host transmission lines have been proven to be useful for the design of elliptic low-pass and high-pass, as well as for band-pass filters with transmission zeros, where a good relation between the electrical size and filter performance has been obtained.

CHAPTER 6

Conclusions and future work

In this thesis, new strategies for the miniaturization of planar non-radiating microwave components have been proposed, and applied to the implementation of multi-band devices and microwave filters, including tunable components. For this purpose, artificial transmission lines based on metamaterial concepts and composed of semi-lumped elements have been considered. These lines provide the design flexibility required to achieve novel functionalities (multi-band operation) on the basis of impedance and dispersion engineering. Moreover, by sacrificing periodicity, such lines can be applied to the design of very compact band-pass filters with standard responses. In addition to metamaterial-based artificial transmission lines (which constitute the main contribution of this thesis), we also considered another approach for device miniaturization: stepped-impedance-resonators (SIRs). Using the conventional filter theory, such resonators have been applied to the design of compact planar filters with transmission zeros.

The contents of this work have been divided into five chapters (excluding the conclusions). Once the motivation and general objectives were pointed out in **chapter 1**, the specific objectives and achieved goals of each chapter are listed below:

In **chapter 2**, a brief general state of the art on the miniaturization of planar non-radiating passive microwave components has been presented, with special emphasis on power dividers, couplers and filters, since these are the components that have been designed in this thesis by means of the novel ideas and generated know-how. The basic metamaterial concepts have also been introduced, providing all the theory and tools that were required in the following chapters, including the CRLH transmission line concept, and the Bloch wave analysis of periodic structures. A review of metamaterial applications, with special emphasis on planar non-radiating microwave components, has been also carried out in this chapter.

In **chapter 3**, a new CRLH transmission line implementation, based on the combination of OSRRs and OCSRRs in microstrip and CPW technology, was proposed. To this end, the accurate circuit models of the OSRR- and the OCSRR-loaded lines (microstrip and CPW) have been deduced. Through these models, it has been found that these OSRR and OCSRR based artificial lines cannot be simply described by means of the canonical CRLH line model. Parasitics must be introduced, although it has been numerically and experimentally confirmed that these additional elements do not prevent the CRLH behavior of the lines, and the advantages of CRLH lines can be fully exploited. Nonetheless, in microstrip technology these CRLH lines are limited in terms of design due to the complexity of the OSRR circuit model. For this reason, only a CRLH line has been designed for this latter case, applying this structure to the design of a band-pass filter. On the other hand, focusing on CPW technology, different applications have been demonstrated by designing, fabricating and characterizing different prototypes, where a synthesis method based on a parameter extraction technique was also reported.

- Firstly, wideband Chebyshev band-pass filters have been presented, where fractional bandwidths from 35% to 100% and third to seventh-order filters have been achieved. The combination of size and performance of these new filters has been found to be competitive.

- Secondly, impedance and dispersion engineering have been applied to the design of a dual-band impedance inverter and a power divider as proof-of-concept demonstrators. The accuracy of the circuit model in predicting the response and the easy design procedure of these devices (through the parameter extraction method) are the main advantages in comparison to the state of the art resonant-type CRLH lines [84], [85].

- By considering additional semi-lumped elements combined with OSRRs and OCSRRs, fully-planar E-CRLH lines have been also implemented both in microstrip and CPW technology, avoiding the use of surface mount elements. Compared to the state of the art E-CRLH lines, accurate circuit models that predict both the simulated and measured responses have been presented

(identical for both microstrip and CPW technologies). This enables the possibility of easily controlling the impedance and phase at different operation frequencies and, since these E-CRLH lines exhibit more than two alternate right- and left-handed bands, it is possible to design devices able to satisfy the requirements or specifications in more than two bands. To demonstrate the applications of the proposed E-CRLH lines, we have reported the detailed procedure for the synthesis of quad-band impedance inverters, which are the building blocks of many microwave components. Through this methodology, quad-band power splitters and branch line hybrid couplers have been designed and fabricated. Furthermore, since the E-CRLH line model (unit cell) is identical to the model of an ideal third-order dual-band band-pass filter, a dual-band band-pass filter has been also designed. The reported devices, designed to operate at the commercial GSM and GPS frequency bands to prove their controllability, exhibit reasonable performance and device dimensions are small on account of the semi-lumped components used in their implementations. Therefore, these results show the potentiality of E-CRLH lines in the design of multi-band microwave components and the possibility of implementing them in fully planar technology.

Chapter 4 is devoted to the study of tunable CRLH lines based on open particles and BST thick-films. For this purpose, a tunable arbitrary CRLH line has been designed and fabricated, where a simulated and measured frequency tunability range of 36.6% has been achieved. The size, the controllability of the different elements as well as the simplicity of the biasing scheme (a single voltage is required to tune the whole structure) are the main advantages of this approach. Once these structures have been experimentally validated, different potential applications such as tunable wideband band-pass filters, phase shifters, tunable dual-band impedance inverters and power dividers have been also analyzed, presenting the design methodology and limitations for each case, as well as potential topologies and simulations. In order to optimally implement some of the aforementioned devices, the independent tuning of the OSRR and OCSRR by means of two voltage sources has been also proposed.

In **chapter 5**, back side etched SIRs in CPW technology have been considered in order to obtain compact filters with sharp responses (due to the inherent transmission zeros of such SIR-loaded CPWs). By means of the conventional filter theory, novel CPW elliptic-function low-pass and high-pass filters, as well as band-pass filters with transmission zeros have been proposed. The deviations from the ideal circuit responses have been analyzed by including parasitics in the circuit model. The good agreement between the filter responses and the different circuit models has been experimentally verified. The combination of filter size and performance (selectivity, in-band losses and stop-band rejection) has been found to be very promising. These filters can be of interest in many applications where size reduction, compatibility with planar technology and high performance are the key aspects.

As a **general conclusion**, the objectives proposed in the first chapter have been satisfactorily achieved. With the work and the investigations carried out in this thesis, we have generated new application-oriented know-how in the field of microwave

engineering. This work has also contributed to the progress and development of metamaterial-based microwave components, specifically within the so-called resonant-type approach, where some limitations present so far have been solved, and novel functionalities have been demonstrated.

Different **future research lines** can emerge from this thesis. For instance, additional microwave components such as dual-band or quad-band rat-race couplers could be implemented with the open particles by combining the CRLH or E-CRLH lines already presented with their dual counterpart implementations. In addition, performance improvement (i.e., losses) of the multi-band components based on the E-CRLH lines could be optimized by considering different alternatives. For example, a different technology with an inherent higher quality factor (such as surface integrated waveguide or SIW) could be considered. Alternatively, the use of impedance inverters to replace either the series or shunt branch of the E-CRLH line could be analyzed for the design of dual-band band-pass filters, since its associate quality factor is much higher than those of the semi-lumped elements. On the other hand, the design methodology of the E-CRLH lines could be reconsidered by including losses from the circuit level (which could lead to the need to consider additional resistors to obtain an optimum response). With this latter method, the conditions of phase and impedance could still be satisfied in the four bands (or two bands considering the dual-band band-pass filter). Furthermore, the implementation of a complete dual-band or quad-band transceiver by means of the components presented herein could also be investigated.

Regarding the tunable CRLH lines, liquid crystals could be studied as an alternative to BST thick-films, which enables similar results to be obtained although with a lower level of losses and higher performance. Thus, with this latter technology, the tunability of E-CRLH lines could be analyzed, making it therefore possible to obtain tunable multi-band components and filters.

Additional research lines based on metamaterial concepts are also being studied in the research group GEMMA/CIMITEC to which the author belongs.

- One of these research lines is focused on the implementation of software tools that enable the automatic synthesis of planar metamaterial microwave circuits based on aggressive space mapping (ASM). So far, this tool has been successfully applied to the synthesis of CSRR-based structures, with one of the aims being to expand its functionality to design open resonator- (OSRR and OCSRR) based structures by means of the parameter extraction methods reported herein.

- The design of artificial lines based on lattice networks is also being studied, which can ideally result in all-pass artificial lines with constant impedances with frequency. The application of these lines to the design of wideband and dual-band components is under study. It is our aim to compare the size and performance with the components designed by means of the approaches presented in this thesis.

- Finally, CSRRs have also been used for the implementation of differential transmission lines with common-mode suppression, maintaining the differential signal integrity thanks to the symmetry of the structure. This research activity is very promising for applications in high speed digital circuits, where differential lines are required. The CSRR-based common mode filters designed so far are competitive, and it is our purpose to implement differential filters (combined with the CSRR common mode filters) based on the open resonators and filters reported in this thesis.

References

[1]   D. Pozar, *"Microwave Engineering"*, John Wiley & Sons, second edition, 1998.

[2]   A. A. Oliner, "Historical Perspectives on Microwave Field Theory", *IEEE Transactions on Microwave Theory and Techniques*, vol. 32, no. 9, pp. 1022-1045, September 1984.

[3]   R. E. Collin, *"Foundations for Microwave Engineering"*, McGraw-Hill, second edition, 1992.

[4]   V. K. Tripathi, H. B. Lunden and J. P. Starski, "Analysis and Design of Branch line Hybrids with Coupled Lines", *IEEE Transactions on Microwave Theory and Techniques*, vol. 32, no. 4, pp. 427-432, April 1984.

[5]   R. K. Settaluri, G. Sundberg, A. Weisshaar and V. K. Tripathi, "Compact Folded Line Rat-Race Hybrid Couplers", *IEEE Transactions on Microwave and Guided Wave Letters*, vol. 10, no. 2, pp. 61-63, February 2000.

[6]   Y. Lai, C. Lin, J. Chiu, C. Lin and Y. Wang, "A Compact Ka-Band Planar Three-Way Power Divider", *IEEE Microwave And Wireless Components Letters*, vol. 17, no. 12, pp. 840-842, December 2007.

[7]   X. Tang and K. Mouthaan, "Analysis and design of compact two-way Wilkinson power dividers using coupled lines", *Proceedings of Asia-Pacific Microwave Conference 2009*, Singapore, Singapore, pp. 1319-1322, 7-10 December 2009.

[8]   W.-L. Chang, T.-Y. Huang, T.-M. Shen, B.-C. Chen and R.-B. Wu, "Design of

REFERENCES

Compact Branch line Coupler with Coupled Resonators", *Proceedings of Asia-Pacific Microwave Conference 2007*, Bangkok, Thailand, pp. 1-4, December 2007.

[9]   F. Hosseini, M. Khalaj-Amir hosseini and M.Yazdani, "Novel compact branch line coupler using non-uniform transmission line", *Proceedings of Asia-Pacific Microwave Conference 2009*, Singapore, Singapore, pp. 1577-1580, December 2009.

[10]   P. Jarry, J. Beneat, *"Design and realizations of miniaturized fractal RF and microwave filters"*, John Wiley & Sons, 2009.

[11]   K. M. Shum, Q. Xue and C. H. Chan, "A Novel Microstrip Ring Hybrid Incorporating a PBG Cell", *IEEE Microwave And Wireless Components Letters*, vol. 11, no. 6, pp. 258-260, June 2001.

[12]   Y. J. Sung, C. S. Ahn and Y.-S. Kim, "Size Reduction and Harmonic Suppression of Rat-Race Hybrid Coupler Using Defected Ground Structure", *IEEE Microwave And Wireless Components Letters*, vol. 14, no. 1, pp. 7-9, January 2004.

[13]   K.-O. Sun, S.-J. Ho, C.-C. Yen and D. van der Weide, "A Compact Branch line Coupler Using Discontinuous Microstrip Lines", *IEEE Microwave And Wireless Components Letters*, vol. 15, no. 8, pp. 519-520, August 2005.

[14]   J. He, B.-Z. Wang and W. Shao, "Compact power divider embedded with zigzag microstrip slow-wave structures", *Electronics Letters*, vol. 45, no. 1, pp. 62-63, January 2009.

[15]   J. Sor, Y. Qian and T. Itoh, "Miniature Low-Loss CPW Periodic Structures for Filter Applications", *IEEE Transactions on Microwave Theory and Techniques*, vol. 49, no. 12, pp. 2336-2341, December 2001.

[16]   F. Martín, F. Falcone, J. Bonache, T. Lopetegi, M. A. G. Laso and M. Sorolla, "New CPW Low-Pass Filter Based On A Slow Wave Structure", *Microwave And Optical Technology Letters*, vol. 38, no. 3, pp. 190-193, August 2003.

[17]   J. García-García, J. Bonache and F. Martín, "Application of Electromagnetic Bandgaps to the Design of Ultra-Wide Bandpass Filters With Good Out-of-Band Performance", *IEEE Transactions on Microwave Theory and Techniques*, vol. 54, no. 12, pp. 4136-4140, December 2006.

[18]   R. K. Settaluri, A. Weisshaar, C. Lim and V. K. Tripathi, "Design of Compact Multilevel Folded-Line RF Couplers", *IEEE Transactions on Microwave Theory and Techniques*, vol. 47, no. 12, pp. 2331-2339, December 1999.

[19]   J. G. Yang, Y. Jeong, S. Choi and K. Yang, "A New Compact 3-D Hybrid Coupler Using Multi-Layer Microstrip Lines at 15 GHz", *Proceedings of the 36th European Microwave Conference, 2006*, Manchester (UK), pp. 25-28, 10-15 September 2006.

[20]   T. H. Duong and I. S. Kim, "Single Section Wilkinson Type UWB Power Divider with Bandpass Filter and DC Block Characteristics in LTCC Technology", *IEEE MTT-S International Microwave Symposium Digest*, Anaheim, California, USA, pp. 117-120, May 2010.

130

[21]   Z.-C. Hao and J.-S. Hong, "Ultra Wideband Bandpass Filter Using Embedded Stepped Impedance Resonators on Multilayer Liquid Crystal Polymer Substrate", *IEEE Microwave And Wireless Components Letters*, vol. 18, no. 9, pp. 581-583, September 2008.

[22]   M. Caulton, B. Hershenov, S. P. Knight and R. E. Debrecht, "Status of Lumped Elements in Microwave Integrated Circuits—Present and Future", *IEEE Transactions on Microwave Theory and Techniques*, vol. 19, no. 7, pp. 588-599, July 1971.

[23]   R. K. Gupta and W. J. Getsinger, "Quasi-Lumped-Element 3- And 4-Port Networks For MIC And MMIC Applications", *International Microwave Symposium Digest*, San Francisco (CA), USA, pp. 409-411, May 1984.

[24]   R. W. Vogel, "Analysis and design of lumped- and lumped- distributed element directional couplers for MIC and MMIC applications", *IEEE Transactions on Microwave Theory and Techniques*, vol. 40, no. 2, pp. 253-262, February 1992.

[25]   G. Matthaei and J. E. Young, *"Microwave filters, impedance matching and coupling structures"*, Artech House, 1985.

[26]   J.-S. Hong and M. J. Lancaster, *"Microstrip Filters for RF/Microwave Applications"*, John Wiley & Sons, 2001.

[27]   R. J. Cameron, C. M. Kudsia and R. R. Mansour, *"Microwave Filters for Communication Systems: Fundamentals, Design, and Applications"*, John Wiley & Sons, 2007.

[28]   J.-S. Hong, "Recent Progress in Miniature Microwave Filters", *2008 IEEE MTT-S International Microwave Workshop Series on Art of Miniaturizing RF and Microwave Passive Components*, Chengdu (China), pp. 1-6, December 2008.

[29]   K. L. Wan, Y. L. Chow and K. M. Luk, "Simple design of dual-frequency unequal power-divider", *Electronics Letters*, vol. 37 no. 19, pp. 1171-1173, September 2001.

[30]   K.-K. M. Cheng and C. Law, "A Novel Approach to the Design and Implementation of Dual-Band Power Divider", *IEEE Transactions on Microwave Theory and Techniques*, vol. 56, no. 2, pp. 487-492, February 2008.

[31]   K.-K. M. Cheng and F.-L. Wong, "A Novel Approach to the Design and Implementation of Dual-Band Compact Planar 90 Branch line Coupler", *IEEE Transactions on Microwave Theory and Techniques*, vol. 52, no. 11, pp. 2458-2463, November 2004.

[32]   Q.-X. Chu and F. Lin, "A Novel Tri-Band Rat Race Coupler With T-Shape Step Impedance Transformers", *Microwave and Optical Technology Letters*, vol. 52, no. 6, pp. 1240-1244, June 2010.

[33]   K.-S. Chin, K.-M. Lin, Y.-H. Wei, T.-H. Tseng and Y.-J. Yang, "Compact Dual-Band Branch line and Rat-Race Couplers With Stepped-Impedance-Stub Lines", *IEEE Transactions on Microwave Theory and Techniques*, vol. 58, no.

REFERENCES

5, pp. 1213-1221, May 2010.

[34]   S.-F. Chang, Y.-H. Jeng and J.-L. Chen, "Dual-band step-impedance bandpass filter for multimode wireless LANs", *Electronics Letters*, vol. 40, no. 1, pp. 38-39, January 2004.

[35]   J. Wang, L. Ge, K. Wang and W. Wu, "Compact microstrip dual-mode dual-band bandpass filter with wide stopband", *Electronics Letters*, vol. 47, no. 4, pp. 263-265, February 2011.

[36]   J. Wang, Y.-X. Guo, B.-Z. Wang, L.C. Ong and S. Xiao, "High-selectivity dual-band stepped-impedance bandpass filter", *Electronics Letters*, vol. 42, no. 9, pp. 538-540, April 2006.

[37]   C. Quendo, E. Rius and C. Person, "An Original Topology of Dual-Band Filter with Transmission Zeros", *International Microwave Symposium Digest*, Philadelphia, Pennsylvania (USA), pp. 1093-1096, June 2003.

[38]   C. Quendo, E. Rius, A. Manchec, Y. Clavet, B. Potelon, J.-F. Favennec and C. Person, "Planar Tri-band Filter based on Dual Behavior Resonator (DBR)", *European Microwave Conference*, Paris (France), October 2005.

[39]   M. Mokhtaari, J. Bornemann, K. Rambabu and S. Amari, "Coupling-Matrix Design of Dual and Triple Passband Filters", *IEEE Transactions on Microwave Theory and Techniques,* vol. 54, no. 11, pp. 3940-3946, November 2006.

[40]   C.-F. Chen, T.-Y. Huang and R.-B. Wu, "Design of Dual- and Triple-Passband Filters Using Alternately Cascaded Multiband Resonators", *IEEE Transactions on Microwave Theory and Techniques*, vol. 54, no. 9, pp. 3550-3558, September 2006.

[41]   J.-H. Sung, G.-Y. Kim, S.-H. Son, H.-J. Lee, Y.-J. Song, Y.-W. Jeong, H.-S. Park and D. Ahn, "Design Method of a Dual Band Balun and Divider", *International Microwave Symposium Digest*, Seattle, Washington (USA), pp. 1177-1180, June 2002.

[42]   H. Uchida, H. Kamino, K. Totani, N. Yoneda, M. Miyazaki, Y. Konishi, S. Makino, J. Hirokawa and M. Ando, "Dual-band-rejection filter for distortion reduction in RF transmitters", *IEEE Transactions on Microwave Theory and Techniques*, vol. 52, no. 11, pp. 2550-2556, November 2004.

[43]   X. Guan, Z. Ma, P. Cai, Y. Kobayashi, T. Anada and G. Hagiwara, "Synthesis of dual-band bandpass filters using successive frequency transformations and circuit conversions", *IEEE Microwave and Wireless Components Letters*, vol. 16, no. 3, pp. 110-112, March 2006.

[44]   P. W. Wong and I. Hunter, "Electronically tunable filters", *IEEE Microwave Magazine*, vol. 10, no. 6, pp. 46-54, October 2009.

[45]   J.-S. Hong, "Reconfigurable planar filters", *IEEE Microwave Magazine*, vol. 10, no. 6, pp. 73-83. October 2009.

[46]   C. Caloz and T. Itoh, *"Electromagnetic Metamaterials: Transmission Line Theory and Microwave Applications"*, John Wiley & Sons, 2006.

132

[47]   G. V. Eleftheriades and K. G. Balmain, *"Negative-Refraction Metamaterials: Fundamental Principles and applications"*, John Wiley & Sons, 2005.

[48]   R. Marqués, F. Martín and M. Sorolla, *"Metamaterials with Negative Parameters: Theory, Design and Microwave Applications"*, John Wiley & Sons, 2008.

[49]   N. Engheta and R. W. Ziolkowski, *"Metamaterials: Physics and engineering explorations"*, John Wiley & Sons, 2006.

[50]   L. Solymar and E. Shamonina, *"Waves in Metamaterials"*, Oxford University Press, 2009.

[51]   V. G. Veselago, "The electrodynamics of substances with simultaneously negative values of ε and μ", *Sov. Phys. Usp.*, vol. 10, no. 4, pp. 509-514, January - February 1968.

[52]   J. B. Pendry, A. J. Holden, D. J. Robbins and W. J. Stewart, "Magnetism from conductors and enhanced nonlinear phenomena", *IEEE Transactions on Microwave Theory and Techniques*, vol. 47, no. 11, pp. 2075-2084, November 1999.

[53]   J. D. Baena, J. Bonache, F. Martín, R. Marqués, F. Falcone, T. Lopetegi, M. A. G. Laso, J. García, I. Gil and M. Sorolla, "Equivalent circuit models for split ring resonators and complementary split rings resonators coupled to planar transmission lines", *IEEE Transactions on Microwave Theory and Techniques*, vol. 53, no. 4, pp. 1451-1461, April 2005.

[54]   D. R. Smith, W. J. Padilla, D. C. Vier, S. C. Nemat-Nasser and S. Schultz, "Composite medium with simultaneously negative permeability and permittivity", *Physics Review Letters*, vol. 84, no. 18, pp. 4184-4187, May 2000.

[55]   R. Marqués, J. Martel, F. Mesa and F. Medina, "Left-handed-media simulation and transmission of EM waves in subwavelength split-ring resonator-loaded metallic waveguides", *Physical Review Letters*, vol. 89, no. 18, pp. 183901-4, October 2002.

[56]   R. A. Shelby, D. R. Smith and S. Schultz, "Experimental verification of a negative index of refraction", *Science*, vol. 292, pp. 77-79, April 2001.

[57]   R. A. Shelby, D. R. Smith, S. C. Nemat-Nasser and S. Schultz, "Microwave transmission through a two-dimensional, isotropic, left-handed metamaterial", *Applied Physics Letters*, vol. 78, no. 4, pp. 489-491, January 2001.

[58]   R. W. Ziolkowski, "Design, Fabrication, and Testing of Double Negative Metamaterials", *IEEE Transactions on Antennas and Propagation*, vol. 51, no. 7, pp. 1516-1529, July 2003.

[59]   R. Marqués, F. Mesa, J. Martel and F. Medina, "Comparative Analysis of Edge- and Broadside-Coupled Split Ring Resonators for Metamaterial Design—Theory and Experiments", *IEEE Transactions on Antennas and Propagation*, vol. 51, no. 10, pp. 2572-2581, October 2003.

[60] D. Schurig, J. J. Mock, B. J. Justice, S. A. Cummer, J. B. Pendry, A. F. Starr and D. R. Smith, "Metamaterial electromagnetic cloak at microwave frequencies", *Science*, vol. 314, no. 5801, pp. 977-980, November 2006.

[61] L. Jelinek, R. Marqués and M. J. Freire, "Accurate modeling of split ring metamaterial lenses for magnetic resonance imaging applications", *Journal of Applied Physics*, vol. 105, no. 2, pp. 024907, January 2009.

[62] J. Valentine, S. Zhang, T. Zentgraf, E. Ulin-Avila, D. A. Genov, G. Bartal and X. Zhang, "Three-dimensional optical metamaterial with a negative refractive index", *Nature*, vol. 455, pp. 376-379, August 2008.

[63] A. K. Iyer and G. V. Eleftheriades, "Negative refractive index metamaterials supporting 2D waves", *IEEE MTT-S International Microwave Symposium Digest*, Seattle, WA, pp. 1067-1070, June 2002.

[64] C. Caloz, H. Okabe, T. Iwai and T. Itoh, "Transmission Line Approach of Left-Handed (LH) Materials", *2002 USNC/URSI Meeting*, San Antonio, TX, June 2002.

[65] C. Caloz and T. Itoh, "Application of the transmission line theory of left-handed (LH) materials to the realization of a microstrip LH line", *IEEE Antennas and Propagation Society International Symposium*, San Antonio, Texas, USA, pp. 412-415, vol. 2, June 2002.

[66] G. V. Eleftheriades, A. K. Iyer and P. C. Kremer, "Planar negative refractive index media using periodically L-C loaded transmission lines", *IEEE Transactions on Microwave Theory and Techniques*, vol. 50, no. 12, pp. 2702-2712, December 2002.

[67] A. Grbic and G. V. Eleftheriades, "Experimental verification of backward-wave radiation from a negative refractive index metamaterial", *Journal of Applied Physics*, vol. 92, no. 10, pp. 5930-5935, November 2002.

[68] A. A. Oliner, "A periodic structure negative refractive index medium without resonant elements", *IEEE AP-S/URSI International Symposium Digest*, San Antonio, Texas, pp. 41, June 2002.

[69] C. Damm, J. Freese, M. Schüβler and R. Jakoby, "Electrically controllable artificial transmission line transformer for matching purposes", *IEEE Transactions on Microwave Theory and Techniques*, vol. 55, no. 6, pp. 1348-1354, June 2007.

[70] C. Caloz, "Dual composite right/left-handed (D-CRLH) transmission line metamaterial", *IEEE Microwave and Wireless Component Letters*, vol. 16, no. 11, pp. 585-587, November 2006.

[71] A. Rennings, T. Liebig, C. Caloz and I. Wolff, "Double-Lorentz transmission line metamaterials and its applications to tri-band devices", *IEEE MTT-S International Microwave Symposium Digest*, pp. 1427-1430, Honolulu, Hawaii, USA, June 2007.

[72] C. Camacho-Peñalosa, T. M. Martin-Guerrero, J. Esteban and J. E. Page, "Derivation and General Properties of Artificial Lossless Balanced Composite Right/Left-Handed Transmission Lines of Arbitrary Order", *Progress In*

Electromagnetics Research B, vol. 13, pp. 151-169, 2009.

[73] A. Rennings, S. Otto, J. Mosig, C. Caloz and I. Wolff, "Extended composite right/left-handed (E-CRLH) metamaterial and its application as quadband quarter-wavelength transmission line", *Asia-Pacific Microwave Conference (APMC)*, Yokohama, Japan, December 2006.

[74] G. V. Eleftheriades, "A generalized negative-refractive-index transmission-line (NRL-TL) metamaterial for dual-band and quad-band applications", *IEEE Microwave and Wireless Components Letters*, vol. 17, no. 6, pp. 415-417, June 2007.

[75] G. Sisó, M. Gil, J. Bonache and F. Martín, "Generalized Model for Multiband Metamaterial Transmission Lines", *IEEE Microwave and Wireless Components Letters*, vol. 18, no. 11, pp. 728-730, November 2008.

[76] R. A. Foster, "A reactance theorem", *Bell System Technical Journal*, vol. 3, pp. 259-267, 1924.

[77] F. Martín, J. Bonache, F. Falcone, M. Sorolla and R. Marqués, "Split ring resonator-based left-handed coplanar waveguide", *Applied Physics Letters*, vol. 83, pp. 4652-4654, December 2003.

[78] F. Aznar, J. Bonache and F. Martín, "Improved circuit model for left-handed lines loaded with split ring resonators", *Applied Physics Letters*, vol. 92, pp. 043512-3, January 2008.

[79] F. Falcone, T. Lopetegui, J. D. Baena, R. Marqués, Ferran Martín and M. Sorolla, "Effective Negative-ε Stopband Microstrip Lines based on Complementary Split Ring Resonators", *IEEE Microwave and Wireless Component Letters*, vol. 14, no. 6, pp. 280-282, June 2004.

[80] F. Falcone, T. Lopetegi, M. A. G. Laso, J. D. Baena, J. Bonache, M. Beruete, R. Marqués, F. Martín and M. Sorolla, "Babinet principle applied to the design of metasurfaces and metamaterials", *Physical Review Letters*, vol. 93, pp. 197401-4, November 2004.

[81] J. Bonache, M. Gil, O. García-Abad and F. Martín, "Parametric analysis of microstrip lines loaded with complementary split ring resonators", *Microwave and Optical Technology Letters*, vol. 50, no. 8, pp. 2093-2096, August 2008.

[82] M. Gil, J. Bonache, I. Gil, J. García-García and F. Martín, "Miniaturization of planar microwave circuits by using resonant-type left handed transmission lines", *IET Microwave, Antennas and Propagation*, vol. 1, pp. 73-79, February 2007.

[83] I. H. Lin, M. De Vincentis, C. Caloz and T. Itoh, "Arbitrary dual-band components using right/left handed transmission lines", *IEEE Transactions on Microwave Theory and Techniques*, vol. 52, no. 4, pp. 1142-1149, April 2004.

[84] J. Bonache, G. Sisó, M. Gil, A. Iniesta, J. García-Rincón and F. Martín, "Application of Composite Right/Left Handed (CRLH) Transmission Lines based on Complementary Split Ring Resonators (CSRRs) to the Design of Dual-Band Microwave Components", *IEEE Microwave and Wireless*

Components Letters, vol. 18, no. 8, pp. 524-526, August 2008.

[85] G. Sisó, J. Bonache and F. Martín, "Dual-Band Y-Junction Power Dividers Implemented Through Artificial Lines Based on Complementary Resonators", *IEEE MTT-S International Microwave Symposium*, Atlanta, USA, pp. 663-666, June 2008.

[86] G. Sisó, J. Bonache and F. Martín, "Miniaturization and Dual-Band Operation in Planar Microwave Components by Using Resonant-Type Metamaterial Transmission Lines", *2008 IEEE MTT-S International Microwave Workshop Series on Art of Miniaturizing RF and Microwave Passive Components*, Chengdu (China), pp. 34-37, December 2008.

[87] M. Studniberg and G. V. Eleftheriades, "Physical Implementation of a Generalized NRI-TL Medium for Quad-Band Applications", *Proceedings of the 37th European Microwave Conference*, Munich (Germany), pp. 408-411, October 2008.

[88] B. H. Chen, Y. N. Zhang, D. Wu and K. Seo, "Novel Composite Right/Left-Handed Transmission Line for Quad-Band Applications", *11th IEEE Singapore International Conference on Communication Systems, 2008 (ICCS 2008)*, pp. 617-620, November 2008.

[89] A. C. Papanastasiou, G. E. Georghiou and G. V. Eleftheriades, "A Quad-Band Wilkinson Power Divider Using Generalized NRI Transmission Lines", *IEEE Microwave and Wireless Components Letters*, vol. 18, no. 8, pp. 521-523, August 2008.

[90] M. Studniberg and G. V. Eleftheriades, "A Dual-Band Bandpass Filter Based on Generalized Negative-Refractive-Index transmission-Lines", *IEEE Microwave and Wireless Components Letters*, vol. 19, no. 1, pp. 18-20, January 2009.

[91] G. V. Eleftheriades, "Correction to "A Generalized Negative-Refractive-Index Transmission-Line (NRI-TL) Metamaterial for Dual-Band and Quad-Band Applications"", *IEEE Microwave and Wireless Components Letters*, vol. 20, no. 2, pp. 130, February 2010.

[92] G. V. Eleftheriades, "Design of generalised negative-refractive-index transmission lines for quad-band applications", *IET Microwave Antennas Propagation*, vol. 4, no. 8, pp. 977-981, August 2010.

[93] F. Martín, F. Falcone, J. Bonache, T. Lopetegi, R. Marqués and M. Sorolla, "Miniaturized CPW stop-band filters based on multiple tuned split ring resonators", *IEEE Microwave and Wireless Component Letters*, vol. 13, no. 12, pp. 511-513, December 2003.

[94] J. García-García, F. Martín, E. Amat, F. Falcone, J. Bonache, I. Gil, T. Lopetegi, Miguel A. G. Laso, A. Marcotegui, M. Sorolla and R. Marqués, "Microwave filters with improved stop-band based on sub-wavelength resonators", *IEEE Transaction on Microwave Theory and Techniques*, vol. 53, no. 6, pp. 1997-2006, June 2005.

[95] M. Gil, J. Bonache, J. García-García, J. Martel and F. Martín, "Composite Right/Left Handed (CRLH) Metamaterial Transmission Lines Based on

Complementary Split Ring Resonators (CSRRs) and Their Applications to Very Wide Band and Compact filter Design", *IEEE Transactions on Microwave Theory and Techniques*, vol. 55, no. 6, pp. 1296-1304, June 2007.

[96]   J. Bonache, M. Gil, I. Gil, J. García-García and F. Martín, "Limitations and Solutions of Resonant-Type Metamaterial Transmission Lines for Filter Applications: the Hybrid Approach", *2006 IEEE MTT-S International Microwave Symposium Digest*, pp. 939-942, San Francisco (CA), USA, June 2006.

[97]   J. Bonache, I. Gil, J. García-García and F. Martín, "Novel microstrip bandpass filters based on complementary split-ring resonators", *IEEE Transactions on Microwave Theory and Techniques*, vol. 54, no. 1, pp. 265-271, January 2006.

[98]   O. Isik and K. P. Esselle, "Analysis of spiral metamaterials by use of group theory", *Metamaterials*, vol. 3, no. 1, pp. 1873-1988, March 2009.

[99]   J. D. Baena, R. Marqués and F. Medina, "Artificial magnetic metamaterial design by using spiral resonators", *Physical Review B*, vol. 69, pp. 014402 (1-5), 2004.

[100] R. Marqués, F. Medina and R. Rafii-El-Idrissi, "Role of bianisotropy in negative permeability and left handed metamaterials", *Physical Review B*, vol. 65, pp. 144441 (1-6), April 2002.

[101] J. Martel, R. Marqués, F. Falcone, J. D. Baena, F. Medina, F. Martín and M. Sorolla, "A new LC series element for compact band-pass filter design", *IEEE Microwave and Wireless Components Letters,* vol. 14, no. 5, pp. 210-212, May 2004.

[102] A. Vélez, F. Aznar, J. Bonache, M. C. Velázquez-Ahumada, J. Martel and F. Martín, "Open complementary split ring resonators (OCSRRs) and their Application to Wideband CPW Band-pass Filters", *IEEE Microwave and Wireless Components Letters*, vol. 19, no. 4, pp. 197-199, April 2009.

[103] J. Martel, J. Bonache, R. Marqués, F. Martín and F. Medina, "Design of Wide-Band Semi-Lumped Bandpass Filters Using Open Split Ring Resonators", *IEEE Microwave and Wireless Components Letters,* vol. 17, no. 1, pp. 28-30, January 2007.

[104] A. Vélez, F. Aznar, M. Durán-Sindreu, J. Bonache and F. Martín, "Stop-band and pass-band filters in coplanar waveguide technology implemented by means of electrically small metamaterial-inspired open resonators", *IET Microwaves, Antennas & Propagation*, vol. 4, no. 6, pp. 712-716, June 2010.

[105] M. Durán-Sindreu, F. Aznar, A. Vélez, J. Bonache and F. Martín, "New Composite Right/Left Handed Transmission Lines based on Electrically Small Open Resonators", *IEEE-MTT-S International Microwave Symposium*, Boston, USA, June 2009, pp. 45-48.

[106] M. Durán-Sindreu, A. Vélez, F. Aznar, G. Sisó, J. Bonache and F. Martín, "Application of Open Split Ring Resonators and Open Complementary Split Ring Resonators to the Synthesis of Artificial Transmission Lines and

Microwave Passive Components", *IEEE Transactions on Microwave Theory and Techniques*, vol. 57, no. 12, pp. 3395-3403, December 2009.

[107]   M. Durán-Sindreu, F. Aznar, A. Vélez, J. Bonache and F. Martin, "Analysis and applications of OSRR- and OCSRR-loaded transmission lines: A new path for the design of compact transmission line metamaterials", *Metamaterials*, vol. 4, no. 2-3, pp. 139-148, August-September 2010.

[108]   S. B. Cohn, "Dissipation loss in multiple coupled resonator filters", *Proc. IRE*, vol. 47, pp. 1342-1348, August 1959.

[109]   M. Dishal, "Design of Dissipative Band-Pass Filters Producing Desired Exact Amplitude-Frequency Characteristics", *Proceedings of the I.R.E.*, vol. 37, pp. 1050-1069, September 1949.

[110]   M. Durán-Sindreu, A. Vélez, G. Sisó, P. Vélez, J. Selga, J. Bonache and F. Martín, "Recent Advances in Metamaterial Transmission Lines Based on Split Rings", *Proceedings of the IEEE, a*ccepted (DOI: 10.1109/JPROC.2011.2114870).

[111]   M. Durán-Sindreu, P. Vélez, J. Bonache and F. Martín, "High-order coplanar waveguide (CPW) filters implemented by means of open split ring resonators (OSRRs) and open complementary split ring resonators (OCSRRs)", *Metamaterials*, accepted (DOI: 10.1016/j.metmat.2011.03.002).

[112]   Z-C. Hao and J-S. Hong, "Ultrawideband filter technologies", *IEEE Microwave Magazine*, vol. 11, no. 4, pp. 56-68, June 2010.

[113]   M. Durán-Sindreu, G. Sisó, J. Bonache and F. Martín, "Fully planar implementation of generalized composite right/left handed transmission lines for quad-band applications", *IEEE-MTT-S International Microwave Symposium*, Anaheim (CA), USA, pp. 25-28, May 2010.

[114]   M. Durán-Sindreu, G. Sisó, J. Bonache and F. Martín, "Planar Multi-Band Microwave Components Based on the Generalized Composite Right/Left Handed Transmission Line Concept", *IEEE Transactions on Microwave Theory and Techniques*, vol. 58, no. 12, pp. 3882-3891, December 2010.

[115]   M. Durán-Sindreu, G. Sisó, J. Bonache and F. Martín, "Compact CPW Dual-Band Bandpass Filters Based on Semi-lumped Elements and Metamaterial Concepts", *2010 Asia-Pacific Microwave Conference Proceedings (APMC)*, Yokohama (Japan), pp. 670-673, December 2010.

[116]   S. Lim, C. Caloz and T. Itoh, "Metamaterial-based electronically controlled transmission line structure as a novel leaky-wave antenna with tunable radiation angle and beam width", *IEEE Transactions on Microwave Theory and Techniques*, vol. 53, no. 1, pp. 161-173, January 2005.

[117]   C. Damm, M. Schüßler, M. Oertel and R. Jakoby, "Compact tunable periodically LC loaded microstrip line for phase shifting", *IEEE MTT-S International Microwave Symposium Digest*, Long Beach, California, USA, pp. 2003-2006, June 2005.

[118] C. Damm, M. Schüßler, J. Freese and R. Jakoby, "Artificial line phase shifter with separately tunable phase and line impedance", *Proceedings of the 36th European Microwave Conference*, Manchester, U.K., pp. 423-426, September 2006.

[119] I. Gil, J. García-García, J. Bonache, F. Martín, M. Sorolla and R. Marqués, "Varactor-loaded split rings resonators for tunable notch filters at microwave frequencies", *Electronic Letters*, vol. 40, pp. 1347-1348, October 2004.

[120] I. Gil, J. Bonache, J. García-García and F. Martín, "Tunable metamaterial transmission lines based on varactor-loaded split-ring resonators", *IEEE Transactions on Microwave Theory and Techniques*, vol. 54, no. 6, pp. 2665-2674, June 2006.

[121] A. Vélez, J. Bonache and F. Martín, "Varactor-Loaded Complementary Split Ring Resonators (VLCSRR) and Their Application to Tunable Metamaterial Transmission Lines", *IEEE Microwave and Wireless Components Letters*, vol.18, no. 1, pp. 28-30, January 2008.

[122] A. Vélez, J. Bonache and F. Martín, "Doubly tuned metamaterial transmission lines based on complementary split-ring resonators", *Electromagnetics*, vol. 28, pp. 523-530, 2008.

[123] I. Gil, F. Martín, X. Rottenberg and W. De Raedt, "Tunable stop-band filter at Q-band based on RF-MEMS metamaterials", *Electronics Letters*, vol. 43, pp. 1153-1154, October 2007.

[124] D. Bouyge, A. Crunteanu, A. Pothier, P. O. Martin, P. Blondy, A. Velez, J. Bonache, J. C. Orlianges and F. Martin, "Reconfigurable 4 Pole Bandstop Filter based on RF-MEMS-loaded Split Ring Resonators", *IEEE-MTT-S International Microwave Symposium*, Anaheim (CA), USA, May 2010.

[125] D. Bouyge, D. Mardivirin, J. Bonache, A. Crunteanu, A. Pothier, M. Durán-Sindreu, P. Blondy and F. Martín, "Split Ring Resonators (SRRs) Based on Micro-Electro-Mechanical Deflectable Cantilever-Type Rings: Application to Tunable Stopband Filters", *IEEE Microwaves and Wireless Components Letters*, vol. 21, no. 5, pp. 243-245, May 2011.

[126] S. Gevorgian, *"Ferroelectrics in Microwave Devices, Circuits and Systems Physics, Modeling, Fabrication and Measurements"*, Springer-Verlag, London, 2009.

[127] O. G. Vendick, E. F. Carlsson, P. K. Petrov, R. A. Chakalov, S. S. Gevorgian and Z. G. Ivanov, "HTS/ferroelectric CPW structures for voltage tuneable phase shifters", *Proceedings of the 34th European Microwave Conference*, vol. 1, pp. 196-202, September 1997.

[128] M. Gil, "Resonant-type metamaterials transmission lines and their application to microwave device design", *Ph.D. Thesis*, Universitat Autònoma de Barcelona, January 2009.

[129] M. Gil, C. Damm, A. Giere, M. Sazegar, J. Bonache, R. Jakoby and F. Martín, "Electrically tunable split-ring resonators at microwave frequencies based on barium-strontium-titanate thick films", *Electronic Letters*, vol. 45, no. 8, pp. 417-418, April 2009.

REFERENCES

[130] M. Gil, C. Damm, M. Sazegar, M. Maasch, A. Giere, M. Schubler, F. Aznar, A. Vélez, J. Bonache, R. Jakoby and F. Martín, "Tunable sub-wavelength resonators based on barium-strontium-titanate thick-film technology", *IET Microwaves, Antennas & Propagation*, vol. 5, no. 3, pp. 316-323, February 2011.

[131] P. Scheele, "Steuerbare passive Mikrowellenkomponenten auf Basis hochpermittiver ferroelektrischer Schichten", *Ph.D. Thesis*, Technische Universität Darmstadt, 2007.

[132] M. Durán-Sindreu, C. Damm, M. Sazegar, Y. Zheng, J. Bonache, R. Jakoby and F. Martín, "Electrically tunable composite right/left handed transmission-line based on open resonators and Barium-Strontium-Titanate Thick films", *IEEE-MTT-S International Microwave Symposium*, Baltimore (Maryland), USA, June 2011.

[133] O. G. Vendick, E. F. Carlsson, P. K. Petrov, R. A. Chakalov, S. S. Gevorgian and Z. G. Ivanov, "HTS/ferroelectric CPW structures for voltage tuneable phase shifters", *Proceedings of the 34th European Microwave Conference*, vol. 1, pp. 196-202, September 1997.

[134] M. Sazegar, Y. Zheng, H. Maune, X. Zhou, C. Damm and R. Jakoby, "Compact Artificial Line Phase Shifter on Ferroelectric Thick-Film Ceramics", *IEEE-MTT-S International Microwave Symposium*, Anaheim (CA), USA, pp. 860-863, May 2010.

[135] J.-S. Hong, "Reconfigurable Planar Filters", *IEEE Microwave Magazine*, vol. 10, no. 6, pp. 73-83, October 2009.

[136] P. Wong and I. Hunter, "Electronically Tunable Filters", *IEEE Microwave Magazine*, vol. 10, no. 6, pp. 46-54, October 2009.

[137] F. Giannini, M. Salerno and R. Sorrentino, "Effects of parasitics in lowpass elliptic filters for MIC", *Electronics Letters*, vol. 18, pp. 284-285, April 1982.

[138] F. Giannini, M. Salerno and R. Sorrentino, "Design of low-pass elliptic filters by means of cascaded microstrip rectangular elements", *IEEE Transaction on Microwave Theory and Techniques*, vol. 30, no. 9, pp. 1348-1353, September 1982.

[139] L. H. Hsieh and K. Chang, "Compact elliptic-function low-pass filters using microstrip stepped-impedance hairpin resonators", *IEEE Transaction on Microwave Theory and Techniques*, vol. 51, no. 1, pp. 193-199, January 2001.

[140] W. Tu and K. Chang, "Microstrip elliptic-function low-pass filters using distributed elements or slotted ground structure", *IEEE Transaction on Microwave Theory and Techniques*, vol. 54, no. 10, pp. 3786-3792, October 2006.

[141] M. C. Velazquez-Ahumada, J. Martel and F. Medina, "Design of compact low-pass elliptic filters using double-sided MIC technology", *IEEE Transaction on Microwave Theory and Techniques*, vol. 55, no. 1, pp. 121-127, January 2007.

[142]   A. Balalem, A. R. Ali, J. Machac and A. Omar, "Quasi-elliptic microstrip low-pass filters using an interdigital DGS slot", *IEEE Microwave and Wireless Component Letters*, vol. 17, no. 8, pp. 586-588, August 2007.

[143]   J. Yang and W. Wu, "Compact elliptic-function low-pass filter using defected ground structure", *IEEE Microwave and Wireless Component Letters*, vol. 18, no. 9, pp. 578-580, September 2008.

[144]   A. A. Omar, K. Hettak and N. Dib, "An elliptic coplanar waveguide low-pass filter", *Proceedings 24th Annual Review of Progress in Applied Computational Electromagnetics*, Niagara Falls (Canada), pp. 636-639, March-April, 2008.

[145]   F. Aznar, A. Vélez, M. Durán-Sindreu, J. Bonache and F. Martín, "Elliptic-function CPW low-pass filters implemented by means of open complementary split ring resonators (OCSRRs)", *IEEE Microwave and Wireless Components Letters*, vol. 19, no. 11, pp. 689-691, November 2009.

[146]   C. Li, K.-Y. Liu and F. Li, "Design of microstrip highpass filters with complementary split ring resonators", *Electronics Letters*, vol. 43, pp. 35-36, January 2007.

[147]   M. Gil, J. Bonache, J. Selga, J. García-García and F. Martín, "Broadband resonant type metamaterial transmission lines", *IEEE Microwave and Wireless Components Letters*, vol. 17, no. 2, pp. 97-99, February 2007.

[148]   J. Selga, G. Sisó, M. Gil, J. Bonache and F. Martín, "Microwave circuit miniaturization with complementary spiral resonators: application to high-pass filters and dual-band components", *Microwave and Optical Technology Letters*, vol. 51, no. 11, pp. 2741-2745, November 2009.

[149]   T. Yasuzumi, T. Uwano and O. Hashimoto, "Microstrip High-pass Filter with Attenuation Poles Using Cross-coupling", *IEEE Asia Pacific Microwave Conference (APMC'10)*, Yokohama (Japan), pp. 107-110, December 2010.

[150]   T.-N. Kuo, S.-C. Lin and C. H. Chen, "Compact Ultra-Wideband Bandpass Filters Using Composite Microstrip–Coplanar-Waveguide Structure", *IEEE Transaction on Microwave Theory and Techniques*, vol. 54, no. 10, pp. 3772-3778, October 2006.

[151]   N. Thomson and J.-S. Hong, "Compact Ultra-Wideband Microstrip/Coplanar Waveguide Bandpass Filter", *IEEE Microwave and Wireless Components Letters*, vol. 17, no. 3, pp. 184-186, March 2007.

[152]   R. Levy, "Filters with single transmission zeros at real or imaginary frequencies", *IEEE Transaction on Microwave Theory and Techniques*, vol. 24, no. 4, pp. 172-181, April 1976.

[153]   J.-S. Hong and M. J. Lancaster, "Design of highly selective microstrip bandpass filters with a single pair of attenuation poles at finite frequencies", *IEEE Transaction on Microwave Theory and Techniques*, vol. 48, no. 7, pp. 1098-1107, July 2000.

[154] U. Rosenberg and S. Amari, "Novel coupling schemes for microwave resonator filters", *IEEE Transaction on Microwave Theory and Techniques*, vol. 50, no. 12, pp. 2896-2902, December 2002.

[155] D. Cañete-Rebenaque, F. Quesada-Pereira, J. Pascual-García, A. Alvarez-Melchon and M. Guglielmi, "Two compact configurations for implementing transmission zeros in microstrip filters", *IEEE Microwave and Wireless Components Letters*, vol. 14, no. 10, pp. 475-477, October 2004.

[156] J. R. Lee, J. H. Cho and S. W. Yun, "New compact bandpass filter using microstrip λ/4 resonators with open stub inverter", *IEEE Microwave and Guided Wave Letters*, vol. 10, no. 12, pp. 526-527, December 2000.

[157] L.H. Hsieh and K. Chang, "Tunable microstrip bandpass filter with two transmission zeros", *IEEE Transaction on Microwave Theory and Techniques*, vol. 51, no. 2, pp. 520-525, February 2003.

[158] S. Amari, G. Tadeson, J. Cihlar and U. Rosenberg, "New parallel λ/2 microstrip line filters with transmission zeros at finite frequencies", *2003 IEEE MTT-S International Microwave Symposium Digest*, pp. 543-546, Philadelphia (Pennsylvania), USA, June 2003.

[159] L. Zhu and W. Menzel, "Compact microstrip bandpass filter with two transmission zeros using a stub-tapped half-wavelenght line resonator", *IEEE Microwave and Wireless Components Letters*, vol. 13, no. 1, pp. 16-18, January 2003.

[160] W. Schwab, F. Boegelsack and W. Menzel, "Multilayer suspended stripline and coplanar line filters", *IEEE Transactions on Microwave Theory and Techniques*, vol. 42, no. 7, pp. 1403-1407, July 1994.

[161] A. Balalem, I. Hamad, J. Machac and A. Omar, "Bandpass filters on a modified multilayer coplanar line", *2006 IEEE MTT-S International Microwave Symposium Digest*, San Francisco, USA, pp 531-534, June, 2006.

[162] M. Miyazaki, H. Asao and O. Ishida, "A Broadband Dielectric Diplexer using a snaked Strip-Line", *1991 IEEE International Microwave Symposium Digest*, vol. 2, pp. 551-554, Boston, Massachusetts, USA, July 1991.

[163] M. Durán-Sindreu, J. Bonache and F. Martín, "Compact Elliptic-Function Coplanar Waveguide Low-Pass Filters Using Backside Metallic Patterns", *IEEE Microwave and Wireless Components Letters*, vol. 20, no. 11, pp. 601-603, November 2010.

[164] J-T. Kuo and E. Shih, "Microstrip stepped impedance resonator bandpass filter with an extended optimal rejection bandwidth", *IEEE Transaction on Microwave Theory and Techniques*, vol. 51, no. 5, pp. 1554-1559, May 2003.

[165] A. Stark, C. Friesicke, J. Muller and A. F. Jacob, "A Packaged Ultrawideband Filter with High Stopband Rejection [Application Notes]", *IEEE Microwave Magazine*, vol. 11, pp. 110-117, August 2010.

Appendix A

Parameter extraction method

The parameters of the circuit model of a CPW line loaded with series OSRR such as the one shown in Figure 3.5(b) can be extracted from the electromagnetic simulation of the structure following a straightforward procedure. From the intercept of the return losses with the unit conductance circle in the Smith chart, we can directly infer the value of the shunt capacitance according to

$$Y_{in}|_{Z_s=0} = Y_o + j\omega 2C \tag{A.1}$$

$$B = 2C\omega|_{Z_s=0} \tag{A.2}$$

$$C = \frac{B}{2\omega|_{Z_s=0}} \tag{A.3}$$

where B is the susceptance in the intercept point. The frequency at this intercept point is the resonance frequency of the series branch

$$\omega^2\big|_{Z_s=0} = \frac{1}{C_s L'_s} \tag{A.4}$$

To determine the two element values of this branch, another condition is needed. This condition comes from the fact that at the reflection zero frequency ω_z (maximum transmission) the Bloch impedance of the structure is Z_0. Thus, by forcing the π-circuit model Bloch impedance of equation (2.21) to Z_0, the second condition results. By inverting equations (A.4) and (2.21), we can determine the element values of the series branch, leading to the following conditions

$$C_s = \left[\frac{\omega_z^2}{\omega^2\big|_{Z_s=0}} - 1\right]\left\{\frac{1}{2Z_0^2\omega_z^2 C} + \frac{C}{2}\right\} \tag{A.5}$$

$$L'_s = \frac{1}{\omega^2\big|_{Z_s=0} C_s} \tag{A.6}$$

The parameters of the circuit model of a CPW line loaded with shunt OCSRRs such as the one shown in Figure 3.7(c) can be extracted following a similar procedure. In this case, the intercept of the return losses with the unit resistance circle in the Smith chart gives the value of the series inductance

$$L = \frac{\chi}{2\omega\big|_{Z_p\to\infty}} \tag{A.7}$$

where χ is the reactance at the intercept point. The shunt branch resonates at this frequency, that is

$$\omega^2\big|_{Z_p\to\infty} = \frac{1}{L'_p C'_p} \tag{A.8}$$

Then, at the reflection zero frequency (ω_z), the characteristic impedance, given by (2.20) must be forced to be Z_0. From these two latter conditions, we finally obtain

$$L'_p = \left[\frac{\omega_z^2}{\omega^2\big|_{Z_p\to\infty}} - 1\right]\left\{\frac{Z_0^2}{2\omega_z^2 C} + \frac{L}{2}\right\} \tag{A.9}$$

$$C'_p = \frac{1}{\omega^2\big|_{Z_p\to\infty} L'_p} \tag{A.10}$$

and the values are univocally determined.

Finally, the parameters of the wideband circuit model of a CPW line loaded with OCSRRs such as the one shown in Figure 3.9(a) can be extracted by applying the same above conditions (but considering the different shunt impedance). Hence, equation (A.7) still applies. In addition, since there is an extra parameter, another condition is required, considering in this case the point at which the electrical length βl is 90°. At such frequency, considering equation (2.16), the following impedance relation results

$$Z_s(\omega)\big|_{\beta l = 90°} = -Z_p(\omega)\big|_{\beta l = 90°} \tag{A.11}$$

Therefore, adding this condition to the system, the following parameters are obtained

$$L'_p = \frac{\left(\omega^2\big|_{Z_p \to \infty} - \omega^2\big|_{\beta l = 90°}\right)\left(\omega_z{}^2 - \omega^2\big|_{Z_p \to \infty}\right)\left(\omega_z{}^2 L^2 - Z_0{}^2\right)}{2L\omega^2\big|_{Z_p \to \infty}\omega_z{}^2\left(\omega_z{}^2 - \omega^2\big|_{\beta l = 90°}\right)} \tag{A.12}$$

$$C'_p = \frac{1}{\omega^2\big|_{Z_p \to \infty}L'_p} \tag{A.13}$$

$$L_{sh} = \frac{\dfrac{L\omega^2\big|_{\beta l = 90°}}{\omega^2\big|_{Z_p \to \infty}} - L'_p - L}{1 - \dfrac{\omega^2\big|_{\beta l = 90°}}{\omega^2\big|_{Z_p \to \infty}}} \tag{A.14}$$

being thus all the values univocally determined again.

Appendix B

Abbreviations and acronyms

ASM	Aggressive space mapping
ASR	Archimedean spiral resonator
BST	Barium-strontium-titanate
CPW	Coplanar waveguide
CSR	Complementary spiral resonator
CSRR	Complementary split ring resonator
CRLH	Composite right-/left-handed
DBR	Dual-behavior resonators
DC	Direct current
D-CRLH	Dual- composite right-/left-handed
EBG	Electromagnetic band gap
E-CRLH	Extended-composite right-/left-handed
EM	Electromagnetic
FoM	Figure of merit
GSM	Global system for mobile

GPS	Global positioning system
HLW	Homogeneity and long wavelength
IL	Insertion losses
LCP	Liquid crystal polymer
LH	Left-handed
LTTC	Low-temperature co-fired ceramic
MEMS	Micro-electro-mechanical systems
MIC	Microwave integrated circuits
MMIC	Monolithic microwave integrated circuits
NB-SRR	Non-bianisotropic split ring resonator
OCSRR	Open complementary split ring resonator
OSRR	Open split ring resonator
RF	Radio frequency
RH	Right-handed
RL	Return losses
SMT	Surface mount technology
SIR	Stepped-impedance-resonator
SIW	Surface integrated waveguide
SR	Spiral resonator
SRR	Split ring resonator
VLSRR	Varactor-loaded split ring resonator
VLCSRR	Varactor-loaded complementary split ring resonator

Author list of publications

International Journals

1. F. Aznar, A. Vélez, M. Durán-Sindreu, J. Bonache and F. Martín, "Elliptic-Function CPW Low-Pass Filters Implemented by Means of Open Complementary Split Ring Resonators (OCSRRs)", *IEEE Microwave and Wireless Components Letters*, vol. 19, no. 11, pp. 689-691, November 2009.

2. M. Durán-Sindreu, A. Vélez, F. Aznar, G. Sisó, J. Bonache and F. Martín, "Application of Open Split Ring Resonators and Open Complementary Split Ring Resonators to the Synthesis of Artificial Transmission Lines and Microwave Passive Components", *IEEE Transactions on Microwave Theory and Techniques*, vol. 57, no. 12, pp. 3395-3403, December 2009.

3. A. Vélez, F. Aznar, M. Durán-Sindreu, J. Bonache and F. Martín, "Stop-Band and Band-Pass Filters in Coplanar Waveguide Technology Implemented by Means of Electrically Small Metamaterial-Inspired Open Resonators", *IET Microwaves, Antennas and Propagation*, vol. 4, no. 6, pp. 712-716, June 2010.

4. F. Aznar, A. Vélez, M. Durán-Sindreu, J. Bonache and F. Martín, "Open complementary split ring resonators: Physics, modelling, and analysis", *Microwave and Optical Technology Letters*, vol. 52, no. 7, pp. 1520-1526, July 2010.

5. M. Durán-Sindreu, F. Aznar, A. Vélez, J. Bonache and F. Martin, "Analysis and Applications of OSRR- and OCSRR-Loaded Transmission Lines: a New Path for the Design of Compact Transmission Line Metamaterials", *Metamaterials*, vol. 4, no. 2-3, pp. 139-148, August-September 2010.

6. M. Durán-Sindreu, J. Bonache and F. Martín, "Compact Elliptic-Function Coplanar Waveguide Low-Pass Filters Using Backside Metallic Patterns", *IEEE Microwave and Wireless Components Letters*, vol. 20, no. 11, pp. 601-603, November 2010.

7. M. Durán-Sindreu, G. Sisó, J. Bonache and F. Martín, "Planar Multi-Band Microwave Components Based on the Generalized Composite Right/Left Handed Transmission Line Concept", *IEEE Transactions on Microwave Theory and Techniques*, vol. 58, no. 12, pp. 3882-3891, December 2010.

8. A. Vélez, G. Sisó, A. Campo, M. Durán-Sindreu, J. Bonache and F. Martín, "Dual-band microwave duplexer based on spiral resonators (SR) and complementary split ring resonators (CSRR)", *Applied Physics A: Materials Science & Processing*, vol. 103, no 3, pp. 911-914, January 2011.

9. A. Vélez, F.Aznar, M. Durán-Sindreu, J. Bonache and F. Martín, "Tunable Coplanar Waveguide Band-stop and Band-pass Filters based on Open Split Ring Resonators and Open Complementary Split Ring Resonators", *IET Microwaves, Antennas and Propagation*, vol. 5, no. 3, pp. 277-281, February 2011.

10. D. Bouyge, D. Mardivirin, J. Bonache, A. Crunteanu, A. Pothier, M. Durán-Sindreu, P. Blondy and F. Martín, "Split Ring Resonators (SRRs) Based on Micro-Electro-Mechanical Deflectable Cantilever-Type Rings: Application to Tunable Stopband Filters", *IEEE Microwave and Wireless Components Letters*, vol. 21, no. 5, pp. 243-245, May 2011.

11. M. Durán-Sindreu, P. Vélez, J. Bonache and F. Martin, "High-order coplanar waveguide (CPW) filters implemented by means of open split ring resonators (OSRRs) and open complementary split ring resonators (OCSRRs)", *Metamaterials*, accepted (DOI: 10.1016/ j.metmat.2011.03.002).

12. M. Durán-Sindreu, A. Vélez, G. Sisó, P. Vélez, J. Selga, J. Bonache and F. Martín, "Recent Advances in Metamaterial Transmission Lines Based on Split Rings", *Proceedings of the IEEE*, accepted (DOI: 10.1109/JPROC.2011.2114870).

13. J. Naqui, M. Durán-Sindreu, J. Bonache and F. Martín, "Implementation of shunt connected series resonators through stepped-impedance shunt stubs: analysis and limitations", IET Microwaves Antennas and Propagation, accepted.

14. M. Durán-Sindreu, J. Bonache and F. Martín, "Elliptic High-Pass Filters with Stepped Impedance Resonators (SIR) in Coplanar Waveguide Technology", *Microwave and Optical Technology Letters*, submitted.

15. M. Durán-Sindreu, J. Bonache and F. Martín, "Compact Wideband CPW Bandpass Filters with Transmission Zeros Based on Stepped Impedance Resonators (SIR)", *IEEE Microwave and Wireless Components Letters*, submitted.

National and International Conferences

1. M. Durán-Sindreu, F. Aznar, A. Vélez, J. Bonache and F. Martín, "Artificial transmission lines exhibiting left handed and right handed wave propagation and implemented by means of open split ring resonators (OSRRs) and open complementary split ring resonators (OCSRRs)", *Days on diffraction '09*, Saint Petersburg (Russia), May 2009.

2. F. Aznar, A. Vélez, M. Gil, M. Durán-Sindreu, J. Bonache and F. Martín, "Recent progress on modelling and conceptions of resonant type metamaterial transmission lines", *Days on diffraction '09*, Saint Petersburg (Russia), May 2009. **Invited.**

3. J. Bonache, A. Vélez, F. Aznar, M. Durán-Sindreu and F. Martín, "Electrically small metamaterial-inspired open resonators: theory and applications", *IEEE International Symposium on Antennas & Propagation and USNC/URSI National Radio Science Meeting (APS-URSI)*, Charleston, SC (USA), June 2009.

4. M. Durán-Sindreu, F. Aznar, A. Vélez, J. Bonache and F. Martín, "New Composite, Right/Left Handed Transmission Lines based on Electrically Small, Open Resonators", *IEEE MTT-S International Microwave Symposium*, Boston (USA), pp. 45-48, June 2009.

5. M. Durán-Sindreu, F. Aznar, A. Vélez, J. Bonache and F. Martín, "Modeling Open Split Ring Resonator (OSRRs) and Open Complementary Split Ring Resonator (OCSRRs) in coplanar waveguide technology", *Young Scientist Meeting on Metamaterials (YSMM)*, Leganés (Spain), July 2009.

6. A. Vélez, F. Aznar, M. Durán-Sindreu, J. Bonache and F. Martín, "Open complementary split ring resonators (OCSRRs): the missing particle", *International Congress on Advanced Electromagnetic Materials in Microwaves and Optics (Metamaterials 2009)*, London (UK), August - September 2009. **Invited.**

7. A. Vélez, F. Aznar, M. Durán-Sindreu, J. Bonache and F. Martín, "Resonadores abiertos y sus aplicaciones en síntesis de filtros de microondas en guía de ondas

coplanar", *XIV Simposium Nacional de la Unión Científica de Radio (URSI)*, Santander (Spain), September 2009.

8. M. Durán-Sindreu, F. Aznar, A. Vélez, J. Bonache and F. Martín, "OSRR and OCSRR-based metamaterial transmission lines", *XIV Simposium Nacional de la Unión Científica de Radio (URSI)*, Santander (Spain), September 2009.

9. A. Vélez, F. Aznar, M. Durán-Sindreu, J. Bonache and F. Martín, "Coplanar Waveguide Stop-Band Filters Implemented by means of Open split ring resonators (OSRRs)", *IEEE Asia Pacific Microwave Conference (APMC'09)*, Singapur, pp. 886-889, December 2009.

10. M. Durán-Sindreu, F. Aznar, A. Vélez, J. Bonache and F. Martín, "Open complementary split ring resonators (OCSRRs): modeling and applications", *12th International Symposium on Microwave and Optical Technology*, New Delhi (India), December 2009. **Invited.**

11. M. Durán-Sindreu, A. Vélez, J. Bonache and F. Martín, "Broadband filters based on OSRR and OCSRR balanced composite right/left handed transmission lines", *2nd International Conference on Metamaterials, Photonic crystals and Plasmonics (META'10)*, February 2010. **Invited.**

12. A. Vélez, G. Sisó, M. Durán-Sindreu, J. Bonache and F. Martín, "Dual-band microwave duplexer based on metamaterial concepts", *2nd International Conference on Metamaterials, Photonic crystals and Plasmonics (META'10)*, February 2010. **Invited.**

13. M. Durán-Sindreu, G. Sisó, J. Bonache and F. Martín, "Fully Planar Implementation of Generalized Composite Right/Left Handed Transmission Lines for Quad-band Applications", *IEEE MTT-S International Microwave Symposium*, Anaheim (EUA), pp. 25-28, May 2010.

14. M. Durán-Sindreu, P. Vélez, J. Bonache and F. Martín, "Broadband Microwave Filters Based on Metamaterial Concepts", *20th International Conference on Applied Electromagnetics and Communications (ICECom 2010)*, Dubrovnik (Croatia), September 2010. **Invited.**

15. M. Durán-Sindreu, G. Sisó, J. Bonache and F. Martín, "Multiband components based on metamaterial concepts", *Fourth International Congress On Advanced Electromagnetic Materials In Microwaves And Optics (Metamaterials 2010)*, Karlsruhe (Germany), September 2010. **Invited.**

16. M Durán-Sindreu, J. Bonache and F. Martín, "Compact CPW Dual-Band Bandpass Filters Based on Semi-lumped Elements and Metamaterial Concepts", *Asia Pacific Microwave Conference (APMC'10)*, Yokohama (Japan), pp. 670-673, December 2010.

17. M. Durán-Sindreu, J. Bonache, P. Vélez and F. Martín, "Recent advances on the applications of artificial transmission lines based on split rings", *Workshop on Metamaterials, 4rth Young Scientist Meeting on Metamaterials (YSMM 2011)*, Valencia, Spain, February 2011.

18. J. Naqui, M. Durán-Sindreu, J. Bonache and F. Martín, "Stepped Impedance Shunt Stubs (SISS): Analysis and Potential Applications in Planar Metamaterials", *4rth Young Scientist Meeting on Metamaterials (YSMM 2011)*, Valencia, Spain, February 2011.

19. M. Durán-Sindreu, C. Damm, M. Sazegar, Y. Zheng, J. Bonache, R. Jakoby and F. Martín, "Electrically tunable composite right/left handed transmission-line based on open resonators and Barium-Strontium-Titanate Thick films", *IEEE-MTT-S International Microwave Symposium*, Baltimore (Maryland), USA, June 2011.

20. J. Naqui, A. Fernández-Prieto, M. Durán-Sindreu, J. Selga, F. Medina, F. Mesa and F. Martín, "Split Rings-Based Differential Transmission Lines with Common-Mode Suppression", *IEEE-MTT-S International Microwave Symposium*, Baltimore (Maryland), USA, June 2011.